Arterial Spin Labelling Magnetic Resonance Imaging of the Brain: Techniques and Development

Ph.D Thesis

Jack Anthony Wells[1,2]

[1]The Advanced Magnetic Resonance Imaging Group
Department of Medical Physics and Bioengineering

[2] Radiology and Physics Unit
UCL Institute of Child Health

University College London

Supervisors

Dr. David Thomas[1,2]

Prof. Roger Ordidge[1]

"Perhaps no other organ of the body is less adapted to an experimental study of its circulation other than the brain" - Carl Wiggers, the "American father of pulmonary circulatory physiology", 1905.

Declaration

I, Jack Anthony Wells, confirm that the work presented in this thesis is my own work except where acknowledged in the text. This work is based on research that was undertaken by myself at University College London during the period 26th September 2005 to 10th August 2008.

Signed.....

Publications

Characterising the Origin of the Arterial Spin Labelling Signal in MRI using a Multi-Echo Acquisition Approach. J A Wells, M F Lythgoe, M Choy, D G Gadian, R J Ordidge, D L Thomas. (2009). Journal for Cerebral Blood Flow and Metabolism. In Press. doi:10.1038/jcbfm.2009.99.

Reduction of Errors in ASL Cerebral Perfusion and Arterial Transit Time Maps using Image De-noising. J A Wells, D L Thomas, M D King, A Connelly, M F Lythgoe, F Calamante. Magnetic Resonance in Medicine. In Press.

In-vivo Hadamard Encoded Continuous Arterial Spin Labelling (H-CASL). J A Wells, M F Lythgoe, D G Gadian, R J Ordidge, D L Thomas. Magnetic Resonance in Medicine. In Press.

Acknowledgements

I would like to thank David Thomas for his enduring expertise and patience. His intellectual contribution to the projects described in this thesis cannot be understated. Though busy with numerous other studies, Dr. Thomas always found time for guidance and discussion. I have taken up a huge amount of his time and have been very fortunate to have him as my Ph.D supervisor. My thanks extend to Roger Ordidge who first taught me the principles of MRI and was always available for advice and discussion throughout my studies.

Many thanks go to Mark Lythgoe for his enthusiasm and encouragement and particularly for helping me to minimise systematic errors in the experimental acquisitions, which was key to the success of the projects. I would also like to thank Mankin Choy for teaching me how to use the 2.35T scanner. Despite interrupting him on many occasions to ask questions, he was always kind and helpful.

I am especially thankful to Martin King who has helped me continually over the course of this work. Dr. King has provided several moments of inspiration which really helped push the projects forward. I consider myself very lucky to have taken up so much of his time and hope to be able to work together on future projects!

I am grateful for the help and support of the many people who I have had the pleasure to work with, in particular (and in no particular order!) Ken Cheung, Rachael Dobson, Panos Kyrtatos, Jon Cleary, Sally Dowsett, John Thornton, Aaron Oliver-Taylor, David Carmichael, Enrico De-Vita, Sati Sohota, Johannes Riegler, Robert Turner and Harry Parkes.

I am also grateful to David Gadian and Fernando Calamante who both offered key guidance and advice over the course of this work. I would also like to thank Ted Proctor who sadly passed away last year. His stories always cheered me up when my experiments we not working as well as I had anticipated!

I would like to thank the Wellcome trust for funding my Ph.D and supporting this research. Finally, I would like to thank my parents, to whom this thesis is dedicated.

Contents Page

ABBREVIATIONS

AD	Anisotropic Diffusion
ADC	Apparent Diffusion Coefficient
ASL	Arterial Spin Labelling
BOLD	Blood Oxygen Level Dependence
CASL	Continuous Arterial Spin Labelling
CBF	Cerebral Blood Flow
DWI	Diffusion Weighted Imaging
EC	Extra-Cellular
EF	Extraction Fraction
EPISTAR	Echo Planar Imaging with Alternating Radio Frequency Pulses
FAIR	Flow Sensitive Alternating Inversion Recovery
FID	Free Induction Decay
fMRI	Functional Magnetic Resonance Imaging
FOV	Field of View
IC	Intra-Cellular
IV	Intra-Vascular
MAD	Median Absolute Deviation
MCA	Middle Cerebral Artery
MR	Magnetic Resonance
MRI	Magnetic Resonance Imaging
MT	Magnetisation Transfer
PASL	Pulsed Arterial Spin Labelling
PET	Positron Emission Tomography
PLD	Post Labelling Delay
POCS	Projection onto Convex Sets
RF	Radio Frequency
ROI	Region of Interest
SAR	Specific Absorption Rate
SEM	Standard Error on the Mean
SNR	Signal to Noise Ratio
SNR_{PWI}	Signal to Noise Ratio of the Perfusion Weighted Images
TE	Echo Time
TI	Inversion Time
TR	Repetition Time
VCGs	Vascular Crusher Gradients

LIST OF FIGURES

ABSTRACT

This thesis centres on the development of arterial spin labelling (ASL) MRI, a non-invasive technique to image cerebral perfusion. In the first chapter I explain the principles of cerebral blood flow (CBF) quantification using ASL beginning with the original implementation through to the most recent advances. I proceed to describe the established theory behind the key additional MRI contrast mechanisms and techniques that underpin the novel experiments described in this thesis (T2 and T1 relaxation, diffusion imaging and half-Fourier acquisition and reconstruction).

In Chapter 2 I describe work undertaken to sample the transverse relaxation of the ASL perfusion-weighted and control images acquired with and without vascular crusher gradients at a range of post-labelling delay times and tagging durations, to estimate the intra-vascular, intra-cellular and extra-cellular distribution of labelled water in the rat cortex. The results provide evidence for rapid exchange of labelled water into the intra-cellular space relative to the transit-time through the vascular bed, and provide a more solid foundation for CBF quantification using ASL techniques.

In Chapter 3 the performance of image de-noising techniques for reducing errors in ASL CBF and arterial transit time estimates is investigated. I show that noise reduction methods can suppress random and systematic errors, improving both the precision and accuracy of CBF measurements and the precision of transit time maps.

In Chapter 4 I present the first *in-vivo* demonstration of Hadamard-encoded continuous ASL (H-CASL); an efficient method of imaging small volumes of labelled blood water in the brain at multiple post labelling delay times. I present evidence that H-CASL is viable for *in-vivo* application and can improve the precision of δa estimation in 2/3 of the imaging time required for standard multi post labelling delay continuous ASL.

CHAPTER 1: INTRODUCTION TO ARTERIAL SPIN LABELLING, DIFFUSION IMAGING AND RELAXATION IN MRI

1.1 INTRODUCTION AND AIMS

Over the last 17 years magnetic resonance imaging (MRI) scientists have conceived and developed a quantitative cerebral perfusion measurement technique that harnesses blood water as an endogenous contrast agent and thus, uniquely, is totally non-invasive. This approach is known as Arterial Spin Labelling (ASL) MRI [Detre *et al.*, 1992]. Perfusion is the rate of delivery of blood to the capillary bed. This nutritive supply is essential to maintain healthy tissue and is an important indicator of viability and function; accurate measurement is of great utility in the study and diagnosis of acute and chronic brain disorder.

In comparison to more established radionucleotide methods such as positron emission tomography (PET), ASL has been shown to have improved spatial and temporal resolution and is non-ionising [Petersen *et al*, 2006]. Furthermore ASL offers an alternative to Dynamic Susceptibility Contrast (DSC) MRI in times of repeated warning by the US Food and Drug Association (FDA) regarding the usage of gadolinium based contrast agents in patients with kidney failures [Golay *et al*., 2007].

However, ASL suffers from intrinsically low SNR and can struggle to produce robust, reliable estimates of perfusion given the complexity of cerebral anatomy and the multifaceted nature of neuropathology. The aim of my thesis is to investigate and help solve some of the issues that have been holding back ASL's progression into a MRI modality that is more widely used for the diagnosis and research of brain disorders.

1.2 ORGANISATION OF PH.D THESIS

This Ph.D thesis is comprised of five chapters. Chapter 1 begins with a detailed summary of Detre and Williams seminal work where the principles of ASL were first proposed [Detre *et al.*, 1992]. It continues to explain the key developments leading to the present state of the field and the main challenges that remain in robust and accurate perfusion quantification using ASL. It concludes with an overview of the theory underlying the key additional MRI methods used in my investigations (diffusion weighted imaging, transverse and longitudinal relaxation and half-Fourier acquisition and reconstruction) and a description of the MRI equipment used in this study.

Chapter 2 reports experiments designed to characterise the origin of the ASL signal in the brain using a multi-echo acquisition approach.

In Chapter 3, I demonstrate that the precision and accuracy of quantitative ASL cerebral perfusion maps can be significantly improved using post-acquisition image de-noising methods.

Chapter 4 describes the first successful *in-vivo* implementation of Hadamard encoded continuous ASL (H-CASL), a novel approach to cerebral perfusion and transit time quantification.

This thesis concludes with Chapter 5: a final discussion of the experimental results described in the previous chapters.

1.3 THE BASIC PRINCIPLES OF ASL

1.3.1 Introduction

Arterial Spin Labelling was first proposed by Detre *et al.* and in 1992 they reported the first results using this new approach to measure cerebral perfusion [Detre *et al.*, 1992]. I will now summarise this work (the basic principles of ASL) before proceeding to describe the notable developments leading to the current state of the field and the main challenges that remain in efficient and robust non-invasive cerebral blood flow (CBF[1]) quantification.

1.3.2 "Perfusion Imaging". The First ASL Experiment

1.3.2.1 METHODS

The first ASL experiments were performed using a spin echo sequence to acquire single slice coronal images of the rat brain [Detre *et al.*, 1992]. Saturation pulses were continuously applied to a plane in the neck during the 2 second relaxation period (TR). This served to magnetically "label" blood water as it flowed through the feeding arteries that supply the brain. If perfect saturation is achieved, the longitudinal magnetisation of the labelled blood is zero immediately after labelling (see 1.9 *T1: The Longitudinal Relaxation Constant*).

Upon image acquisition the measured signal intensity within a given pixel was attenuated according to the number of labelled spins that have travelled to that pixel within the observation slice (ignoring all longitudinal relaxation of the tagged blood water following saturation) since the labelled blood water acts to reduce the net longitudinal magnetisation before initial excitation prior to image readout. This CBF-weighted acquisition is known as the "labelled" image.

[1] The term "Cerebral blood flow" is often used as a replacement for perfusion, particularly by physiologists and clinicians. For those not familiar with the field, the concept of CBF is more recognisable and easier to grasp, though it should not be confused with the flow velocity (in m/s). As is common in the ASL literature, the terms CBF and perfusion are used interchangeably in this thesis.

The continuous saturation pulses induced magnetization transfer (MT) effects within the imaging plane (see below). The labelled image was hence CBF and MT weighted. To differentiate the two effects and extract the CBF related signal, it was necessary to acquire an image with identical MT effects but with no perfusion weighting. This is known as the control acquisition. Hence the saturation pulse was applied outside the head so that the imaging slice was equidistant between the tagging and control planes. Assuming the saturation planes (symmetrical about the imaging plane) induce identical MT effects in the observation slice, a simple subtraction of the labelled and control acquisitions yields a perfusion-weighted (ΔM) image. Although this approach to MT cancellation was shown to be effective, it did not permit multi-slice acquisitions.

1.3.2.1.1 Magnetisation Transfer (MT)

Magnetisation transfer is an ever-present consideration in ASL. With naive application, MT can significantly influence the measured ΔM signal and confound CBF quantification. Mobile protons have sufficiently long T2 relaxation times to ensure that the transverse signal has not completely decayed in the time between excitation and acquisition (TE), where spatial encoding takes place (see 1.8 *T2: Transverse Relaxation*). Protons associated with macromolecules and membranes posses a very short T2 (less than 1ms) and therefore do not directly contribute to the measured signal at typical echo times. However exchange of magnetisation between the mobile and macromolecular protons will influence the spin state of the mobile or liquid protons, affecting the measured signal. In the majority of ASL experiments an off-resonance labelling/control pulse is applied that preferentially saturates macromolecular spins due to their broad absorption line-shapes. Therefore the off-resonance labelling/control pulse will indirectly affect the magnetisation of the mobile protons which can significantly reduce the measured signal. Consequently MT is an important factor in ASL; due care must be taken to avoid errors in CBF quantification from a MT mismatch between the labelled and control acquisitions.

1.3.2.2 CBF Quantification

Detre *et al.*, reasoned that the perfusion weighted, subtracted, images could be converted into quantitative cerebral perfusion maps with the additional measurement of certain parameters combined with sensible assumptions regarding the state of the

cerebral anatomy [Detre *et al.*, 1992]. They built these measurements and assertions into an ASL CBF quantification model based on the Bloch equations.

Blood flow was quantified by first modifying the Bloch equation to include flow effects:

$$\frac{dM_b}{dt} = \frac{M_b^o - M_b}{T_1} + fM_a - \frac{f}{\lambda}M_b \qquad [1.1]$$

where f = blood flow in ml g^{-1} s^{-1} ; λ = blood:brain partition coefficient, defined as (quantity of tracer/gm brain)/(quantity of tracer/ml blood); T_1 = relaxation time of brain water in the absence of flow or exchange between blood and brain water; M_b = Z magnetization of brain water in arbitrary intensity units/g brain; M_b^o = fully relaxed value of M_b; M_a = Z magnetization of blood water in arbitrary intensity units/ml blood.

In order to estimate quantitative CBF, Detre makes several important assumptions, i) the labelled spins instantaneously exchange with the tissue; ii) the number of protons leaving the brain through the veins, fM_v, is equal to the amount f M_b/ λ. It is then assumed that iii) directly after the labelling pulse (t = 0), there is efficient saturation (i.e. the labelled blood has no longitudinal magnetisation, M_a = 0) and that iv) negligible MT effects are introduced in the imaging volume by the labelling pulse (not the case in practice in their *in-vivo* data). Given these assumptions, equation [1.1] can be solved to give:

$$M_b(t) = \frac{M_b^0}{1 + \frac{fT_1}{\lambda}}\left\{1 + \frac{fT_1}{\lambda}\exp(-t(\frac{1}{T_1} + \frac{f}{\lambda}))\right\} \qquad [1.2]$$

Thus M_b will be a function of the blood flow and the T_1 of the brain water. Following saturation, the brain magnetisation decreases with an apparent time constant given by:

$$\frac{1}{T_{1app}} = \frac{1}{T_1} + \frac{f}{\lambda} \qquad [1.3]$$

Detre then makes another key assumption v) the tissue is in a steady state such that the increase in perfusion weighted signal due to the arrival of labelled blood water to the tissue is balanced by T1 decay and the removal through the veins. In this case, M_b tends to M_b^{ss} which can be calculated by setting $t = \infty$ in equation 1.2:

$$\frac{M_b^{ss}}{M_b^0} = \frac{1}{1 + \frac{fT_1}{\lambda}} \qquad [1.4]$$

Equations [1.3] and [1.4] can then be rearranged to show that blood flow can be calculated by measuring M_b^{ss}, M_b^o and T_{1app}:

$$f = \frac{\lambda}{T_{1app}}\left(1 - \frac{M_b^{ss}}{M_b^0}\right) \qquad [1.5]$$

To measure the apparent relaxation constant the repetition time ($T1_{app}$) was varied from 0.5 to 4s. The control magnetisation as a function of TR was then fitted to a simple T1 recovery model (see section 1.9 *T1: The Longitudinal Relaxation Time*). The paper continues to describe the results of the first experiments using these methods to measure blood flow in the rat brain.

1.3.2.3 RESULTS

The mean signal intensity in the subtracted images was reduced by an average of 3.1% of the control signal. This signal change would be expected given a cerebral perfusion of 100ml min^{-1} $100g^{-1}$, a T_1 of rat brain at 4.7 T of 1.7s and a blood:brain partition coefficient of 0.9 ml/g.

In the dead rat the subtracted, perfusion-weighted, image was uniform with a mean intensity difference of 1%. Theoretically, with no flow, the difference image should be made up of noise with a mean value of zero. Such imperfect subtractions point to issues within the imaging protocol which are detrimental to the accuracy of ASL measurements. The finding was attributed to spectrometer instability.

The authors acknowledge that a significant proportion of the labelled spins may reside in the macro-vasculature during image acquisition. These spins, which have not exchanged into the tissue, can cause an overestimation in the estimated CBF since they may flow through the tissue of interest. Therefore to suppress the contribution from arterial spins, spoiler gradients were used in the imaging sequence around the 180^{o} pulse in both labelled and control acquisitions.

The theory presented assumes that there is no longitudinal relaxation of the tagged spins en route to the cerebral tissue and that relaxation occurs once the labelled protons exchange with tissue water. This may result in an underestimation in the measured blood flow. However (according to [Detre *et al.*, 1992]) the proximity of the tagging plane to the observation slice means the saturated water takes a maximum of 425ms to exchange with the tissue water (although there is no reference to support this remark). Indeed, the authors claim most of the saturated blood water will have exchanged in a significantly shorter time. Hence, they argue, this assumption results in only a small underestimation of flow.

The average CBF over the whole brain was calculated to be 106 ml $100g^{-1}$ min^{-1}, in agreement with values previously reported in the literature. In hindsight it is likely that a) dismissing the T_1 decay of the endogenous tracer in transit and b) imperfect suppression of labelled arterial spins served to counteract one another to produce apparently accurate CBF measurements. Further validation of the technique was achieved by the measurement of significantly increased flow during hypercapnia.

1.3.2.4 EVALUATION

In the closing remarks, Detre describes sensible proposals within the imaging protocol to improve the efficiency of this new technique. In this initial work, the labelling pulse acts to saturate rather then invert the arterial blood. The author concedes an inversion would clearly act to increase the SNR of the measurements. Detre also points to interleaved, rapid imaging methods such as echo planar imaging and surface coil detection. His sensible conclusions have been implemented in many subsequent ASL imaging studies. Indeed, all the ASL experiments conducted for this thesis have adopted these adaptations.

Soon after the introduction of this technique, ASL divided into two main categories; Continuous and Pulsed ASL.

1.3.3 Continuous Arterial Spin Labelling (CASL): Principles

A few months later, the same group [Williams *et al.,* 1992] used adiabatic fast passage to invert, rather than saturate, the arterial blood water by a process known as flow induced adiabatic inversion (see below), with improved results. In this work the term continuous ASL was defined (CASL) due to the relatively long duration of the labelling pulse (2s) (see *Figure 1.1*). The CASL method was further validated during cold injuries [Williams *et al.,* 1992] and amphetamine stimulation in rats [Silva *et al.,* 1995].

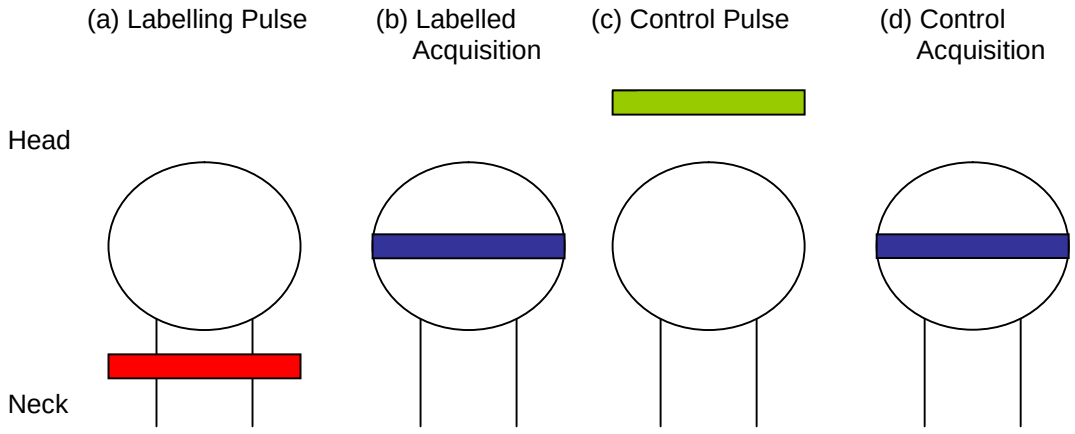

Figure 1.1
A schematic representation of CASL. In the tagging phase (a), arterial spins are inverted as they flow through the labelling plane by flow induced adiabatic inversion. The signal in the observation slice will then be attenuated depending on the concentration and position of the labelled spins upon acquisition and the extent of longitudinal relaxation in transit. In the control phase(c), the off-resonance pulse is applied outside the head to induce identical MT effects as the labelling pulse, whilst leaving the magnetization of blood in the feeding vessels unaltered.

The implementation of CASL to humans was challenging due to the specialist hardware requirements necessary to facilitate labelling over a few seconds as well as the specific absorption rate (SAR) restrictions. Consequently, the continuous labelling pulse was replaced by a brief inversion extended over a larger slab proximal to the imaging plane. This approach is term pulsed arterial spin labelling (PASL). It was the introduction of PASL that helped first make it possible to apply ASL in human studies.

1.3.3.1 Flow Induced Adiabatic Inversion

In CASL, inversion of blood water in the feeding arterials is accomplished using flow induced adiabatic inversion. This technique harnesses the movement of the blood itself to label arterial spins. The motion of spins along a gradient sweeps the frequency of the spins from far above resonance to far below the resonant frequency of the applied RF pulse. So from the blood water spins' frame of reference, when the blood is far from the labelling plane, the RF frequency it "sees" is far off resonance. As it flows towards the brain it sweeps through the labelling plane and is on resonance. As it passes beyond the tagging plane the RF frequency (in its frame of reference) becomes more off resonance. As the frequency of the spins is swept toward and through resonance, the effective field (B_{eff}) rotates and eventually becomes inverted. In the rotating frame, the effective field can be described as the vector sum of the field of the applied RF pulse (B_1) and an additional field proportional to $\Delta\omega/\gamma$ where $\Delta\omega$ is the frequency offset between the resonant frequency of the spins and that of the labelling pulse and γ is the gyromagnetic ratio. However, the arterial spins must obey the adiabatic condition in order to achieve inversion. This states that the rate of the change of the effective field must be considerably greater than T1 and T2 relaxation but must be less than the rate of precession of the magnetisation. In the case of velocity-driven adiabatic inversion schemes used in continuous ASL, the frequency sweep is determined by the velocity of the arterial blood water spins along the direction of the gradient, and the adiabatic condition can be expressed accordingly:

$$\frac{1}{T_2}, \frac{1}{T_1} << \frac{Gv}{B_1} << \gamma B_1 \qquad [1.6]$$

Where G is the strength of the labelling gradient and v is the spin velocity.

1.3.4 Pulsed Arterial Spin Labelling (PASL): Principles

1.3.4.1 EPISTAR

In 1994, Robert R. Edelman introduced a technique known as EPISTAR (echo-planar imaging and signal targeting with alternating radio frequency pulses) [Edelman *et al.,* 1994]. The short duration of the tagging pulse (23ms) meant this method was later to be categorised as a Pulsed Arterial Spin Labelling (PASL) approach (see *Figure 1.2*).

This novel sequence was applied to Functional Magnetic Resonance Imaging (fMRI) in humans. Blood Oxygen Level Dependence (BOLD) imaging is the most common approach to fMRI [Ogawa *et al.,* 1990]. However, Edelman argued that it is sensitive to shifts in venous oxygen saturation and therefore sensory activation changes may be detected downstream, somewhat removed from the specific area of heightened metabolic rate within the brain tissue. Edelman argued increases in blood flow as detected by the EPISTAR sequence were better localised to the active region. The paper reports the results using this new method to measure qualitative changes in CBF due to sensory activation.

A 23 msec inversion pulse was applied to a slab inferior to the slice of interest. After a delay to allow inflow of the tagged blood, an EPI image was then acquired. MT effects were accounted for using an identical approach to [Detre *et al.*, 1992]. However in these experiments, the proximity of the tagging plane to the observation slice meant that the control inversion slab also intersected the brain. As a result, signal arising from the veins was apparent upon subtraction of the labelled and control images due to the inadvertent tagging of venous spins by the control inversion. This was unrelated to perfusion and introduced some uncertainty into the measurements.

The EPISTAR sequence differs in several respects in comparison to Detre and Williams' initial work. The inclusion of EPI dramatically increases the efficiency of the measurements and allows interleaved tagged and control acquisitions, reducing the extent of mis-registration and scanner instability and allowing good time resolution (necessary for fMRI experiments). In addition, MT effects are moderate due to the

reduced duration of the tagging pulse. MT acts to reduce the T_1 of the labelled water (that has exchanged into the tissue) and hence the tagged spins will have relaxed to a lesser extent upon image acquisition, providing superior contrast per labelled spin. The reduction in SAR was also a considerable advantage.

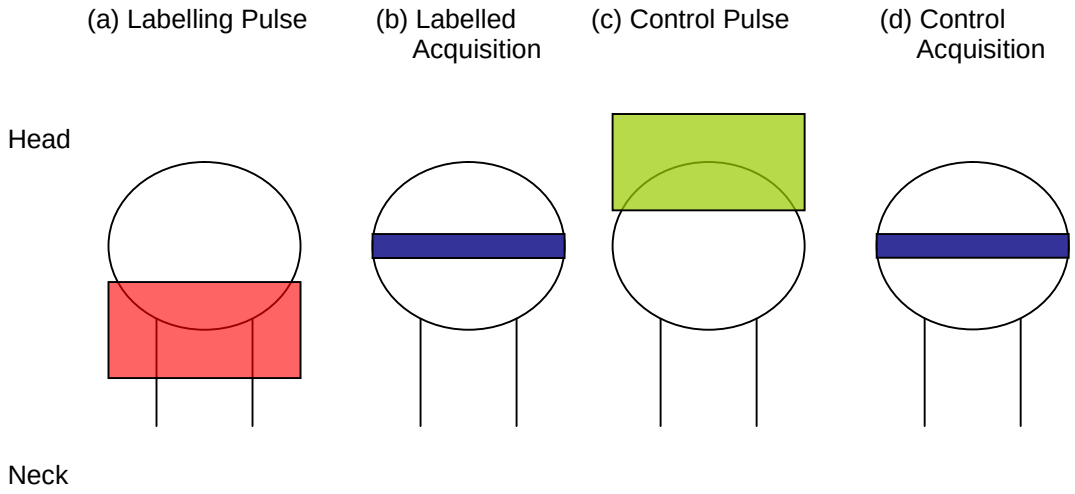

Figure 1.2
A schematic representation of EPISTAR. The labelling pulse (a) is designed to invert spins over a large area proximal to the observation slice after brief application. In EPISTAR's original design, the control pulse (c) is identical but situated symmetrically above the observation slice, the same approach used in CASL.

1.3.4.2 FAIR

In 1992 Kwong *et al.*, performed slice-selective inversion recovery imaging experiments during a sensory activation paradigm in humans [Kwong *et al.*, 1992]. Qualitative CBF changes between activation and rest were then estimated by accounting for the inflow of fully relaxed blood into the imaging slice during the inversion time (TI). Kwong *et al.*, later adapted the imaging protocol and interpreted the measurements to quantify CBF [Kwong *et al.*,1995]. This technique was later termed flow-sensitive alternating inversion recovery (FAIR) by Kim [Kim., 1995]. In this sequence, alternate images were acquired, first after a slice selective inversion and then after a global inversion, using EPI (see *Figure* 1.3). During the slice selective inversion time, the inflowing intra-vascular spins were fully relaxed. During the global inversion time, the inflowing spins were relaxing back to M_0 according to T_1. Static tissue within both images should have relaxed to the same extent and subtract to zero to give a flow

weighted image. To estimate quantitative CBF, it was necessary to measure the T_1 of the brain tissue in order to calculate the effect of the inflowing spins on the apparent T_1 relaxation constant (T_{1app}) following the slice selective inversion. The symmetric nature of this sequence automatically compensates for MT-effects. In both FAIR and EPISTAR, the imperfect RF profile of the preparation pulses meant that there was always a minimum transit time for the labelled spins to reach the imaging slice, though this is reduced in comparison to CASL (where labelling takes place in the larger feeding arteries).

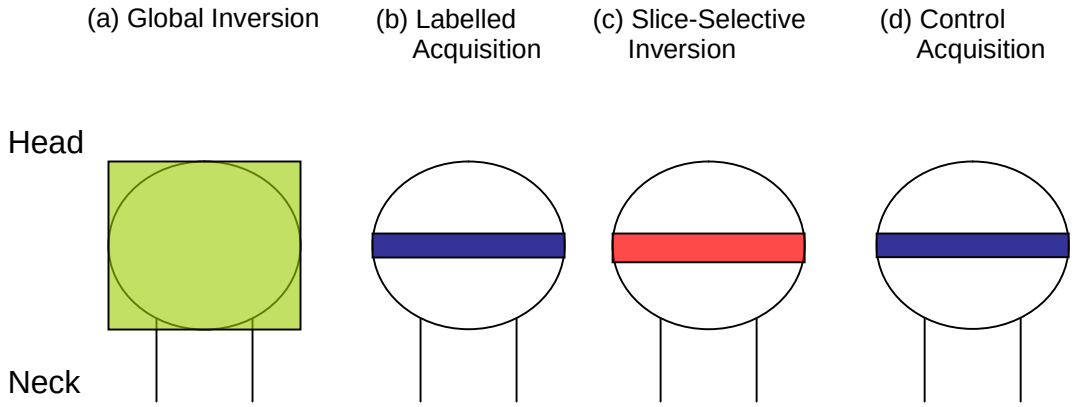

Figure 1.3
A schematic representation of FAIR. A global inversion (a) is applied before the first acquisition (b). This can be thought of as the labelled phase. The control is achieved by using a slice-selective inversion (c) before the second acquisition (d).

1.4 THE DEVELOPMENT OF ASL

1.4.1 CASL Techniques and Development

The prolonged labelling time means, in their basic forms, CASL has a theoretical signal advantage of roughly 2.7 times that of PASL [Wong *et al.*, 1998]. However the increased extent of MT may cause the results to be confounded if the MT effects are asymmetrical and may reduce the SNR of the measurements due to the associated reduction of the T_1 of the labelled spins that have exchanged into the tissue during labelling.

The conventional (see *Figure 1.1, 1.2*) approach to MT cancellation only allows single slice acquisitions. To overcome the single-slice limitation, Alsop and Detre proposed a

sinusoidal modulation of the RF labelling waveform during the control phase while keeping the frequency offset the same as for the labelling phase [Alsop *et al.*, 1998]. The application of such an RF pulse together with a gradient will continuously invert two planes at the same time, theoretically leaving the net magnetization of the arterial blood unaltered. The power of the amplitude modulated control is configured to produce an identical MT profile in the brain during the tag and control imaging stages, permitting multi-slice acquisitions. However, perfect control is difficult to achieve thus reducing the effective labelling efficiency (i.e. the longitudinal magnetisation of blood in feeding vessels during tagging – the longitudinal magnetisation of blood in feeding vessels during control). They estimated the effective efficiency to be around 70%.

Talagala *et al* introduced an alternative pulse sequence aimed to overcome MT asymmetry by distributing the control RF power evenly on both sides of the acquisition volume [Talagala *et al.*, 1998]. Although this approach successfully allowed multi-slice CASL acquisitions, it resulted in substantial RF deposition which may have limited its application in humans, particularly at high field (~ 3T).

An effective way to reduce MT is to use a separate labelling coil positioned on the neck. [Silva *et al.*,1995, Zhang *et al.*,1995(a)]. The spatial extent of the off-resonance RF is thus limited to the tagging region, inducing negligible MT in the imaging slab, significantly reducing SAR and allowing multi-slice acquisitions. This also enabled vessel selective labelling of the left or right carotid artery [Zaharchuk *et al.*, 1999, Mildner *et al.*, 2003]. Vessel selective labelling is an exciting new development within ASL and enables the assessment of the supply of blood to the brain from individual arteries. Selective labelling of the ventral arteries and feeding arteries proximal to the middle cerebral artery (MCA) has been achieved using conventional MRI hardware without a separate labelling coil [Davies and Jezzard, 2003; Guenther, 2006(a); Kansagra and Wong, 2008]. In addition, a recent study has provided evidence that territorial ASL methods in combination with MR angiography yielded results that were in good agreement with digital subtraction angiography measurements (the “Gold Standard” approach) in the assessment of collateral circulation (which plays a vital role in patients with steno-occlusive disease, in particular for predicting stroke outcome [Chng *et al*., 2008]). There is likely to be a good deal of interest in vessel selective ASL in the near future.

As previously discussed, RF deposition is an important issue within CASL and can limit its efficiency in human studies. Reducing this was a motivation behind pseudo-continuous ASL [Garcia *et* al., 2005(a), Wu *et al.*, 2007(a)]. This relatively new approach to flow driven adiabatic inversion employed repeated rather than continuous RF pulses to reduce SAR and MT. This was a welcome modification and is more compatible with standard MRI RF hardware in comparison to CASL. Many recent ASL experiments have used this labelling scheme to good effect [e.g. Wong *et al.*, 2006, Fernandez-Seara *et al.*, 2008] and it represents a promising approach to spin tagging for future studies.

1.4.2 PASL Techniques and Development

1.4.2.1 FAIR Sequence Development

Uninverted flow-sensitive alternating inversion recovery (UNFAIR) modified the original FAIR sequence to include an additional inversion to the imaging slice just after the first so that theoretically the static tissue signal is fully relaxed [Tanabe *et al.*, 1999]. Consequently the imaging conditions are identical for the control and labelled acquisitions (apart from the changing width of the hyperbolic secant pulse). The authors claim that this serves to avoid artefacts such as eddy currents, though in the light of recent developments which demonstrate the benefit of suppressing the static tissue signal to improve the SNR of ASL images [Garcia *et al.*, 2005(b)], this approach may have limited value. A similar strategy was also developed by Berr *et al.*, [Berr *et al.*, 1999].

The Acronym “FAIRER” was used to describe two different adaptations to the original FAIR technique. “FAIR excluding radiation damping” includes an additional gradient during TI to reduce radiation damping effects which may be problematic at high field strength [Zhou *et al.*, 1998, Zhou *et al.*, 1999]. In contrast, “FAIR with an extra radiofrequency pulse” consists of the standard FAIR sequence followed by an additional saturation pulse to null the signal from the static tissue [Mai and Berr, 1999]. This was developed with intended application to the lung in combination with cardiac gating.

Unprepared BAsis and SElective inversion (BASE) was introduced in 1998 with its initial application in fMRI [Schwarzbauer and Heink., 1998]. This approach does not

require a global inversion and therefore can be used with smaller transmit coils. In addition it is robust against a mismatch of inversion and slice selective profiles though it is only able to measure CBF changes rather than absolute values. In 1999, Pell *et al.* increased the time resolution of FAIR by reducing the TR of the sequence [Pell *et al.*, 1999]. This was achieved using a global saturation pulse just prior to the FAIR sequence. Furthermore, "FAIR exempting separate T_1 measurement" incorporates an additional saturation recovery acquisition interleaved within the standard FAIR protocol for the combined measurement of both perfusion and BOLD contrast at a cost of about 15% greater imaging time [Lai *et al.*, 2001].

1.4.2.2 EPISTAR SEQUENCE DEVELOPMENT

Three years after its first application, Edelman and Chen published work addressing the problem of inadvertent venous tagging in EPISTAR [Edelman and Chen, 1998]. They replaced the conventional control inversion with a 360^o pulse situated at the site of labelling. Hence MT effects could be accounted for without the introduction of spurious venous signal. This adaptation also enabled multi-slice acquisitions. By this time, it had also been shown that the half-Fourier single shot turbo spin-echo (HASTE) imaging sequence in combination with an EPISTAR spin preparation could overcome some of the artefacts associated with EPI and produce better quality perfusion images [Chen *et al.*, 1997].

Wong *et al.* introduced a simple adaptation termed PICORE or Proximal Inversion with Control for Off Resonance Effects [Wong *et al.*, 1997]. In this approach the slice gradient is turned off in the control phase, controlling for MT whilst avoiding unintended tagging of the veins distal to the imaging slice. However the different tagging and control gradients meant eddy currents can be problematic [Jahng *et al.*, 2003]. Better MT and eddy current cancellation was the main motivation behind the recently conceived "Double Inversion with Proximal Labelling of Both Tagged and Control Images (DIPLOMA)" [Jahng *et al.*, 2003]. In this sequence, tagging is achieved using an off resonance pulse followed by a slab selective inversion. The control is achieved using two consecutive slab selective inversions in a similar way to the Edelman's modification [Edelman and Chen, 1998]. Overall the MT and eddy current

compensation worked as intended to produce superior perfusion weighted images in comparison to PICORE and EPISTAR.

1.5 ISSUES IN ACCURATE, EFFICIENT AND ROBUST ASL CBF QUANTIFICATION

1.5.1 Transit time

1.5.1.1 INTRODUCTION

In 1994, Walsh *et al.* performed important validation experiments comparing the new ASL methods with the well established radioactive microsphere approach in the healthy and partially occluded rat brain [Walsh *et al.*, 1994]. Although the baseline results were in good agreement, they observed a consistent underestimation of flow by the MRI measurement for the successful occlusions. This discrepancy was attributed to long transit times through the middle cerebral artery (MCA) in the occluded state. The rapid decay, according to T_1, during this transitional period severely reduces the perfusion weighted signal. Transit time effects have since become accepted as an important possible confounder in the interpretation of ASL perfusion weighted images and still represent a major obstacle in robust and accurate CBF quantification.

1.5.1.2 INTRODUCING A POST-LABELLING DELAY TIME

In 1996 Alsop and Detre published a theoretical framework with experimental methods to more accurately account for transit effects within ASL [Alsop and Detre, 1996]. They state that although in rats the transit time is negligible, it is significant in human studies where it can vary considerably across the brain, even in healthy patients. For the most accurate quantification it should be determined by measurement of the perfusion weighted signal at a range of delay times [Buxton *et al.*, 1998]. However this would reduce the sensitivity and temporal resolution of the method. Alsop reasoned that the inclusion of a post labelling delay (PLD) between the end of the tagging pulse and image acquisition would markedly reduce the sensitivity of the CBF estimates to variable transit time providing the delay is greater than the arterial transit time (δa). The arterial transit time is the time taken for the blood water to travel from the labelling plane to the imaging region. Therefore in healthy volunteers the PLD should be chosen to be around 1s, and extended for patients with cerebrovascular disease. This relies on

the similarity of the T_1 of arterial blood and grey matter which only differ by around 10% at 1.5 Tesla. Although an extended PLD will result in a decrease in the perfusion weighted signal due to increased T_1 relaxation of the labelled spins, it will also render the CBF estimates relatively insensitive to transit time variations provided it is greater then δa.

However the T_1 of white matter is considerably shorter then in grey matter and therefore the proposed delay has a limited effect at reducing transit time sensitivity in this case. Alsop adapted Detre's original model [see 1.3.2.2 *CBF Quantification*] to include several new parameters: the arterial transit time (δa); the tissue transit time (δ) (which represents the time taken for blood water that has been labelled to exchange into the tissue); the T1 relaxation constant of labelled water in the blood (T1a); the T1 relaxation constant of labelled water in the tissue during application of the off resonance labelling or control pulse (T1s); the T1 relaxation constant of labelled water in the tissue following application of the off resonance labelling or control pulse (T1n). These parameters were incorporated into the model to better account for longitudinal relaxation effects in order to more accurately quantify CBF. According to the model, precise knowledge of these parameters will account for the longitudinal relaxation of labelled blood in transit to and within the tissue of interest. T1n can be estimated by fitting the control signal to a simple T1 recovery model (see section 1.9 *T1: The Longitudinal Relaxation Constant*). T1s can be calculated using the T1n and Mo measurements [Alsop and Detre, 1996]. The arterial and tissue transit time can be calculated by acquiring ASL images at a range of PLD times and fitting the data to the model described in their work [Alsop and Detre, 1996] (N.B *w* is standard notation used in the literature for the PLD time):

$$f = \frac{-\lambda(M^{tag} - M^{ctrl})}{2\alpha M_b^0} C(T_{1ns}, T_{1s}, T_{1a}, \delta, \delta a) \qquad [1.7]$$

$$\frac{1}{C} = T_{1ns}\exp(-\delta / T_{1a})\left[\exp(\min(\delta - w,0)/T_{1ns}) - \exp(-w/T_{1ns})(1 - \frac{T_{1s}}{T_{1ns}})\right] \qquad [1.8]$$
$$+ T_{1a}[\exp((\min(\delta a - w,0) - \delta a)/T_{1a}) - \exp((\min(\delta - w,0) - \delta)/T_{1a})]$$

The way in which changes in CBF, δ and δa affect the modelled ASL signal acquired over a range of PLD times is shown in Figure 1.4. In their model CBF (the principle parameter of interest for the majority of ASL applications) is directly proportional to the measured ΔM signal. The arterial transit time determines the point of inflection of the inflow curve; the shape of the inflow curve displays marked sensitivity to this parameter. The tissue transit time affects the PLD dependant ΔM signal in a way that is more difficult to distinguish from CBF changes. Therefore given the low SNR of the ΔM signal, in practice it is difficult to estimate δ from the bolus inflow curve as a small degree of noise can introduce marked imprecision into the δ and CBF estimates. For this reason δ is often a fixed parameter or is measured using diffusion sensitised ASL measurements [Wang *et al.,* 2003, Petersen *et al.,* 2005]:

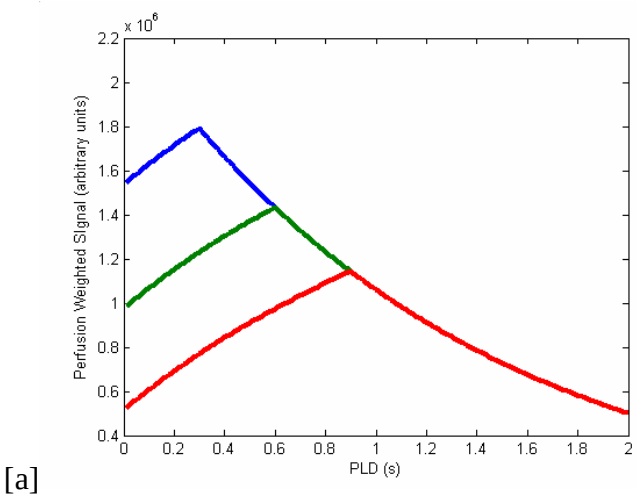

[a]

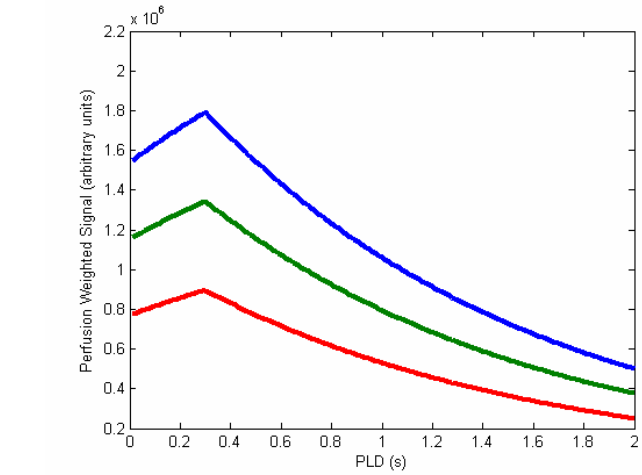

[b]

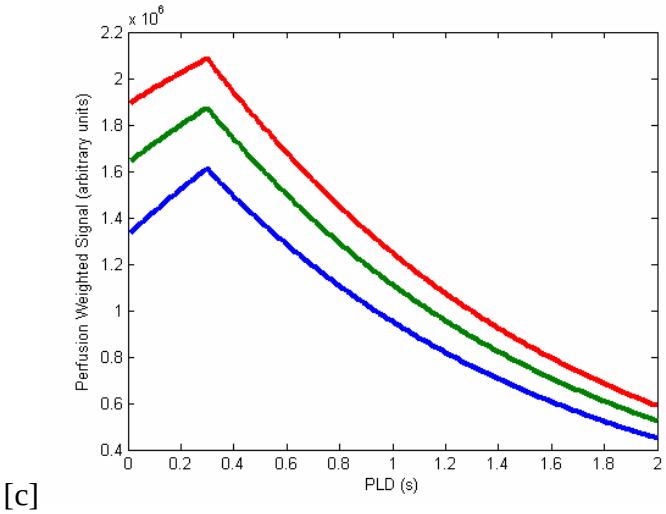

[c]

Figure 1.4

Figure 1.4 [a] shows the perfusion weighted signal at variable δa (0.3s blue line, 0.6s green line and 0.9s red line) and fixed CBF and δ. Figure 1.4 [b] shows the perfusion weighted signal at variable CBF (400 blue line, 300 green line and 200ml/min/100g red line) and fixed δa and δ. Figure 1.4 [c] shows the perfusion weighted signal at variable δ (0.3s blue line, 0.6s green line and 0.9s red line) and fixed CBF and δa.

The problem with measuring the ASL signal at a range of inflow times instead of a single PLD value is that it reduces the temporal resolution of the method. In their work the authors showed that the single extended PLD acquisition could produce reliable perfusion estimates in patients with cerebrovascuar disease (with the associated heightened range of transit times within the brain) and is still arguably the most practical and robust approach to avoiding confounding transit time effects in ASL [Alsop and Detre, 1996]. The model in this publication is considered to be the standard approach for ASL CBF quantification. For this reason I have generally used this (and a later version that incorporates variable tagging duration [Wang *et al.,* 2002]) for CBF estimation in this thesis.

1.5.1.3 The Look-Locker Readout

In 2001 Matthias Gunther *et al.* implemented a Look-Locker readout in combination with spin tagging to measure the progression of the tagged bolus at multiple delay times in a single excitation, thus allowing simultaneous measurement of CBF and arterial transit time in a single shot [Guenther *et al.,* 2001]. The magnetisation was sampled using a low flip angle excitation as the tagged bolus progressed through the cerebral vasculature following pulsed labelling. For a given imaging time, this approach was shown to produce results with an SNR advantage of 1.2 over separate acquisitions at each delay time, making perfusion measurements at multiple PLD times more practical. However image quality can be hampered by artefacts due to stimulated echoes and this perhaps explains the questionable quality of the perfusion weighted images presented in this work. However it seems such problems have been ironed out as this image read-out technique was used as part of a promising semi-automated ASL CBF and transit time quantification protocol for Philips MRI systems. This has recently been shown to produce reproducible CBF and transit time maps between scans and between sites [Petersen *et al.,* 2008]. A new model has recently been developed to describe the progression of the look-locker ASL signal in greater detail [Francis *et al.,* 2008]. Their findings highlighted the importance of accounting for the transit time of labelled blood water through the arteriolar compartment for accurate perfusion quantification in the Look-Locker FAIR acquisitions.

1.5.1.4 DEFINING THE WIDTH OF THE BOLUS: QUIPSS

Wong *et al.* devised an adaptation to PASL using additional saturation pulses to improve the definition of the tagged bolus [Wong *et al.,* 1998]. This attempted to address two main issues: i) to minimise errors in the quantification of perfusion due to spatially varying transit times and ii) to reduce the errors associated with vascular artefacts (see 1.5.2 *Vascular Artefacts*). This technique was termed Quantitative Imaging of Perfusion using a Single Subtraction and exists in two main forms, QUIPSS I and QUIPSS II. Unlike CASL where the site of labelling is narrow and the duration of the tagged bolus is known, the tagged slab in PASL will possess spatially variable transit delays for a given imaging region and the tagged bolus has unknown duration. After an inflow time (TI1) a saturation pulse is applied to the imaging slab (in QUIPSS I) or to the labelling slab (QUIPSS II). The authors claim that in principle and with careful selection of image parameters, CBF measurements can be made transit time insensitive. However the authors concede that tagged blood water en route to an alternate location within the imaging slice and the changing T_1 properties of the labelled spins as they perfuse are important possible confounders. Signal that appeared to be from large vessels was apparent in the subtracted QUIPSS I images. In contrast QUIPSS II measures a bolus of tagged blood that leaves the tagging area relatively early and has more time to flow into the capillaries and exchange into the tissue. However because the signal derives mainly from the tissue compartment in QUIPSS II, knowledge of δ (a parameter that is not accounted for in their model) is more crucial for accurate CBF quantification in comparison to QUIPSS I. They state that there is still much work to do in the characterization of these known sources of error. QUIPPS II is analogous to the approach by Alsop and Detre described above [Alsop and Detre, 1996] in that both methods aim to measure the signal from a defined bolus of labelled blood that has had sufficient time to reach the microvasculature. By saturating the adjacent plane, the idea is to remove the signal from blood that would otherwise be present in the arterial vessels during image acquisition (i.e. blood that was labelled further downstream from the imaging plane and in effect has a longer transit time).

A modification termed Q2TIPS [Luh *et al.,* 1999] was proposed with a train of thin-slice saturation pulses applied to the distal end of the tagged region. This improved the

accuracy of the QUIPSS II measurements by improving the definition of the labelled bolus and reducing intravascular contamination of the imaging volume.

1.5.1.5 Velocity Selective Labelling

A recent idea uses velocity, rather than spatially, selective labelling pulses with the intention of saturating flowing spins situated in feeding vessels very close to the tissue of interest [Wong *et al.*, 2006(a)]. The global nature of these velocity selective pulses means intravascular spins are tagged in and around the imaging slice. Thus in theory the transit time is minimised. The labelling pulse saturates spins flowing above a certain velocity. The subsequent acquisition is sensitive to the tagged spins which flow below a certain velocity. Thus the sequence is designed to be sensitive to blood as it decelerates during entry to the micro-vessels and in this way is sensitive to perfusion. The control acquisition includes identical RF pulses with low velocity encoding gradients.

This technique has been shown to produce sensible CBF values in normal volunteers and in patients with cerebrovascular disease [Wong *et al.*, 2006(a)]. However CBF quantification may be confounded by irregular vascular distribution to the tissue of interest and errors may be introduced if the velocity selective tagging is applied off the direction of blood supply [Wu *et al.*, 2007(b)]. Indeed it seems that more work needs to be done to validate the accuracy of this new technique and compare the accuracy and precision of VS-ASL with a range of optimised spatially selective ASL approaches. However thus far the SNR of this technique has been constrained as labelled blood could only be saturated rather than inverted. Wong *et al.*, have reported preliminary results using a sequence of RF pulses to invert, rather than saturate, blood flowing in a certain velocity range [Wong *et al.*, 2009].

1.5.2 Vascular Artefacts

1.5.2.1 Introduction

As previously described, the first ASL experiments [Detre *et al.*, 1992] incorporated spoiler gradients around the refocusing pulse to attenuate signal from flowing spins in the vasculature to avoid overestimating CBF. For accurate quantification it is necessary to distinguish regions of heightened perfusion from regions where signal increases come

from blood that is simply in transit to its eventual location for oxygen and nutrient delivery and exchange.

1.5.2.2 When Perfusion meets Diffusion

Ye *et al.* found that, in humans, spoiler gradients (of small duration, separation and amplitude) around the refocusing pulse (the approach implemented in the first ASL experiment [Detre *et al*., 1992]) were not sufficient to crush all the arterial signal and therefore proposed the inclusion of bipolar crusher gradients, with a relatively high *b*-value [YE *et al.,* 1997]. The *b*-value is the standard unit defining the extent of diffusion weighting due to the gradients in a sequence and is given in s/mm^2 (see 1.10 *Principles of Diffusion MRI*). They measured a decrease in the perfusion weighted signal (ΔM) of approximately 50% in humans with the inclusion of the bipolar vascular crushers. The signal intensity of the base images, the majority (~95%) of which arises from the tissue, was reduced by 3%. This led them to conclude that when the ASL signal was sampled, ΔM arises almost equally from arterial water and extra-vascular water, whereas in the presence of bipolar crushers, ΔM arises predominantly from extra-vascular water. However it is perhaps not surprising that the diffusion gradients reduced the signal to such an extent given that there was no PLD prior to image acquisition. With negligible PLD it is likely that a significant proportion of the labelled water will reside in the vascular compartment during image acquisition. There has subsequently been a good deal of interest in investigating and interpreting the dual weighted ASL perfusion and diffusion signal.

Silva *et al.* measured ΔM with diffusion gradients at a range of *b*-values in the rat brain. The results were interpreted to estimate the fraction of the labelled blood in the vascular compartment relative to that which has exchanged into the cerebral tissue [Silva *et al.,* 1997(a)]. They argued that these values were equivalent to the first pass extraction fraction (EF) and investigated the possible correlation of this parameter with CBF. The results provided evidence for a strong correlation between the EF of labelled blood water and CBF. This was an important finding and suggested ASL was susceptible to overestimating cerebral perfusion at high CBF unless EF was taken into account. The same group exploited the different susceptibility of the vascular and tissue compartments to MT to measure EF in the rat brain [Silva *et al.*, 1997(b)]. The

longitudinal magnetisation of the arterial spins is less severely attenuated by MT from an off-resonance pulse in comparison to the tissue spins. The reported relationship between CBF and EF was in good agreement with their previous results.

The recent advances in ASL and in MRI hardware (pseudo continuous labelling, EPI, background suppression, higher field magnets) helped the combined diffusion and perfusion experiment at multiple *b*-values to be repeated in humans [Wang *et al.,* 2007]. This provided further evidence, concordant with previous work, [e.g. Parkes and Tofts, 2002] for the limited exchange of cerebral blood water in humans. However the authors reported marked variance in the estimated pseudo-ADC values assigned to the vascular and tissue compartments, limiting the extent of interpretation of their results.

Overall, these experiments provide a convincing argument for the inclusion of vascular crusher gradients within single-PLD ASL experiments for more accurate CBF quantification in both animal and human studies.

1.5.3 CBF Quantification Models

Detre's original quantification model [Detre *et al.,* 1992] assumes the brain tissue to be a single compartment with instantaneous exchange of the labelled spins from the vessels. However CBF quantification may be confounded given the cumulating evidence for the restricted exchange of blood water and the dependence of EF on CBF [Silva *et al.,* 1997a, Ewing *et al.,* 2001, Zaharchuk *et al.,* 1998].

In order to account for this, more complex multi-compartment models have been proposed [Li *et al*., 2005, Parkes and Tofts, 2002, Zhou *et al.,* 2001, St Lawrence *et al.,* 2000, St Lawrence and Wang, 2005]. In general these models have shown the effect of limited exchange on measured CBF to be minimal in human studies provided the relaxation rates in tissue and blood are similar. However they may benefit CBF quantification in white matter which has marked difference in T1 relaxation properties in comparison to blood [Calamante *et al.,* 1996; Parkes and Tofts, 2002; Li *et al.,* 2005; St Lawrence *et al.,* 2000; St Lawrence and Wang, 2005].

As a general point, at present many of those applying ASL in experimental and clinical applications may argue that it does not have the SNR to support many additional complexities in the CBF quantification model due to the possible associated reduction in precision.

Recently an investigation was performed to model the affects of blood dispersion and pulsatility in pulsed ASL experiments. The established models assume plug flow from the tagging to the imaging plane. A new model was proposed that assumes parabolic flow (a more realistic assumption) in the larger feeding arteries and accounts for cardiac pulsatility. It was found that fitting the acquired ΔM data to this new model yielded greater CBF estimates. However the precision of the calculated CBF was reduced due to the model's added complexity. They found that when no cardiac-gating was used the mean curve over several cardiac cycles was predicted to closely match the curve which assumes constant flow [Gallichan and Jezzard, 2008].

A model-free approach to perfusion quantification [Petersen *et al.*, 2005] has been proposed. A sequence which combined interleaved vascular crushers with a Look-Locker readout was implemented. CBF is quantified using a deconvolution with an arterial input function in a similar way to dynamic susceptibility contrast imaging [Ostergaard, 2005]. Simulations demonstrated that this approach improved the precision of CBF estimation in comparison to standard parametric modelling. Furthermore these measurements (with and without vascular crusher gradients) can also be used to estimate the arterial blood volume and the mean transit time. This protocol was used in a semi-automated ASL sequence for Philips MRI systems, recently shown to produce reproducible CBF and transit time maps between scans and between sites [Petersen *et al.*, 2008].

1.5.4 Measuring CBF in White Matter

Accurate CBF quantification in white matter using ASL is challenging for 3 main reasons: i) Perfusion tends to be substantially lower in comparison to grey matter, reducing the SNR of the measurements; ii) In general, the transit time of white matter is considerably greater than grey matter and consequently there is more longitudinal relaxation of the tagged spins en route to the tissue; iii) although the T1 of blood and

grey matter is similar, it is significantly reduced in white matter and therefore knowledge of the tissue transit time of blood is more crucial for accurate CBF quantification in this case. For these reasons the SNR_{pwi} in deep white matter perfusion territories has recently been measured to be less than 1 using FAIR [van Gelderen *et al*., 2008]. Indeed a recent comparison of ASL with perfusion computed tomography has shown that ASL can yield inaccurate white matter CBF estimates [Koziak *et al.,* 2008].

The recent multi scan, multi centre MRI ASL study measured good reproducibility in white matter in healthy volunteers [Petersen *et al.,* 2008]. However this was after spatially averaging over all the white matter pixels in the brain. Detecting more focal changes in white matter perfusion is likely to be significantly more challenging and represents a major disadvantage of ASL over PET.

1.6 GENERAL ASL OPTIMISATION AND DEVELOPMENT

There is some controversy within MR as to the optimal field strength for many applications. However the introduction of high field (~3T) scanners has generally been welcomed by ASL users due to the increase in signal together with the increase in T_1 (less relaxation in transit). The growing trend for high field magnets is likely to greatly enhance ASL's appeal.

The low SNR of the ASL measurements is arguably most responsible for its relatively limited use. In humans the difference in signal intensity between the labelled and control image is of the order of 1% of the base signal; scanner stability is crucial for reliable measurements. This makes rapid single-shot interleaved tagged and control imaging methods such as EPI [Edelman *et al.,* 1994, Kwong *et al.,* 1995] or spiral imaging [Yang *et al.,* 1998] highly advantageous. However, these can be accompanied by severe susceptibility artefacts. Therefore alternative readout methods based on single line [Zhang *et al.,* 1995(b), Branch *et al.,* 1999], fast-spin echo [Chen *et al*., 1997; Crelier *et al.,* 1999; Liu *et al*., 2001] or snapshot FLASH (fast low angle shot) [Calamante *et al,* 1999] methods have been suggested as viable alternatives. These have important applications in imaging outside the brain. A single shot 3D sequence has recently been designed that was shown to increase the SNR of the perfusion weighted images by a factor of 2.8 in comparison to 2D EPI at the same nominal resolution. This

sequence is known as 3D GRASE [Gunther *et al*., 2005] and is becoming increasingly popular in ASL applications.

Background suppression was proposed for better cancellation of the static tissue through the reduction of physiological noise [Ye *et al.*, 2000, Garcia *et al.*, 2005(b)]. An inversion pulse is applied during TR and the image is subsequently acquired at the null point of the tissue (IE when the longitudinal magnetisation of the tissue is zero). Two spin populations (e.g. Grey and CSF) with different T_1 values may be both nulled using two inversion pulses with appropriate sequence timing. Indeed, up to three saturation pulses were applied (one before the inversion pulse) in the original implementation of this technique [Ye *et al.*, 2000]. However background suppression must be implemented with caution to ensure that bias is not introduced to the perfusion measurements due to noise rectification. Recent studies have used this in combination with the aforementioned pseudo-continuous labelling and 3D GRASE readout with encouraging results [e.g. Fernandez-Seara *et al.*, 2007].

1.7 APPLICATIONS

1.7.1 Cerebrovascular Disease

Acute and marked reduction of perfusion is the cause of stroke and ischemic attacks; ASL has considerable potential in the study and diagnosis of cerebrovascular disease. For example there is evidence that ASL CBF maps can provide identification of salvageable brain tissue (the “penumbra”) following an ischemic attack [Chalela et al., 2000]. Previous studies have attempted to provide some identification of these regions by measuring the so-called perfusion-diffusion mismatch in the brain– where the region of reduced perfusion is mismatched to the region of tissue changes as identified by diffusion weighted imaging. There is evidence that CASL is able to map regions of hypoperfusion during acute stroke [Chalela et al., 1998], chronic cerebrovascular disease [Detre et al., 1998] and in response to perfusion changes induced by pharmacological stimuli [Detre et al., 1998].

A comparison of FAIR ASL and DCS was performed by Hunsche *et al*., in both patients with ischemic stroke and normal volunteers [Hunsche *et al*., 2002]. They found a good correlation between the measured CBF as well as a modest correlation between cerebral blood volume and transit time estimates using the two techniques. Yoneda *et al*.,

compared relative perfusion measurements (the “diseased” side in comparison to the “healthy” side) generated using FAIR (at two different inversion times (TI =800ms and 1600ms)) and DSC MRI [Yoneda *et al.,* 2003]. By studying 11 stroke patients they found that the relative perfusion measurements at a TI of 1600 correlated best with the transit time measurements from the DCS method. The correlations were not so strong with the CBF and blood volume estimates generated using the gadolinium technique”

“To try to account for extended transit time effects, Hendrikse *et al.,* implemented single-slice, pulsed ASL to acquire perfusion weighted images over a range of inflow times (200 to 1600 msec) in nine patients with carotid artery occlusion [Hendrikse *et* al., 2004]. Apart from at the longest and shortest inversion times, the perfusion-weighted signal in gray matter was less in the hemisphere containing the occlusion in comparison to the contralateral hemisphere or with control values. Quantitative CBF estimates were also found to be significantly different between the affected hemisphere and the healthy side or the control values”

“Kimura *et al.,* implemented CASL and CO_2 PET to assess regional CBF and transit times in patients with unilateral occlusive disease [Kimura *et al*., 2005]. ASL CBF was correlated with PET CBF across 48 ROIs for each subject (11 in total). The mean correlation over all subjects was 0.71. However, the ASL CBF estimates were found to be significantly reduced in comparison to PET CBF within gray matter ROIs on the diseased side. The transit times were subsequently found to be significantly greater in the affected hemisphere suggesting that the underestimation of CBF by ASL in the affected hemisphere appears to be due to longer transit times to this region. However, their results do show fairly good agreement between CBF estimated using ASL and PET for patients with unilateral occlusions”

“ASL has recently been employed to characterise alterations in CBF in paediatric patients with arterial ischemic stroke [Chen *et al*., 2009]. This was the first study to demonstrates the clinical utility of ASL in the diagnosis of this patient group. They found the inter-hemisphere perfusion deficit (a similar measure to the relative perfusion estimates taken by Yoneda *et al* [Yoneda *et al.,* 2003]) to correlate with the degree of stenosis, diffusion lesion, and follow-up infarct volumes. Furthermore they claim that brain regions presenting delayed arterial transit effects (as measured using ASL) were

(to a limited extent) associated with positive outcome. Pollock *et al* recently attempted to use ASL to characterize the perfusion patterns encountered after anoxic injury to the brain [Pollock *et al.,* 2008]. They found that global GM CBF was significantly higher in anoxic injury subjects in age-matched control groups and concluded that their study provided evidence that pulsed ASL can quantify the severity of the cerebral hyper-perfusion after a global anoxic injury.

1.7.2 Functional MRI

ASL has several benefits over BOLD measurements (the standard approach to functional MRI (fMRI)). Perhaps the greatest advantage is the absolute quantification that ASL can provide. This allows more rigorous inter- and intra-subject comparisons and can remove the necessity for task related paradigms inside the MRI scanner, which may particularly benefit studies focussing on certain patient groups. For example the possible correlation of resting perfusion to task performance outside the MRI scanner in Alzheimer's patients has previously been investigated. (e.g. Grossman *et al.,* 2001). Secondly, standard functional studies are performed using gradient echo based imaging sequences that are sensitive to the BOLD effect. Thus in regions of high static susceptibility such as the orbital- frontal cortex, the measured signal may be severely reduced. ASL does not require such T2* weighted acquisitions and therefore such "image drop out" of the imaging region can be reduced using spin-echo based image-readout techniques, for example. In addition, there is evidence to suggest that perfusion changes have superior spatial specificity and closer temporal fidelity to the neuronal activation in comparison to BOLD changes during a typical fMRI paradigm [Silva *et al*., 2000; Duong *et al*., 2001]; as previously mentioned, BOLD is sensitive to shifts in venous oxygen saturation and therefore sensory activation changes may be detected downstream, somewhat removed from the specific area of heightened metabolic rate within the brain tissue. Changes in perfusion as detected by ASL are better localised to the active region in the brain. However it is widely accepted that the SNR of the ASL measurements is considerably lower than the BOLD measurements and therefore ASL may require longer scan times for many fMRI studies in comparison to BOLD imaging experiments.

1.8 T2: THE TRANSVERSE RELAXATION TIME

1.8.1 Introduction

Chapter 2 describes experiments designed to estimate the transverse relaxation decay constant (T2) of the ASL signal in order to understand more about the origin of labelled blood in the brain. In this section I will describe the principles behind transverse relaxation and explain why it can yield information about the cerebral-vascular location of the measured ASL signal. In order to understand the processes behind transverse relaxation, I will first present a brief overview of the mechanisms underlying the NMR phenomenon.

1.8.2 NMR Phenomena: How we Generate a Signal

The nucleus of a hydrogen atom consists of a single proton which possesses the quantum mechanical property known as spin. In combination with its positive charge, the spin of the proton generates a magnetic moment. When the proton experiences a strong magnetic field, it exerts a turning force (or torque) that causes the proton to precess around the applied field (see *Figure 1.5*). The frequency of this precession is given by the Larmor equation:

$$\omega_0 = \gamma B_0 \qquad [1.9]$$

where γ is the gyromagnetic ratio ($42.\text{MHzT}^{-1}$ for hydrogen); ω_0 is the frequency of precession and B_0 is the strength of the applied magnetic field

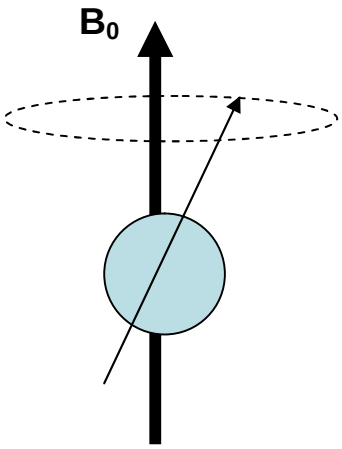

Figure 1.5

A proton rotates around the main magnetic field (B_0) at the Larmor frequency.

The axis parallel to the main magnetic field is known as the longitudinal or z-axis. In quantum mechanical terms, the protons precess in one of two states – parallel (or up) and anti-parallel (or down) to the applied magnetic field (see *Figure 1.6*). The anti-parallel direction requires fractionally more energy and so overall there are slightly more protons parallel to the magnetic field. The distribution of the two states can be quantified using Boltzman statistics. The probability p_i that a system is in quantum state ψ_i is equal to the number of quantum states associated with ψ_i divided by the total number of states (Z) as given by:

$$p_i = \frac{e^{\frac{-E_i}{k_B T}}}{Z} \qquad [1.10]$$

Where E_i is the energy of the system, k_B is the Boltzmann constant and T is the temperature of the system. The energy of the parallel and anti-parallel states are given by:

$$E_{up} = -1/2\ \gamma h B_0 \text{ and } E_{down} = +1/2\ \gamma h B_0. \qquad [1.11]$$

Therefore the relative population of the two spin states can be given by:

$$\frac{N_{down}}{N_{up}} = \frac{\exp-(\frac{\gamma\hbar B_0}{2k_B T})}{\exp+(\frac{\gamma\hbar B_0}{2k_B T})} = \exp-(\frac{\gamma\hbar B_0}{k_B T}) \qquad [1.12]$$

Equation 1.12 shows that the extent of the difference is directly proportional to the strength of the magnetic field which explains why it is desirable to image using a high field MRI scanner: there is more signal.

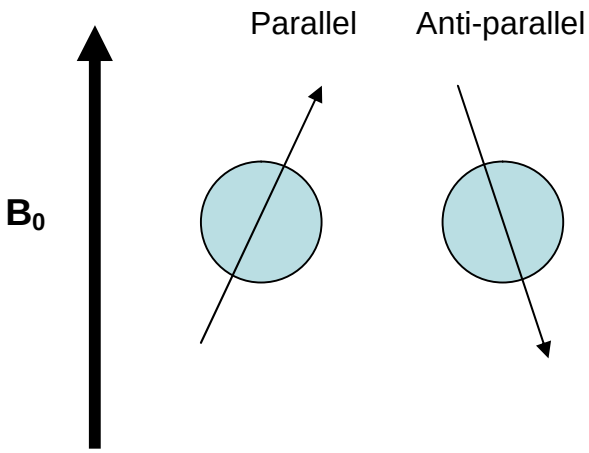

Figure 1.6
Protons are aligned parallel or anti-parallel to the applied magnetic field. Slightly more protons are aligned in parallel to the main magnetic field as this state is of lower energy.

When a subject is at rest in an MRI scanner, there is no consistency between the transverse magnetisation of their protons i.e the component perpendicular to the longitudinal axis. As a result the net magnetisation (M_0 - the vector sum of all the magnetic moments) is aligned with the magnetic field and has no transverse component (see *Figure 1.7*).

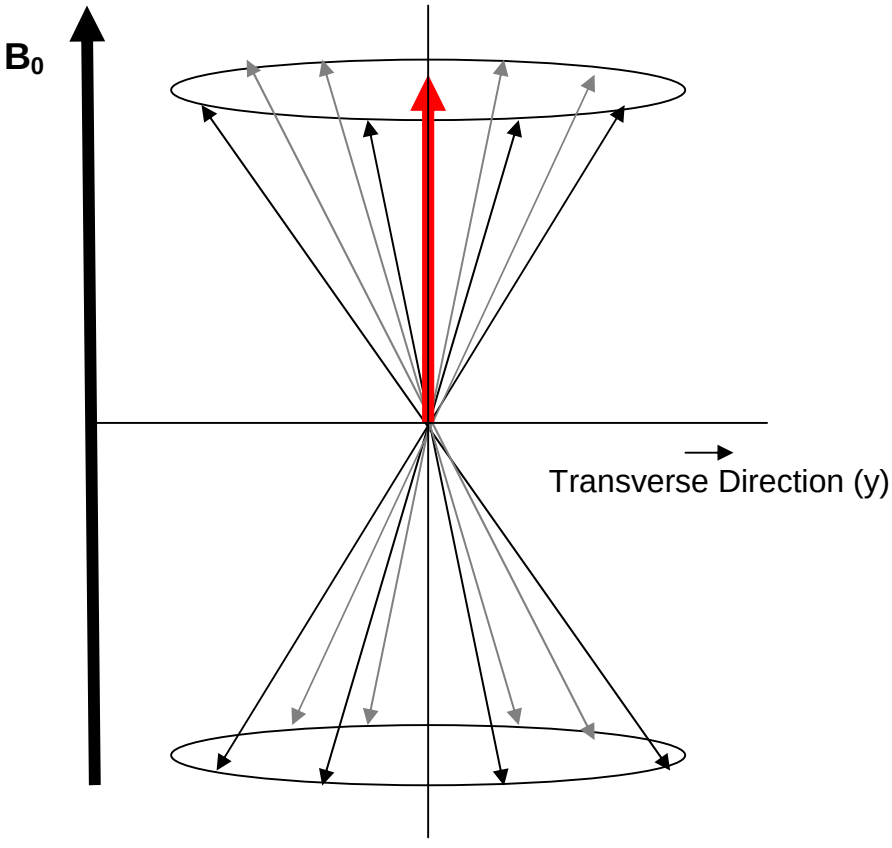

Figure 1.7
When a subject is at rest in the scanner, protons are fully relaxed and are out of phase. As a result the net magnetisation (red arrow) is aligned with B_0 and possesses no transverse component.

To generate the measured signal, radio frequency (RF) pulses are used to tip M_0 into the transverse plane. The time varying magnetisation vector is now represented by M. The RF pulse oscillates at the Larmor frequency. M moves away from B_0 during the application of the pulse. In the laboratory frame of reference this is a spiral motion as M precesses about B_0. In the rotating frame (at the Larmor frequency), the net magnetisation moves monotonically towards the transverse plane. If the applied B_1 field acts to bring M into the transverse plane then a 90^o RF pulse has been applied. This is also known as an excitation pulse. For a simple constant-amplitude RF pulse the flip angle (α) can be expressed as:

$$\alpha = \gamma B_1 t_p \quad [1.12]$$

where t_p is the pulse duration and B_1 is its RF magnetic field strength.

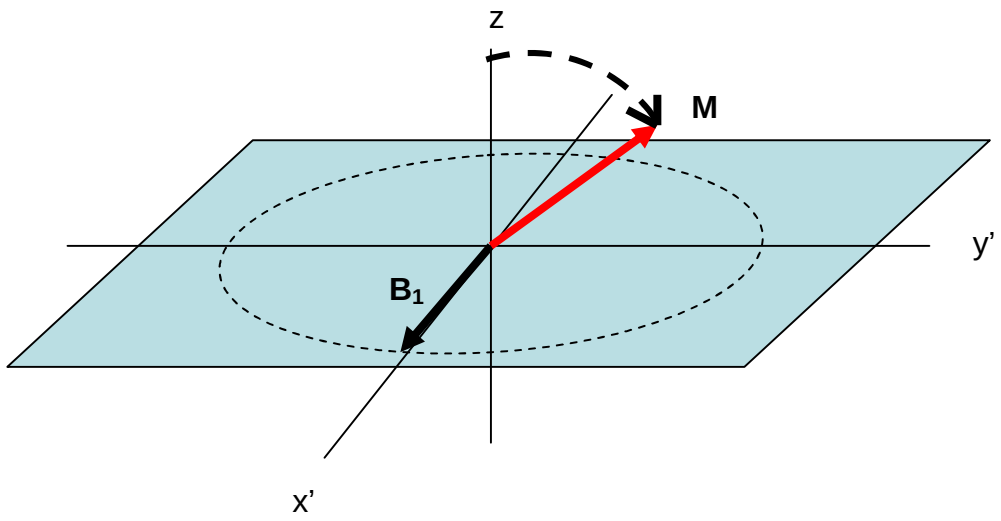

Figure 1.8

The effect of a radio-frequency excitation pulse on the net magnetisation vector in the rotating frame. The application of a radio-frequency excitation pulse with magnetic field B_1 applied along the x axis acts to tilt M_0 toward the transverse axis.

The application of a 90^o pulse acts to bring the spins into phase coherence so M possesses a large amplitude in the transverse plane. Thus a signal can be detected as the transverse rotation induces voltage in a receiver coil (see *Figure 1.9*).

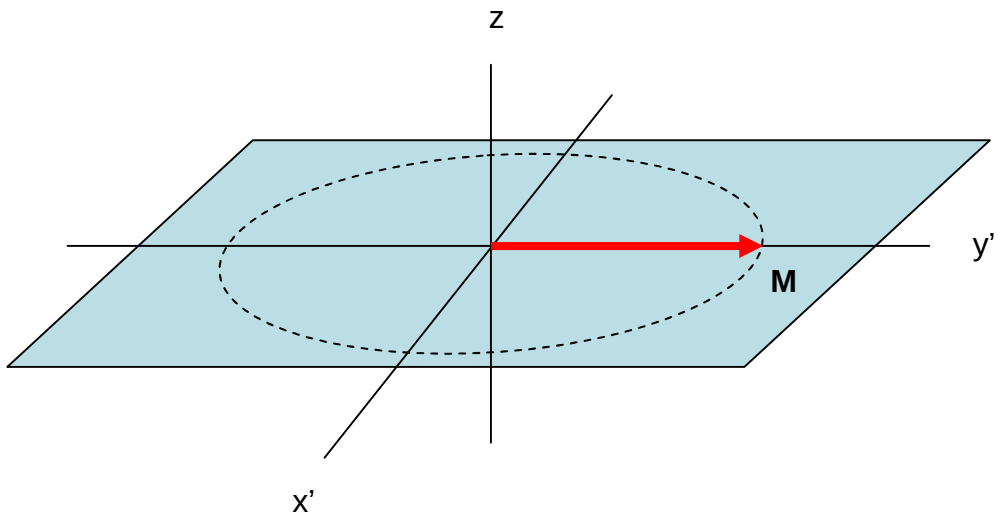

Figure 1.9
The net magnetisation in the rotating frame directly after a 90^o excitation RF pulse in the rotating frame. The application of a 90^o RF pulse acts to bring M into phase coherence in the transverse plane.

1.8.3 Spin-Spin Relaxation and the Spin Echo Acquisition

M decays rapidly in milliseconds following excitation due to the dephasing of the protons, known as the free induction decay (FID). However in MRI, this signal is not generally measured to generate an image. We use magnetic gradients to generate a gradient echo or an additional RF "refocusing" pulse to generate a spin echo (see *Figure 1.10*).

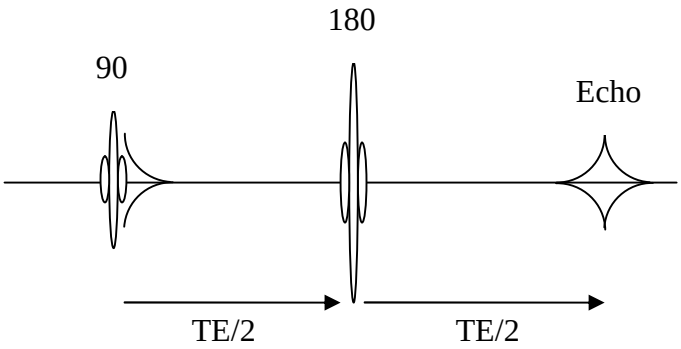

Figure 1.10
The basic spin echo acquisition. A 90^0 RF pulse is applied before a 180^0 or refocusing pulse to generate an echo which is measured using a receiver coil. The total time for transverse de-phasing is the echo time (TE = TE/2+TE/2).

In a spin echo sequence, spins de-phase following the excitation pulse resulting in a reduction in the net transverse magnetisation. This is because each of the spins experiences a different magnetic field following the 90^o pulse due to inhomogeneities in the main field. In the rotating frame depicted in Figure 1.11, spins which experience a strong magnetic field relative to the average magnetic field of the sample move clockwise, spins which experience a weak magnetic field relative to the average magnetic field move anticlockwise.

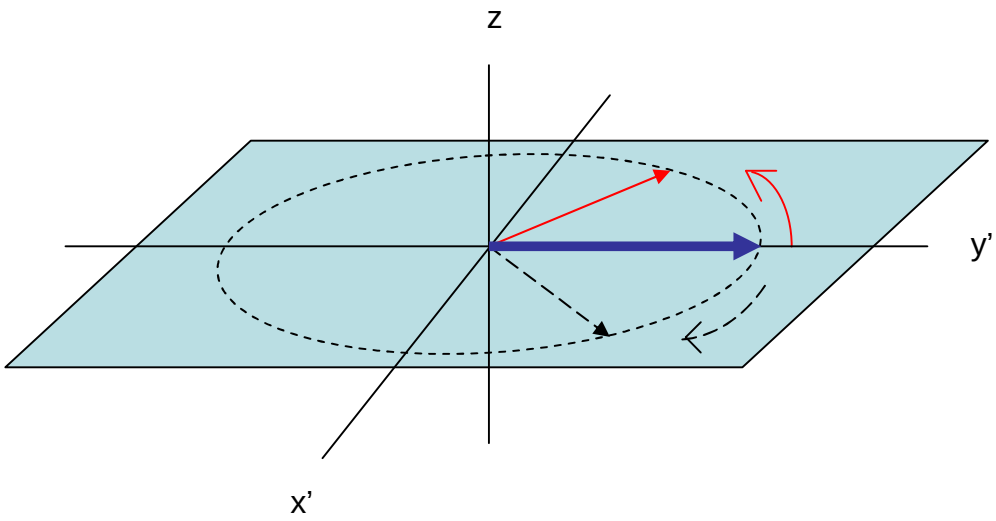

Figure 1.11

The de-phasing of the signal following excitation into the transverse plane (rotating frame). Directly after the 90^0 RF pulse, the spins are in phase and the transverse component of M_0 (blue arrow) has relatively large amplitude. The excited spins within the imaging volume experience different local magnetic fields. As a result, some precess slightly slower and some precess slightly faster than the Larmor frequency. This causes the transverse magnetisation of the spins to fan out thus reducing the magnitude of M_0.

After a half echo time (TE/2) a 180^o pulse is applied. This acts to flip the spins 180^o about the *y*'-axis and reverses their phase. The different field strengths that the spins experience now act to re-phase the net magnetisation (see *Figure 1.12*).

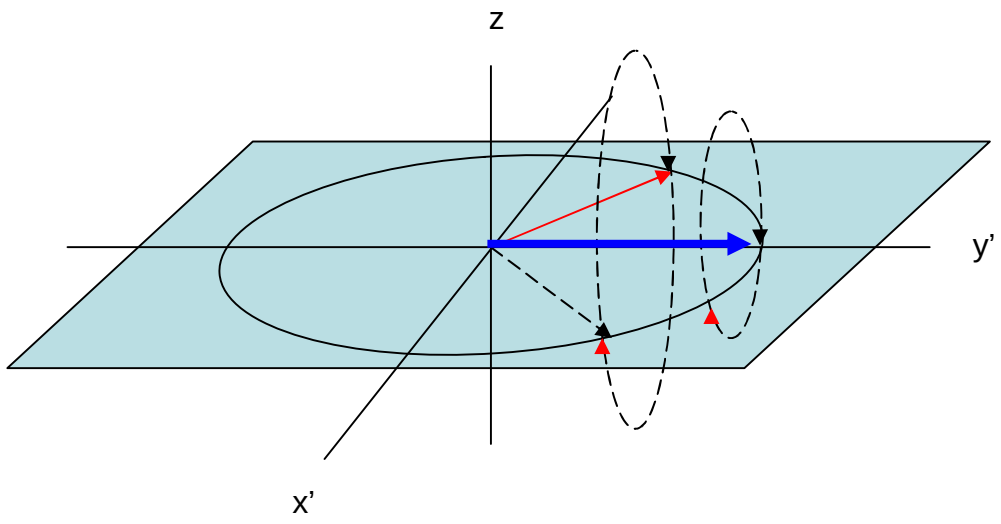

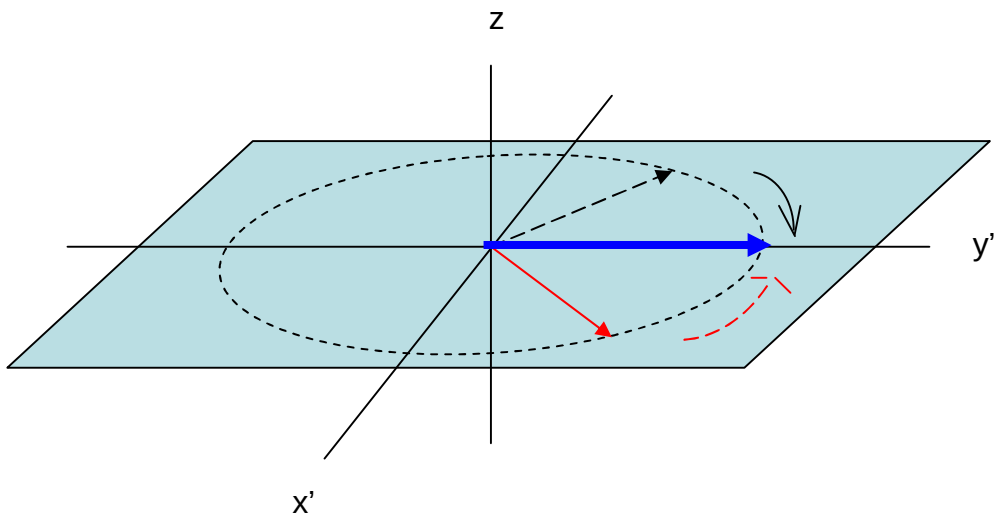

Figure 1.12
The action of the 180^0 refocusing pulse (applied along the y-axis) to the spins in the transverse plane (rotating frame). The 180^o RF pulse acts to invert the "fan" of transverse magnetisation 180^o about the y-axis. As a result, spins that were rotating faster than ω_0 now move clockwise towards M (blue arrow), spins that were precessing slower than ω_0 move towards M.

However at the time of the echo, the spins are not perfectly refocused. This is a result of spin-spin or transverse relaxation. If each of the spins just experienced a single resonance frequency (ω_o) the magnetisation would precess coherently about the z axis with frequency ω_o. However if there is a range of different frequencies ($\Delta\omega_o$) nuclei will precess at different frequencies and in the rotating frame will disperse resulting in the decay of M_{xy} (the magnetisation in the transverse plane). Spin-spin relaxation involves phenomenon that cause an inherent broadening of the resonant linewidths. This is caused by two processes. First of all, the nuclear spins have a finite lifetime in a given energy state due to spin-lattice relaxation processes (see section1.9. *T1: The Longitudinal Relaxation Constant*). Consequently there is an inherent uncertainty in the resonance frequency resulting in a 'lifetime' broadening of the resonant frequencies by the amount $\Delta\omega_o \approx 1/T1$. Thus the processes that contribute to spin-lattice relaxation also influence transverse relaxation. However in *in-vivo* MRI, 'lifetime' broadening plays a more minor role in the T2 of different tissue types in comparison to the relaxation processes described below:

If one imagines a collection of excited spins in a perfect magnetic field, ignoring longitudinal relaxation (see *T1: The Longitudinal Relaxation Constant)*, if the spins were stationary they would all precess at the Larmor frequency and would remain in phase.

However the spins in biological tissue posses considerable kinetic energy and thus frequently collide. If two protons come together then each of them will experience a slightly higher or lower magnetic field, as the magnetic moment of the other proton adds or subtracts from the main field (see *Figure 1.13*). This causes the processional frequencies of the protons to change and thus the bulk magnetisation becomes de-phased. When the protons are again separated, they return to the Larmor frequency but each has acquired a different phase. Over a few ms this interaction will occur many thousands of times for each proton and the vector sum in the transverse direction (that gives the measured signal) gradually decays to zero. No energy is lost from the system of spins during this process, only phase coherence. The decay is an exponential process, the speed of which is characterised by the transverse decay or T2 constant:

$$S = S_0(\exp^{(-TE/T2)}) \qquad [1.13]$$

Where S is the measured signal; S_0 is the measured signal when there is no spin-spin relaxation and TE is the echo time.

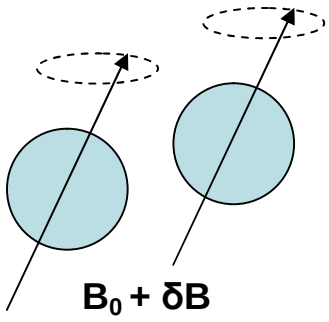

Figure 1.13

Protons collide with other protons and as a result experience a slightly different magnetic field (δB). Thus their rate of precession deviates slightly from the Larmor frequency by the amount ωδB.

The molecular interactions that cause spin-spin relaxation were investigated by Bloembergen, Purcell and Pound, commonly known as the BBP theory of relaxation [Bloembergen *et al.*, 1948]. They devised the theory based on the principle that every atom or molecule is in constant motion; rotating, vibrating and translating in random directions. Molecules exist in each state of motion for approximately 10^{-12} seconds before colliding with another molecule thus changing its state of motion. This time is known as the correlation time (τ_c). τ_c is short in gasses where molecules have relatively high levels of kinetic energy and posses relatively high mean velocity whereas τ_c tends to be longer in solids where molecules move relatively slowly. τ_c is also sensitive to temperature as higher temperatures give molecules more kinetic energy and shorter τ_c. When spins are tumbling very rapidly (short τ_c) then a particular spin will experience a local magnetic field with a high frequency that effectively averages out over a few milliseconds. This behaviour is termed "motional averaging" and results in a relatively homogenous local field. In this instance de-phasing occurs relatively slowly (high T2 constant). In contrast, a slowly tumbling molecule will see a relatively low frequency magnetic field inhomogeneity and will become rapidly de-phased following excitation. Different types of biological tissue possess a marked difference in the speed of molecular tumbling and as a result have different transverse relaxation times. For example, in arterial blood or CSF protons are frequently colliding and therefore the spin-spin magnetic field inhomogeneities are generally high frequency, yielding relatively slow transverse relaxation. Conversely, protons that are "bound" to larger macromolecules (e.g. in myelin) undergo rapid spin-spin relaxation as their motion is restricted by their molecular environment (very short T2 constant). Consequently, such structure is often invisible to MRI as the signal will have almost totally de-phased by the time an echo is detected. In brain tissue, water molecules are in a mixed state of bound and free and the rate of transverse de-phasing (T2 constant) will be intermediate. Most biological tissues possess a mixture of free and bound protons and behave in this way. Therefore by estimating the T2 of a voxel we can gain information as to the type of tissue that we are imaging. For example, if a voxel contains mostly grey matter the T2 will be approximately 60-70ms whereas if we measure the T2 of a voxel that

represents blood in an artery we would expect a marked increase (200ms) at the same field strength (Stanitz *et al.*, 2005). In practice, voxels in MRI exhibit partial volume effects and contain more than one tissue type with more than one associated T2 value. If the sampled protons are in fast exchange (relative to the experimental echo times) then the relaxation behaviour will be mono-exponential, representing a weighted average of the tissues present. If there is slow or restricted exchange then bi-exponential transverse decay (if there are two tissue types in slow exchange) may be observable.

In chapter 2 we measure the ASL, perfusion weighted signal at several different echo times. Using equation 1.13, we can use these measurements to estimate the T2 of this signal. The T2 will be determined by the distribution of labelled blood water in different molecular environments during image acquisition. In this way we can estimate the cerebral vascular location of labelled blood water that has flowed into the brain.

1.9 T1: THE LONGITUDINAL RELAXATION CONSTANT

Following excitation by a RF pulse, the spins will gradually relax back to equilibrium, parallel to the longitudinal axis. This process is known as longitudinal or spin-lattice relaxation, the rate of which is characterised by relaxation constant T1. Typically the rate of this decay will be significantly less than the rate of spin-spin (T2) relaxation. Unlike transverse relaxation, a loss of energy occurs in this process. This is to be expected given that energy (from the RF excitation pulse) is required to bring the spins into the transverse plane. The T1 constant can be described as the rate at which this energy to transferred to the lattice

In normal tissues, T1 values are related to macromolecular concentration, water binding and water content. For a detailed description of the mechanisms involved in T1 relaxation, see [Gadian, 1995].Spin-lattice relaxation is a particularly important consideration in ASL as differences in the longitudinal magnetisation gives the flow related contrast that we measure. Longitudinal relaxation of labelled blood water occurs after labelling. Like T2 decay, the rate of longitudinal relaxation is dependent on the molecular environment of the labelled blood water. For example the rate of T1 decay will be relatively slow in the blood but will increase when the labelled blood water exchanges into the tissue. Thus longitudinal relaxation of labelled spins not only acts to

reduce to magnitude of the ASL signal, decreasing the SNR of the measurements but must also be carefully accounted for to avoid errors in CBF quantification.

1.10 PRINCIPLES OF DIFFUSION MRI

The measured NMR signal can be made sensitive to the extent of diffusion (random molecular motion) of the sampled protons. The effect of diffusion on the measured signal can be understood from a simple pulsed gradient spin echo (or Stejskal and Tanner) method. This consists of a standard spin echo acquisition with identical gradients placed on either side of the 180^o pulse (see *Figure 1.14*).

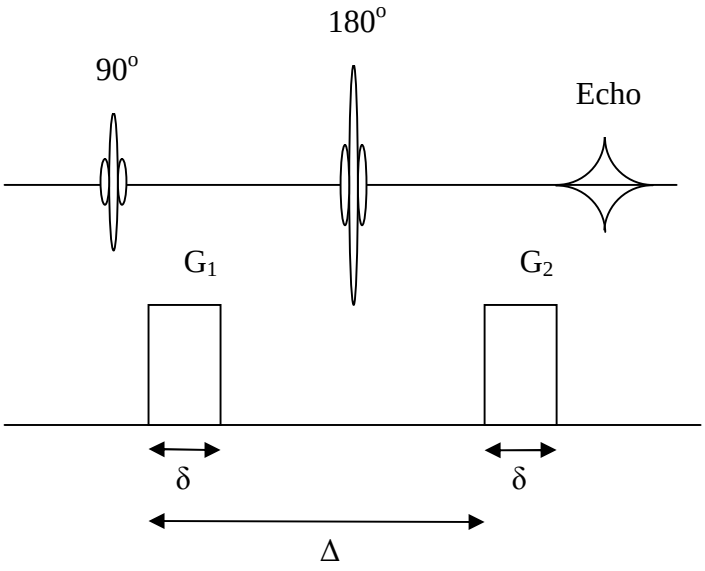

Figure 1.14

The Stejskal Tanner experiment. Gradients of equal duration and amplitude are placed either side of the 180^0 re-focussing pulse in a spin echo acquisition. In this example, for conceptual clarity, the gradient separation (Δ) is considered to be considerably greater than the gradient duration (δ).

The first gradient pulse induces a phase shift φ_1 of the spin traverse magnetisation, which depends on the spin position. If the first gradient (amplitude G1) is applied along the slice select (z) axis, then the phase shift is equal to the following:

$$\phi_1 = \gamma \int_0^{\delta} G_1 z_1 dt = \gamma G \delta z_1 \qquad [1.14]$$

where δ is the gradient duration; ΔM is the gradient separation; γ is the gyromagntic ratio; z_1 is the spin position during the first gradient and for conceptual simplicity is considered to be constant as δ is relatively short. After the 180° refocusing pulse, the second gradient (amplitude G2) will result in a phase shift φ_2:

$$\phi_2 = \gamma \int_{\Delta}^{\Delta+\delta} G_2 z_2 dt = \gamma G \delta z_2 \qquad [1.15]$$

where z_2 is the spin position during the second gradient (G_2). The overall phase shift μ(φ) can therefore be expressed as:

$$\mu(\varphi) = \varphi_2 - \varphi_1 = \gamma G \mu(z_1 - z_2) \quad [1.16]$$

So static spins (where $z_1 = z_2$) will not experience any dephasing as $\varphi_1 = \varphi_2$. However moving spins (where $z_1 \neq z_2$) will accumulate a net phase shift ($\varphi_1 - \varphi_2$). When we measure the echo, we sample the total magnetisation of the volume of tissue that has been excited. This can be thought of as the vector sum of the magnetic moments of the individual nuclei whose magnetic moments will depend on the extent of their motion during time interval Δ. The measured signal (M) relative to the signal with no diffusion weighting (M_0) can then be expressed as:

$$\frac{M}{M_0} = \sum_{j=1}^{N} \exp(i\mu(\phi_j)) \qquad [1.17]$$

This equation can be resolved with knowledge of the net phase distribution. Firstly, assuming free diffusion in a uniform medium the probability of finding a spin at position z_1 is constant. If we then define $\mathbf{P}(z_2|z_1,\Delta)dz_2$ as the conditional probability of finding a spin at z_1 during gradient G_1 and then between z_2 and dz_2 after Δ, the measured signal can be defined as follows:

$$\frac{M}{M_0} = \int_{-\infty}^{\infty}\int_{-\infty}^{\infty} \exp(i\gamma G \mu(z_1 - z_2)) \times \mathbf{P}(z_2 \mid z_1, \Delta) dz_1 dz_2 \quad [1.18]$$

For free diffusion in one direction the conditional probability is given by [Le Bihan, 1995]:

$$\mathbf{P}(z_1 \mid z_2, \Delta) = \frac{1}{\sqrt{4\pi D\Delta}} \exp\left[\frac{-(z_1 - z_2)^2}{4D\Delta}\right] \qquad [1.19]$$

where D is the diffusion coefficient, representing to the extent of diffusion in the medium. We can then combine equations 1.18 and 1.19 to obtain:

$$\frac{M}{M_0} = \exp(-(\gamma G\mu)^2 D\Delta) \qquad [1.20]$$

Or by taking the logarithm,

$$\ln\left(\frac{M}{M_0}\right) = -(\gamma G\mu)^2 \Delta D \qquad [1.21]$$

Equation 1.21 equates the measured signal attenuation to the diffusivity and is the basis for diffusion measurement using MRI. However equation 1.21 only gives an approximation as to the measured signal attenuation, since the duration (δ) of each diffusion gradient (G_1 & G_2) may not be negligible in comparison to Δ (as we have assumed so far). Therefore a more precise solution can be found when taking δ into account:

$$\ln\left(\frac{M}{M_0}\right) = -(\gamma G\delta)^2 (\Delta - \delta/3) D \qquad [1.22]$$

The quantity (Δ-δ/3) is known as the diffusion time τ and is related to molecular motion through the Einstein equation:

$$\left\langle r^2 \right\rangle = 6D\tau \qquad [1.23]$$

where (r^2) is the mean displacement of a collection of molecules. The *b*-value is the established term to describe the extent of diffusion weighting in the sequence.

$$b = \left(\gamma G \mu\right)^2 (\Delta - \delta / 3) \qquad [1.24]$$

Therefore:

$$\ln\left(\frac{M}{M_0}\right) = -bD \qquad [1.25]$$

In biological tissue there are many complicated processes that render the “free diffusion” model an oversimplification. Therefore D is referred to as the “apparent” diffusion coefficient (ADC). An established approach to estimating the ADC of a sample is to measure the signal over a range of *b*-values using the sequence shown in Figure 1.14. According to equation 1.25, the measured signal will have a linear dependence on the applied *b* -value, assuming free diffusion in a homogenous medium. The ADC can then be estimated by calculating the gradient of this plot (see *Figure 1.15*).

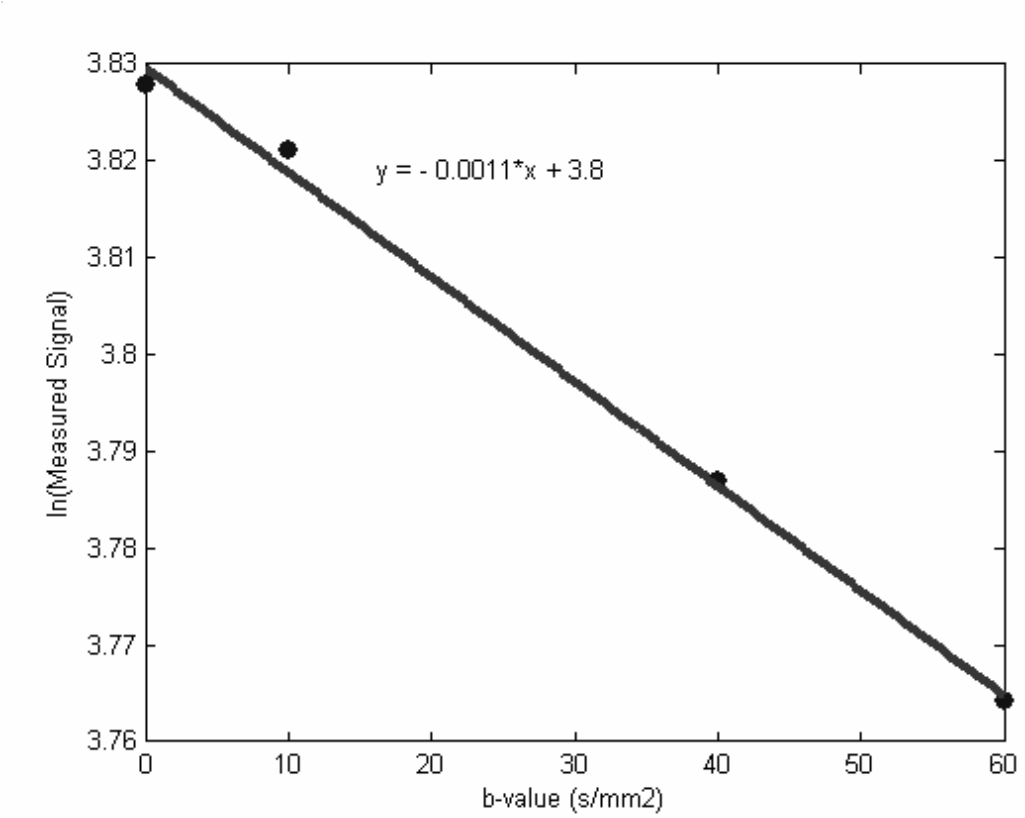

Figure 1.15
In-vivo results showing the measured signal from a ROI in the cortex of the rat brain. The slope is equal to the ADC (estimated to be approximately 0.11 x 10^{-3} mm^2/sec).

In chapter 4 we implement diffusion gradients as illustrated in Figure 1.14 with the intention of selectively suppressing the signal from the intra-vascular compartment. The brain capillary vasculature may be described as a network of randomly oriented segments where direction of flow changes frequently. Blood flowing in the micro-vasculature and capillaries can be thought of as possessing a fast pseudo-coefficient [Le Bihan, 1995]. This pseudo-ADC is around 10 times greater than that of the tissue. This effect can be seen in Figure 1.16. Figure 1.16 shows the mean cortical perfusion-weighted signal (×10) generated using ASL as a function of *b*-value in addition to the tissue signal reported in Figure 1.15. The tissue signal was taken from the control acquisitions (used to generate the perfusion-weighted images) and so the tissue and perfusion-weighted signal can be thought of as effectively being acquired simultaneously. These *in-vivo* data are shown here to aid the clarity of this explanation. By fitting a simple linear model to the data, the ADC of the labelled blood in the cortex is calculated to be approximately 8 times that of the static tissue. This result reflects the fact that labelled blood in the microvasculature makes up a significant proportion of the

ASL signal [Silva *et al*., 1997(a)] whereas if we consider the entire tissue, the blood volume is around 3% in the rat brain [Shockley and LaManna, 1998]]. Therefore this fast-pseudo coefficient is more dominant in the ASL signal and as a result the estimated ADC of the perfusion-weighted signal (over the *b*-values used in the experiment) is considerably greater than the control.

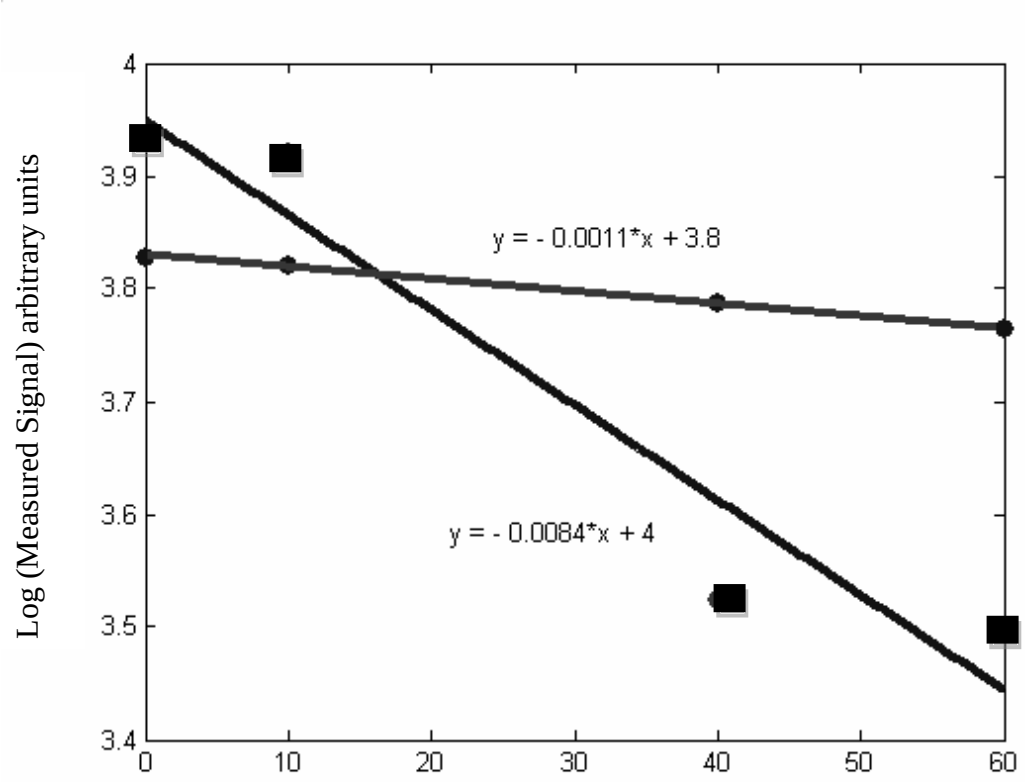

Figure 1.16
In-vivo results showing the measured perfusion weighted (labelled blood water- black squares) and control (static tissue – black dots) signal from a ROI in the cortex of the rat brain. The amplitude of the perfusion weighted signal has been multiplied by 10 so it is of the order of the control signal for clarity of display. The solid lines represent the linear fits to the data. The gradient of the fits represents the calculated ADC.

1.11 HALF-FOURIER ACQUISITIONS AND THE POCS RECONSTRUCTION

In chapter 2 we implement half-Fourier acquisitions. In this approach we do not sample the whole of k-space but rather, just over half. We then used a constrained reconstruction technique to generate the images from the acquired data. Our motivation was to reduce the minimum echo time of the acquisitions to improve the range of coverage of the transverse decay. In addition we aimed to keep each acquisition short so that we could acquire several images during the decay. Half-Fourier imaging takes advantage of the conjugate symmetry of *k*-space. Specifically, if the frequency representation S(k) of a real-valued function I(x) is known for $k \geq 0$ then S(-k) can (in theory) be generated based on the Hermitian symmetry:

$$S(-k) = S^{*}(k) \qquad [1.26]$$

Therefore, in theory it is only necessary to acquire one half of k-space. In practice subject motion and magnetic field inhomogeneities introduce a non-zero phase into the image function. However this can be adequately overcome by acquiring a few additional lines of encoding across the centre of k space as illustrated in Figure 1.17.

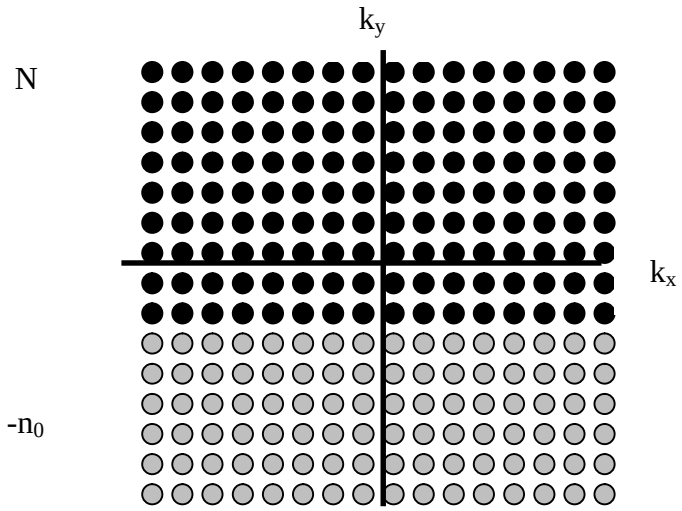

Figure 1.17
A typical sampling regime used for half-Fourier acquisitions. ● *represents points in k-space that are sampled and* ◍ *represents points that are not sampled [Liang and Lauterbur, 2000].*

In Chapter 4 we acquire half of *k*-space (32 lines) plus 4 additional lines in the phase encoding direction. The half-Fourier reconstruction problem can be formally described as follows:

Given:

$$S[n] = \int_{-\infty}^{\infty} I(x) e^{-i2\pi n \Delta k x} dx \qquad -n_0 \le n \le N \qquad [1.27]$$

Determine: I*(x)*

where n_o is much smaller than N. In chapter 4 we use the projection onto convex sets (POCS) algorithm to reconstruct the images [Liang *et al.*, 1992]. This is an automated iterative approach where a phase correction is first estimated and then combined with the measured data to compute the final reconstruction.

First of all S(k) is zero filled to generate a 64 by 64 data set. The first image estimate is performed using:

$$I_1(x) = F^{-1}(S(k))$$

Then the phase estimate ($e^{i\varphi(x)}$, generated from the central, symmetric k-space data) is combined with the magnitude of the estimated image:

$$\tilde{I}_1(x) = |I_1(x)| e^{i\phi(x)}$$

Then the data is Fourier transformed to create a new data set:

$$\hat{S}_1(x) = F(\tilde{I}_1(x)))$$

$S_{new}(k)$ is then formed by merging $S^{\wedge}_1$ where the lines of k-space were not acquired in S(k). The process is then repeated until no significant change occurs.

1.12 MRI APPARATUS

All the MRI experiments described in this thesis were performed by myself using a 2.35T horizontal magnet (see *Figure 1.18*) with a 120mm bore (Oxford Instruments Eynsham, UK), interfaced to a Surrey Medical Imaging Systems (SMIS, UK) console. The operating system for the console was Windows 3.1.

Figure 1.18 *The Experimental MRI scanner used in the imaging studies described in this thesis. The scanner was installed on the fourth floor of the UCL Institute of Child Health in 1984.*

An Alderman-Grant volume coil (60mm length) was used for RF transmission, and signal was received using a passively decoupled, single loop surface coil of 1cm diameter (see *Figure 1.19*).

In all the experiments, anaesthesia was induced using 3% halothane in 100% O_2 and was maintained via a nose cone at 2% halothane in 100% O_2 whilst the animal was placed on a custom designed Perspex probe (see *Figure 1.19*). The rodent's head was secured using ear bars to minimise motion during the data acquisition. Once the probe was fixed in the scanner, halothane concentration was reduced to 1.25% in 60% N_2O and 40% O_2. Body core temperature was measured throughout using a rectal thermometer and maintained at 36.5 ± 0.5^{o}C using a heated blanket during preparation and warm air flow into the magnet throughout the data acquisition period.

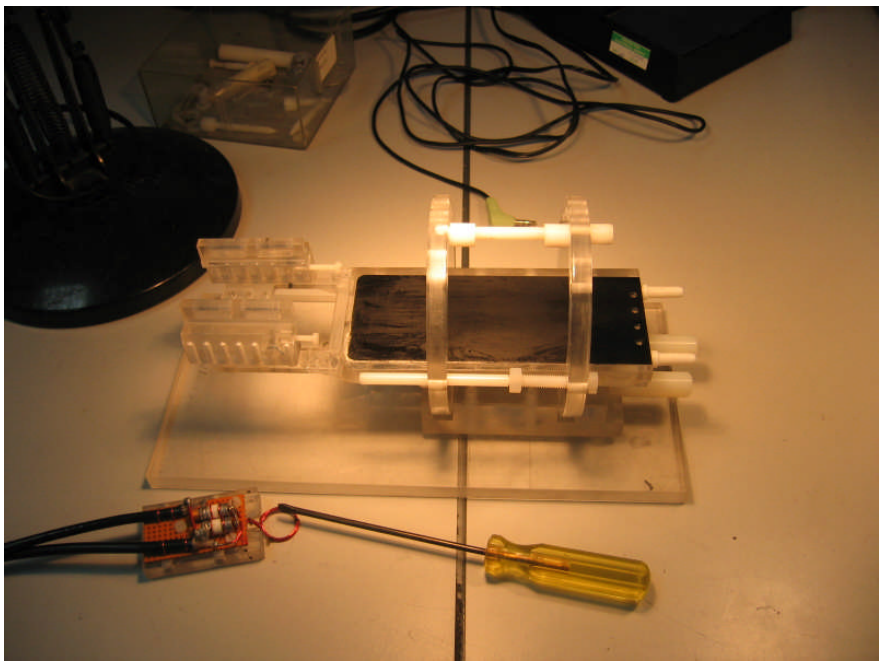

Figure 1.19
The probe used to transport and hold the rodent in position inside the magnet. The surface coil (diameter 1cm) used for MR signal detection is also shown. This coil was smaller than those used by other users of the scanner. As a result the SNR in the brain regions proximal to the coil (e.g. cortex) was relatively high. Conversely, marked sensitivity "drop off" means that the SNR decreases rapidly with the distance from the coil and brain regions far from the coil possess relatively low SNR.

All experiments were performed in accordance with the UK Home Office animals act (1986).

1.13 CONCLUSION AND CLOSING REMARKS

In this chapter I have explained the principles of CBF quantification using ASL techniques beginning with the original implementation [Detre *et al*., 1992] through to the most recent advances. I have also explained the potential difficulties that may confound accurate, efficient and robust ASL CBF quantification, all of which require careful consideration during ASL application. In addition I have described the established theory behind the key additional MRI contrast mechanisms and techniques that underpin the experiments detailed in Chapter 2 (T2 and T1 relaxation, diffusion imaging and half-Fourier acquisition and reconstruction). Now I continue to Chapter 2 which describes experiments designed to characterise the origin of the ASL signal in the rat brain using Multi-Echo acquisitions.

1.14 REFERENCES

Alsop DC, Detre JA.(1996). Reduced transit-time sensitivity in noninvasive magnetic resonance imaging of human cerebral blood flow. Journal of Cerebral Blood Flow And Metabolism 16, 1236-1249.

Alsop DC, Detre JA.(1998). Multisection cerebral blood flow MR imaging with continuous arterial spin labelling. Radiology 208, 410-416

Berr SS, Mai VM.(1999) Extraslice Spin Tagging (EST) magnetic resonance imaging for the determination of perfusion. Journal of Magnetic Resonance Imaging 9,146-150.

Bloembergen N, Purcell EM, Pound RV. (1948) Relaxation effects in nuclear magnetic resonance absorption. Physical Review 73, 679-712.

Branch CA, Hernandez L, Yongbi MN, Huang NC, Helpern JA.(1999) Rapid and continuous monitoring of cerebral perfusion by magnetic resonance line scan assessment with arterial spin tagging. NMR In Biomedicine 12, 15-25.

Buxton RB, Frank LR, Wong EC, Siewert B, Warach S, Edelman RR.(1998). A general kinetic model for quantitative perfusion imaging with arterial spin labelling. Magnetic Resonance in Medicine 40, 383-396.

Calamante F, Williams SR, van Bruggen N, Kwong KK, Turner R.(1996) A model for quantification of perfusion in pulsed labelling techniques. NMR Biomed. 9:79-83. Erratum in: NMR Biomed 1996 9:277.

Calamante F, Lythgoe MF, Pell GS, Thomas DL, King MD, Busza AL, Sotak CH, Williams SR, Ordidge RJ, Gadian. (1999). Early changes in water diffusion, perfusion, T1 and T2 during focal cerebral ischemia in the rat studied at 8.5T. Magnetic Resonance in Medicine 41, 479-485.

Carr JP, Buckley DL, Tessier J, Parker GJ.(2007). What levels of precision are achievable for quantification of perfusion and capillary permeability surface area product using ASL? Magnetic Resonance in Medicine 58(2), 281-9.

Chalela JA, Alsop DC, Gonzalez-Atavales JB, Maldjian JA, Kasner SE, Detre JA.(2002). Magnetic resonance perfusion imaging in acute ischemic stroke using continuous arterial spin labelling. Stroke, 31:680-687

Chen Q, Siewert B, Bly BM, Warach S, Edelman RR.(1997). STAR-HASTE: perfusion imaging without magnetic susceptibility artefact. Magnetic Resonance in Medicine 38, 404-8.

Chen J, Licht DJ, Smith SE, Agner SC, Mason S, Wang S, Silvestre DW, Detre JA, Zimmerman RA, Ichord RN, Wang J.(2009). Arterial spin labeling perfusion MRI in pediatric arterial ischemic stroke: initial experiences. Journal of Magnetic Resonance Imaging. 29:282-90.

Chng SM, Petersen ET, Zimine I, Sitoh YY, Lim CC, Golay X.(2008) Territorial arterial spin labelling in the assessment of collateral circulation: comparison with digital subtraction angiography. Stroke 39,3248-54.

Davies NP, Jezzard P.(2003). Selective arterial spin labelling (SASL): perfusion territory mapping of selected feeding arteries tagged using two-dimensional radiofrequency pulses. Magnetic Resonance In Medicine 49,1133-1142.

Detre JA, Leigh JS, Williams DS, Koretsky AP.(1992). Perfusion imaging. Magnetic Resonance in Medicine 23,37-45.

Detre JA, Alsop DC, Vives LR, Maccotta L, Teener JW, Raps EC,(1998). Noninvasive MRI evaluation of cerebral blood flow in cerebrovascular disease. Neurology 50, 633-641.

Duang TQ, Kim DK, Ugurbil K, Kim SG.(2001). Localised cerebral blood flow response at submilimeter columnar resolution. Proceeding of the national academy of sciences 98, 10904-10909.

Eastwood JD, Holder CA, Hudgins PA, Song AW.(2002). Magnetic resonance imaging with lateralized arterial spin labelling. Magnetic Resonance Imaging 20, 583-586.

Edelman RR, Siewert B, Darby DG, Thangaraj V, Nobre AC, Mesulam MM.(1994). Qualitative mapping of cerebral blood-flow and functional localization with echo-planar mr-imaging and signal targeting with alternating radio-frequency. Radiology 192,513-520.

Edelman RR, Chen Q.(1998). EPISTAR MRI: multislice mapping of cerebral blood flow. Magnetic Resonance in Medicine 40, 800-805.

Ewing JR, Cao Y, Fenstermacher JD.(2001).Single-coil arterial spin tagging for estimating cerebral blood flow as viewed from the capillary: relative contributions of intra- and extravascular signal. Magnetic Resonance in Medicine 46,465-475.

Fernandez-Serra MA, Edlow BA, Hoang A, Wang J, Detre JA.(2007). Snap-Shot ASL Presented at the 15th ISMRM, Berlin.

Fernandez-Seara MA, Edlow BL, Hoang A, Wang J, Feinberg DA.(2008). Minimizing acquisition time of arterial spin labelling at 3T. Magnetic Resonance in Medicine 59,1467-71.

Francis ST, Bowtell R, Gowland PA (2008) Modeling and optimization of Look-Locker spin labeling for measuring perfusion and transit time changes in activation studies taking into account arterial blood volume. Magnetic Resonance in Medicine 59 316-25

Gadian DG. NMR and its applications to living systems (1995, second edition). Chapter 6.3 Relaxation.Oxford Science Publications.

Gallichan D, Jezzard P.(2008). Modelling the effects of dispersion and pulsatility of blood flow in pulsed arterial spin labelling. Magnetic Resonance in Medicine 60, 53-63.

Garcia DM, Duhamel G, Alsop DC.(2005). Efficiency of inversion pulses for background suppressed arterial spin labelling. Magnetic Resonance in Medicine 54,366-372.

Golay X, Petersen ET, Zimine I.(2007). Novel Developments in Arterial Spin Labelling based Perfusion Imaging. MRI Perfusion and Diffusion Workshop, Brazil.

Grossman M, Alsop D, Detre JA.(2001). Perfusion fMRI using arterial spin labelling in Alzheimer's disease and frontal temporal dementia: correlations with language. Brain Language 79, 94-95.

Guenther M, Bock, Schad LR.(2001). Arterial spin labelling in combination with a look-locker sampling strategy: inflow turbo-sampling EPI-FAIR (ITS-FAIR). Magnetic Resonance in Medicine. 46, 974-84.

Guenther M, Oshio K, Feinberg. (2005). Single-Shot 3D Imaging Techniques Improve Arterial Spin Labelling Perfusion Measurements. Magnetic Resonance in Medicine, 54, 491-498.

Guenther M. (2006(a)). Rapid Imaging of Multiple Vascular Territories Using Cycled Arterial Spin Labelling with Independent Component Analyses. Presented at the 15th ISMRM , Seattle.

Guenther M.(2006(b)). Highly Efficient Accelerated Acquisition of Perfusion Inflow Series by Cycled Arterial Spin Labelling. Presented at the 15th ISMRM ,Seattle.

Hendrikse J, van Osch MJ, Rutgers DR, Bakker CJ, Kappelle LJ, Golay X, van der Grond J. (2004). Internal carotid artery occlusion assessed at pulsed arterial spin-labeling perfusion MR imaging at multiple delay times. Radiology.233(3):899-904.

Hunsche S, Sauner D, Schreiber WG, Oelkers P, Stoeter P. (2002). FAIR and dynamic susceptibility contrast-enhanced perfusion imaging in healthy subjects and stroke patients. Journal of Magnetic Resonance Imaging.16:137-46.

Jahng G-H, Zhu X-P, Matson GB, Weiner MW, Schuff N.(2003). Improved perfusion-weighted MRI by a novel double inversion with proximal labelling of both tagged and control images. Magnetic Resonance in Medicine 49, 307-314.

Kansagra AP, Wong EC.(2008). Mapping of Vertebral Artery Perfusion Territories using Arterial Spin Labelling MRI. Journal of Magnetic Resonance Imaging 28, 762- 766.

Kim SG. (1995). Quantification of Regional Cerebral Blood Flow Change by Flow Sensitive Alternating Inversion Recovery (FAIR). Application to functional mapping. Magn Reson Med 34, 293-301.

Kimura H, Kado H, Koshimoto Y, Tsuchida T, Yonekura Y, Itoh H. (2005). Multislice continuous arterial spin-labeled perfusion MRI in patients with chronic occlusive cerebrovascular disease: a correlative study with CO2 PET validation. Journal of Magnetic Resonance Imaging 22(2):189-98.

Koziac AM, Winter J, Lee TY, Thompson RT, St Lawrence. (2008). Magnetic Resonance Imaging 26, 543-53.

Kwong KK, Belliveau JW, Chesler DA, Goldberg IE, Weisskoff RM, Poncelet BP, Kennedy DN, Hoppel BE, Cohen MS, Turner R, Cheng HM, Brady TJ, Rosen BR. (1992). Dynamic magnetic resonance imaging of human brain activity during primary sensory activation. Proceedings of the National Academy of Sciences 89, 5675-5679.

Kwong KK, Chesler DA, Weisskoff RM, Donahue KM, Davis TL, Ostergaard L.(1995). MR perfusion studies with T1-weighted echo-planar imaging. Magnetic Resonance in Medicine 34,878-887.

Lai S, Wang J , Jahng GH.(2001).FAIR exempting separate T(1) measurements (FAIREST): a novel technique for online quantitative perfusion imaging and multi-contrast fMRI. NMR in Biomedicine 14, 507-516.

Li KL, Zhu X, Hylton N, Jahng GH, Weiner MW, Schuff N. (2005). Four-phase single-capillary stepwise model for kinetics in arterial spin labeling MRI. Magnetic Resonance in Medicine 53,511-518.

Z.-P. Liang, F. B. Boada, R. T. Constable, E. M. Haacke, P. C. Lauterbur, and M. Smith. (1992) Constrained reconstruction methods in MR imaging. Reviews of Magnetic Resonance in Medicine, vol. 4, no. 2, pp. 67–185, 1992.

Liu HL, Kochunov P, Hou J, Pu Y, Mahankali S, Feng CM, Yee SH, Wan YL, Fox PT, Gao JH. (2001). Perfusion-weighted imaging of interictal hypoperfusion in temporal lobe epilepsy using FAIR-HASTE: comparison with H(2)(15)O PET measurements. Magnetic Resonance in Medicine 45, 431-435.

Luh WM, Wong EC, Bandettini PA, Hyde JS.(1999).QUIPSS II with thin-slice TI1 periodic saturation: a method for improving accuracy of quantitative perfusion imaging using pulsed arterial spin labelling. Magnetic Resonance in Medicine 41, 1246-1254.

Mai VM, Berr SS.(1999). MR perfusion imaging of pulmonary parenchyma using pulsed arterial spin labelling techniques: FAIRER and FAIR. Journal of Magnetic Resonance Imaging 9, 483-487.

Mildner T, Trampel R, Möller HE, Schäfer A, Wiggins CJ, Norris DG.(2003). Functional perfusion imaging using continuous arterial spin labeling with separate labeling and imaging coils at 3T. Magnetic Resonance in Medicine 49, 791-795.

Ogawa S, Lee TM, Kay AR, Tank DW.(1990). Brain magnetic resonance imaging with contrast dependant on blood oxygenation. Proceedings of the national academy of sciences U S A. 87(24):9868-72.

Ostergaard L. (2005). Principles of cerebral perfusion imaging by bolus trackin. Journal of Magnetic Resonance Imaging 22, 710-7.

Parkes LM, Tofts PS.(2002). Improved accuracy of human cerebral blood perfusion measurements using arterial spin labeling: accounting for capillary water permeability. Magnetic Resonance in Medicine 48, 27-41.

Pell GS, Thomas DL, Lythgoe MF, Calamante F, Howseman AM, Williams SR.(1999) .Implementation of quantitative FAIR perfusion imaging with a short repetition time in time course studies. Magnetic Resonance in Medicine 41, 829-840.

Petersen ET, Zimine I, Ho YC, Golay X.(2006). Non-invasive measurement of perfusion: a critical review of arterial spin labelling techniques. British Journal of Radiology.79, 688-701.

Petersen ET, Lim T, Golay X.(2006). Model-free arterial spin labelling quantification approach for perfusion MRI. Magnetic Resonance in Medicine 55, 219-32.

Petersen ET, Golay X Is Arterial Spin Labelling Ready for the Prime time? (2008). Prilimary Results from the QUASAR Reproducibility Study. Proceedings of the 16th Annual Meeting of ISMRM, Toronto, Cananda, 2008 (Abstract 191)

Pollock JM, Whitlow CT, Deibler AR, Tan H, Burdette JH, Kraft RA, Maldjian JA (2008). Anoxic injury-associated cerebral hyperperfusion identified with arterial spin-labeled MR imaging. American Journal of Neural Radiology. 29:1302-7.

Quirk JD, Bretthorst GL, Duong TQ, Snyder AZ, Springer Jr CS, Ackerman JH, Neil JJ.(2003). Equilibrium Water Echange Between the Intra- and Extracellular Spaces of Mammalian Brain. Magnetic Resonance in Medicine 50, 493-499.

Schwarzbauer C, Heinke W.(1998). BASE imaging: a new spin labelling technique for measuring absolute perfusion changes. Magnetic Resonance in Medicine. 39, 717- 722.

Shockley RP, LaManna JC (1998). Determination of rat cerebral cortical blood volume changes by capillary mean transit time analysis during hypoxia, hypercapnia and hyperventilation. Brain Research 28;454; 170-178.

Silva AC, Zhang WG, Williams DS, Koretsky AP.(1995). Multi-slice MRI of rat brain perfusion during amphetamine stimulation using arterial spin labeling. Magnetic Resonance in Medicine 33, 209-214.

Silva AC, Williams DS, Koretsky AP.(1997a). Evidence for the exchange of arterial spin labeled water with tissue water in rat brain from diffusion-sensitized measurements of perfusion. Magnetic Resonance in Medicine 38, 232-237.

Silva AC, Zhang WG, Williams DS, Koretsky AP.(1997). Estimation of water extraction fractions in rat brain using magnetic resonance measurement of perfusion with arterial spin labelling. Magnetic Resonance in Medicine 37, 58-68.

Silva AC, Lee SP, Iadecola C, Kim SG. (2000). Early temporal characteristics of cerebral blood flow and deoxyhaemaglobin changes during somatosensory stimulation. Journal of Cerebral Blood Flow and Metabolism 20, 201-206.

Stanitz GJ, Odrobina EE, Pun J, Escaravage M, Graham SJ, Bronskill MJ, Henkelman RM (2005). T1, T2 relaxation and magnetization transfer in tissue at 3T. Magnetic Resonance in Medicine 54, 507-12.

St.Lawrence KS, Frank JA, Mclaughlin AC. (2000). Effect of restricted water exchange on cerebral blood flow values calculated with arterial spin tagging: a theoretical investigation. Magnetic Resonance in Medicine 44, 440-449.

St.Lawrence KS, Wang J.(2005). Effects of the apparent transverse relaxation time on cerebral blood flow measurements obtained by arterial spin labelling. Magnetic Resonance in Medicine 53, 425-433.

Talagala SL, Barbier EL, Williams DS, Silva AC, Koretsky AP. (1998). Multi-slice perfusion MRI using continuous arterial water labelling controlling for MT effects with simultaneous proximal and distil RF irradiation. Proceedings of the 6th Annual Meeting of ISMRM, Sydney.

Tanabe JL, Yongbi MN, Branch CA, Hrabe J, Johnson G, Helpern JA.(1999). MR perfusion imaging in human brain using the UNFAIR technique. Journal of Magnetic Resonance Imaging 9, 761-767.

Van Gelderen P, de Zwart JA, Duyn JH.(2008). Pittfalls of MRI Measurement of White Matter Perfusion Based on Arterial Spin Labelling. Magnetic Resonance in Medicine 59,788-795.

Yang YH, Frank JA, Hou L, Ye FQ, Mclaughlin AC, Duyn JH.(1998). Multislice imaging of quantitative cerebral perfusion with pulsed arterial spin labeling. Magnetic Resonance in Medicine 39, 825-832.

Ye FQ, Pekar JJ, Jezzard P, Duyn T, Frank JA, Mclaughlin AC.(1996). Perfusion imaging of the human brain at 1.5T using a single-shot EPI spin tagging approach. Magnetic Resonance in Medicine 36, 219-224.

Ye FQ, Mattay VS, Jezzard P, Frank JA, Weinberger DR, McLaughlin AC. (1997). Correction for vascular artefacts in cerebral blood flow values measured by using arterial spin tagging techniques. Magnetic Resonance in Medicine. 37, 226-235.

Ye FQ, Frank JA, Weinberger DR, McLaughlin AC. (2000). Noise reduction in 3D perfusion imaging by attenuating the static signal in arterial spin labelling (ASSIST). Magnetic Resonance in Medicine 44, 92-100.
Yoneda K, Harada M, Morita N, Nishitani H, Uno M, Matsuda T. (2003). Comparison of FAIR technique with different inversion times and post contrast dynamic perfusion MRI in chronic occlusive cerebrovascular disease. Magnetic Resonance Imaging. 21:701-5.Walsh EG, Minematsu K, Leppo J, Moore SC.(1994). Radioactive microsphere validation of a volume localised continuous saturation perfusion measurement. Magnetic Resonance in Medicine 31,147-153.

Wang J, Alsop DC, Song HK, Maldjian JA, Tang K, Salvucci AE, Detre JA. (2003). Arterial transit time imaging with flow encoded arterial spin tagging (FEAST). Magnetic Resonance in Medicine 50;599-607;

Wang J, Fernandez-Serra MA, Wang S, St. Lawrence KS.(2007). When perfusion meets diffusion: in vivo measurements of water permeability in human brain. Journal of Cerebral Blood Flow & Metabolism 27, 839-49.

Williams DS, Detre JA, Leigh JS, Koretsky AP.(1992). Magnetic resonance imaging of perfusion using spin inversion of arterial water. Proceedings of the National Academy of Sciences 89, 212-216.

Wong EC, Frank LR, Buxton RB.(1997). Implementation of quantitative perfusion imaging techniques for functional brain mapping using pulsed arterial spin labelling. NMR in Biomedicine 10, 237-49.

Wong EC, Buxton RB, Frank LR.(1998). A theoretical and Experimental Comparison of Continuous and Pulsed Arterial Spin Labelling Techniques for Quantitative Perfusion Imaging. Magnetic Resonance in Medicine 40, 348-355.

Wong EC, Buxton RB, Frank LR.(1998).Quantitative imaging of perfusion using a single subtraction (QUIPSS and QUIPSS II). Magnetic Resonance in Medicine 39, 702-708.

Wong EC, Cronin M, Wu WC, Inglis B, Frank LR, Liu TT.(2006(a)). Velocity Selective Arterial Spin Labelling. Magnetic Resonance in Medicine 55, 1334-41.

Wong EC.(2006(b)). Vessel Encoded Arterial Spin Labelling Using Pseudo Continuous Tagging. Presented at the 14th ISMRM , Seattle.

Wong E, Guo J. Velocity Selective Inversion Pulse Trains for Velocity Selective Arterial Spin Labelling. Presented at the 17th ISMRM , Hawaii.

Wu WC, Wong EC.(2007(a)). Feasibility of velocity selective arterial spin labelling in functional MRI. Journal of Cerebral Blood Flow and Metabolism 27(4), 831-8.

Wu WC, Fernandes-Seara F, Wehrli JA, Detre JA, Wang J.(2007(b)). A Theoretical and Experimental Investigation of the Tagging Efficiency of Pseudo-Continuous Arterial Spin Labelling. Presented at the 15th ISMRM, Berlin.

Zaharchuk G, Bogdanov Jr. AA, Marota JJA, Shimizu-Sasamata M, Weisskoff RM, Kwong KK.(1998). Continuous Assessment of Perfusion by Tagging Including Volume and water Extraction (CAPTIVE): a steady-state contrast agent technique for measuring blood flow, relative blood volume fraction and the water extraction fraction. Magnetic Resonance in Medicine 40, 666-678.

Zaharchuk G, Ledden PJ, Kwong KK, Reese TG, Rosen BR, Wald LL.(1999). Multislice perfusion and perfusion territory imaging in humans with separate label and image coils. Magnetic Resonance in Medicine 41,1093-1098

Zhang W, Silva AC, Williams DS, Koretsky AP.(1995). NMR measurement of perfusion using arterial spin labelling without saturation of macromolecular spins. Magnetic Resonance in Medicine 33, 370-376.

Zhang W.(1995(b)) A quantitative analysis of alternated line scanning in k-space and its application in MRI of regional tissue perfusion by arterial spin labeling. Journal of Magnetic Resonance Series B 107, 165-171.

Zhou J, Mori S, van Zijl PCM.(1998). FAIR excluding radiation damping (FAIRER). Magnetic Resonance in Medicine 40, 712-719.

Zhou J, Mori S, van Zijl PCM.(1999). Perfusion Imaging using FAIR with a short pre-delay. Magnetic Resonance in Medicine 41, 1099-1107.

Zhou JY, Wilson DA, Ulatowski JA, Trajstman RJ, van Zijl PCM.(2001). Two-compartment exchange model for perfusion quantification using arterial spin tagging. Journal of Cerebral Blood Flow and Metabolism 21(4), 440-455.

CHAPTER 2: CHARACTERISING THE ORIGIN OF THE ARTERIAL SPIN LABELLING SIGNAL IN MRI USING A MULTI-ECHO ACQUISITION APPROACH

2.1 ABSTRACT

Arterial spin labelling can non-invasively isolate the MR signal from arterial blood water that has flowed into the brain. In grey matter, the labelled bolus is dispersed within three main compartments during image acquisition: the intra-vascular compartment; intra-cellular tissue space; and the extra-cellular tissue space. Changes in the relative volumes of the extra-cellular and intra-cellular tissue space are thought to occur in many pathological conditions such as stroke and brain tumours. Accurate measurement of the distribution of the ASL signal within these three compartments will yield better understanding of the time-course of blood delivery and exchange, and may have particular application in animal models of disease to investigate the relationship between the source of the ASL signal and pathology. In this study we sample the transverse relaxation of the ASL perfusion-weighted and control images acquired with and without vascular crusher gradients at a range of post-labelling delays and tagging durations, to estimate the tri-compartmental distribution of labelled water in the rat cortex. Our final results provide evidence for rapid exchange of labelled blood water into the intra-cellular space relative to the transit-time through the vascular bed, and provide a more solid foundation for CBF quantification using ASL techniques.

2.2 INTRODUCTION

As discussed in chapter 1, arterial spin labelling MRI [Detre *et al.*, 1992] is increasingly being used to measure cerebral perfusion non-invasively with good spatial and temporal resolution. In ASL, a bolus of arterial blood is magnetically labelled in the feeding arteries and then imaged in the brain. Though such measurements are most commonly used to estimate the rate of delivery of blood to the capillaries, the labelled bolus of arterial blood water becomes distributed between several cerebral-vascular compartments prior to image acquisition. In grey matter, these can be broadly separated into three main compartments: i) the intra-vascular (IV – arterioles, capillaries, venules) compartment; ii) the extra-vascular, intra-cellular (IC) tissue space; iii) the extra-

vascular, extra-cellular (EC) tissue space. Changes in the relative volume of the extra- and intra-cellular tissue space (EC relative to IC) are thought to occur in many common pathological conditions such as stroke [Moseley *et al.,* 1990] and brain tumours [Bakey, 1970]. Non-invasive estimation of this parameter using MRI may lead to a better understanding of disease processes. Previous studies have observed multi-exponential transverse (T2) decay in skeletal muscle, attributing the slow relaxation component to the extra-cellular space [Belton *et al.,* 1972; Hazlewood *et al.,* 1974; Gambarota *et al,* 2001]. Further studies provide evidence that the transverse decay of extra-vascular rat brain tissue is bi-exponential due to a marked difference between the T2 of the IC (fast transverse relaxation) and EC (slow transverse relaxation) compartments [Haida *et al.,* 1987; Matsumae *et al.,* 2003; Lascialfari *et al.,* 2005]. Another study observed slow exchange between the IC and EC space in the *in-vivo* rat brain relative to the timescale of T2 measurement [Quirk *et al.,* 2003]. In [Matsumae *et al.,* 2003], the volume of the extracellular space, as estimated from the T2 relaxation curve, was found to be in good agreement with electron microscopy imaging experiments. In this chapter, we measure the transverse decay of the ASL perfusion-weighted signal to estimate the origin (EC relative to IC) of nutritive blood flow-related signal that has exchanged into the tissue. Such measurements could lead to better understanding of the time-course of blood delivery and exchange and may have particular application in animal models of disease to investigate the relationship between the IC/EC origin of the ASL signal and pathology.

The distribution of ASL labelled water within the three compartments during image acquisition will also have direct implications for cerebral perfusion quantification. For example, perfusion may be overestimated by standard quantification methods if a significant proportion of the tagged spins reside in the intra-vascular compartment, as this blood may still be in transit to its eventual location for oxygen and nutrient delivery and exchange [Silva *et al.,* 1997(a)]. Several studies have attempted to address this uncertainty by estimating the proportions of labelled spins in the vascular space relative to the tissue space (IV relative to (EC +IC)) using a variety of methods which take advantage of differences in apparent diffusion, the effect of contrast agents, or magnetisation transfer in the two compartments [Silva *et al.,* 1997(a), Silva *et al.,* 1997(b), Wang *et al.,* 2003, Wang *et al.,* 2007, Zaharchuk *et al.,* 1998].See section 1.5.2 (*Vascular Artefacts)* for further details. Recently, initial data has been presented

investigating the potential use of T2 differences to observe compartmentation of the ASL signal in the human brain using a FAIR-CPMG approach [He & Yablonskiy, 2007].

A common approach to ASL CBF measurement is to acquire multiple images at a range of inflow times and fit the dynamic time-course data to a model for cerebral parameter quantification. An assumption of this approach is that the T2 of the labelled water is constant and is independent of the PLD [Buxton *et al.*, 1998, Petersen *et al.*, 2006, Petersen *et al.*, 2008, Francis *et al*., 2008]. Marked sensitivity of the T2 of the tagged bolus to the PLD will influence the accuracy of the estimates. Indeed, a recent study cited T2 as an explanation for CBF quantification errors [Kober *et al.*, 2008] but, unlike T2* effects [St.Lawrence *et al.*, 2005], this potential source of error has not been previously examined.

In this chapter we present a novel technique to estimate non-invasively the proportion of the ASL perfusion-weighted signal originating from the three distinct cerebral-vascular compartments (IV, EC and IC). We sample the transverse relaxation of the perfusion-weighted and control images acquired with a range of post labelling delays (PLDs) and labelling durations (τ) with and without vascular crusher gradients (VCGs) in the rat brain. It is known that the T2 of arterial blood is significantly greater than that of the cerebral parenchymal tissue [Stanitz *et al.*, 2005]. Previously, my colleagues have used this T2 difference to estimate the cerebral blood volume using a double echo pulsed ASL approach [Thomas *et al.*, 2002]. In this work, I extend this concept using a multi-echo CASL sequence to examine the possibility that the T2 of the ASL signal is a sensitive indicator of the intra-vascular (IV) to extra-vascular (IC and EC) ratio when compared to the more established diffusion-sensitised ASL measurements. [Silva *et al.*, 1997(a)]. Furthermore multi-echo ASL data (with VCGs to eliminate any intra-vascular contribution) was acquired to estimate the proportion of the perfusion-weighted signal originating from the intra- and extra-cellular tissue space. The measurements are also used to estimate the T2 of labelled blood in the vessels which may provide a surrogate index of the intra-vascular blood oxygen saturation [Turner *et* al., 1998; Golay *et al.*, 2001]. By acquiring images at a range of PLDs and τ we can follow the dynamic changes in these parameters as the labelled bolus is delivered to the brain. In this way, we provide further insight into the time-course of blood delivery and exchange within

cerebral tissue, and demonstrate the proof of principle of this method for possible future application in brain pathology. Finally, by investigating the dependence of the T2 of the ASL and control signal on τ and PLD we examine the possible implications on the accuracy of standard CBF quantification methods [e.g. Buxton *et al.*, 1998].

In this chapter I begin by describing experiments undertaken to investigate potential confounding factors that may have otherwise influenced the reliability of the results described in the optimised implementation of the methods (referred to as the "final experiments", see section 2.8 *Characterising the Origin of the Arterial Spin Labelling Signal in MRI using a Multi-Echo Acquisition Approach: Final Experiments*). I then go on to describe two pilot studies that preceded the final experiments. Although these pilot studies were intended to fulfil the aims of the investigation, subsequent analyses revealed significant limitations in the imaging protocol. However, they are described in this chapter as they nonetheless provided useful information that influenced the design of the optimised imaging protocol. This chapter concludes with a full description and discussion of the final experiments. The chapter is presented in this way in order to demonstrate the methodological development that led to the methods adopted in the final experiments.

2.3 DEPENDENCE OF THE POWER OF THE SPIN ECHO IMAGING PULSES ON THE DELAY BETWEEN THE END OF LABELLING AND IMAGE ACQUISITION

It was important to establish that the measured T2 of a phantom was independent of the post-labelling delay time, since we aimed to estimate T2 over a range of PLD times to investigate possible changes in this parameter as the bolus of labelled blood progresses through the vascular tree. In a pilot study, ASL images of the rat brain were acquired at a range of post-labelling delays and echo times using a standard spin-echo EPI acquisition. The $T2_{app}$ of the mean cortical signal in the control images appeared to display marked dependence on the post-labelling delay time; rising with increasing PLD. This may have been a consequence of the different susceptibility of cerebral compartments with different T2 constants to magnetisation transfer from the off-resonance labelling/control pulse [Harrison *et al.*, 1995]. However previous work has

shown that the short T2 component of tissue is more susceptible to MT [Harrison *et al.*, 1995]. Therefore we may expect the $T2_{app}$ of the control signal to decrease with increasing PLD (as the extent of MT within the tissue is reduced), in direct contradiction to our findings. We hypothesised that the prolonged power demand of the 3second labelling pulse was affecting the subsequent output of the RF amplifier which would in turn affect the flip angles of the 90^o and 180^o imaging pulses. This would likely result in a systematic PLD-dependence of the power of the 90^o and 180^0 pulses in the spin-echo EPI acquisitions as the RF amplifier has a greater time to "recover" after the labelling pulse at longer PLD. It was important to investigate whether the demand on the RF hardware from the 3 second continuous labelling pulse was influencing the accuracy of the 90^o and/or the 180^0 RF pulses in the spin-echo EPI acquisitions. Imaging experiments on a copper sulphate phantom and direct RF amplitude observation (using a high sampling frequency oscilloscope) were performed to investigate this potentially confounding factor.

A copper sulphate solution was prepared with a concentration of $2mmol/dm^3$ to give a T2 of approximately 50-100ms (to match brain tissue, based on previous measurements taken by other users of the MRI scanner). A simple copper sulphate solution is not susceptible to magnetisation transfer effects. Therefore theoretically, the measured signal intensity of the phantom image should be independent of the time between the end of the 3 second off-resonance labelling/control pulse and the spin-echo EPI image acquisition (the PLD). The solution was transferred into a small test tube, taking care to minimise any bubbles that may cause susceptibility artefacts. The phantom was placed flat on the probe. MRI studies were performed using the 2.35T scanner. Single slice "coronal" EPI images were then acquired after a 3 second labelling pulse at 5 different post-labelling delay times (50, 300, 500, 1000 and 1500ms) at echo times of 37, 51, 71 and 99ms. In order to confirm any systematic dependence of the RF excitation pulse power as a function of PLD, an oscilloscope was later connected to the input of the volume coil. The amplitude of the 90^o spin-echo EPI excitation pulse RF envelope was then directly observed at short (50ms) and extended (500ms) PLD.

Figure 2.1 shows the mean signal within a large ROI in the control images at different PLD times from separate acquisitions at increasing echo times (a-d). Visual assessment

reveals a trend of increasing signal with the duration of the PLD and provides evidence that the measured signal intensity was correlated to the PLD; the likely explanation being a PLD dependence of the power of the 90^{o} and/or 180^{o} spin-echo excitation and re-focusing pulses following the 3 second tagging/control phase. It is possible that the demand for a long RF pulse may cause marked changes in the temperature of the coil which may alter its quality factor, thus affecting the power output. Figure 2.2 shows the estimated T2 (calculated by fitting the measured signal to a simple mono-exponential model) at each post-labelling delay from the multiple echo- time data reported in Figure 2.1.

Following the imaging experiments, myself and two of my colleagues observed a consistent increase in the amplitude of the 90^{o} RF envelope as the PLD increased from 50ms to 500ms using the oscilloscope to directly measure the input to the volume coil (data not shown).

An electrical inspection of the volume coil was performed by my colleague. A faulty capacitor was detected and replaced. Subsequent direct observation of the envelope of the 90 and 180 RF excitation pulses indicated that this intervention had fixed the problem; the amplitude was constant and independent of the PLD. This highlights the importance of thoroughly checking the performance of the system before carrying out highly sensitive experiments to measure small variations in quantitative MR parameters. We proceeded to conduct further experiments, keeping a careful eye on the estimated T2 of the control signal as a function of PLD as this was likely to be an indication of the possible re-occurrence of this fault.

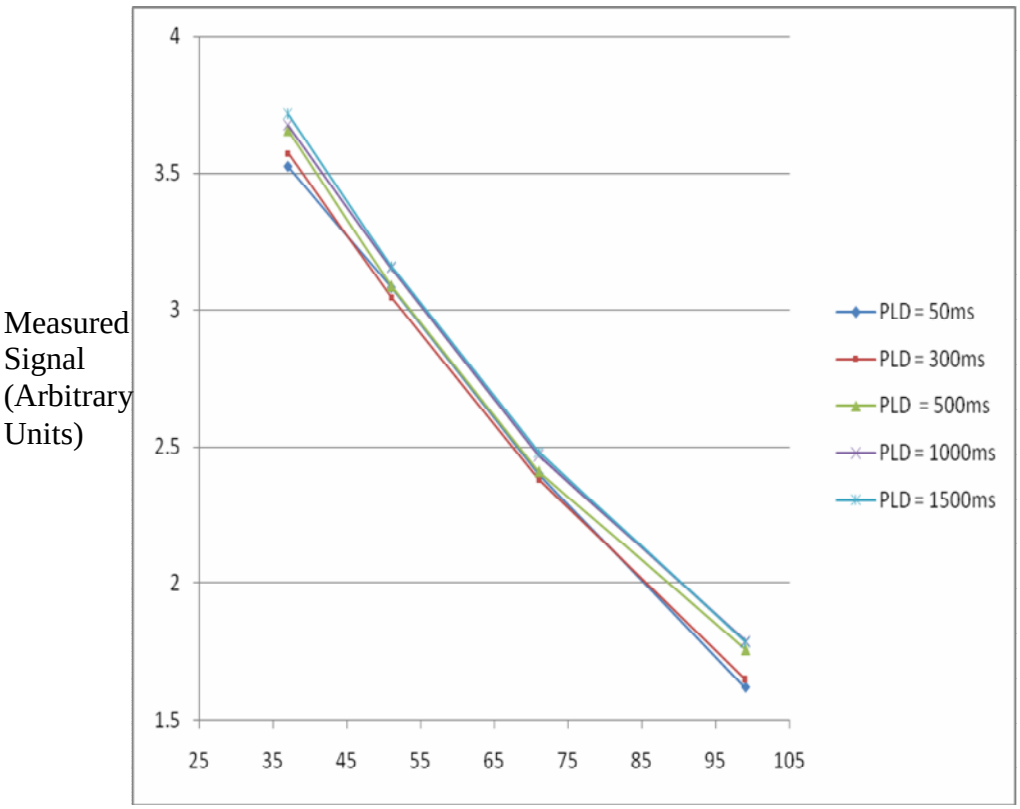

Figure 2.1

The mean signal of the control images of the copper sulphate phantom as a function of echo time. Each plot shows data acquired at different PLD times.

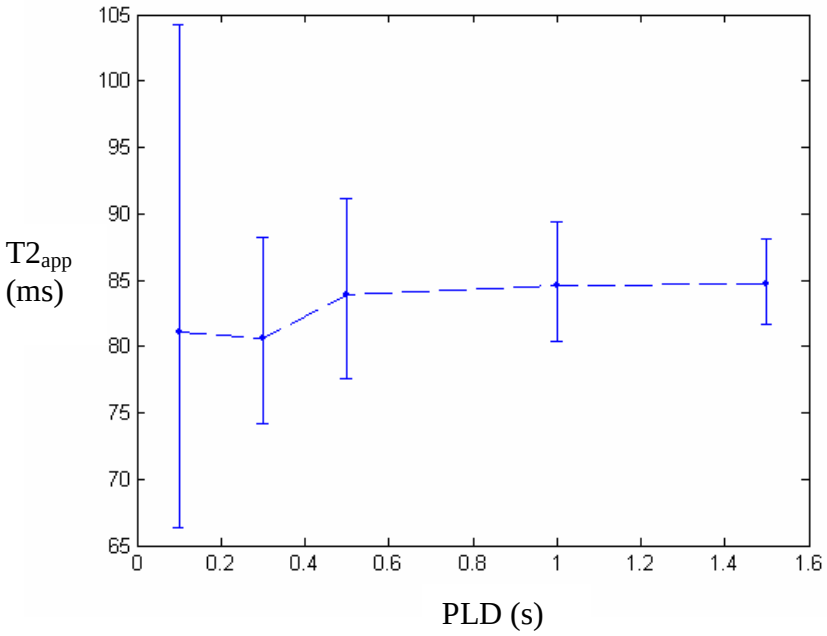

Figure 2.2
The estimated $T2_{app}$ of the copper sulphate phantom at increasing post-labelling delay time. The error bars reflect the upper and lower confidence intervals (95%) of the TE dependant fit of the data to a mono-exponential model.

2.4 REMOVAL OF IMAGE ARTEFACTS USING SPOILER GRADIENTS AND PHASE CYCLING

The experiments described above in section 2.3 were performed using a standard single slice CASL sequence with a single shot EPI readout at a single TE. From this point forward we made the decision to use a half-Fourier multi-echo EPI CASL sequence (see *Figure 2.3*) to improve the efficiency of data acquisition at multiple echo times for increased precision of T2 estimation in a given imaging time. The sequence was designed to acquire images at four different echo times following a single excitation. Therefore it can be considered to be four times more efficient then the single echo equivalent in this, single slice, application. In addition the half-Fourier image readout reduces the minimum echo time of the first acquisition and the echo times of the subsequent 3 acquisitions in the echo-train. This ensures that the sequence is able to sample a greater dynamic range of the transverse decay for more accurate T2 estimation in comparison to the standard EPI readout.

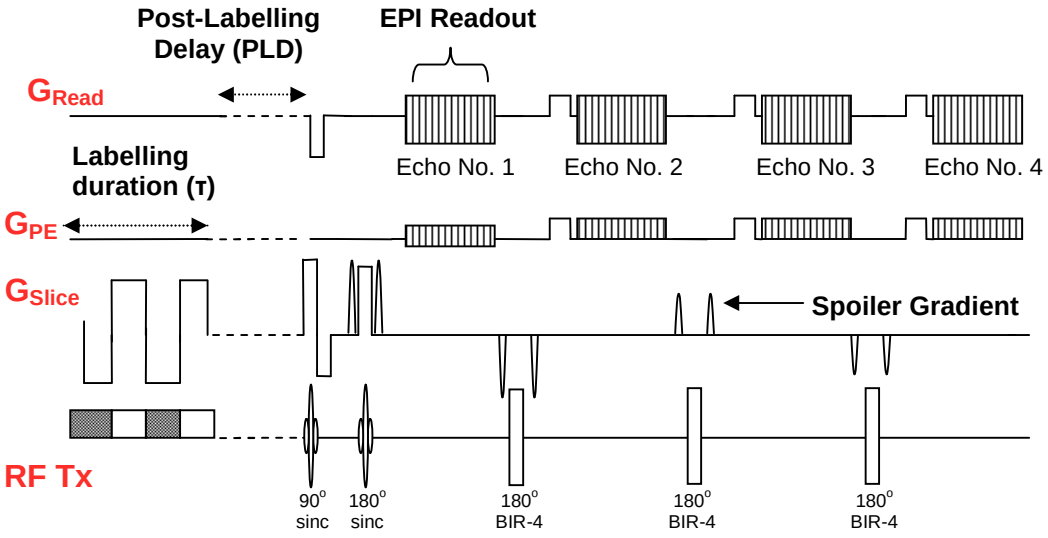

Figure 2.3
The half-Fourier multi-echo EPI CASL sequence. Spolier gradients are arranged on the slice select axis as recommended in [Poon and Henkleman, 1992].

The first *in-vivo* implementation of the half-Fourier multi-echo EPI CASL sequence revealed noticeable artefacts in the reconstructed images (see *Figure 2.4*). RF pulse imperfections in a multi-echo sequence can generate spurious echo signal that can cause such artefacts. Importantly these pulse imperfections may cause magnetisation to be stored on the longitudinal axis during TE. Consequently the multi-echo relaxation curve will exhibit some T1 dependence, confounding accurate T2 quantification. Previous work has suggested that spoiler gradients are the only practical and accurate technique for suppression of spurious echo signal in quantitative T2 studies [Poon and Henkleman, 1992]. The authors go on to recommend an optimal configuration of spoiler gradients for effective artefact removal. However preliminary experiments showed artefacts were still present with this "optimal" configuration, using a spoiler gradient duration of 1ms (data not shown). Ideally we did not want to extend the duration of the spoiler gradients beyond the minimum that could produce artefact-free images. This would increase the minimum TE, thus reducing the range of coverage of the transverse decay of the measured signal. Therefore calibration experiments were performed to investigate the optimal spoiler gradient configuration (with a fixed duration of 1ms) to remove these artefacts.

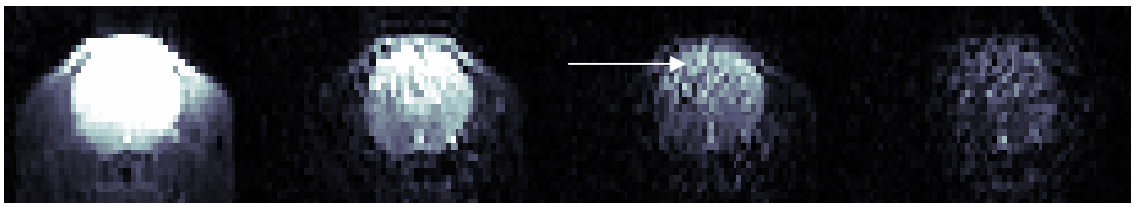

TE 23 ms 62 ms 101 ms 140 ms

Figure 2.4

The control base images acquired using the multi-echo sequence without any spoiler gradients or phase cycling. The images at TE =62, 101 and 140ms are corrupted with artefacts (as highlighted by an arrow) most likely as a result of imperfect RF pulses. The artefacts can be more clearly identified by visual comparison to Figure 2.5 where they have been significantly reduced. Such artefacts may have a particularly detrimental effect on the reliability of the perfusion weighted measurements where we expect differences in the tagged and control signal due to spin tagging to be on the order of 5% of base signal intensity.

One male Sprague Dawley rat was used. The animal preparation and MRI hardware was identical to that detailed in section 1.12. Balanced spoiler gradients of 1ms duration were inserted directly before and after each of the 180^{o} refocusing pulses on all three axis (see *Figure 2.3*). The amplitude of the spoiler gradients was systematically varied and after each iteration, the multi-echo sequence was implemented to acquire four images at echo times of 23, 62,101 and 140ms. The images were rapidly reconstructed and the extent of artefacts was assessed by visual inspection.

The optimal crusher gradient configuration for removal of image artefacts as determined from visual inspection was 1000, 1400, 1950 and -2000 DAC. DAC is the unit of gradient amplitude on the SMIS console and ranges from -2048 to +2048. The strength of each of the three orthogonal gradients was different on the 2.35T scanner. 1 DAC represented 0.077 mT/m, 0.019 mT/m, and 0.021 mT/m on the X, Y and Z axis respectively. The images showed a marked improvement with this sequence of crusher gradients (see *Figure 2.5*).

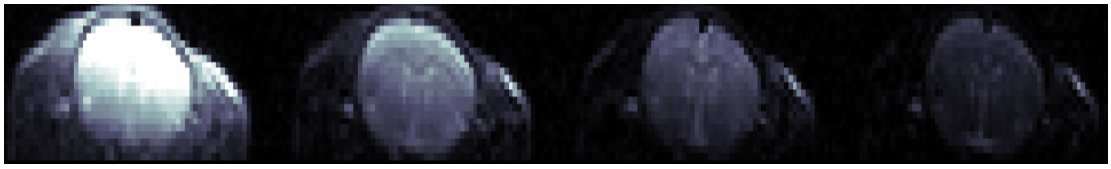

TE 23 ms 62 ms 101 ms 140 ms

Figure 2.5
The control base images acquired with crusher gradients each of duration 1ms, on all three axis, having been optimised through visual inspection. The crusher gradients were 1000, 1400, 1950 and -2000 DAC around the four 180^{o} refocusing pulses respectively.

This crusher gradient configuration was used in pilot study 1. However the estimated $T2_{app}^{\Delta M}$(VCGs-on) at τ = 500ms and PLD =50ms (see 2.6 *Pilot Studies; Figure 2.11 [a]*) led us to conclude that perhaps the complex spoiler gradient arrangement was influencing the accuracy of the $T2_{app}$ estimates. At this time we concluded that simply configuring the spoiler gradients based on visual inspection of the images was perhaps a naive approach that raised some uncertainty regarding the accuracy of our T2 estimates.

Therefore, in pilot study 2 and in the final experiments the spoiler gradients were configured based on a sound theoretical basis [Poon and Henkleman, 1992] and were positioned on a single axis rather than all three. By extending the duration of the spoiler gradients to 2ms and introducing phase cycling, the artefacts appeared to have been removed (*see Figure* 2.6). Therefore phase cycling and spoiler gradients configured as +2000, -2000, +1000, 1000 DAC on the slice select (z) axis were used in pilot study 2 and in the final experiments.

TE 29 ms 68 ms 107 ms 146 ms

Figure 2.6
The control base images acquired with crusher gradients each of duration 2ms, on the slice select axis. This crusher gradient configuration was implemented in the final experiments. The crusher gradients were 2000, -2000, 1000 and -1000 DAC around the four 180^{o} refocusing pulses respectively. Phase cycling was also used in these acquisitions.

2. 5 INVESTIGATING THE POSSIBLE DIFFUSION WEIGHTING INTRODUCED TO THE MEASURED SIGNAL BY THE IMAGING GRADIENTS IN THE MULTI-ECHO ACQUISITIONS

The half Fourier multi echo EPI CASL sequence includes four sets of switching EPI imaging gradients preceded by a spin echo preparation (see *Figure 2.3*). It was important to determine the extent of any possible diffusion weighting introduced to the acquired signal at echo numbers 2, 3 and 4 by the preceeding imaging gradients. If the signal from echo numbers 2, 3 and 4 were diffusion weighted we would not be estimating the true T2 but rather an unknown mixture of diffusion and T2 weighted effects. This would confound the results with one clear difficulty being that signal from the vascular compartment (high apparent ADC [le Bihan, pg 270-271]) would be considerably attenuated at the later echo times and the estimated T2 of the ASL signal originating from the IV compartment ($T2_{IV}$) would be systematically underestimated. I conducted experiments to examine the extent of this potentially confounding factor.

Phantom and *in*-vivo experiments were performed. A small test tube filled with copper sulphate solution was secured to the Perspex probe. The phantom has a relatively high ADC (see section 1.10 *Principles of Diffusion MRI*) and is therefore sensitive to any diffusion weighting within the sequence. The half-Fourier multi-echo EPI CASL sequence was implemented with a 3s labelling duration and a 50ms post labelling delay. There were no vascular crusher gradients. The sequence was implemented with all the imaging gradients present to acquire 4 images with echo times of 25, 64, 103 and 142ms. After an inter-experimental delay of 6 seconds the respective control scan was then acquired. The protocol was repeated but now without the imaging gradients for the first acquisition in the echo train. The corresponding control was then acquired. The same procedure was repeated but in this case without the first two imaging gradients in the pulse train and then finally with only the last imaging gradients (see *Figure 2.7*). Images were acquired with phase cycling and spoiler gradients arranged as recommended in [Poon and Henkleman, 1992]. The interleaved acquisitions were repeated for a total of 6 repeats for each sequence configuration (i.e. number from 1-4 of EPI imaging gradients present in the sequence – see *Figure 2.7*). The mean signal was taken within a large ROI in the homogenous phantom. Figure 2.8 shows the mean signal as a function of echo time for all the acquisitions. The T2 estimated from all 4 image readouts, 3 image readouts and 2 image readouts was 69 (46, 137), 75(40, 558) and 56ms . The confidence intervals of the 2 TE fit cannot be estimated.

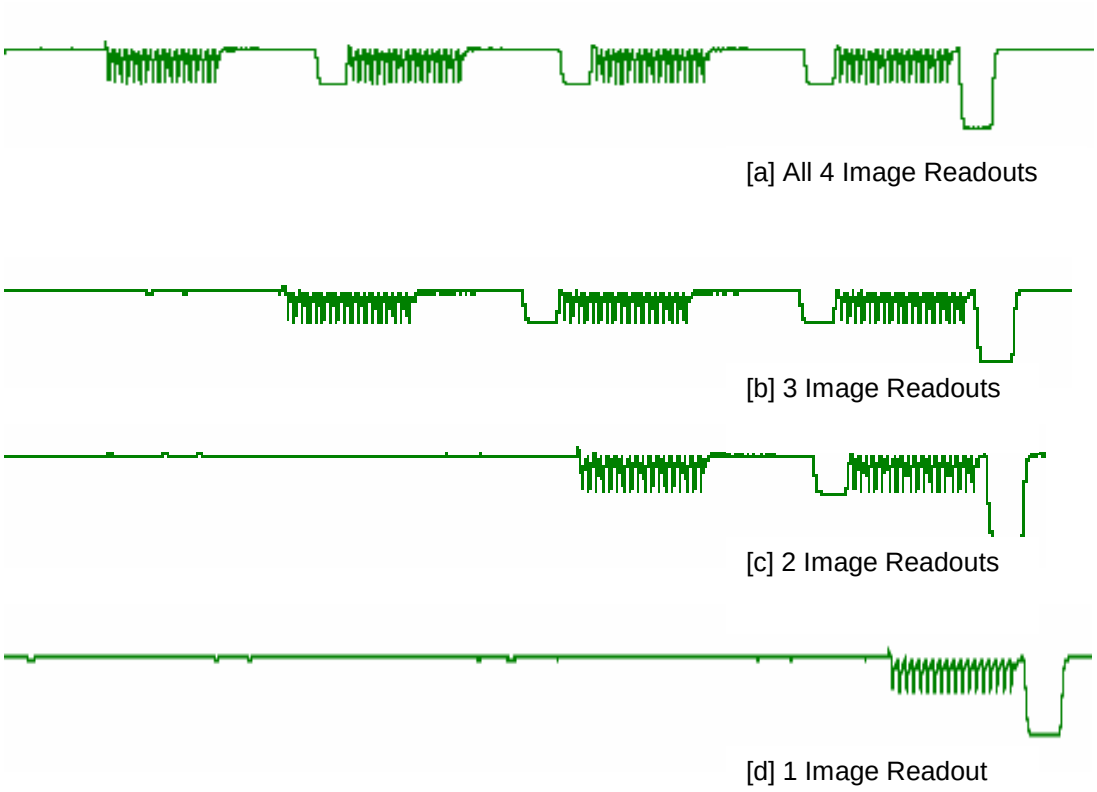

Figure 2.7
A schematic representation of the data acquisition protocol to investigate the possible diffusion weighting of the imaging gradients. The measured Y gradient amplitude (phase) following the 180^{o} refocusing pulse is shown, with all the imaging gradients present (a) followed by successive reduction in the number of switching EPI imaging gradients present in the sequence (b-d). The gradient waveform data was captured using Micro1401 data acquisition unit made by Cambridge Electronic Design Ltd (www.ced.co.uk), connected to a PC running the Spike 2 software package (also provided by CED) to directly measure the output of the y(phase) gradient amplifier during the phantom experiment.

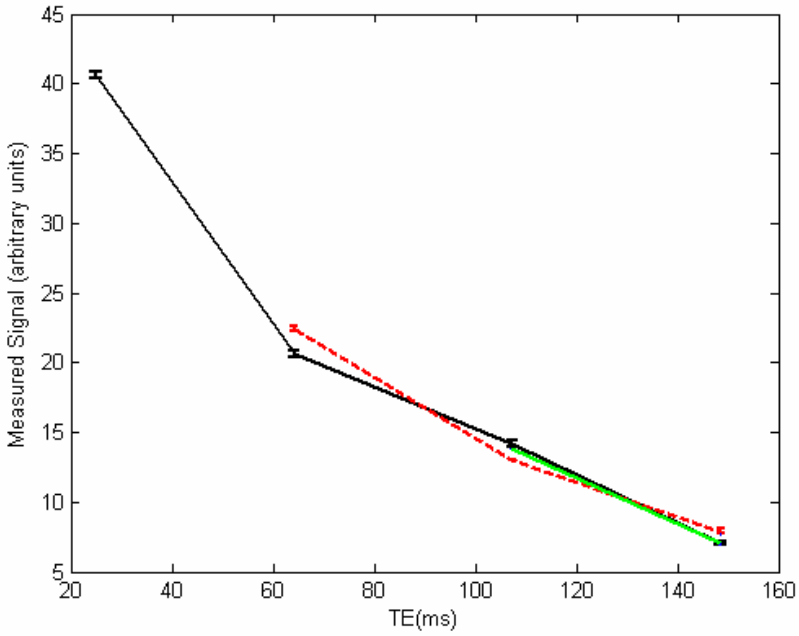

[a]

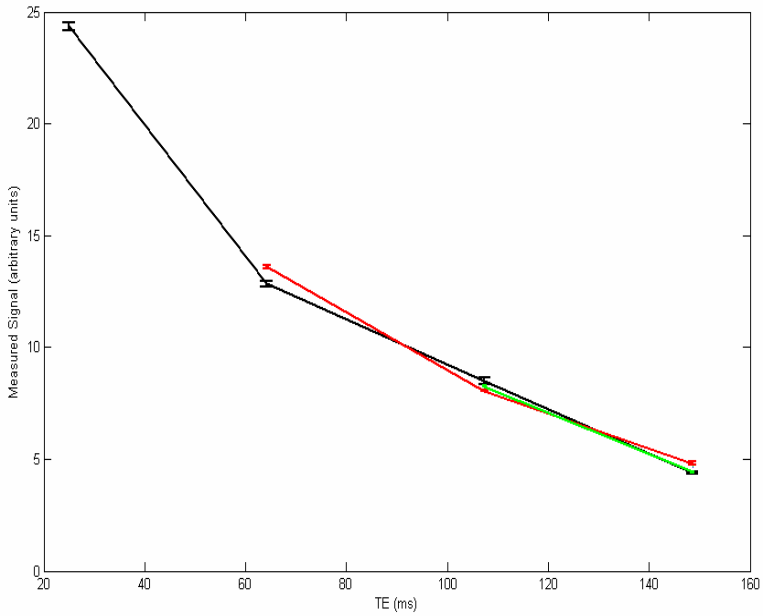

[b]

Figure 2.8

The mean measured signal (± 1 SEM) from a large ROI within a copper sulphate phantom as a function of echo time acquired with all four imaging gradients present in the echo train (solid black line), then three (red dashed line), then two (green solid line) and finally just the last (blue dashed line). The data reported is for the tagged (a) and control (b) acquisitions. Error bars represent the standard error across the 6 repeats at each TE.

The results indicate that the measured signal at echo times of 64, 103 and 142ms is dependent on the application of the previous imaging gradients in the echo train. The measured signal appears to display a small deviation from mono-exponential decay that is dependent on the application of the proceeding imaging gradients in the echo train. This is possibly a result of residual gradient moments affecting the position of the echo in *k*-space. However this small deviation appears to add and subtract to the "true" signal sequentially and has negligible influence on the rate of transverse decay. Although the phantom imaging experiments provided some evidence that the extent of diffusion weighting introduced to the measured signal by the imaging gradients was relatively small, it was important to examine the effect on the ASL, perfusion- weighted, signal. This signal will be more susceptible to any possible diffusion weighting introduced by the imaging gradients given that a large proportion (relative to the control) of the labelled spins are flowing in the vasculature during image acquisition.

One male Sprague Dawly rat was used. The animal preparation and MRI hardware was identical to that described in section 1.12 with τ = 3000ms and PLD = 50ms and number of averages = 30.

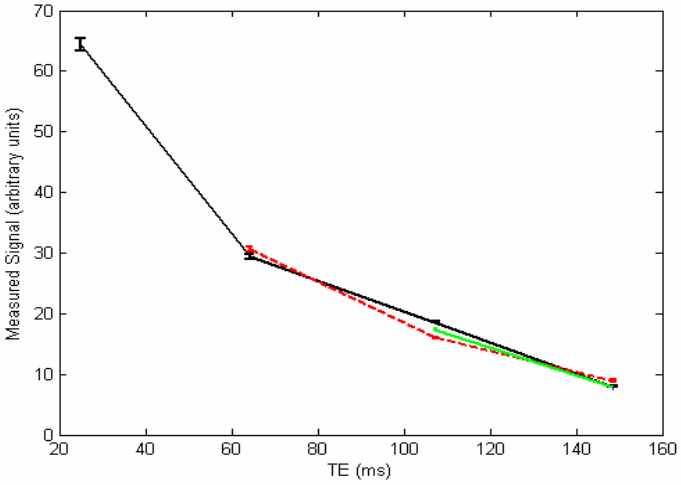
Measured Signal (arbitrary units)
TE (ms)
0
10
20
30
40
50
60
70
20
40
60
80
100
120
140
160

[a]

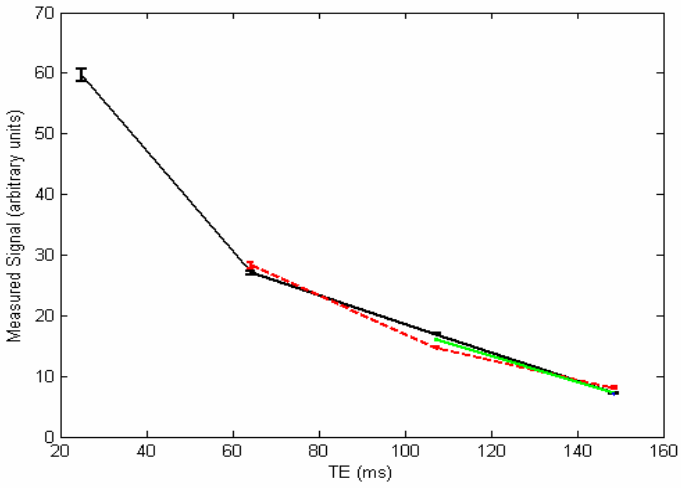
Measured Signal (arbitrary units)
TE (ms)
0
10
20
30
40
50
60
70
20
40
60
80
100
120
140
160

[b]

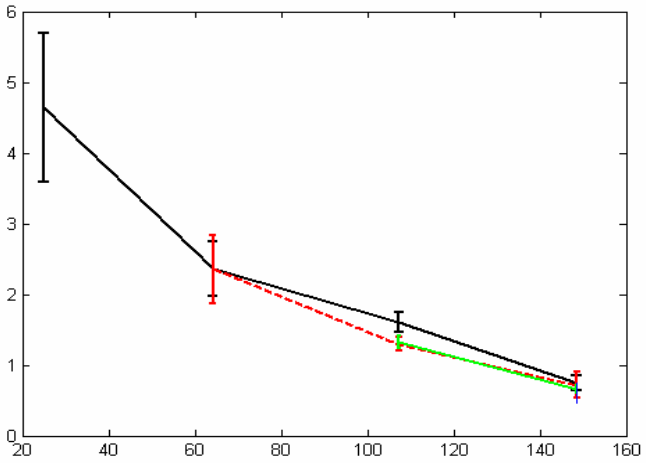
0
1
2
3
4
5
6
20
40
60
80
100
120
140
160

[c]

Figure 2.9

The mean in-vivo cortical signal (±1 SEM) as a function of echo time acquired with all four imaging gradients in the echo trains (solid black line), then three (red dashed line line), then two (green solid line) and finally just the last (blue marker). The data reported is for the tagged (a) control (b) and subtracted (ΔM) images (c). Error bars represent the standard error across the 6 repeats at each TE

The echo train possesses the even-odd echo behaviour associated with multi-echo acquisitions [Pell *et al.*, 2006; Poon and Henkleman 1992]. The odd/even behaviour of the echo train is due to the phase cycling present in the sequence (see McRobie *et al*, page 149-150 for a detailed explanation). However, as one can see from visual inspection of Figures 2.8 and 2. 9, no systematic underestimation occurs at the greatest echo time when all 4 echoes are acquired in comparison to when the acquired image at this echo time is not preceded by any EPI gradients. Indeed at the final echo time, the measured signal is very similar irrespective of the "history" of the extent of the EPI imaging gradients. Any such effects are likely to be apparent in a copper sulphate phantom which has a high ADC and in particular in the *in-vivo* perfusion weighted signal (where at τ = 3000ms and PLD = 50ms a considerable proportion of the labelled spins are likely to reside in the vascular compartment). The T2 of the control signal, estimated from all 4 image readouts, 3 image readouts and 2 image readouts was 59 (40, 108), 64(37, 211) and 49ms.The T2 of the ASL signal, estimated from all 4 image readouts, 3 image readouts and 2 image readouts was 59 (40, 108), 64(37, 211) and 49ms.The confidence intervals of the 2 TE fit cannot be estimated.

Figure 2.9 provides convincing evidence that the extent of signal attenuation at echo numbers 2, 3 and 4, due to the proceeding imaging gradients, is negligible. This applies to the control (*Figure 2.9[a]*), tagged (*Figure 2.9[b]*) and most importantly the perfusion weighted (*Figure 2.9 [c]*) signal.

These experiments provide reassurance that the estimated T2 of the control and ASL signal will be negligibly affected by the diffusion weighting of the imaging gradients.

2.6 CHARACTERISING THE ORIGIN OF THE ARTERIAL SPIN LABELLING SIGNAL IN MRI USING A MULTI-ECHO ACQUISITION APPROACH: PILOT STUDIES

The following experiments were undertaken with the intention that they would fulfil the aims of the investigation (described in the introduction to this chapter). However subsequent analyses revealed oversights within the imaging protocol, limiting the extent of interpretation of these results. However the experiments are described here as they provided information which was useful in optimising the protocol used in the final experiments (see section 2.8 *Characterising the Origin of the Arterial Spin Labelling Sequence in MRI using a Multi Echo Acquisition Approach: Final Experiments*). These investigations are referred to as pilot study 1 and pilot study 2.

The animal preparation and MRI hardware was identical to that detailed in section 1.12.In pilot study 1, 10 male Sprague Dawley rats were used, in pilot study 2 there were 9. The half-Fourier multi-echo EPI CASL sequence was implemented to acquire images. In order to monitor the progression of labelled water within the cerebral vessels and tissue, the tagging pulse duration was varied over the range of values: 500, 750, 1000, 1500 and 3000ms with additional acquisitions at PLD = 50ms, 300ms and 500ms after the 3s labelling pulse. After the PLD, single slice coronal images were then acquired 0.3mm caudal to the bregma using a multi-echo spin echo half-Fourier EPI sequence to produce 4 images in a single shot. Previous work has found evidence to support the use of acquisitions at multiple echo times for more accurate and precise T2 estimates in comparison to multiple average data at a smaller number of echo times [Poon and Henkleman]. The multi-echo EPI sequence can acquire images at 4 TEs in a single shot. To increase the number of echo times, the sequence timing was altered in order to acquire images at 4 different TEs. The sequence timing was again altered for a total of 12 echo times (3 different sequence timings, each able to acquire images at 4 different echo times). . The echo times in pilot study 1 were (23, 35, 47, 62.2, 74.2, 86.2, 101.4, 113.4, 125.4, 140.6, 150.6, and 164.6ms), and in pilot study 2 were (25, 37, 49, 64.2, 76.2, 88.2, 103.4, 115.4, 127.4, 142.6, 152.6, and 166.6ms), due to the increase in the duration of the spoiler gradients in pilot study 2 from 1ms to 2ms. In these pilot studies, 36 averages were acquired.. Mono-polar diffusion gradients were arranged on the read, slice select and phase axis to increase the magnitude of the net diffusion

gradient (see *Figure 2.10*). The *b*-value of the mono-polar diffusion gradients was 20s/mm^2.

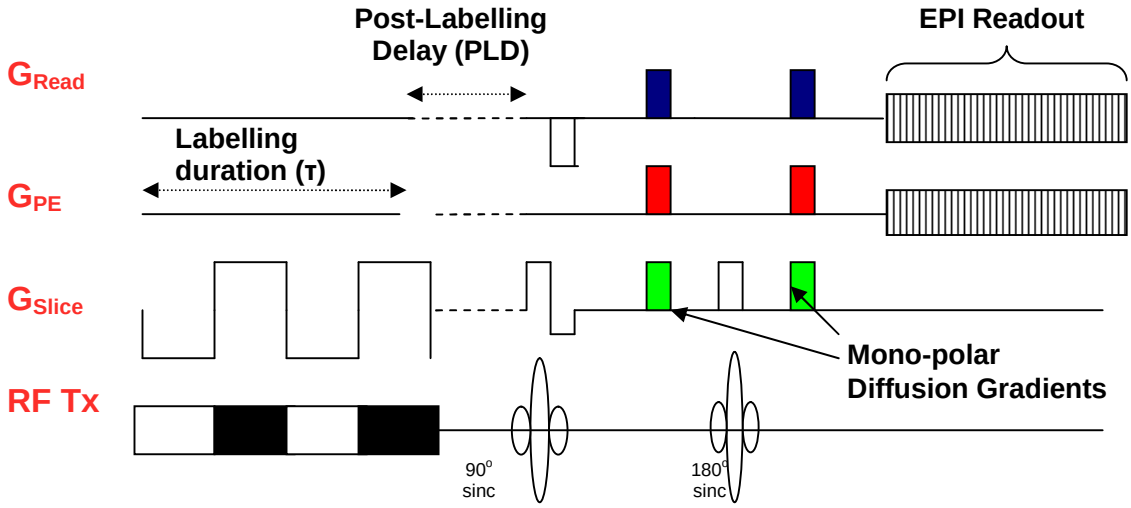

Figure 2.10
The initial stages of the half-Fourier multi-echo EPI CASL sequence showing the arrangement of the vascular crusher gradients in pilot studies 1 and 2.

In addition to the echo times, the only other discernable difference between pilot study 1 and pilot study 2 was the arrangement of the spoiler gradients (see 3.4 *Spoiler Gradients*)**.**

Figure 2.11(a) shows the mean $T2_{app}$ of the ASL and control signal across the 10 experiments from pilot study 1. The $T2_{app}$ is calculated by fitting the TE dependant signal to a simple mono-exponential model. The mean $T2_{app}^{\Delta M}$(VCGs-on) estimates at τ =500 was less than $T2_{app}^{Ctrl}$(VCGs-on) at τ =500ms. Assuming that the vascular crusher gradients were effectively suppressing the vascular signal, then $T2_{app}^{\Delta M}$(VCGs-on) reflects the transverse decay of labelled blood water that has exchanged into the tissue. This result was particularly difficult to interpret physiologically: given that (intuitively) the ASL signal at short τ and with VCGs should be weighted toward the extracellular compartment (high T2) in comparison to the intracellular compartment (low T2) it was surprising that $T2_{app}^{\Delta M}$ was less then $T2_{app}^{ctrl}$ (which represents the T2 of the static tissue) at these imaging parameters. We reasoned that this curious result may be a consequence of the crusher gradient configuration. Previous work has shown the

arrangement of the crusher gradients in multi-echo acquisitions to have a marked effect on the transverse decay of images acquired in the echo train [Poon and Henkleman, 1992]. For this reason we proceeded to pilot study 2 having introduced phase cycling and an established spoiler gradient arrangement to the sequence (see section 2.4 *Spoiler Gradients*). Figure 2.11(b) shows the mean T2 of the ASL and control signal across the 9 experiments from pilot study 2.

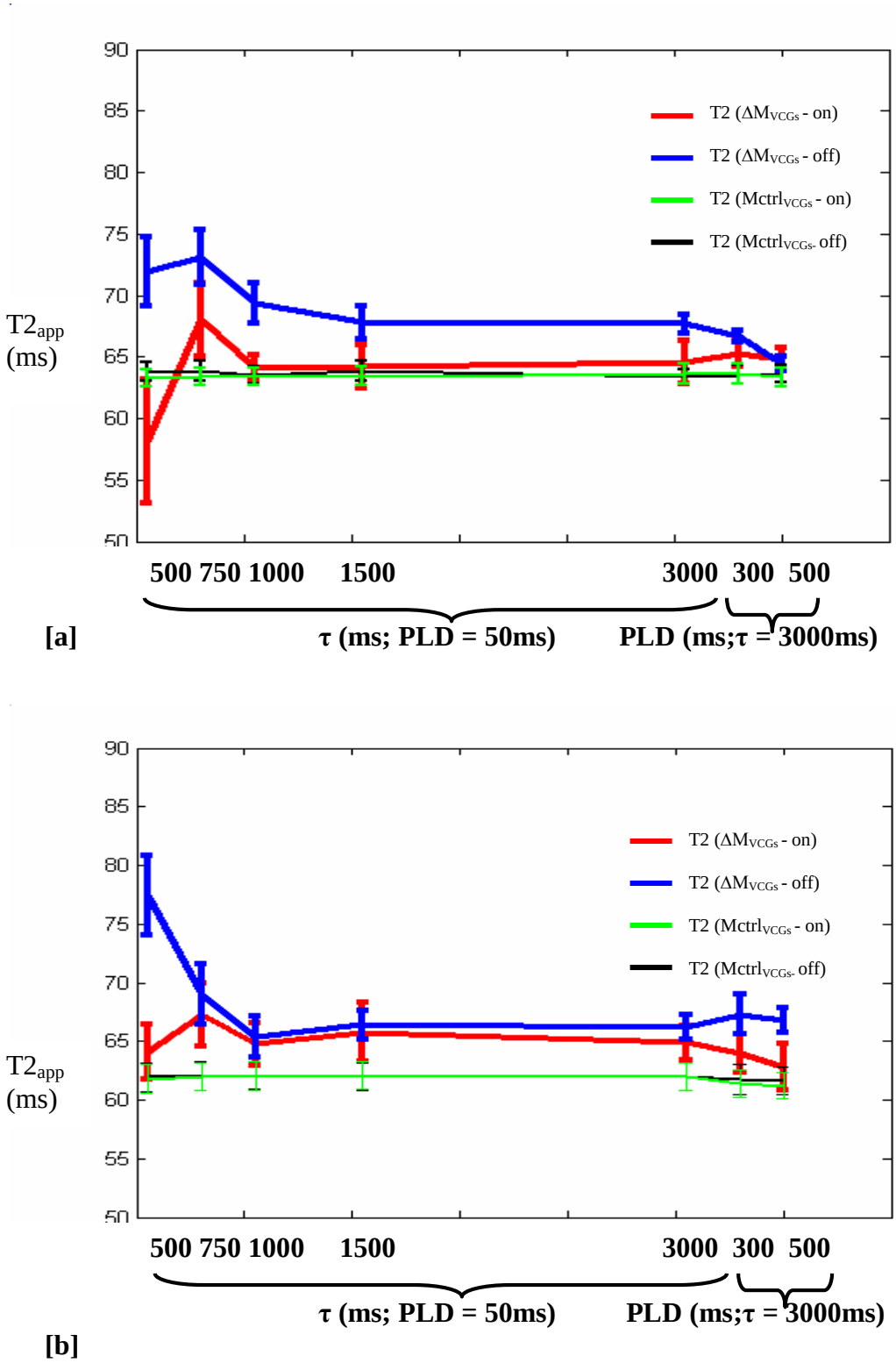

Figure 2.11
The mean $T2_{app}^{\Delta M}$ (VCGs–on) (red line), $T2_{app}^{\Delta M}$ (VCGs–off) (blue line), $T2_{app}^{Ctrl}$ (VCGs–on) (green line) and $T2_{app}^{Ctrl}$ (VCGs–on) (black line) at different PLD and τ times from pilot study 1 [a] and pilot study 2 [b]. Error bars represent the standard error across the experiments (9 in pilot study 1, 10 in pilot study 2). The $T2_{app}$ is estimated by fitting the data acquired at 12 echo times to a mono-exponential model.

Subsequent analysis revealed limitations in the design of the acquisition protocol. The first issue lies in how the echo times at which the signal was sampled using the multi-echo acquisition were changed. This was achieved by increasing the delay between the 90^{o} excitation pulse and the first 180^{o} RF pulse (the half echo-time) and the first 180^{o} and the echo at the centre of k-space. However in the pilot studies, the delay was inserted between the mono-polar diffusion gradients thus increasing the diffusion time (see *Figure 2.12*).

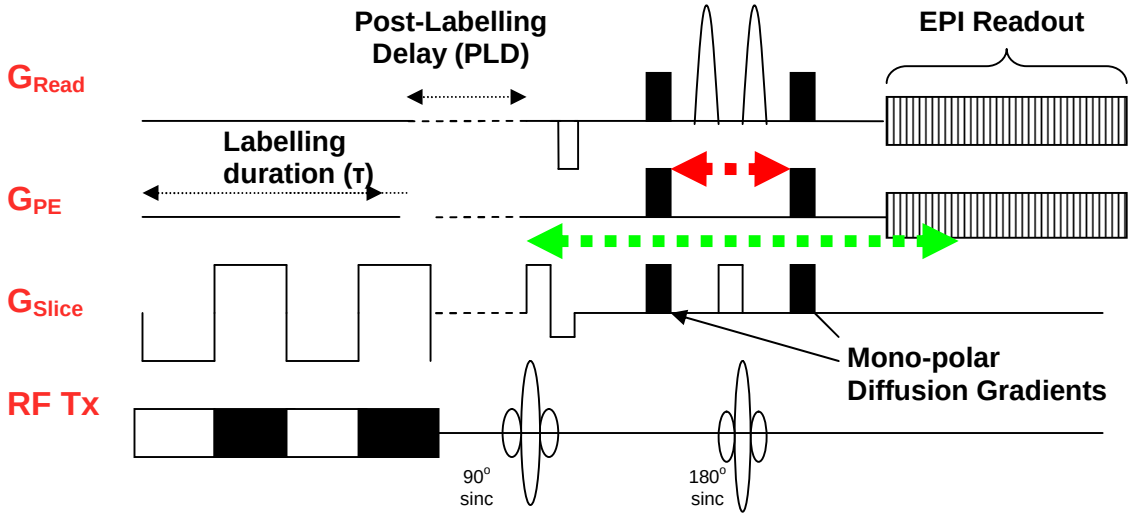

Figure 2.12
The initial stages of the half-Fourier multi-echo EPI CASL sequence. The red arrow shows the separation of the mono-polar diffusion gradients, which determines their b-value (see 1.10 Principles of Diffusion MRI). The green arrow shows the echo time of the first acquisition in the echo train. In pilot studies 1 and 2, I increased the echo time (green arrow) by increasing the separation of the diffusion gradients (red arrow). In doing this I unintentionally increased the b-value of the sequence in addition to the echo time.

Therefore the *b*-value of the sequence was increasing with the echo time of the first image in each of the three echo trains. Consequently Figure 2.11 does not reflect the true $T2_{app}$ of the ASL and control signal acquired with VCGs. The $T2_{app}$ estimates are confounded by the TE dependant variation in the *b*-value of the applied diffusion gradients. The *b*-value of the diffusion gradients was approximately 20, 30 and 40 $s/mm^{2,}$ as the first echo time in the echo train increases from 25, 37 and 49ms in pilot

study 2 and 18, 28, 38 s/mm^2 as the first echo time in the echo train increases from 23, 35 and 47ms in pilot study 1. Therefore the measured signal as a function of TE does not just reflect the transverse decay but an unknown mixture of T2 and diffusion effects. This explains why the mean $T2_{app}{}^{\Delta M}$(VCGs-on) estimate at τ =500 in pilot study 1 was less than the $T2_{app}{}^{Ctrl}$(VCGs-on) at the same imaging parameters, a result that was previously difficult to explain. The signal acquired from echo trains at long TEs will be more attenuated by the diffusion gradients than the signal acquired from echo trains at short TEs. This will act to decrease $T2_{app}$. At the time of analysis I was not aware of this problem and therefore this appeared as an increased rate of transverse decay, particularly at short tagging durations where the proportion of ASL signal in the vascular compartment was relatively high. In addition, subsequent analysis (see section 2.7 *Calibration of Vascular Crusher Gradients*) revealed that the mono-polar diffusion gradients (VCGs), when applied on all three axes as in pilot 1 and 2, were affecting the measured signal in a way that contradicted established diffusion MRI theory (see 1.10 *Principles of Diffusion MRI*). The properties of the VCGs and the extent of vascular suppression were not rigorously addressed prior to pilot studies 1 and 2. The next section (2.7 *Calibration of Vascular Crusher Gradients*) describes experiments designed to investigate the properties of the vascular crusher gradients.

To summarise, the results from pilot studies 1 and 2 were unreliable due to systematic errors in the imaging protocol. Consequently it was necessary to repeat the experiments (see section 2.8 *Characterising the Origin of the Arterial Spin Labelling Signal in MRI using a Multi-echo Acquisition Approach: Final Experiments*) whilst ensuring that the methodological limitations of the pilot studies were accounted for. In the final experiments, the TE of the echo trains was changed without increasing the separation of the mono-polar diffusion gradients. In addition the properties of the vascular crusher gradients were investigated prior to the final experiments to ensure that they did not introduce systematic errors due to eddy currents (see section 2.7 *Calibration of Vascular Crusher Gradients*). Furthermore because of the similarity of the $T2_{app}$ estimates at τ = 3000ms and changing PLD in pilot studies 1 and 2 (see *Figure 2.13*), we extended the PLD to 700 and 1200ms in the final experiments to investigate the origin of the ASL signal at greater inflow times as we may expect a greater range of estimated $T2_{app}{}^{\Delta M}$ at these imaging parameters. The experience of the many imaging experiments also led me to the observation that slightly heavier rats allowed the surface

coil to be positioned closer to the head of the animal resulting in improved SNR_{pwi}. Consequently the weight of the rats in the final experiments increased to (182-242g) from (164 -222g) yielding improved SNR_{pwi}. Finally the acquisitions were "more interleaved" in the final experiments in comparison to the pilot studies; image files corresponding to 2 averages were saved rather than 6 averages. For example, in pilot studies 1 and 2 data was acquired with VCGs-on for 6 averages and then with VCGs-off for 6 averages. In the final experiments data was acquired over 2 averages with VCGs and then 2 averages without VCGs. This should reduce the influence of scanner instability or physiological drift on any apparent differences in the measured signal with and without VCGs.

2.7 CALIBRATION OF VASCULAR CRUSHER GRADIENTS

The final experiments were intended to acquire images with and without the signal from labelled water in the cerebral vasculature. To achieve this, I implemented the half-Fourier multi-echo CASL sequence with and without diffusion gradients (referred to as "Vascular Crusher Gradients"). It was important to ensure that the diffusion gradients were indeed achieving effective vascular suppression. The experiments described below were performed following pilot studies 1 and 2 and are divided into two parts: Firstly I present results that demonstrate that the diffusion gradients used in pilot studies 1 and 2 were introducing eddy current that confounded the interpretation of the measured signal. I will then describe experiments undertaken to circumnavigate this problem and investigate the necessary *b*-value of the adapted diffusion gradients to effectively suppress the vascular signal.

In pilot studies 1 and 2, mono-polar diffusion gradients were applied simultaneously on all three axis (see *Figure 2.13*). This was to increase the net amplitude of the gradients to maximise the *b*-value of the sequence for a given duration and separation (see 1.10 *Principles of Diffusion MRI*).

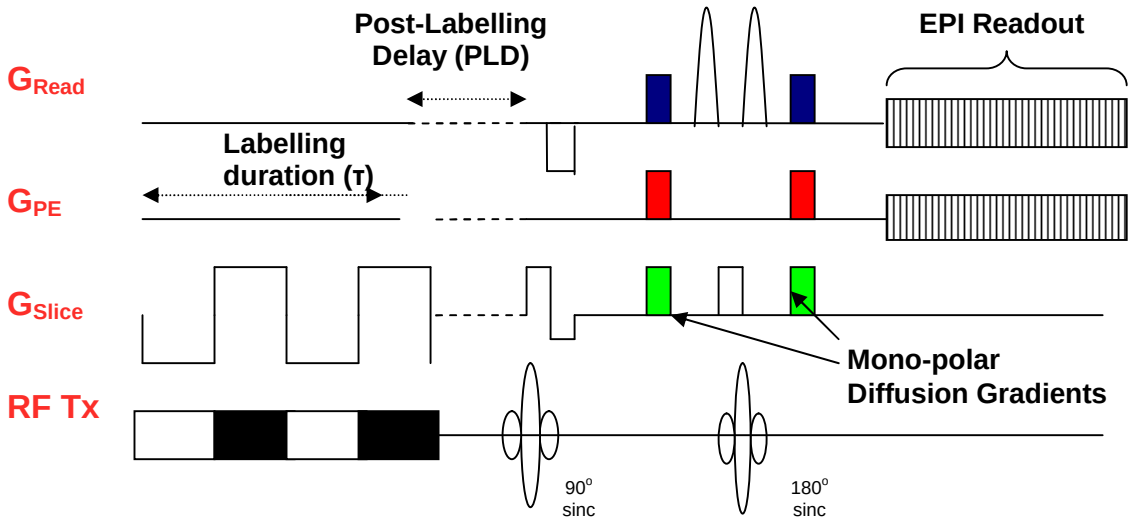

Figure 2.13
The initial stages of the half-Fourier multi-echo EPI sequence. Mono-polar diffusion gradients were applied simultaneously on all three axis in pilot studies 1 and 2.

Figure 2.14 [a] shows the difference images generated by subtracting the control base images acquired with VCGs from the control base images acquired without VCGs at τ = 500ms and PLD =50ms for all 9 experiments in pilot study 2. The Figure is windowed so that any pixels that have greater signal intensity without VCGs than with VCGs are black. The VCGs have no affect on the background signal intensity and therefore in this region, the difference images display noise; approximately half of the pixels are black. In the brain, we would expect the difference images to be black as the VCGs should act to reduce the measured signal from the brain. However, Figure 2.14 clearly demonstrates that the difference images display marked structure in the cortex (the tissue of interest in our study). This demonstrated that eddy currents caused by the application of the diffusion gradients resulted in a distortion of the images (acquired in pilot studies 1 and 2) along the PE direction. In pilot studies 1 and 2, the ROI was manually adjusted to try to account for the apparent shift of the brain within the FOV due to the application of the VCGs; however this was not ideal and assumes the eddy currents were causing a rigid translation of the brain within the FOV which is unlikely to have been the case.

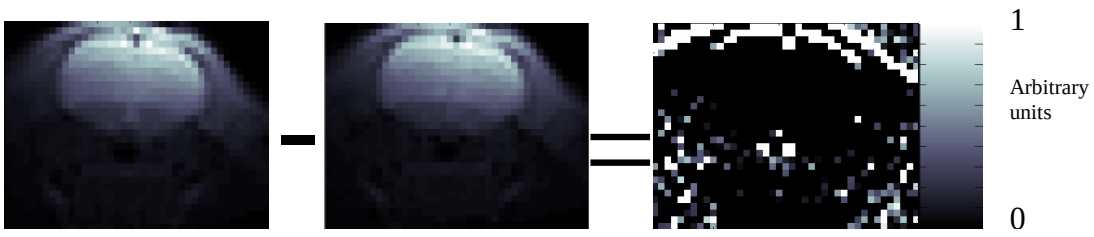

[a]

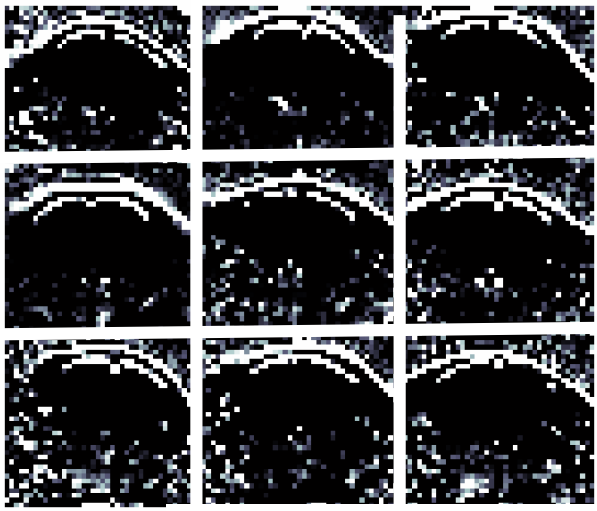

Pilot Study 2

Control Images (VCGs –on) –
Control Images (VCGs –off).

[b]

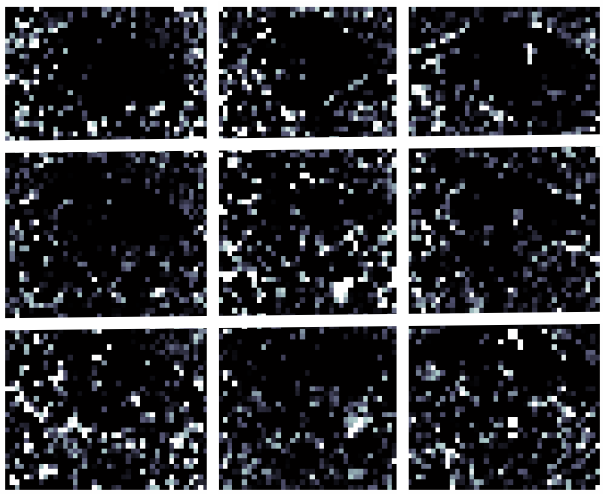

Final Experiments

Figure 2.14

The difference images of the base images acquired with VCGs – the base images acquired without VCGs at τ =500ms and PLD = 50ms for all 9 experiments in pilot study 2 [a] and in the final experiments [b]. The difference images are scaled ("windowed") so that any pixels that have a greater signal intensity than without VCGs

than with VCGs are black. Each of the 9 difference images (1 for each experiment) are separated by a white border.

Phantom studies were subsequently performed to check the calibration of the mono-polar diffusion gradients. An oil phantom was used as this is known to possess a very low ADC. Therefore the amplitude of the diffusion gradients should have no noticeable effect on the measured signal. Any systematic change in the measured signal intensity from the oil phantom as a function of diffusion gradient strength suggests that unwanted eddy current effects are influencing the measured signal. Such potential eddy current problems associated with mono-polar diffusion gradients can often be negated by the use of bi-polar diffusion gradients where the diffusion gradients are of the same amplitude but of opposite direction. However as we see from Eq. 1.24, the *b*-value of diffusion gradients is approximately proportional to their separation. Diffusion gradients should be applied between the initial excitation pulse and the image readout. Therefore their separation will affect the echo time of the acquisition. Mono-polar diffusion gradients have a considerable advantage in this application as they can be implemented before and after the first 180^{o} refocusing pulse. Consequently for a given time delay between the 90^{o} and 180^{o} pulses (the half echo time) mono-polar diffusion gradients can generate a significantly greater *b*-value (see 1.10 *Principles of Diffusion MRI*) which may be necessary to effectively remove the vascular signal.

All images were acquired using the half–Fourier multi-echo EPI CASL sequence. Mono-polar diffusion gradients, arranged either side of the first 180^{o} refocusing pulse, were implemented on each separate axis at a range of *b* values (0, 20, 40) - (see *Figure 2.13*). Twelve images (6 labels and 6 controls) were acquired at each different *b*-value with diffusion gradients applied separately on each axis. The images at the first echo time (25ms) were analysed. Figure 2.15 shows the measured signal as a function of *b*-value when the mono-polar diffusion gradients are positioned on each axis. The results demonstrated that diffusion gradients positioned on the y-axis considerably increased the measured signal. This suggested that the mono-polar diffusion gradients on the phase axis were introducing eddy currents which acted to transform the image within the field of view thus changing the measured signal as the amplitude of the gradients is increased. This finding introduces doubt as to the reliability of the measurements acquired with the inclusion of vascular crusher gradients in pilot studies 1 and 2.

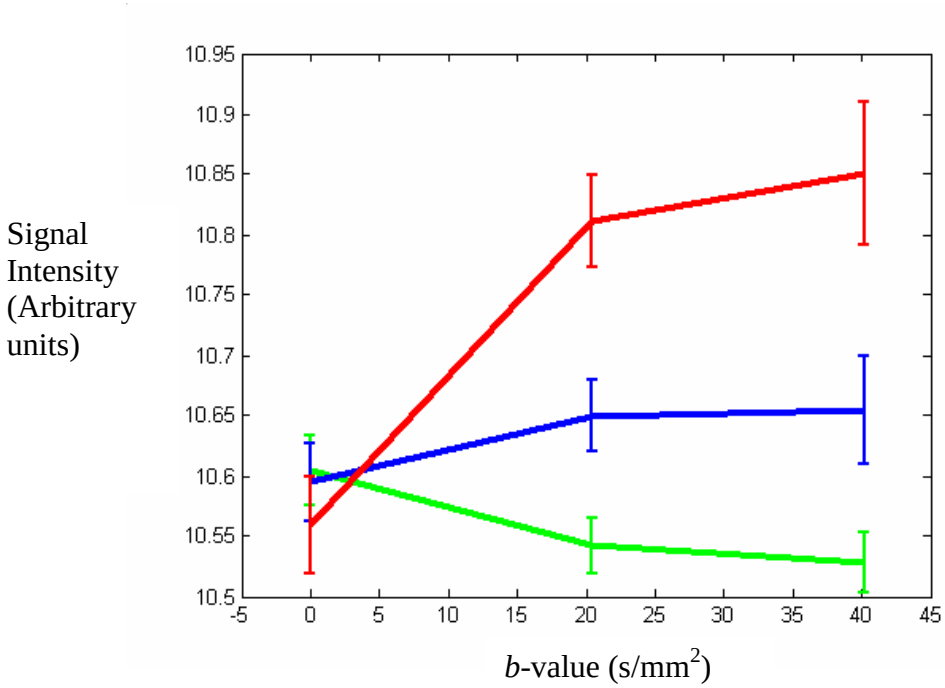

Figure 2.15

The mean signal from a large ROI within the oil phantom at increasing b value. Data is reported with mono-polar diffusion gradients applied on the read axis (x-axis – blue line); phase (y-axis – red line) and slice select (z-axis – green line). Error bars represent the standard error of the mean signal across the 12 images at each b-value.

Figure 2.15 also suggests that the measured signal displays some sensitivity to the *b*-value of the mono-polar diffusion gradients arranged on the slice select axis. However these results were not conclusive. We performed further experiments to investigate whether this was indeed the case. Images were acquired of an oil phantom with diffusion gradients applied on the z-axis over a greater number of *b*-values (0, 10, 20, 30, 40 and 70 mm^2/s). Six images (3 tag and 3 control) were acquired at each *b*-value. The mean signal within a ROI in the oil phantom was taken. Figure 2.16 shows the results and confirms that the measured signal was influenced by the *b*-value of the z-axis diffusion gradients. Therefore the z-axis diffusion gradients were causing additional eddy currents, introducing systematic errors to the signal acquired with vascular crusher gradients in pilot studies 1 and 2.

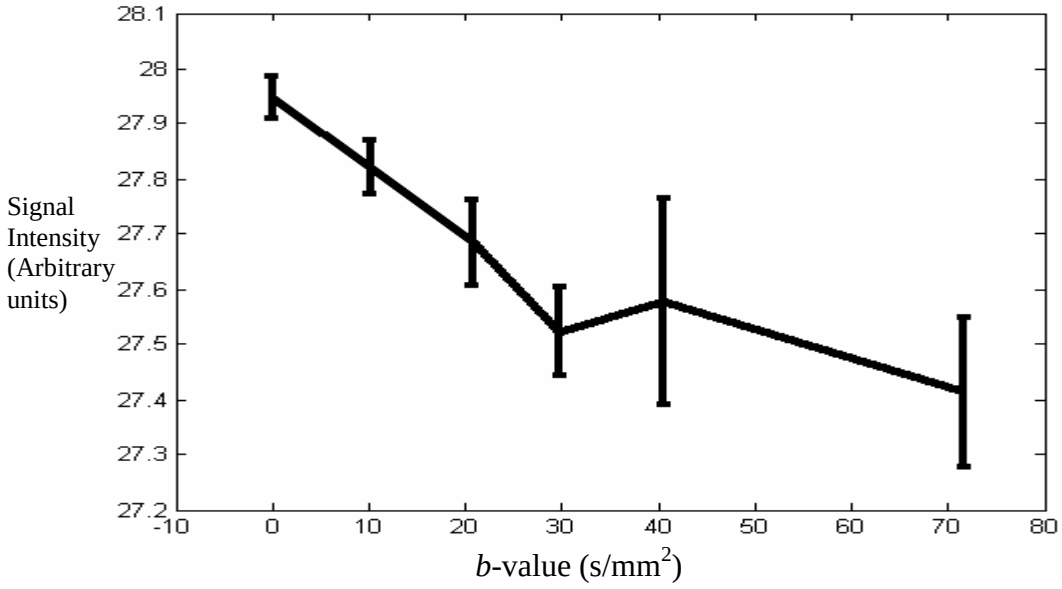

Figure 2.16

The measured signal from q large ROI within the oil phantom with increasing b value from diffusion gradients positioned on the slice select axis. Error bars represent the standard error of the mean signal across the 6 images at each b-value

I then performed the same experiment but in this case the direction of the mono-polar diffusion gradients on the z axis was reversed (see *Figure 2.17*). The results are shown in Figure 2.18. In this case the measured signal did not possess any such monotonic dependence on the *b*-value of the crusher gradients. This suggested that diffusion gradients applied on the slice-select axis in this way did not introduce significant eddy currents and would not confound future experiments. Given that the principle direction of flow in the rat brain positioned in our scanner was parallel to the z-axis, it seemed sensible to proceed to the final experiments with the diffusion gradients arranged in this way on the slice-select axis, the same approach used in [Wang *et al*., 2007; Petersen *et al*., 2006; Wang *et al*., 2003]. Figure 2.14 [b] shows the equivalent images (with the same windowing) to Figure 2.14 [a] for the final experiments with the new diffusion gradient calibration. The lack of noticeable coherent signal in these images provides some evidence that eddy current effects are minimal in these acquisitions.

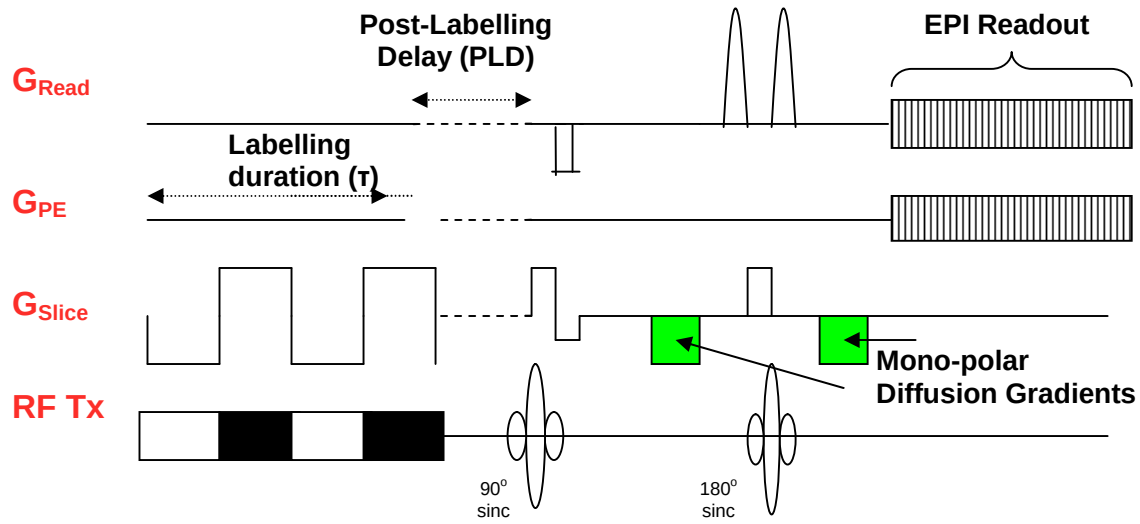

Figure 2.17
The initial stages of the half-Fourier Multi-Echo EPI CASL sequence. In the final experiments the mono-polar diffusion gradients were arranged on the z (slice-select) axis with a 4ms duration (δ) and 16ms separation (Δ).

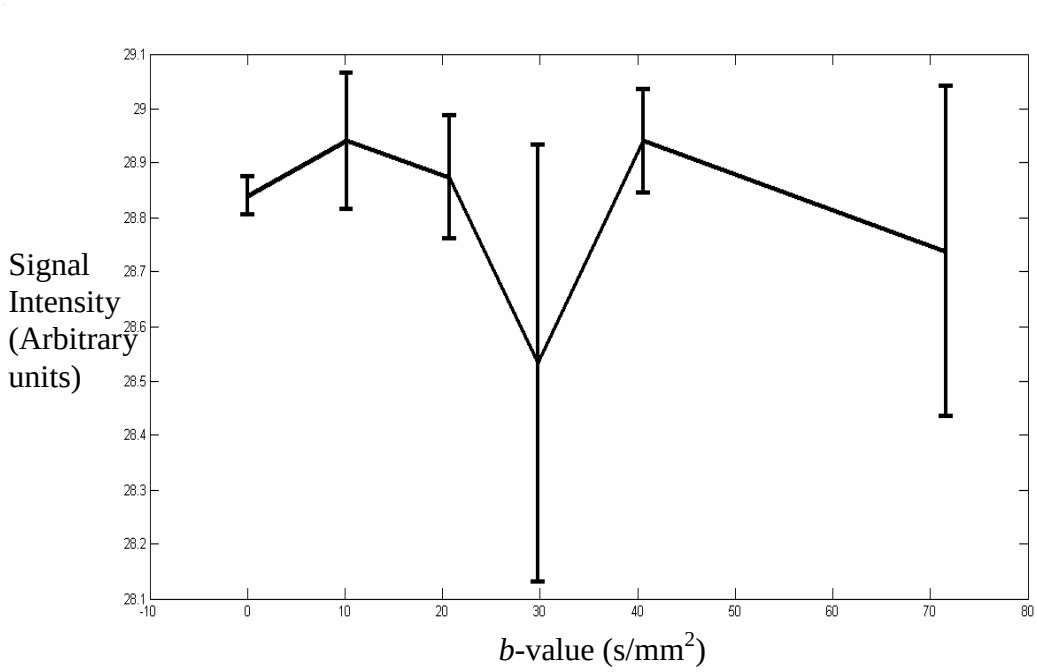

[a]

Figure 2.18
The measured signal from a large ROI within an oil phantom with increasing b value from diffusion gradients situation on the z-axis (of opposite sign to those reported in

Figure 2.16). Error bars represent the standard error of the mean signal across the 6 images at each b-value.

2.7.1 Diffusion Gradient Calibration for Vascular Suppression

Given that we were now satisfied that the mono-polar diffusion gradients arranged in this way on the z-axis were not introducing spurious signal due to eddy currents into the images, we proceeded to investigate the *b*-value necessary for suppression of the vascular signal. We performed three separate experiments on two male Sprague Dawley rats. One rat was recovered and then re-scanned the next day. The multi-echo half-Fourier CASL sequence was used with a labelling duration of 3s and PLD of 50ms. The 3s tagging duration ensured that the ΔM signal would be relatively high and the short 50ms PLD should maximise the proportion of tagged blood residing in the vascular compartment [Silver *et al.,* 1997 (a)]. Silva *et al.,* concluded that diffusion gradients applied on the read axis with a *b* value of 20 s/mm^2 are sufficient to remove signal from the vascular compartment [Silva *et al.,* 1997(a)]. However the extent of vascular suppression is likely to depend on the time delay between the gradients (Δ). This should be of sufficient duration to allow blood water molecules to flow parallel to the direction of the applied diffusion gradient for a time. If the direction of flow is totally perpendicular to the direction of the diffusion gradients then minimal vascular crushing will occur. In their work Δ was 33ms. However having a long Δ requires a long TE (see *1.10 Principles of Diffusion MRI*). It was important to keep the minimum TE of our experiments short relative to the expected $T2_{app}$ of our sample to ensure greater coverage of the transverse decay curve to improve the accuracy of $T2_{app}$ estimation. To this end it was important to minimise the diffusion time whilst ensuring that the vascular signal was effectively suppressed. Previous work has demonstrated that mono-polar diffusion gradients, applied in one direction, with 19ms separation and a *b*-value of approximately 90s/mm^2 suppressed the signal from labelled blood water in the vascular compartment [Silva *et al.,* 1997(b)]. An alternative study found that vascular suppression could be achieved using mono-polar diffusion gradients of 20ms separation and *b*-value of approximately 20s/mm^2 [Neil *et al.,* 1991]. In these experiments, we implement diffusion gradients with a similar separation (16ms) giving a minimum echo time of 29ms. Images were acquired at *b*-values of 0 (no diffusion gradients), 10, 40 and 60 using mono-polar diffusion gradients positioned on the slice select axis. The protocol was repeated a total of 6 times. Figure 2.19 shows the logarithm of the measured

perfusion weighted and control signal as a function of *b*-value. The gradient of this plot is equal to the apparent diffusion coefficient (ADC). Previous work has shown the dependence of the perfusion weighted signal on the *b*-value of the applied diffusion gradients to be bi-exponential due to a high pseudo-ADC from labelled spins in the vasculature and a low ADC from labelled blood that has exchanged into the tissue [Silva *et al.*, 1997(a); Neil *et al.*, 1991]. Visual inspection of Figure 2.19 suggests that the portion of the signal with a fast pseudo-ADC is attenuated at a *b*- value of 40s/mm^2. This provides evidence that the vascular component of the ASL signal has been effectively attenuated at a *b*-value of 40s/mm^2. Therefore we chose a *b*-value of 40 s/mm^2 for the vascular crusher gradients in the final experiments. I now continue to describe the final experiments undertaken to fulfil the aims of the investigation.

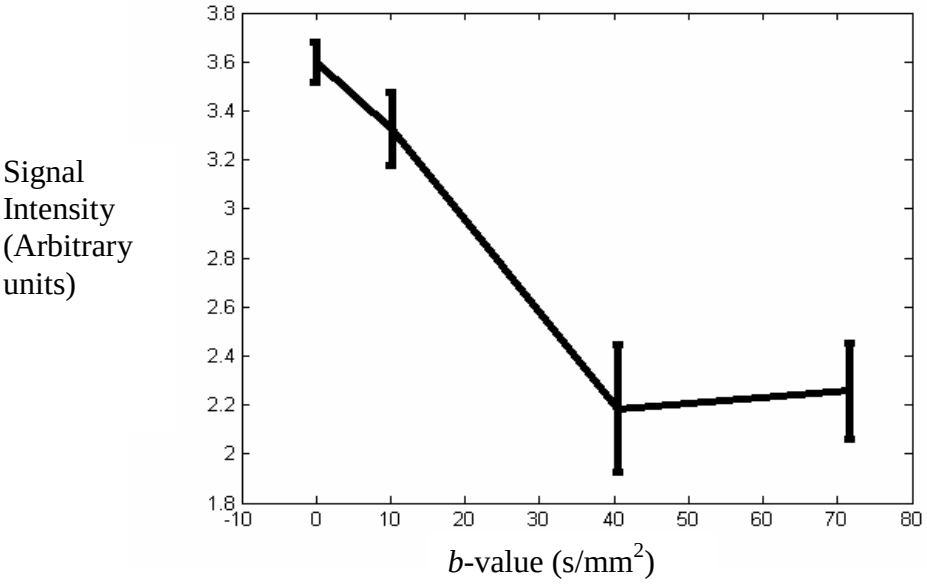
Signal Intensity (Arbitrary units)
3.8
3.6
3.4
3.2
3
2.8
2.6
2.4
2.2
2
1.8
-10
0
10
20
30
40
50
60
70
80
b-value (s/mm2)

[a]

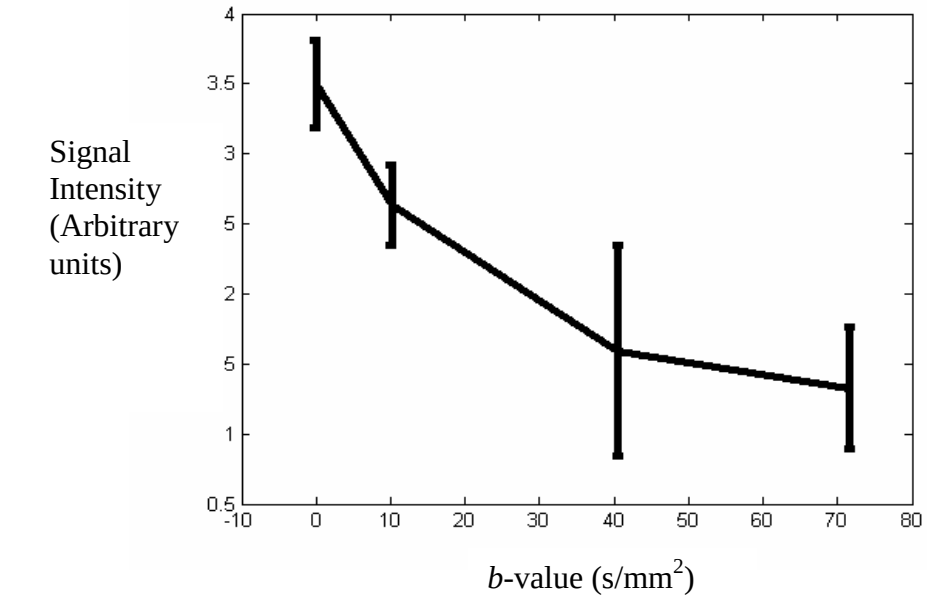
Signal Intensity (Arbitrary units)
4
3.5
3
5
2
5
1
0.5
-10
0
10
20
30
40
50
60
70
80
b-value (s/mm2)

[b]

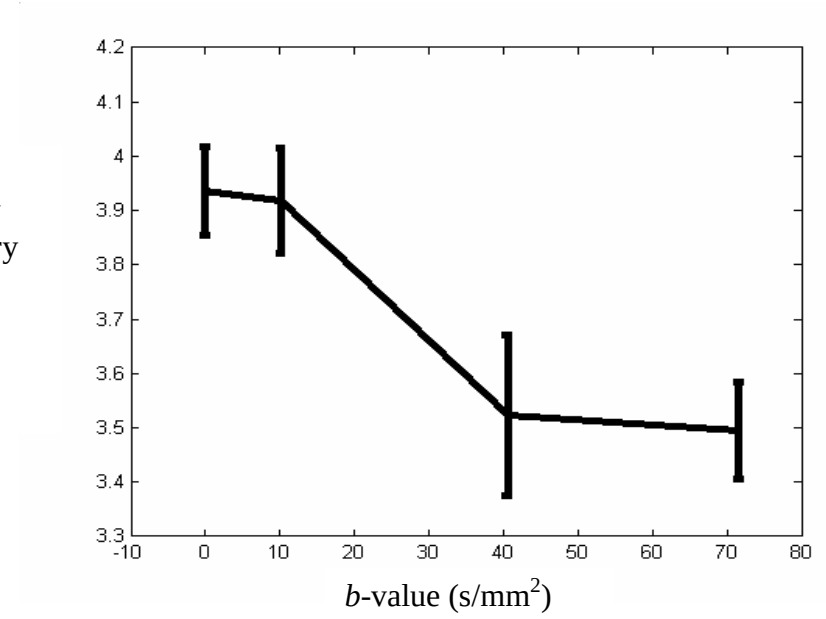

[c]

Figure 2.19
The mean perfusion weighted signal within a cortical ROI as a function of the b-value of the applied mono-polar diffusion gradients for the 3 experiments (a – c). Error bars represent the standard deviation of the mean across the 6 repeats.

2.8 CHARACTERISING THE ORIGIN OF THE ARTERIAL SPIN LABELLING SIGNAL IN MRI USING A MULTI-ECHO ACQUISITION APPROACH: FINAL EXPERIMENTS

2.8.1 Introduction

These experiments were performed following the stages of methodological development described above. The experiments below were performed with an optimised spoiler gradient and vascular crusher gradient configuration. Images were also acquired over a wide range of τ and PLD combinations relative to the pilot studies. The acquisitions also benefitted from reduced random and systematic errors in comparison to the pilot studies due to my accumulated experience in experimental imaging using the 2.35T scanner.

2.8.2 METHODS

2.8.2.1 Animal Preparation

9 male Sprague Dawley rats (182-242g) were used in this study. The animal preparation and MRI hardware was identical to that detailed in section 1.12. N_2O and halothane have been previously shown to increase CBF from baseline [Austin *et al.*, 2005].

2.8.2.2 Continuous Arterial Spin Labelling

A continuous arterial spin labelling (CASL) sequence [Alsop *et al.*, 1996] was implemented with an alternating adiabatic spin tagging pulse to minimise eddy current effects. The offset frequency of the labelling pulse oscillated in accordance with the slice select gradient to maintain a constant tagging plane (see Figure 2.17). The switched gradient scheme was implemented to suppress eddy currents that found to be causing systematic errors as a function of delay time. The switched gradient scheme consisted of 2 positive and 2 negative lobes giving single lobe duration of 0.75 for a 3s tagging duration. The control images were acquired by reversing the offset frequency of the tagging pulse. The labelling pulse was applied 2mm caudal to the cerebellum, perpendicular to the carotid and vertebral arteries, to ensure efficient spin tagging.

In order to monitor the progression of labelled water within the cerebral vessels and tissue, the tagging pulse duration was varied over the range of values: 500, 750, 1000 and 3000ms. After a PLD, single slice coronal images were then acquired 0.3mm caudal to the bregma using a multi-echo spin echo half-Fourier EPI sequence to produce 4 images in a single shot. This was twice repeated, with different sequence timings to achieve a total of 12 echo times (29, 41, 53, 68.2, 80.2, 92.2, 107.4, 119.4, 131.4, 146.6, 158.6, and 170.6ms). A slice selective 90°-180° pulse combination was used to generate the first spin echo and subsequent echoes were generated using non-selective adiabatic BIR-4 pulses, to ensure efficient spin refocusing and accurate T2 measurements. The PLD was 50 ms, and was also extended for additional acquisitions at 300, 700 and 1200 ms after the 3 second labelling pulse to investigate the provenance of the ASL signal further downstream, an approach commonly used to negate possible

confounding transit time effects [Alsop *et al.*, 1996]. The protocol was then repeated with the addition of mono-polar diffusion gradients (or vascular crusher gradients (VCGs)) around the first 180° refocusing pulse in the slice select direction. The time delay between diffusion gradients was 16ms, resulting in a *b*-value of 40 s/mm^2. As previously discussed, diffusion-weighting is frequently used to attenuate signal from the labelled spins in the vasculature to avoid overestimating perfusion and previous work has shown diffusion gradients of similar separation and *b*-value to achieve effective vascular suppression in the rat brain [Silva *et al.*, 1997(b]; Neil *et al.*, 1991]. The entire set of acquisitions was repeated for a total of 30 averages at each echo time, τ /PLD combination, with VCGs on and off. Other acquisition parameters were: inter-experiment delay time = 4s; half-Fourier matrix size =36x64; FOV = 32 x 32mm; slice thickness = 2mm.

Phase cycling and spoiler gradients applied along the slice select axis (modulated as a function of echo number using the scheme recommended in [Poon and Henkelman, 1992]) were implemented for all the acquisitions, as described in section 2.8.This is designed to remove spurious magnetisation pathways arising from a succession of imperfect RF pulses.

2.8.2.3 Image Analyses

Images were first averaged in k-space and then reconstructed to 64 x 64 using the POCS algorithm [Liang and Lauterbur, 2000; Liang et al. 1992].The images were masked and independent component analysis (ICA) was applied to the subtracted images to reduce random errors (See *Chapter 3*). The mean signal of the ASL difference image (ΔM) within a cortical ROI was taken (see *Figure 2.21*) and the data were fitted to a mono-exponential model. A mono-exponential model was used to yield a single apparent T2 estimate ($T2_{app}^{\Delta M}$) reflecting the contribution to the total ASL signal from the different cerebral compartments, each with their associated T2 constants. $T2_{app}^{\Delta M}$ provides a simple summary measure *i.e.* the apparent T2 of the ASL signal with minimal interpretation. Mono-exponential fits were also applied to the multi-echo ASL control images (giving $T2_{app}^{Ctrl}$) to investigate differences in $T2_{app}$ between the ASL ΔM signal and the control images (which represent the mean T2 of all the tissue in the ROI). A balanced one-way ANOVA with correction for multiple

comparisons was performed to determine the probability that the means of the $T2_{app}$ values with the different sequence parameters (τ, PLD, VCGs-on, VCGs-off, ΔM, ASL control image) were significantly different. For visualisation of spatial variations in $T2_{app}{}^{\Delta M}$, maps were also generated. Following ICA de-noising, $T2_{app}{}^{\Delta M}$ was calculated on a pixel-by-pixel basis by fitting to a simple mono-exponential model.

The fraction of the ASL signal from the intra-vascular compartment ($\Phi_{IV}{}^{\Delta M}$) was estimated for each animal at each τ and PLD using:

$$\Phi_{IV}{}^{\Delta M} = 1 - (\Delta M_{VCGs\text{-}on} / \Delta M_{VCGs\text{-}off}) \qquad [2.1]$$

from the perfusion-weighted images acquired at the earliest echo time (29ms) and assuming the VCGs crushed the entire vascular signal [Silva *et al*., 1997(a)]. Appendix B highlights the difficulties encountered when trying to estimate $T2_{IC}$ and $T2_{EC}$ from our data. Therefore we use values from previous studies that were designed to measure these parameters with reasonable precision. As previously discussed, there is convincing evidence that extravascular tissue has multiple T2 components in slow exchange (relative to the timescale of the T2 measurement) that can be attributed to intra- and extra-cellular space [Matsumae *et al.*,2003; Haida *et al.*,1987; Lascialfari *et al.*, 2005; Belton *et al.*, 1972; Hazlewood *et al.*, 1974; Gambarota *et al*, 2001]. However to our knowledge there are few studies that have estimated $T2_{IC}$ and $T2_{EC}$ in the rat brain. Indeed although these parameters were recently measured *in-vivo* at 4.7T, the authors reported marked variance in their estimates ($T2_{EC}$ = 184 ±50ms, $T2_{IC}$ =64 ±10ms) [Lascialfari *et al.*, 2005].Therefore in recognition of this possible source of uncertainty, we present results using $T2_{EC}$ and $T2_{IC}$ values from two alternative studies we found to have estimated these parameters . Firstly, we assume T2 values of the intra- and extra-cellular compartments to be 57ms and 174ms respectively from previous measurements of the 8 week old rat brain cortex at the same field strength as the present study [Haida *et al*., 1987]. Secondly, we assume T2 values of the intra- and extra-cellular compartments to be 53ms and 133ms respectively from previous measurements of the 6 week old rat mid-brain at 4.7T [Matsumae *et al.*, 2003] The proportion of intra- to extra-cellular ASL signal is then estimated by fitting the $\Delta M_{VCGs\text{-}on}$ observations to a bi-exponential model:

$$\Delta M_{VCGs-on} = \Delta M^{0}_{VCGs-on}\left[EC^{\Delta M} \exp(\frac{-TE}{T2_{EC}}) + IC^{\Delta M} \exp(\frac{-TE}{T2_{IC}}) \right] \qquad [2.2]$$

where $EC^{\Delta M}$ is the proportion of the $\Delta M_{VCGs\text{-}on}$ signal deriving from the extra-cellular compartment with transverse decay constant $T2_{EC}$ (174ms or 133ms), $IC^{\Delta M}$ is the proportion of the $\Delta M_{VCGs\text{-}on}$ signal originating from the intra-cellular compartment with transverse decay constant $T2_{IC}$ (57ms or 53ms) and $\Delta M^{0}_{VCGs\text{-}on}$ is the $\Delta M_{VCGs\text{-}on}$ signal at TE = 0ms. These estimates were then multiplied by the $\Delta M_{VCGs\text{-}on}$/ $\Delta M_{VCGs\text{-}off}$ measurements ($1\text{-}\Phi_{IV}^{\Delta M}$) to calculate the overall fraction of the total ASL signal ($\Delta M_{VCGs\text{-}off}$) from labelled water in the extra- and intra-cellular tissue space at a range of PLD and τ for each of the nine experiments ($\Phi_{EC}^{\Delta M}$ and $\Phi_{IC}^{\Delta M}$ respectively). The same analyses were performed on the control images to give the equivalent fractional contributions to these images (i.e Φ_{IV}^{Ctrl}, Φ_{EC}^{Ctrl} and Φ_{IC}^{Ctrl}). Since a three compartment model was assumed, the following equalities apply: $\Phi_{IV}^{\Delta M} + \Phi_{EC}^{\Delta M} + \Phi_{IC}^{\Delta M} = 1$; $\Phi_{IV}^{Ctrl} + \Phi_{EC}^{Ctrl} + \Phi_{IC}^{Ctrl} = 1$.

To estimate the T2 of the vascular compartment ($T2_{IV}$) we fitted the perfusion-weighted signal acquired without VCGs ($\Delta M_{VCGs\text{-}off}$) to a tri-exponential model assuming labelled blood water is in slow exchange between each of the vascular and the intra- and extra-cellular compartments in the tissue [Quirk *et al.*, 2002, Eichling *et al.*, 1974]:

$$\Delta M_{VCGs\text{-}off} = \Delta M^{0}_{VCGs\text{-}off}\left[\Phi_{EC}^{\Delta M} \exp\left(\frac{-TE}{T2_{EC}}\right) + \Phi_{IC}^{\Delta M} \exp\left(\frac{-TE}{T2_{IC}}\right) + \Phi_{IV}^{\Delta M} \exp\left(\frac{-TE}{T2_{IV}}\right) \right] \qquad [2.3]$$

For this fit, $T2_{EC}$ and $T2_{IC}$ were assumed to be 174ms and 57ms respectively, and the values of $\Phi_{EC}^{\Delta M}$, $\Phi_{IC}^{\Delta M}$ and $\Phi_{IV}^{\Delta M}$ calculated above were used. The fit therefore estimated two parameters: $T2_{IV}$ and $\Delta M^{0}_{VCGs\text{-}off}$. The choice of $T2_{EC}$ and $T2_{IC}$ has negligible effect on the estimated $T2_{IV}$.

In summary, the calculations used to estimate the tri-compartmental origin of the ASL and control signal (and $T2_{IV}$) were as follows:

1. Calculate the proportion of intra-vascular signal using data acquired with and without VCGs at the earliest echo time [Eq. 2.1]

2. Estimate $EC^{\Delta M}$ and $IC^{\Delta M}$ by fitting data acquired with VCGs to a bi-exponential model [Eq. 2.2] using assumed values for T2 of the two compartments
3. Calculate $\Phi_{EC}{}^{\Delta M}$ and $\Phi_{IC}{}^{\Delta M}$ by multiplying the $EC^{\Delta M}$ and $IC^{\Delta M}$ estimates by 1-$\Phi_{IV}{}^{\Delta M}$.
4. Estimate $T2_{IV}$ using the $\Phi_{IV}{}^{\Delta M}$, $\Phi_{EC}{}^{\Delta M}$ and $\Phi_{IC}{}^{\Delta M}$ measurements and fitting the data acquired without VCGs to a tri-exponential model [Eq. 2.3]:

The mean cortical signal in the perfusion-weighted images acquired with VCGs at τ = 3000ms and PLD = 700ms were used to estimate CBF for each experiment based on [Alsop and Detre, 1996].

2.8.3 RESULTS

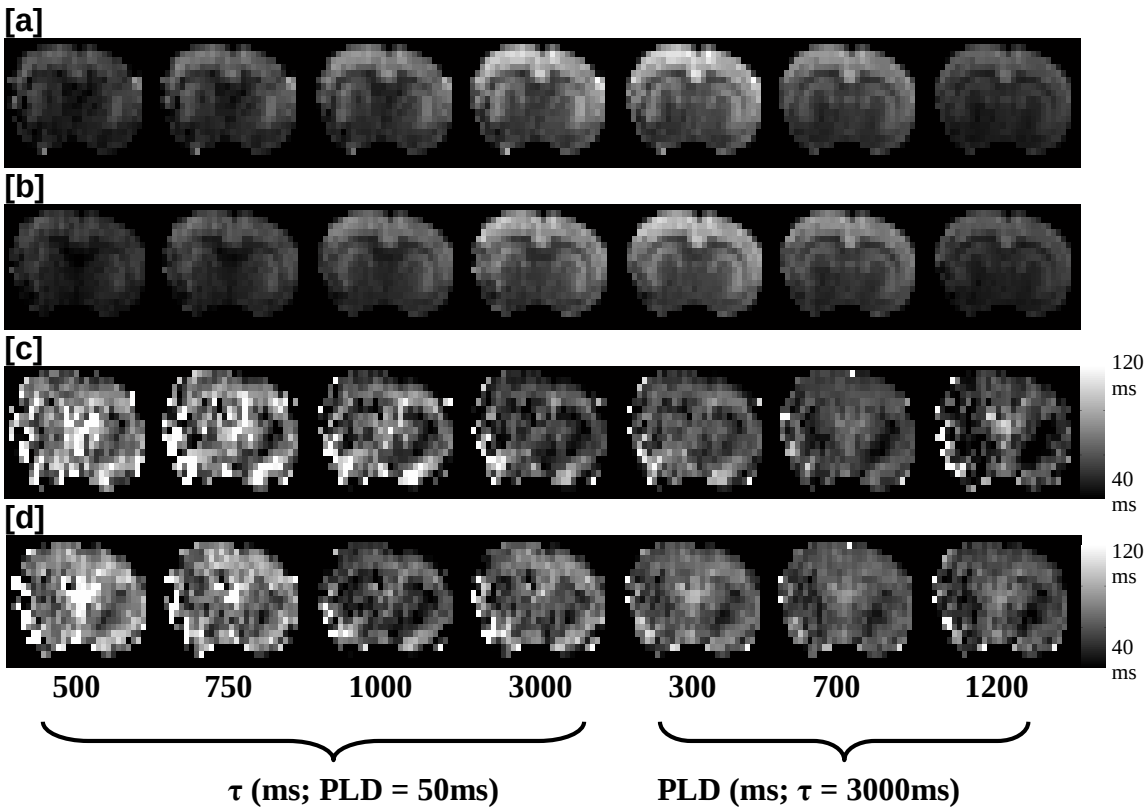

Figure 2.20

Typical perfusion-weighted images (number of averages=30) acquired at the shortest TE (29ms) and the PLD/ τ combinations shown below the respective images without [a] and with [b] VCGs. Calculated $T2_{app}{}^{\Delta M}$ maps without [c] and with [d] VCGs are also shown. At PLD=50ms and τ=500-750ms, there are regions of significantly reduced signal intensity in comparison to later τ due to longer transit times to these brain regions. As a result, the pixel by pixel $T2_{app}{}^{\Delta M}$ fits are essentially fitting noise which can return erroneously high values. At later τ and PLD, the acquired perfusion weighted signal in these regions increases and therefore the T2 fits return more sensible values.

This was one of the reasons a ROI in the cortex was chosen for our analyses; the transit times in this region are relatively homogenous.

The mean CBF across the 9 experiments (±1 SEM) was 233 ± 12 ml/min/100g, in good agreement with previous ASL measurements in rat cortex made in our laboratory using a similar approach [Thomas *et al.*, 2006]. Figure 2.20 shows typical perfusion-weighted images acquired over a range of τ and PLD, with and without the application of VCGs, together with calculated $T2_{app}^{\Delta M}$ maps. The SNR of the base images at the maximum TE (176.6ms) was considerably greater than 3 in all of the experiments. Therefore random noise in the cortex was assumed to be Gaussian [Gudbjartsson and Patz, 1994], with negligible noise rectification within the ROI of the subtracted images. Figure 2.21 shows the mean cortical transverse decay of the ASL signal from the same experiment.

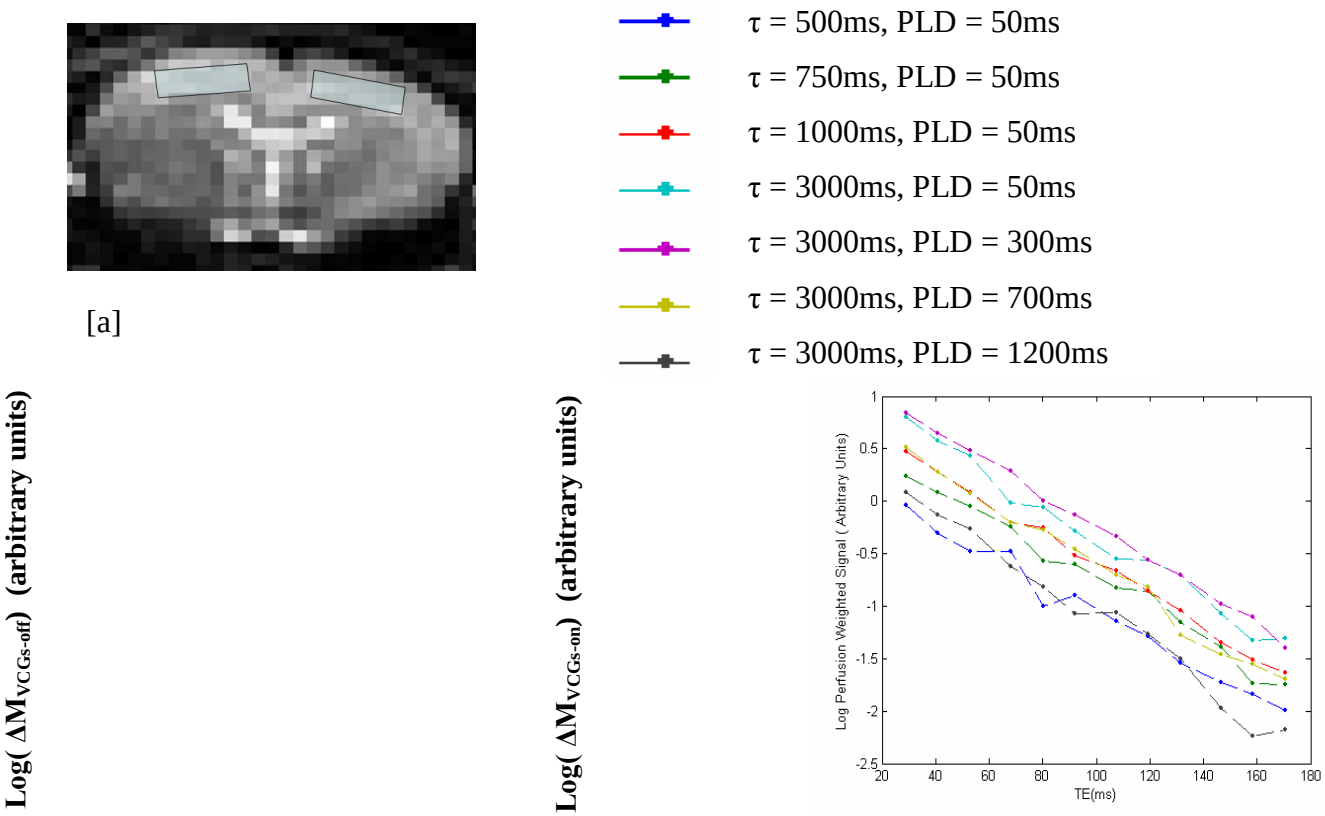

Figure 2.21

The mean perfusion-weighted signal within the cortical ROI (shown in [a]) for each set of PLD and τ combinations without [b] and with [c] VCGs against TE for the same subject as shown in Figure 2.20.

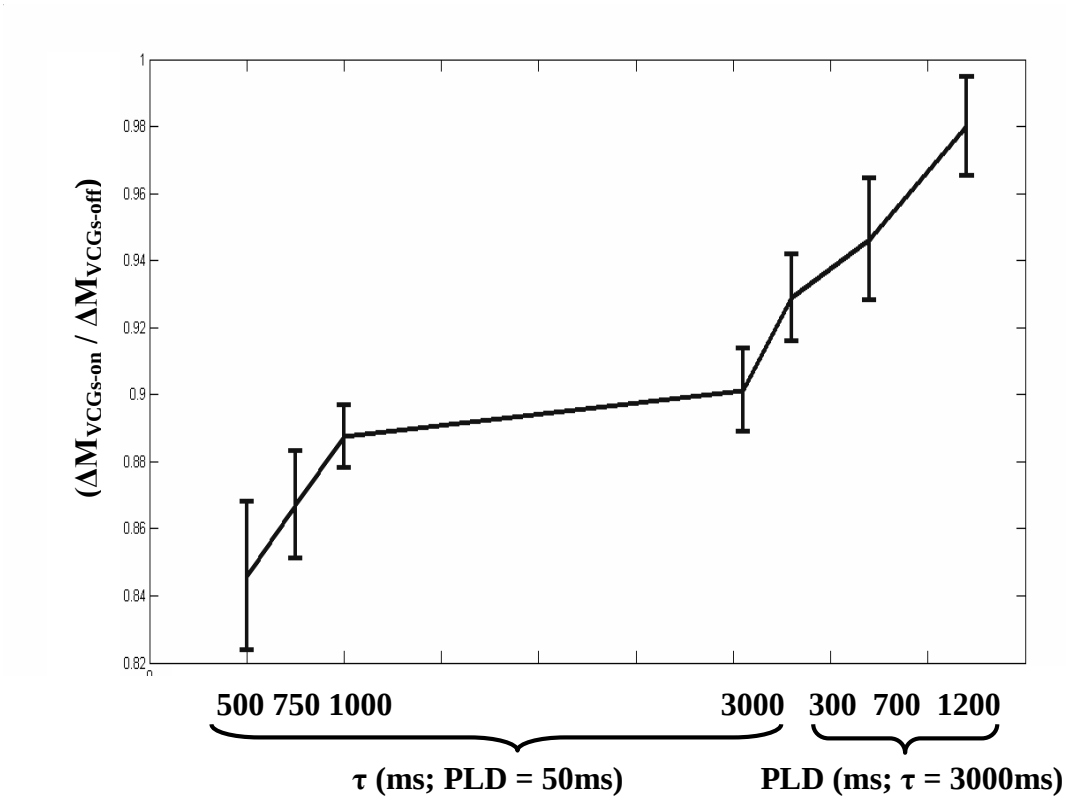

Figure 2.22
The mean of the measured $\Delta M_{VCGs\text{-}on}$ / $\Delta M_{VCGs\text{-}off}$ (i.e. 1 - $\Phi_{IV}^{\Delta M}$) at the different τ and PLD combinations. Error bars denote the standard error across the 9 subjects.

Figure 2.22 shows measured $\Delta M_{VCGs\text{-}on}$ / $\Delta M_{VCGs\text{-}off}$ (*i.e.* 1 - $\Phi_{IV}^{\Delta M}$) at fixed PLD (50ms) and increasing τ and then at fixed τ (3000ms) and increasing PLD. The monotonic increase, as is apparent from visual inspection, reflects the apparent shift of the source of the ASL signal from the vascular to the tissue compartment as τ and PLD increase. This is likely to be due to exchange of vascular water into the tissue combined with outflow of labelled blood from the observation slice that does not exchange. Figure 2.23 shows the mean apparent T2 of the ASL and control signal ($T2_{app}^{\Delta M}$ and $T2_{app}^{Ctrl}$) over the range of τ and PLDs across the 9 experiments. As previously discussed, $T2_{app}$ was estimated using a mono-exponential fit to provide a simple summary measure of the apparent T2 of the labelled water in the different compartments. $T2_{app}^{\Delta M}$(VCGs-on) and $T2_{app}^{\Delta M}$(VCGs-off) measured at τ = 500ms and PLD = 50ms were significantly greater than the equivalent estimates acquired at τ = 3000ms and PLD = 1200ms providing evidence that the $T2_{app}^{\Delta M}$ is decreasing with increasing τ and PLD, as inferred through visual inspection of Figure 2.23. The decrease in $T2_{app}^{\Delta M}$(VCGs-on) may reflect the shift of the perfusion-weighted signal

from the EC to the IC tissue space with increasing τ and PLD (see below). Each of the $T2_{app}^{\Delta M}$ (VCGs-on) estimates are significantly greater than the $T2_{app}^{Ctrl}$ (VCGs-on) observations acquired at the same τ and PLD, which provides evidence that the balance between the IC and EC signal contributions is more weighted towards the EC tissue space in the ΔM images compared to the controls (see below). There was no significant difference between $T2_{app}^{\Delta M}$ acquired with and without VCGs at the same τ and PLD. The $T2_{app}$ estimates from the individual 9 experiments are shown in Figures 2.24 and 2.25.

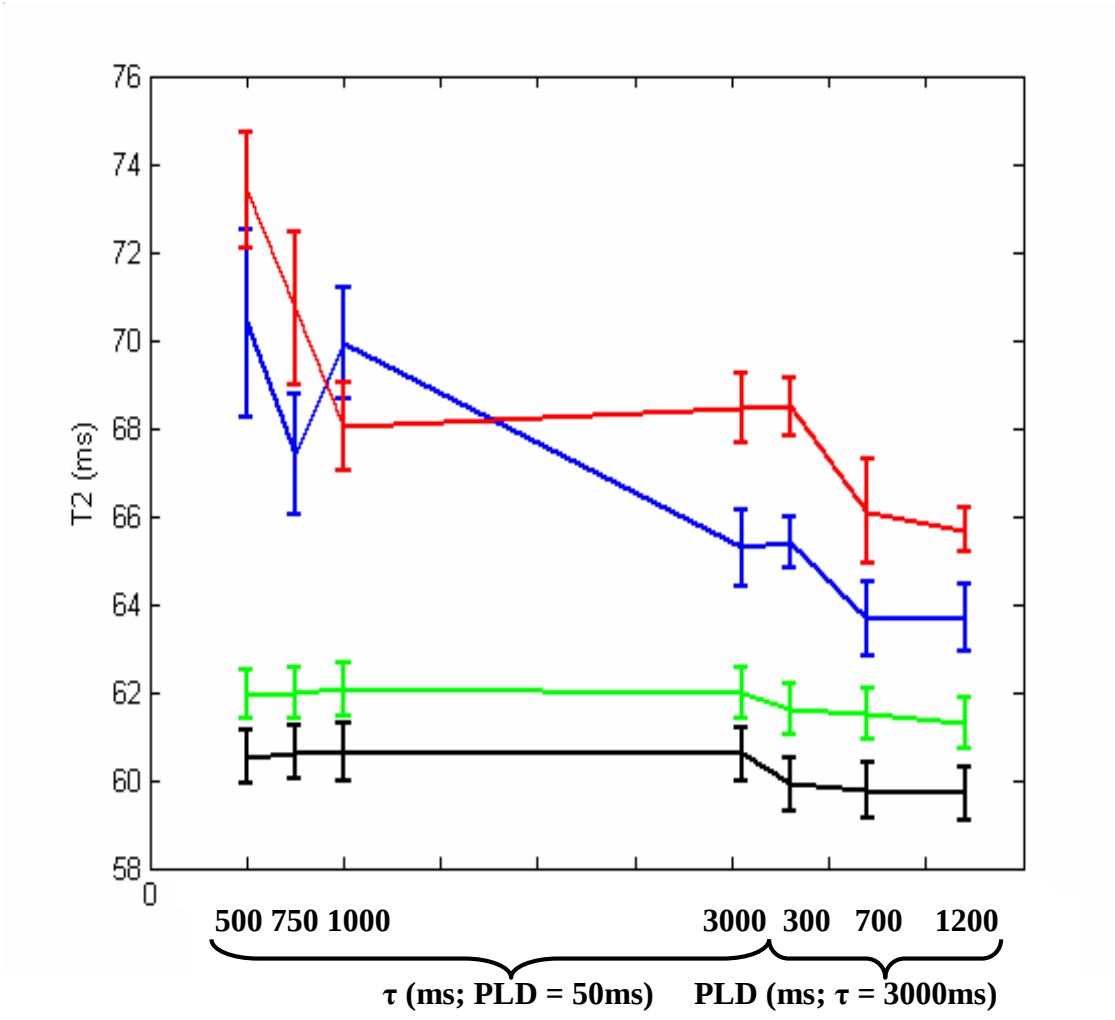

Figure 2.23
The mean T2 of the subtracted signal with VCGs ($T2_{app}^{\Delta M}$(VCGs-on) - red line) and without VCGs ($T2_{app}^{\Delta M}$(VCGs-off) - blue line) and of the control data with crushers ($T2_{app}^{Ctrl}$(VCGs-on) - green line) and without ($T2_{app}^{Ctrl}$(VCGs-off) - black line) at different PLD and τ times across all 9 experiments. Error bars represent the standard error across the 9 subjects.

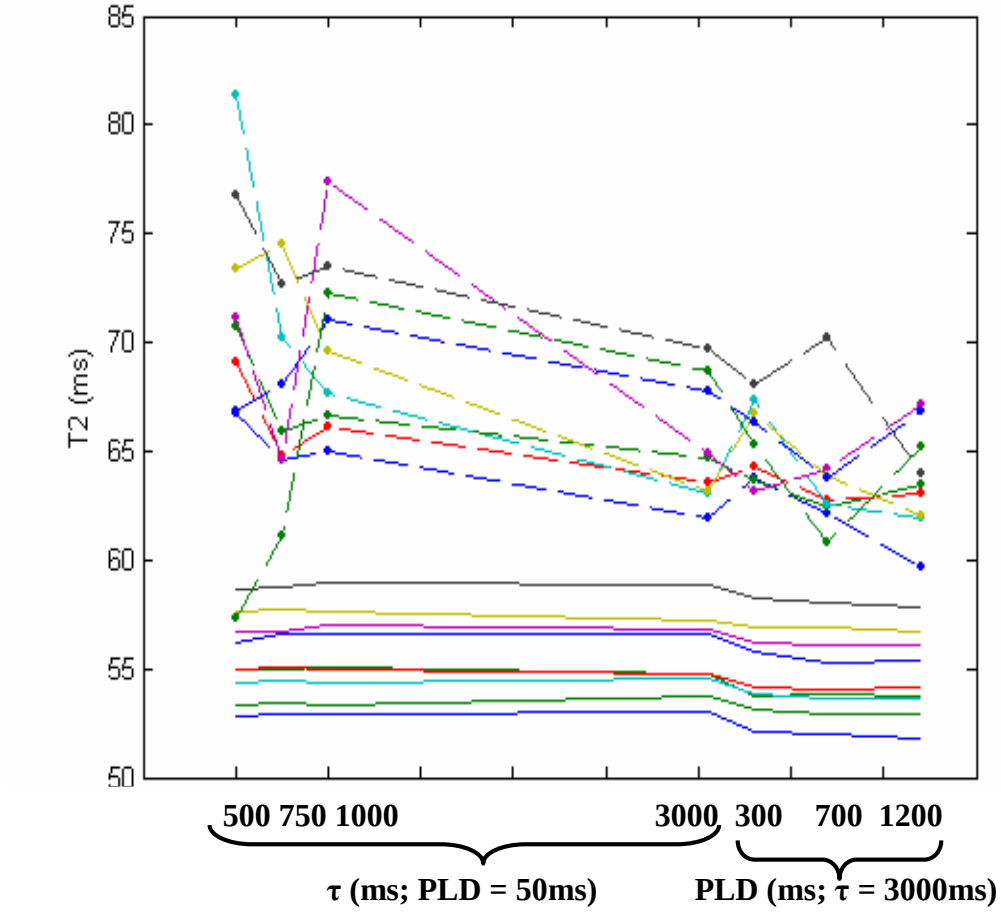

Figure 2.24
The $T2_{app}^{\Delta M}$(VCGs-off) and $T2_{app}^{Ctrl}$(VCGs-off)-5 for each of the 9 experiments (represented by different colour lines). I emphasise that the T2 of the control signal -5ms is reported here for clarity.

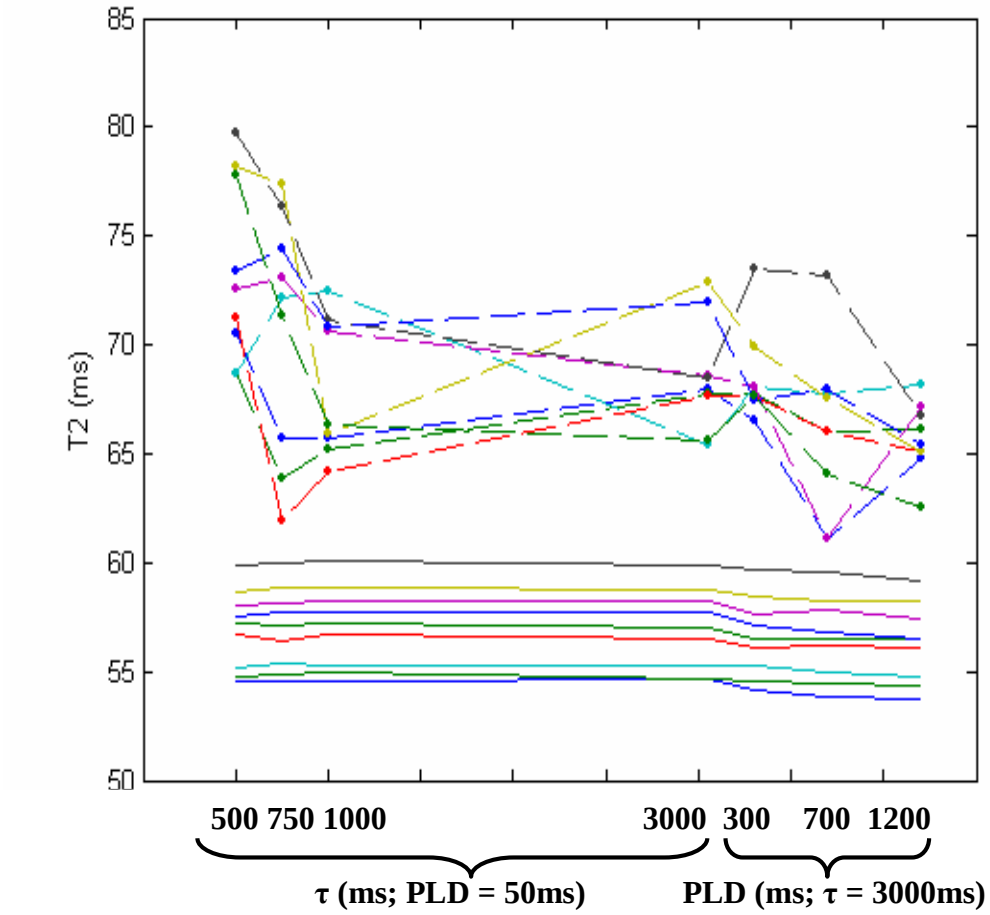

Figure 2.25
The $T2_{app}^{\Delta M}$(VCGs-on) and $T2_{app}^{Ctrl}$(VCGs-on)-5 for each of the 9 experiments (represented by different colour lines). I emphasise that the T2 of the control signal -5ms is reported here for clarity.

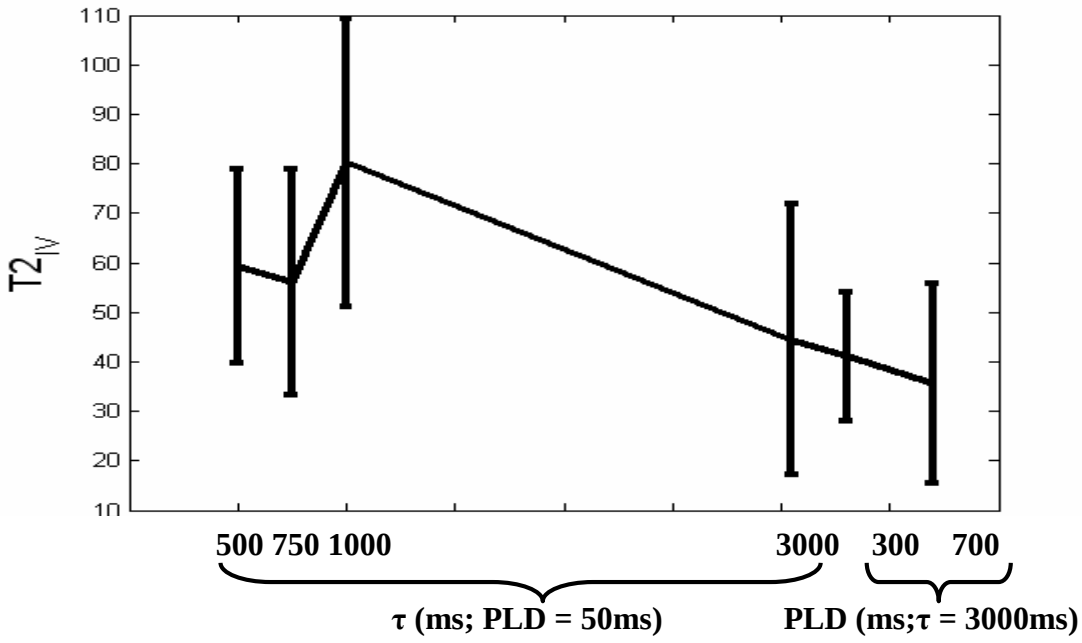

Figure 2.26
The median T2 of the vascular compartment ($T2_{IV}$) at increasing τ and PLD. Error bars (dashed lines) denote the standard error of the median across the 9 subjects.

Figure 2.26 shows the estimated T2 of the ASL signal located in the vascular compartment ($T2_{IV}$). $\Delta M_{VCGs\text{-}on}$/ $\Delta M_{VCGs\text{-}off}$ observations that are very close to 1 can result in fairly extreme $T2_{IV}$ estimates, due to the small intra-vascular component of these measurements. In this case, if there is a marked difference between $T2_{app}^{\Delta M}$(VCGs-on) and $T2_{app}^{\Delta M}$(VCGs-off) then $T2_{IV}$ will converge on a very high or very low value. For this reason, results from one of the nine experiments at four of the seven different τ and PLD combinations are not included in the analysis (criteria for exclusion was: $T2_{IV} > 500$ms). Furthermore for this reason, the median T2 across the remaining experiments is reported. At τ = 3000ms and PLD = 1200ms, $\Phi_{IV}^{\Delta M}$ is approximately 2.5 % of the total ASL signal, severely limiting the precision of $T2_{IV}$ estimation in this case. As a result the marked variance of the $T2_{IV}$ estimates across the 9 experiments restricts the interpretation of $T2_{IV}$ at these imaging parameters and is therefore not reported in Figure 2.26 (criteria for exclusion was: mean $\Phi_{IV}^{\Delta M} < 0.05$). At short τ (0.5-1s) and PLD (50ms) we may have expected the $T2_{IV}$ observations to be larger based on previous *ex-vivo* estimates of the T2 of arterial blood [Stanisz *et al.*, 2005]. This finding is likely to reflect the oxygen saturation of blood in the vessels that

contain the labelled water, given the sensitivity of blood T2 to this parameter [Zhao *et al.*, 2007]. .The median $T2_{IV}$ estimates at τ = 3000ms are lower than those at shorter τ. This may reflect the shift of the labelled blood that remains in the vessels from the arterial to the venous side of the vasculature (see 2.5 *Discussion*).

Figure 2.27 reports the proportion of the ASL and control signal in the vascular space and in the extra- and intra-cellular tissue space at increasing τ and PLD. The results are shown for $T2_{EC}$ and $T2_{IC}$ values of 174 and 57ms [a] and 133 and 53ms [b]. The VCGs will have a very small effect on the tissue compartment given the relatively low *b* value of 40s/mm^2. Any signal attenuation caused by the VCGs is likely to be similar between the intra- and extra-cellular tissue spaces [Duong *et al.*, 2001].

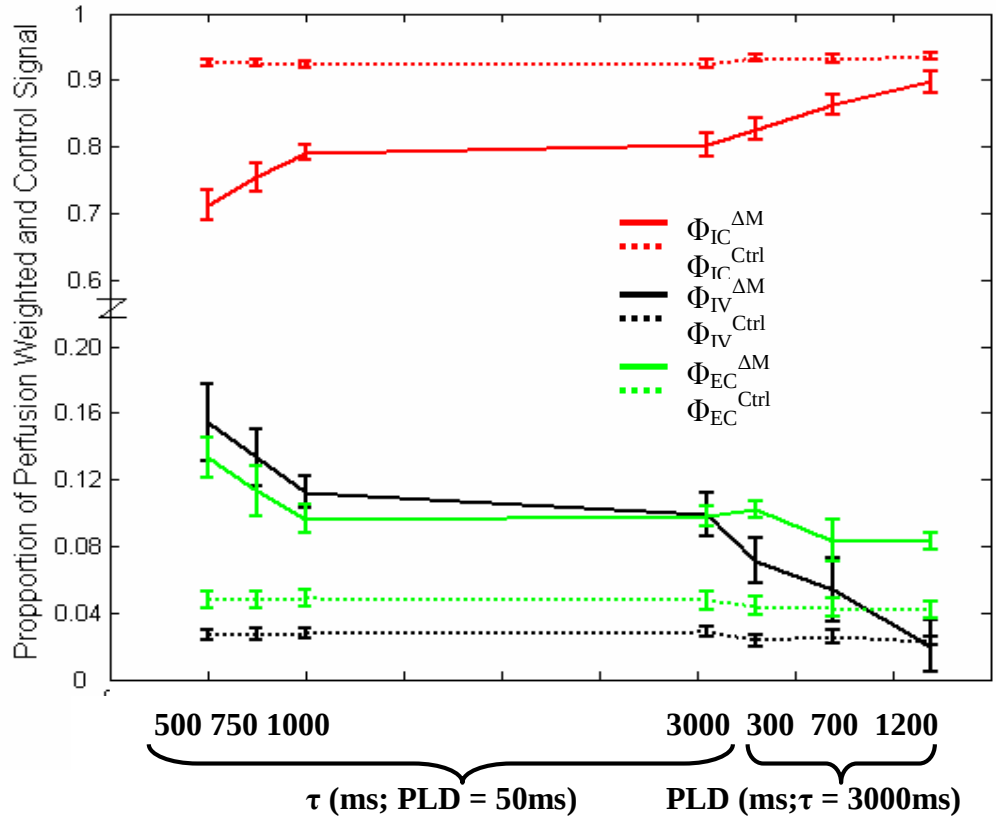
Propportion of Perfusion Weighted and Control Signal
1
0.9
0.8
0.7
0.6
0.20
0.16
0.12
0.08
0.04
0
$\Phi_{IC}^{\Delta M}$
Φ_{IC}^{Ctrl}
$\Phi_{IV}^{\Delta M}$
Φ_{IV}^{Ctrl}
$\Phi_{EC}^{\Delta M}$
Φ_{EC}^{Ctrl}
500 750 1000
3000
300 700 1200
τ (ms; PLD = 50ms)
PLD (ms;τ = 3000ms)

[a]

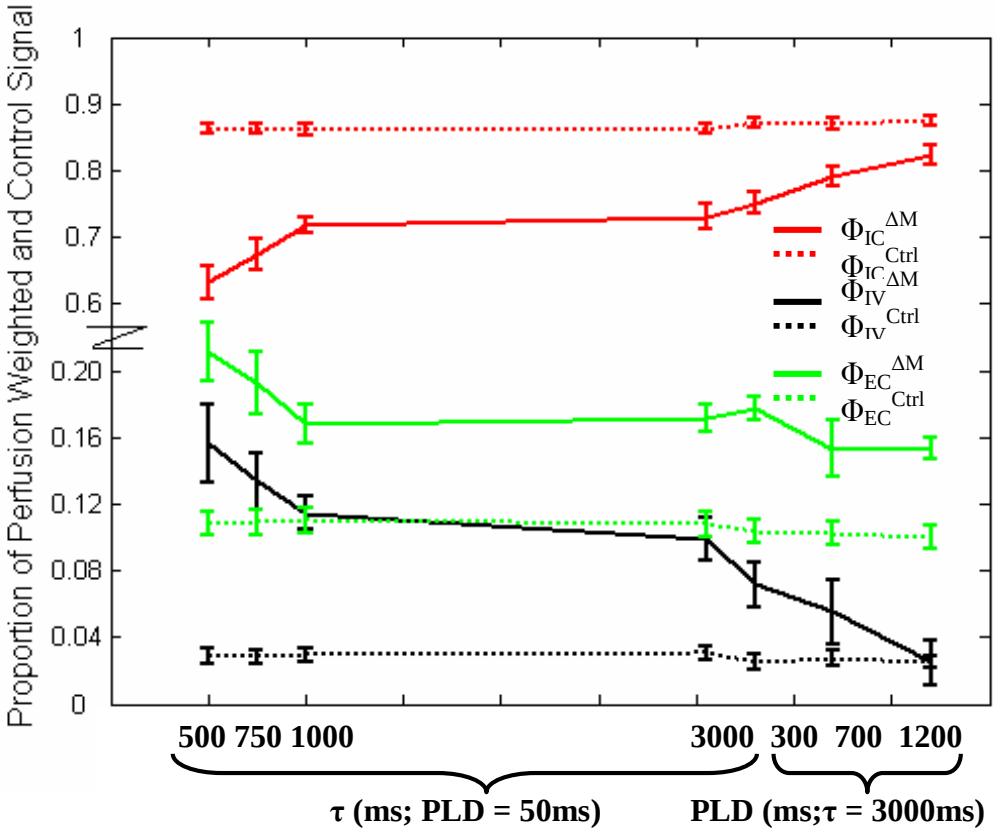
Proportion of Perfusion Weighted and Control Signal
1
0.9
0.8
0.7
0.6
0.20
0.16
0.12
0.08
0.04
0
$\Phi_{IC}^{\Delta M}$
Φ_{IC}^{Ctrl}
$\Phi_{IV}^{\Delta M}$
Φ_{IV}^{Ctrl}
$\Phi_{EC}^{\Delta M}$
Φ_{EC}^{Ctrl}
500 750 1000
3000
300 700 1200
τ (ms; PLD = 50ms)
PLD (ms;τ = 3000ms)

Figure 2.27
The proportion of ASL signal originating from the intra-vascular compartment ($\Phi_{IV}^{\Delta M}$ - black line) and in the intra-cellular ($\Phi_{IC}^{\Delta M}$ - red line) and extra-cellular ($\Phi_{EC}^{\Delta M}$ - green line) tissue space at the various τ and PLD combinations. The proportion of the control signal in the 3 different compartments is represented by a dotted line. Results are reported for $T2_{EC}$ and $T2_{IC}$ values of 174 and 57ms [a] and 133 and 53ms [b]. For clarity the scale of the y axis has been adjusted and is non linear. Error bars denote the standard error across the 9 experiments.

2.8.4 DISCUSSION

These are the first results to report the T2 of the ASL signal over a range of labelling durations and inflow times with and without the application of vascular crusher gradients. We have estimated the dynamic distribution of the ASL signal originating from the intra-vascular space and within the intra- and extra-cellular tissue space. This provides a novel insight into the destination of arterial blood water that has flowed into the brain as well as proof of principle of this non-invasive approach for possible future applications in humans and in animal models of disease where changes in the distribution of water within the intra- and extra-cellular tissue space are notoriously difficult to investigate.

Figure 2.27 indicates that the source of the ASL signal shifts further into the intra-cellular compartment from the intra-vascular and extra-cellular spaces as τ increases from 500 to 1000ms. The subsequent constancy of the $\Phi_{IC}^{\Delta M}$ and $\Phi_{EC}^{\Delta M}$ estimates at τ = 1s and τ =3s suggests that a dynamic equilibrium is established between labelled water in the intra-and extra-cellular tissue space by τ = 1s. This is perhaps not surprising given the previously measured mean residence time of spins in the extra-cellular space of ~120ms [Quirk *et al*, 2003]. Figure 2.27 also shows that the ΔM signal is weighted towards the extra-cellular space, relative to the control signal, even when τ=3s and with extended PLD. The short mean residence time (120ms) of the extra-cellular spins relative to the τ and PLD timescale, as well as the aforementioned evidence for establishment of a dynamic equilibrium, suggests this may be due to gradual exchange of labelled blood from the vascular compartment to the tissue at increasing PLD as implied from Figure 2.27. Indeed Figure 2.27 suggests that as the PLD increases at τ =3000ms the ASL signal from the intra-vascular compartment seems to effectively shift into the intra-cellular space while the signal from the extra-cellular space appears

relatively stable, perhaps acting as a "buffer" for the movement of labelled blood between the two compartments.

It was hypothesised that the heightened T2 of the arterial blood in comparison to the tissue would render the $T2_{app}^{\Delta M}$(VCGs-off) estimates sensitive to the fraction of labelled blood in the vascular compartment. However, Figure 2.23 demonstrates that the $T2_{app}^{\Delta M}$(VCGs-off) estimates are similar to the equivalent observations with vascular suppression gradients applied ($T2_{app}^{\Delta M}$(VCGs-on)) at brief tagging durations (τ = 500 to 1000ms) and PLD (50ms) where the majority of labelled blood in the vascular compartment is expected to be arterial. $T2_{IV}$ at these imaging parameters was calculated to be approximately 60-80ms (see *Figure 2.26*). As τ increases to 3000ms, the mean $T2_{app}^{\Delta M}$(VCGs-off) is less than the mean$T2_{app}^{\Delta M}$(VCGs-on). This suggests that upon image acquisition the portion of tagged blood in the vascular compartment has a reduced T2 relative to the labelled spins that have exchanged into the tissue. Indeed, $T2_{IV}$ at these imaging parameters was estimated to be 30-50ms (see *Figure 2.26*). Previous work has estimated the arterial and venous oxygen saturation in the rat brain to be 0.9 and 0.6 respectively [Lin *et al.*, 1998]. Zhou *et al*., measured the T2 of blood *in-vitro* at 3 Tesla and 37^{o}C [Zhou *et al.*, 2001]. They found the T2 of blood with an oxygen saturation of 0.9 and a hematocrit fraction of 0.44 to be approximately 74ms. The T2 of blood with an oxygen saturation of 0.6 was approximately 31ms. These measurements are of the order of those reported in Figure 2.26 and suggests that the source of the vascular portion of the ASL signal becomes increasingly weighted to the venous side of the vascular bed as τ increases from 1 to 3s. This observation may reflect the time taken by labelled blood that does not exchange (due to the limited permeability of the blood:brain barrier [Parkes and Tofts, 2002, Zhou *et al.*, 2001]) to traverse the capillary bed.

In equation 2.3, slow exchange (relative to the timescale of T2 measurement) is assumed between in the intra- and extra-vascular space in order to estimate $T2_{IV}$ from our data. However Figure 2.22 indicates that labelled blood water rapidly exchanges into the tissue. This casts doubt as to the validity of applying the model described in equation 2.3 to our data. However, Figure 2.24 provides some evidence that there is a difference between $T2_{app}^{\Delta M}$(VCGs-on) and $T2_{app}^{\Delta M}$(VCGs-off) at τ = 3000ms. This suggests that the rate of exchange between labelled blood water in the intra- and extra-

vascular space is indeed limited over the timescale of T2 measurement. This supports the validity of the model represented in equation 2.3. This apparent contradiction may reflect the heterogonous distribution of blood vessels. The dominant contribution to the measured $\Phi_{IV}^{\Delta M}$ may be from blood water in the larger arteries and veins rather than the capillaries (where the blood water may be in fast exchange)"

In this study we estimate the proportion of ASL signal from the vascular compartment ($\Phi_{IV}^{\Delta M}$) by calculating $\Delta MC_{VCGs\text{-}on}/ \Delta M_{VCGs\text{-}off}$, assuming the vascular crusher gradients (b = 40 s/mm^2) achieve complete vascular suppression [Silva *et al*., 1997(a)] (see section 2.7 *Calibration of Vascular Suppression*). Our $\Phi_{IV}^{\Delta M}$ estimates at τ = 3s and PLD = 50ms are in good agreement with previous Sprague Dawley rat ASL studies using similar anaesthetic regimes and very similar imaging parameters (τ and PLD). This provides some evidence that the crusher gradients are working as intended to severely attenuate the vascular signal. In [Silva *et al.*, 1997(a)], $\Phi_{IV}^{\Delta M}$ was estimated by differentiating the vascular and tissue portion of the ASL signal based on their diffusion characteristics (the same approach used in this work). They studied rats under halothane anaesthesia and found that the contribution of vascular water to the measured perfusion can be efficiently eliminated with b- values of approximately 20 s/mm^2. With τ = 3.5s and negligible PLD they calculated $\Phi_{IV}^{\Delta M}$ to be about 0.9 at normal CBF, in excellent agreement with our results (see *Figure 2.22*). In [Silva *et al*., 1998(b)] EF was estimated by exploiting the different susceptibility of blood and tissue to magnetisation transfer (MT) effects. In their work the extent of MT in the volume of interest was manipulated without affecting tagging efficiency by using a separate labelling coil for spin tagging. The estimated EF after labelling for 2 seconds with negligible PLD was around 0.9 in agreement with our findings. In [Zaharchuk *et al*,1998] a long half-life intra-vascular magnetopharmaceutical with a high tissue;blood susceptibility difference was used in combination with ASL for the continuous measurement of blood flow and blood volume. In this study $\Phi_{IV}^{\Delta M}$ was calculated to be about 0.8 at τ = 3.7s and PLD =0.2s at a blood flow of 200ml/100g/min. However they report a large spread in the $\Phi_{IV}^{\Delta M}$ estimates acquired over a relatively narrow range of blood flows (1.1 to 0.6 over 100 - 200 ml/min/100g). Therefore the estimated $\Phi_{IV}^{\Delta M}$ in the present work is likely to fall within the confidence intervals of this previous study. Nonetheless, this may introduce some uncertainty as to the extent of vascular suppression in our experiments. Previous work has measured a persistent microvascular signal despite the presence of large

crusher gradients [Henkelman *et al.,* 1994]. This may be due the variability in microvascular flow during the application of the diffusion-weighting gradients in the sequence [Villringer *et al*., 1994]. This could additionally explain the $\Delta M_{VCGs\text{-}on}$/ $\Delta M_{VCGs\text{-}off}$ reported in the present work at brief tagging durations (Figure 2.22, τ =500 and 750ms): given that the transit time from the labelling to the imaging plane [Thomas *et al.,* 2006] in the CASL experiments has been reproducibly measured to be about 0.2s, intuitively one may expect the vascular proportion occupied by the labelled blood to be greater than 0.2. However, this result may simply indicate rapid exchange of labelled water into the tissue after entering the capillary bed. In humans, a greater proportion of labelled water resides in the intra-vascular compartment during image acquisition [Wang *et al.,* 2007]. This discordance principally reflects the marked difference in CBF (~50 ml/min/100g) and transit time (1s) in the human brain in comparison to the rat brain (where CBF ~200 ml/min/100g and transit time ~ 0.2s).

Although visual inspection of Figure 2.23 suggests $T2_{app}^{\Delta M}$(VCGs-on) is increased in comparison to $T2_{app}^{\Delta M}$(VCGs-off) at τ =3000ms, we found no significant difference between the $T2_{app}^{\Delta M}$ estimates acquired at the same τ and PLD with and without VCGs. This finding provides some indication that the sensitivity of $T2_{app}^{\Delta M}$ to $\Phi_{IV}^{\Delta M}$ is limited and suggests that diffusion sensitised measurements ($\Delta M_{VCGs\text{-}on}$/ $\Delta M_{VCGs\text{-}off}$) are a much more efficient way of calculating the proportions of vascular and tissue signal in the rat brain.

In general, the relatively narrow range of measured T2 estimates (see *Figure 2.23*) suggests this approach has limited sensitivity to the vascular origin of the labelled blood, even over a wide range of CASL sequence timings (*i.e.* τ, PLD; see *Figure 2.23*). Alternatively, this finding does provide some reassurance that $T2_{app}^{\Delta M}$ is unlikely to be a confounding factor for CBF estimation using a range of tagging pulse lengths and/or PLDs, particularly if TE is relatively short. However the significantly increased $T2_{app}$ (VCGs-on) of the perfusion-weighted signal in comparison to the control may result in a small overestimation in CBF using standard quantification methods [e.g. Alsop and Detre, 1996, Buxton *et al.,* 1998] as the equilibrium magnetisation of the tissue (M_0) is assumed to decay with the same T2 as the labelled ASL signal in the brain.

The volume of extra-cellular space in the static tissue as estimated from our control data is around 5% based on assigning T2 values of 57 and 174ms to the intra- and extra-cellular compartments [Haida *et al.*, 1987]. Although this is in broad agreement with a number of previous studies, it is rather small in comparison to others [Rall and Zubrod, 1962]. This may suggest that $T2_{EC}$ and $T2_{IC}$ values of 133ms and 53.4ms respectively are more accurate as this yields EC volume estimate of approximately 12% (see *Figure 2.27*) This lies within the range of previously reported values in the rat cortex: 9.3% [Reulen *et al.*,1970]; 16.1% [Rees *et al*.,1982], 14.5% [Woodwood *et al*., 1967], 14-22% [Davson H and Spaziani E, 1959] and 7-14% [Rall *et al*., 1962].

In this chapter we use a bi-exponential model to estimate the proportion of the ASL signal originating from the intra-and extra-cellular tissue space (see equation 2.2). As demonstrated by the simulations described in Appendix B, our data is not able to provide evidence as the viability of the bi-exponential model. For example, the fit to the data displayed in figure B1 has an R-square of 0.997 but provides no evidence as to whether a mono-exponential or bi-exponential fit is more appropriate for the data (as indicated from the confidence intervals of the fitted parameters). Therefore we have used values from previous studies designed to precisely estimate $T2_{IC}$ and $T2_{EC.}$ However the reliance on published $T2_{EC}$ and $T2_{IC}$ values is a limitation of this work. In future studies it would be ideal to fit the control data acquired with VCGs to a bi-exponential model to simultaneously estimate the relative distribution of the intra- and extra-cellular signal of the static tissue in addition to the T2 constants of the two compartments. However, this would require a greater number and range of echo times than used in the present work (e.g. see [Matsumae *et al.*, 2003] for a typical acquisition protocol used for this purpose). See Chapter 5 and Appendix B for further discussion of this issue.

It is important to note that the experiments were performed on rats anaesthetised on N_2O and halothane. These substances have been previously shown to increase CBF from baseline [Austin *et al.*, 2005]. This is likely to affect the tri-compartmental distribution of the ASL signal at the different τ and PLD times. However the increased CBF will have improved the SNR of the ΔM measurements which in turn improved the precision of T2 estimation.

2.8.5 SUMMARY

In summary, ASL can non-invasively isolate the MR signal from arterial blood water that has flowed into the brain. We have shown that it is possible to measure the transverse decay of this signal over a range of bolus durations and delivery times to estimate the dynamic origin of nutritive flow-related signal in the intra- and extra-cellular tissue space, accepting that the accuracy of $\Phi_{IC}^{\Delta M}$ and $\Phi_{EC}^{\Delta M}$ estimation is restricted by the limited validation of $T2_{IC}$ and $T2_{EC}$. Furthermore, by taking measurements with and without vascular crusher gradients we have calculated the proportion of the perfusion-weighted signal originating from the cerebral vasculature, together with the associated T2 constant of this compartment (which may represent a surrogate index of blood oxygen saturation). We hope that this technique may be useful for future application in animal models of disease to better understand the relationship between the time-course for blood delivery and exchange and pathology.

2.7 REFERENCES

Alsop DC, Detre JA (1996) Reduced transit-time sensitivity in noninvasive magnetic resonance imaging of human cerebral blood flow. Journal of Cerebral Blood Flow and Metabolism 16, 1236-1249

Austin VC, Blamire AM, Allers KA, Sharp T, Styles P, Matthews PM, Sibson NR (2005). Confounding effects of functional activation in rodent brain: a study of halothane and alpha-chlorose anaesthesia. Neuroimage 24, 92-100.

Bakay L (1970). The extracellular space in brain tumours. I. Morphological considerations. Brain 93, 693-698

Belton PS, Jackson RR, Packer J (1972). Transverse nuclear relaxation and spin effects. Biochimica Biophysica ACTA 286 16-25

Buxton RB, Frank LR, Wong EC, Siewert B, Warach S, Edelman RR (1998) A general kinetic model for quantitative perfusion imaging with arterial spin labelling. Magnetic Resonance in Medicine 40:383-396

Davson H, Spaziani E (1959). The blood-brain barrier and the extracellular space of brain. Journal of physiology. 149; 135-143.14-22%.

Detre JA, Leigh JS, Williams DS, Koretsky AP. (1992). Perfusion imaging. Magnetic Resonance in Medicine 23:37-45

Duong TG, Sehy JV, Yablonskiy DA, Snider BJ, Ackerman JJH, Neil JJ. (2001) .Extracellular Apparent Diffusion in Rat Brain. Magnetic Resonance in Medicine 45:801-810

Eichling J, Raichle M, Grubb R, Ter-Pogossian M. (1974). Evidence of the limitations of water as a freely diffusible tracer. Circulation Research 35, 358-364

Francis ST, Bowtell R, Gowland PA (2008) Modeling and optimization of Look-Locker spin labeling for measuring perfusion and transit time changes in activation studies taking into account arterial blood volume. Magnetic Resonance in Medicine 59 316-25

Gambarota G, Cairns BE, Berde CB, Mulkern RV (2001). Osmotic effects on the T2 relaxation decay of in vivo muscle. Magnetic Resonance in Medicine 26, 592-599

Golay X, Silvennoinen MJ, Zhou J, Clingman CS, Kauppinen RA, Pekar JJ, Van Zijl PC (2001). Measurement of tissue oxygenation extraction rations from venous blood T(2): Increased precision and validation of principle. Magnetic Resonance in Medicine 46, 282-91

Gudbjartsson H, Patz P (1994). The rician distribution of noisy MRI data. Magnetic Resonance in Medicine 34, 910-914

Haida M, Yamamoto M, Matsumura H, Shinohara Y, Fukuzaki M. (1987). Intracellular and extracellular spaces of normal adult rat brain determined from the proton nuclear magnetic resonance relaxation times. Journal of Cerebral Blood Flow and Metabolism 7:552-556

Harrison R, Bronskill MJ, Henkleman M. (1995). Magnetization Transfer and T_2 Relaxation Components in Tissue. Magnetic Resonance in Medicine 33, 490 – 496.

Hazlewood CF, Chang DC, Nichols BL, Woessner DE (1974). Nuclear magnetic resonance relaxation times of water protons in skeletal muscle. Biophysics Journal 14:583-606

He, Yablonskiy. Transverse relaxation of the perfusion MRI signal. ISMRM Perfusion Workshop 2007, Brazil.

Henkelman RM, Neil JJ, Xiang QS (1994) A quantitative interpretation of IVIM measurements of vascular perfusion in the rat brain. Magnetic Resonance in Medicine 32:464-469

Kober F, Duhamel G, Cozzone PJ (2008) Experimental comparison of four FAIR arterial spin labelling techniques for quantification of mouse cerebral blood flow at 4.7 T. NMR in Biomedicine 21, 781-792

Lascialfari A, Zucca I, Asdente M, Cimino M, Guerrini U, Paoletti R, Tremoli E, Lorusso V, Sironi L (2005). Multiexponential T2-relaxation analysis in cerebrally damaged rats in the absence and presence of a gadolinium contrast agent. Magnetic Resonance in Medicine 53, 1326-1332.

Le Bihan D. Diffusion and Perfusion Magnetic Resonance Imaging. Applications to functional MRI. Raven Press 1995.

Liang Z-P, Boada FE, Constable RT, Haacke EM, Lauterbur PC, Smith MR. (1992). Constrained Reconstruction Methods in MR Imaging. Reviews in Magnetic Resonance Imaging 4, 67-185.

Liang Z and Lauterbur PC (2000) Principles of Magnetic Resonance Imaging; A Signal Processing Perspective. IEEE press.

Lin W,Paczynski RP, Celik A, Karthikeyan K, Hsu CY, Powers WJ. (1998). Experimental Hypoxia: Changes in R_2* of Brain Parenchyma Accurately Reflect the Combined Effects of Changes in Arterial and Cerebral Venous Oxygen Saturation. Magnetic Resonance in Medicine 39,374-481.

Matsumae M,Oli S, Watanabe H, Okamoto K, Y Suzuji, Sato K, Atsumi H, Goto T, Tsugane R (2003) Distribution of intracellular and extracellular water molecules in developing rat's midbrain: comparison with fraction of multicomponent T2 relaxation time and morphological findings from electron microscopic imaging. Childs Nervous System 19, 91-5

McRobie DW, Moore EA, Graves MJ, Prince MR. NMR MRI: From picture to proton. (first edition). Cambridge university press.

Moseley ME, Cohen Y, Mintorovitch J, Chileuitt L, Shimizu H, Kucharczyk J, Wendland MF, Weinstein PR. (1990). Early detection of regional cerebral ischemia in cats: comparison of diffusion and T2-weighted MRI and spectroscopy. Magnetic Resonance in Medicine 14, 330-346

Neil JJ, Scherrer LA, Ackerman JJH. (1991). An approach to Solving the Dynamic Range Problem in Measurement of the Pseudodiffusion Coefficient in Vivo with Spin Echoes. Journal of Magnetic Resonance 95,607-614

Parkes LM, Tofts PS (2002) Improved accuracy of human cerebral blood perfusion measurements using arterial spin labelling: accounting for capillary water. Magnetic Resonance in Medicine 48, 27-41

Pell GS, Briellmann RS, Waites AB, Abbott DF, Lewis DP, Jackson GD.(2006). Optimized clinical T2 relaxometry with a standard CPMG sequence. Journal of Magnetic Resonance Imaging 23, 248-52.

Petersen ET, Lim T, Golay X. (2006). Model-free arterial spin labelling quantification approach for perfusion MRI. Magnetic Resonance in Medicine 55, 219-32

Petersen ET, Golay X. (2008). Is Arterial Spin Labelling Ready for the Prime time? Prilimary Results from the QUASAR Reproducibility Study Presented at the 16th ISMRM , Berlin. (Abstract 191)

Poon CS, Henkelman RM.(1992). Practical T2 Quantification for Clinical Applications. Journal of Magnetic Resonance 2, 541-553

Quirk JD, Bretthorst GL, Duong TQ, Snyder AZ, Springer Jr CS, Ackerman JH, Neil JJ (2003) Equilibrium Water Exchange Between the Intra- and Extracellular Spaces of Mammalian Brain. Magnetic Resonance in Medicine 50:493-499

Rall DP, CG Zubrod (1962) Mechanisms of Blood Absorption and Excretion :Passage of Drugs in and out of the central nervous system. Annual Review of Pharmacology of Toxicology 2, 109-128

Rall DP, Oppelt WW, Patlak CS (1962). Extracellular space of brain as determined by diffusion of inulin from the ventricular system. Life Sciences 2;43-44;7-14%.

Reulen. *H.J,*, U. Hase. A. Fenske. M. Samii and K. Schiirmann (1970) Extrazellul/irraum und lonenverteilung in grauer und weisser Substanz des Hundehirns, *Aeta Neuroehir. (Wien).* 22:305 325. 9.3% in the cortex

Rees S, Cragg I, Everitt AV (1982). Comparison of extracellular space in the mature and ageing rat brain using a new technique. Journal of the Neurological Sciences 53(2):347-57. 16.1%

Silva AC, Williams DS, Koretsky AP. (1997(a)). Evidence for the exchange of arterial spin labeled water with tissue water in rat brain from diffusion-sensitized measurements of perfusion. Magnetic Resonance in Medicine 38:232-237

Silva AC, Zhang WG, Williams DS, Koretsky AP. (1997(b)). Estimation of water extraction fractions in rat brain using magnetic resonance measurement of perfusion with arterial spin labeling. Magnetic Resonance in Medicine 37: 58-68

Stanisz GJ, Odrobina EE, Pun J, Escaravage M, Graham SJ, Bronskill MJ, Henkelman RM. (2005). T1, T2 relaxation and magnetization transfer in tissue at 3T. Magnetic Resonance in Medicine 54:507-12.

St Lawrence KS, Wang J. (2005). Effects of the apparent transverse relaxation time on cerebral blood flow measurements obtained by arterial spin labelling. Magnetic Resonance in Medicine 53:425-33.

Thomas DL, Lythgoe MF, Calamante F, Gadian DG, Ordidge RJ. (2001). Simultaneous non-invasive measurement of CBF and CBV using double-echo FAIR (DEFAIR). Magnetic Resonance in Medicine 45, 853-63

Thomas DL, Lythgoe MF, van de Weerd L, Ordidge RJ, Gadian DG. (2006). Regional variation of cerebral blood flow and arterial transit time in normal and hyperfused rat brain measured using continuous arterial spin labelling MRI. Journal for Cerebral Blood Flow and Metabolism. 26, 274-82

Turner R, Howseman A, Rees GE, Josephs O, Friston K. (1998). Functional magnetic resonance imaging of the human brain: data acquisition and analysis. Experimental Brain Research. 123, 5-12

Villringer A, Them A, Lindauer U, Einhaaupl K, Dirangl U. (1994). Capillary perfusion of the rat brain cortex: an in vitro confocal microscopy study. Circulation Research 75,55-62

Wang J, Fernandez-Serra MA, Wang S, St. Lawrence KS. (2007). When perfusion meets diffusion: in vivo measurements of water permeability in human brain. Journal of Cerebral Blood Flow and Metabolism 27, 839-49

Wang J, Alsop DC, Song HK, Maldjian JA, Tang K, Salvucci AE, Detre JA. (2003). Arterial transit time imaging with flow encoding arterial spin tagging (FEAST). Magnetic Resonance in Medicine 50, 599-607

Woodwood DL, Reed DJ, Woodbury DM (1967). Extracellular space of rat cerebral cortex. American Journal of Physiology 212(2):367-70.14.5%.

Zaharchuk G, Bogdanov Jr. AA, Marota JJA, Shimizu-Sasamata M, Weisskoff RM, Kwong KK, Jenkins BG, Weissleder R, Rosen BR .(1998). Continuous Assessment of Perfusion by Tagging Including Volume and water Extraction (CAPTIVE): a steady-state contrast agent technique for measuring blood flow, relative blood volume fraction and the water extraction fraction. Magnetic Resonance in Medicine. 40, 666-678

Zhou JY, Wilson DA, Ulatowski JA, Trajstman RJ, van Zijl PCM. (2001). Two-compartment exchange model for perfusion quantification using arterial spin tagging. Journal of Cerebral Blood Flow and Metabolism 21, 440-455

Zhao JM, Clingman CS, Narvainen MJ, Kauppinen RA, van Zijl PCM. (2007). Oxygenation and Hematocrit Dependence of Transverse Relaxation Rates of Blood at 3T. Magnetic Resonance in Medicine 58, 592-596

CHAPTER 3: REDUCTION OF ERRORS IN ASL CEREBRAL PERFUSION AND ARTERIAL TRANSIT TIME MAPS USING IMAGE DE-NOISING

3.1 ABSTRACT

In this chapter, the performance of image de-noising techniques for reducing errors in arterial spin labelling (ASL) cerebral blood flow (CBF) and arterial transit time estimates is investigated. Simulations were used to show that the established ASL CBF quantification method exhibits the bias behaviour common to non-linear model estimates and as a result, the reduction of random errors using image de-noising can improve accuracy. To assess the effect on precision, multiple ASL data-sets acquired from the rat brain were processed using a variety of common de-noising methods (Wiener filter, anisotropic diffusion filter, Gaussian filter, wavelet decomposition and

independent component analyses). The various de-noising schemes were also applied to human ASL data to assess the possible extent of structure degradation, due to excessive spatial smoothing. The animal experiments and simulated data show that noise reduction methods can suppress both random and systematic errors, improving both the precision and accuracy of CBF measurements and the precision of transit time maps. A number of these methods (and particularly independent component analysis) were shown to achieve this aim without compromising image contrast.

3.2 INTRODUCTION

As previously discussed, arterial spin labelling (ASL) [Detre *et al*., 1992] is a non-invasive magnetic resonance imaging (MRI) technique to measure cerebral blood flow (CBF), an important physiological parameter of interest in many research and clinical applications [Calamante *et al*., 1999]. Arterial transit time (δa) measurements provide complementary information, can indicate possible pathology and may reflect the status of the arterial vasculature [Thomas *et al*., 2000, Thomas *et al*., 2006(a)]. The relatively low cerebral blood volume and rapid decay of the endogenous tracer means ASL measurements suffer from low signal-to-noise ratio (SNR). Achieving an adequate SNR at a suitable spatial resolution usually requires considerable data averaging, which can be problematic given the practical acquisition time restrictions for clinical MR scanning. Despite its current relatively limited use, ASL is likely to become more prevalent in clinical and research applications given the continued progression of modern scanner hardware and the associated SNR increases [Petersen *et al*., 2006].

Image de-noising techniques are intended to remove noise whilst retaining the "true" signal. Spatial filters are commonly used to reduce noise in images. These filters usually smooth the data to reduce the high frequency noise but in the process can also blur the data. The idea is that you smooth pixels to suppress the noise whilst maintaining the important structure within the image. An example of such a smoothing method is the Gaussian filter which is frequently applied in fMRI data analyses. Another example is the Wiener filter which smoothes adaptively depending on the distribution of pixel values within each kernel and an estimate of the noise present in the image. In recent years new methods have been devised that seek to spatially smooth

within homogenous regions while preserving edges in the data. An example used in this work is the anisotropic diffusion filter, an iterative approach that is intended to smooth within and not between important structures.

A different class of methods performs decomposition of the images into wavelet basis functions and shrinks the high frequency wavelet coefficients in order to de-noise the data. Advocates of this de-noising technique argue that it can better distinguish signal from noise in comparison to a simple Fourier transform. Wavelet decomposition concentrates the majority of a smooth signal in a few wavelet coefficients and in this way small coefficients that represent the noise can be thresholded, while the large ones that contain the signal's important features should be maintained.

Independent component analysis (ICA) is not a spatial filter but rather a method for extracting mixed signals into subcomponents assuming the statistical independence of the non-Gaussian source signals. An intuitive description is the "cocktail party problem". In this scenario several people are talking at the same time and there are a number of microphones at different positions in the room recording the many conversations. The aim of ICA is to take the many recordings and extract the individual voices. In this work we aim to use ICA to remove the background noise whilst preserving the source signal. Unlike the spatial de-noising methods described above, our implementation of ICA operates on 3D data (a time course of 2D images).

Post-acquisition de-noising methods have been exploited in many MRI modalities. For example, the anisotropic diffusion (AD) filter has been shown to have the potential to decrease the scan time of diffusion-weighted imaging (DWI) acquisitions [Parker *et al*., 2000] and to improve the reliability of CBF measurements using dynamic susceptibility contrast (DSC) MRI [Murase *et al*., 2001]. Wavelet filtering can be highly beneficial in conjunction with fMRI analyses [Wink *et al.,* 2004], DWI data [Wirestam *et al.,* 2006], and DSC-MRI data [Wirestam *et al.,* 2005]. The Wiener filter can aid 3D structural MRI processing [Martin-Fernandez *et al.,* 2006], and independent component analysis (ICA) has been shown to improve functional MRI [Thomas *et al.,* 2002], DWI [Arfanakis *et al.,* 2002] and DSC-MRI [Calamante *et al.,* 2004]. Despite these useful applications, the use of noise reduction algorithms in ASL has so far been mainly restricted to fMRI modelling [Restom *et al.,*2006; Behzadi *et al.,*2008]. Given the poor

SNR typically obtained in ASL, image de-noising could form an essential pre-processing step to make ASL more robust and more efficient, benefiting both its clinical and research applications.

In this chapter we investigate the performance of a number of common image de-noising techniques in reducing errors of ASL CBF and arterial transit time (δa) estimates. The study is divided into three main strands focussing on the effect of de-noising methods on accuracy, precision and structural degradation. Firstly, using simulations (where the true cerebral parameter estimates are known) we demonstrate that fitting to the established ASL CBF quantification method [Alsop and Detre.,1996] exhibits the bias behaviour common to non-linear model estimates and that the reduction of random errors using de-noising can enhance the *accuracy* of quantitative cerebral perfusion estimates. Secondly, ASL data acquired from the rat brain with several repeated measurements were used principally to assess the performance of the de-noising methods on the *precision* of CBF and δa measurements. Finally the various de-noising schemes are also applied to typical human ASL data to illustrate their potential use in clinical studies and, in particular, to assess the possible extent of *structure degradation*, due to excessive spatial smoothing, in the perfusion-weighted images.

3.3 MATERIALS AND METHODS

3.3.1 Computer Simulations

Two different sets of simulations were performed. In the first set we investigated the bias of the CBF estimates using the standard quantification model over a range of $SNR_{pwi.}$ The second set mirrors the *in-vivo* protocol; simulated images of the rat brain were generated and then de-noised using ICA to investigate the possible introduction of bias using this de-noising technique. The two different approaches are referred to as simulated data 1 and simulated data 2.

3.3.2 Simulated Data 1

In a preliminary analysis of the animal data, we have observed the mean and median CBF (as calculated by fitting to an established quantification model [Alsop and Detre, 1996]) within homogenous brain regions to increase in accordance with the noise level.

With Gaussian noise, the introduction of bias to maximum likelihood non-linear model estimates is widely recognised within the statistics literature [Box. 1971]. Therefore, the presence of Gaussian noise introduces both random and systematic errors to the CBF estimates. To the best of our knowledge, however, this is an issue that has not yet been raised in the context of the ASL CBF and δa estimation model [Alsop and Detre, 1996]. We therefore performed simulations to investigate and characterise this effect.

Continuous arterial spin labelling (CASL) data with a CBF of 250ml/min/100g and δa of 0.3s (corresponding to typical values in the rat brain) were simulated for 12 post-labelling delay (PLD) times (w = 0.15, 0.2, 0.3, 0.4, 0.5, 0.6, 0.7, 0.8, 0.9, 1, 1.5 and 2s; NB. These values correspond to those used in the experimental studies (see below)). The ASL data were generated using the established CBF quantification model [Alsop and Detre, 1996]. Zero mean Gaussian noise was added to the simulated time-course data to generate images with a mean SNR_{PWI} of 40, 30, 20, 10, 5, 4, 3, 2, 1.5, where SNR_{PWI} is the mean SNR of the perfusion-weighted images across all the PLD times. CBF and δa were then estimated by fitting the same model. The process was repeated 1000 times at each SNR.

3.3.2 Simulated data 2

An additional set of simulations was also performed. The purpose of this analysis was to investigate whether ICA introduces bias to the CBF estimates. Unlike the spatial filters, ICA uses the “time dimension” (or different PLD times) to de-noise the data. In the animal experiments, ICA is applied to the high SNR base images (control and tagged). The differences between the tagged and control acquisitions (that are proportional to CBF) are small relative to the changes in the base image signal intensity as a function of PLD due to MT effects (See *Figure 3.1*).

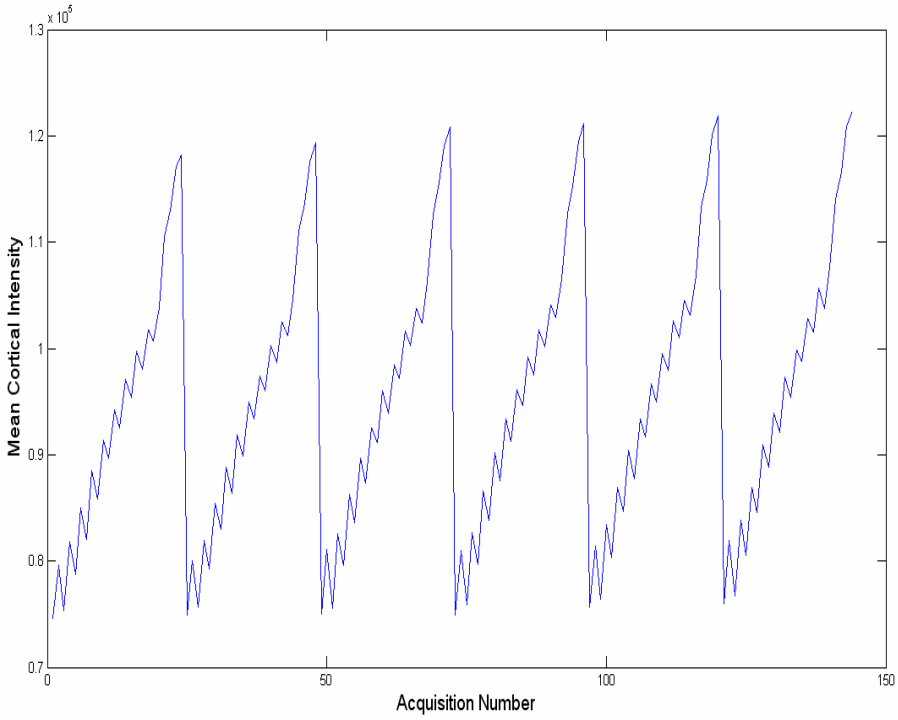

Figure 3.1
The mean cortical signal intensity of the base images across all the "5 average" in-vivo acquisitions for one of the three experiments. There are 6 repeats each consisting of 24 acquisitions (tag and control acquisitions at 12 PLDs). The "low frequency" changes in the measured signal are due the PLD dependant changes of the extent of MT effects in the tissue. The "high frequency" changes are due to blood flow. Conceptually, there is a risk that de-noising methods that act in the time domain may "smooth" the "high frequency" component of the time-course. This would underestimate the calculated CBF.

Therefore in the time-course of ASL image acquisitions (see *Figure 3.1*), the changes in signal intensity between the tagged and control acquisition can be considered to be high frequency and low amplitude relative to the changes in signal intensity due the PLD dependence of MT recovery. It was therefore important to ensure that ICA preserved these high frequency, low amplitude signal differences (that yield ΔM) and do not bias the resultant CBF estimates. This potential confounder is unique to ICA in this study as the other filters work on an image-by-image basis and do not incorporate the time dimension. To investigate this possible source of error we conducted further simulations, referred to as simulated data 2.

Simulated data were constructed to mirror the experimental *in vivo* data set with images generated at 12 post-labelling delay times. The time course of the pixels in the simulated images was calculated by using the established CBF quantification model [Alsop and Detre, 1996]. The majority of the brain pixels represented grey matter with a CBF of 250ml/min/100g and δa of 0.3s with a large region in the striatum of flow 150ml/min/100g and δa of 0.3s. There was no flow present in a thin strip that represents CSF within the ventricles. The signal intensity of the images decreased ventrally in accordance with the surface coil sensitivity (see *Figure 3.2*).

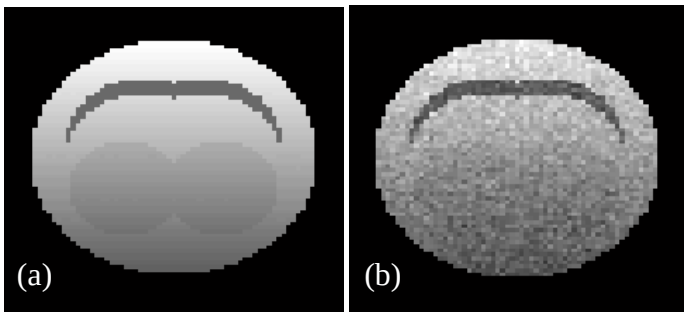

Figure 3.2
Simulated ASL control image before (a) and after (b) the addition of zero mean Gaussian noise.

Complex Gaussian noise (mean value = 0) was added to the raw images to generate 6 'noisy' data sets with a mean SNR of 31.9 to match the *in vivo* data (see *Figure 3.2*). The absolute signal intensities were taken to produce magnitude images. The images were then de-noised using ICA (see 3.3.6.5 *Independent component analyses*) and processed to generate CBF and δa maps before and after de-noising in an identical manner to the *in vivo* data (see 3.3.5 *CBF and δa quantification*).

A further set of simulations were performed to investigate the possible introduction of bias into CBF estimates when ICA is used to de-noise a sequence of images where perfusion is changing. An example of where this would be expected to occur is in fMRI experiments where blood flow changes may take place during a specified paradigm. In this application ASL images at a single PLD time are acquired due to the demand for good time resolution. Accordingly, simulated tagged and control images were generated as described in section 3.32 at a single delay time of 0.5s. "High CBF" maps were interleaved with "low CBF maps". The CBF oscillated from 250ml/min/100g to 200ml/min/100g between each tagged image. 200 images (tagged and control) were generated to give 100 CBF maps (50 images at each "high" or "low" CBF value). The

SNR in the control images was 30 in agreement with the *in-vivo* data. The controlled and tagged images were then de-noised using ICA (see 3.3.6.5 *Independent component analyses*) and processed to generate CBF maps. The mean CBF within a cortical ROI was taken across all 50 CBF maps for each CBF value (200 and 250ml/min/100g).

3.3.3 Animal Preparation

The *in-vivo* experimental protocol was designed to facilitate multiple repeated acquisitions to enable the assessment of the variability of the CBF and δa measurements to estimate their precision before and after de-noising. Errors due to subject motion and time-dependent variation in perfusion caused by changes in physiology were minimised by performing measurements on the anaesthetised rat brain, allowing a scan time of 1 hour and rigid motion prevention.

Three male Sprague Dawley rats (168-184g) were used in this study. Anaesthesia was induced and maintained as described in section 1.12.

3.3.4 Animal MRI: Continuous ASL

MRI animal studies were performed using a 2.35T horizontal magnet as described in section 1.12.

A CASL sequence was implemented with an alternating adiabatic spin tagging pulse (total duration 3 seconds) to minimise eddy current effects. The offset frequency of the labelling pulse oscillated in accordance with the slice select gradient to maintain a constant tagging plane. The labelling pulse was applied 2mm caudal to the cerebellum, perpendicular to the carotid and vertebral arteries, to ensure efficient spin tagging. Single slice coronal images, 0.3mm caudal to the bregma, were then acquired using spin echo EPI after a PLD time. For robust and accurate quantification, it is necessary to measure the perfusion-weighted signal over the time course of the delivery of the tagged bolus. This reduces the number of physiological assumptions and allows the simultaneous measurement of CBF and δa. Consequently 12 PLD times (w = 0.15, 0.2, 0.3, 0.4, 0.5, 0.6, 0.7, 0.8, 0.9, 1, 1.5 and 2s) were employed for each tag/control pair. Other acquisition parameters were: slice thickness = 2mm; image matrix size = 128×64; field of view = 40×20mm^2; TE = 36ms; inter-experiment delay = 2s. Data were

acquired with 5 averages at each *w*, giving a measurement time of 10 minutes. This process was repeated 6 times, resulting in a total scan time of 60 minutes.

For the remainder of this chapter, the 6 sets of tagged and control images acquired with 12 PLDs are referred to as the original 'noisy' images. The de-noising methods listed below were then applied to these 6 groups of ASL images. Application of the de-noising methods prior to CBF quantification suppresses the noise in the raw images and thus reduces the magnitude of propagated noise-based errors in CBF calculations. Preliminary analysis revealed the difference in the effect of de-noising the base images (i.e. control and labelled images) and subtraction images (control minus labelled images) to be negligible in this context because of the similar contrast present in the perfusion-weighted and base images. Therefore the base images were de-noised so that the fit of the control image signal intensity as a function of post-labelling delay time (a procedure required for CBF and δa quantification) could also benefit from reduced random errors. In addition, the raw data before subtraction were averaged across the entire experiment (all 6 repeats) for each *w* to produce a high SNR data set. These data were treated as the ''Gold Standard''. However, the extent of interpretation of these findings is limited as the "Gold Standard" only represents an approximation to the true CBF value (see SNR dependency of PWI signal, Figure 3.3 below). Therefore the simulations described above were used to investigate the possible implications of random errors on the accuracy of CBF quantification.

3.3.5 Human MRI: 3D GRASE ASL

Given the relatively small amount of white matter tissue in the rat brain, CBF maps in the rat tend to have few boundaries between areas with very marked perfusion difference (especially at the typical spatial resolution used for ASL). In contrast, the large amount of white matter in the human brain leads to many interfaces between areas with markedly different perfusion values (e.g. grey and white matter regions). Human ASL data are therefore ideal for assessing the effect of the various de-noising methods on structure degradation (*i.e.* spatial smoothing).

MRI human studies were performed on a single healthy subject using a 3T clinical whole-body MRI scanner (Magnetom Trio, Siemens Erlangen, Germany) with a

standard 12-channel receive-only head coil. A 3D GRASE pseudo-CASL sequence was used with background suppression [Fernandez-Seara *et al.*, 2005]. The following imaging parameters were used: Inflow time = 600ms; TE/TR = 57.7/3750ms; slice thickness = 4mm; image matrix size = 64×56×48; field of view = 250×219×192 mm^3. Sixty four pairs of label-control images were acquired on a healthy adult volunteer. In contrast to the experimental acquisitions, multi-PLD data were not acquired due to practical limitations on the scan time.

The 64 acquisitions were averaged over sets of 8 repeats to create 8 labelled and control images to increase the SNR_{PWI}. A data set was also generated by averaging all 64 tagged and control acquisitions, which was used as a reference or "Gold Standard" dataset for the purposes of this study. The images were masked to remove tissue outside the brain. The subtraction of the labelled and control acquisitions in the human data revealed many sharp boundaries between regions of contrasting CBF (*e.g.* between white and grey matter), which were not apparent in the base images for the pseudo-CASL sequence parameters used. This limits the benefit of edge-preserving filters (e.g. AD filter) when applied to the base images. Consequently in this case the 8 'noisy' and 'Gold Standard' control and labelled images were pair-wise subtracted and then de-noised. This approach must be employed with caution as in some instances the perfusion-weighted images may be so noisy as to impair the effectiveness of the de-noising strategies [Parker *et al.*, 2000]. In order to quantify the potential structural degradation effect of image de-noising, the contrast (i.e. the mean PWI signal difference) and the contrast-to-noise ratio ($CNR = SNR_{PWI}(ROI1) – SNR_{PWI}(ROI2)$) across a structural boundary was calculated before and after de-noising. Any significant changes in the 8 CNR estimates following de-noising were investigated using a paired t-test.

3.3.6 Noise Reduction Methods

In this work we chose to implement established threshold selection algorithms for each of the noise reduction techniques, rather than using an empirical optimisation by visual inspection (apart from the simple Gaussian filter, where a fixed level of smoothing was chosen). In this way, the spatial extent of the filter and/or degree of smoothing is determined based on an estimate of the level of noise within the image. Hence the level

of smoothing changes according to the image parameters and data quality. The adaptive nature of this approach should make the findings of this investigation relevant to future studies with alternate imaging parameters (number of averages, number of post-tagging delay times, *etc.*). This is the most straightforward and objective approach, requiring the least amount of user input, while providing a suitable optimisation of filter parameters given the underlying quality of the data. In future studies the extent of smoothing should be judged subjectively by the experimenter with knowledge of the application and the experimental protocol used. However in taking our approach we examine the possibility that image de-noising within ASL can be beneficial even with minimal subjective optimisation.

3.3.6.1 WIENER FILTER

An adaptive 2D Wiener method was applied, optimised based on statistics estimated from the local neighbourhood of each pixel. First estimates of the mean, μ, and variance, σ^2, were calculated within a 3×3 kernel centred on each pixel (pixel signal intensity = C). The data were then filtered on a pixel by pixel basis according to:

$$b = \mu + \frac{\sigma^2 - v^2}{\sigma^2}(C - \mu) \qquad [3.1]$$

where v^2 is the noise variance and b is the filtered pixel [Lim and Jae., 1990].

3.3.6.2 ANISOTROPIC DIFFUSION (AD) FILTER

For this work the method is similar to that used by Parker *et al.* [Parker *et al.*, 2000], but with the constant K (also known as the conduction coefficient or scale parameter) optimised as in reference [Murase *et al.*, 2001]:

$$K = 1.4826 \cdot MAD(\nabla I) \qquad [3.2]$$

where *MAD* denotes the median absolute deviation, and ∇I the image intensity gradient (a small blur with a Gaussian kernel with standard deviation equal to 0.8 in-plane voxel units was used to stabilise the local derivative gradient calculation [Parker *et al.*, 2000]). The number of iterations was set to 5 based on a preliminary analysis (data not shown). The AD filtering was performed using the MatLab and Octave Functions for Computer Vision and Image Processing (P.D. Kovesi, School of Computer Science &

Software Engineering, The University of Western Australia. http://www.csse.uwa.edu.au/~pk/research/matlabfns/).

3.3.6.3 GAUSSIAN FILTER

The standard deviation of the 2D Gaussian filter was fixed at 0.5 voxels and the kernel size to 3×3; these relatively small values were chosen to limit the degree of structural degradation.

3.3.6.4 WAVELET ANALYSES

For this work the Harr wavelet was employed, as it has been shown to be effective at preserving fine details within the MR image [Nowak *et al*., 1999]. Wavelet processing was implemented using the MatLab wavelet toolbox (The Mathworks inc). An optimal global threshold was selected based on

$$thr = \sqrt{2\log(y)} \times v \qquad [3.3]$$

where v = standard deviation of the noise and y is the number of pixels in the image [Donoho and Johnson., 1993]. The standard deviation of the noise is estimated using: $Std = 1.3826 \cdot MAD(\gamma)$, where γ is the finest scale wavelet coefficients. This threshold has been shown to effectively attenuate noise over a range of SNR conditions [Wink *et al.*, 1993]. In this work we implemented both the soft and hard thresholding schemes [Donoho. 1995].

3.3.6.5 INDEPENDENT COMPONENT ANALYSIS (ICA)

ICA is a set of methods designed to extract separate signals from measurements comprised of a mixture of statistically independent observations [Mckeown *et al*., 2003]. Our aim was to use these techniques to distinguish and extract random noise from the ASL data. More formally, the signal, *C(x,t)*, was assumed to be a linear combination of the source signal components:

$$C(x,t) = \sum_{j=1}^{M} a_j(x) \cdot S_j(t) + noise \qquad [3.4]$$

where $a_j(x)$ are the spatially independent source and $S_j(t)$ denotes the mixing coefficients that quantify the contribution of signal sources *j* at time *t*. The number of sources *M* was set to 7 empirically, based on a preliminary analysis. The results of the *in vivo* data (animal and human) included in this study were found to be relatively insensitive to the exact choice of this value (*e.g.* similar results were obtained with *M*=6-10); however, de-noising of data with a large range of transit times across the imaging volume may require a larger *M* value. The ICA Matlab code used is based on the software available from the web site http://isp.imm.dtu.dk/toolbox [T. Kolenda et al, DTU:Toolbox, ISP Group, Informatics and Mathematical Modelling, Tehcnical University of Denmark, 2002].

ICA was applied to the experimental animal data in two ways: first, to all 6 'noisy' data sets *simultaneously* in a single analysis (labelled ICA_{all}), and second to each of the 6 groups separately (labelled ICA_{each}). In both cases, all the data to be analysed (i.e. the 6 sets of 12 delay-times for ICA_{all}, and 1 set of 12 delay-times for ICA_{each}) were treated as a pseudo-temporal time series. ICA was applied to these series, thus de-noising each individual image. For ICA_{all}, the resultant images are then separated back into the 6 groups, each containing 12 tag and control images at different *w*. This approach would apply when a large series of images was continuously acquired to monitor the progression of CBF estimates with good temporal resolution, as is often required in fMRI experiments for example. For ICA_{each}, each of the 12 delay-times is de-noised as a separate time series. This approach would be applicable when a single multi-*w* data-set was acquired to efficiently capture a single CBF and δa map in a short scan time. For the human data, since data from a single inflow time was acquired, ICA_{each} would correspond to de-noising of a single image. Therefore, only ICA_{all} (de-noising of *all* the 64 perfusion-weighted images) was performed.

3.3.7 CBF and δa Quantification

CBF quantification of the *in vivo* animal data was performed according to the model proposed by Alsop and Detre [Alsop and Detre. 1996] that is described in section 1.5.1.2 of this thesis. The images were first pair-wise subtracted to form the ΔM perfusion-weighted images. The images were then masked to remove tissue outside the brain. From the recovery of the control magnetization as a function of *w*, the fully

relaxed magnetisation (M_0), the steady state magnetization during labelling (Mss), the brain tissue longitudinal relaxation constant during the post-labelling delay (T1n) and the brain tissue longitudinal relaxation constant during labelling (T1s) were calculated [Alsop and Detre. 1996]. CBF and *δa* maps were then generated for the "Gold Standard'' data set and for each of the 6 'noisy' sets of images before and after de-noising by fitting the model to the ΔM(*w*) data. The efficiency of the tagging pulse has been estimated to be 0.7 [Utting *et al.*, 2003]. The blood:brain partition coefficient for water (λ) was assumed to be 0.9 [Herscovitch and Raichle. 1985] . The tissue transit time (δ) was assumed to be 0.5s based on previous measurements (data not shown). The T1 of the blood (T1a) was assumed to be 1.5s based on previous measurements [Thomas *et al.*, 2006(b)]. The trust-region non-linear least squares fitting algorithm was used to fit the model to the data [Branch *et al*., 1999]. If the least-squares fit to the data returns a *δa* that is less than the minimum PLD (PLD_{min}), the precision of this estimate is restricted by the choice of experimental PLD times: for $\delta a < PLD_{min}$, the *δa* term drops out of the objective function (see Eq. 9 in (Alsop *et al.*, 1996)) and cannot be estimated with defined precision. All that remains is the evidence that *δa* lies in the interval 0 to PLD_{min}. It should be noted however that this limitation does not affect CBF, the principal parameter of interest in this work: the CBF estimates will be unaffected as the measured perfusion-weighted signal is proportional to flow and any variation in *δa* within this region ($0 \leq \delta a \leq PLD_{min}$) will not influence the fitted CBF value. However, for future studies for which the measurement of short *δa* is a priority, a very short PLD should be chosen. For more information see Appendix A. PLD_{min} was 0.15s in the current study as we hypothesised that a shorter PLD following the 3 second labelling pulse may cause the gradient amplifier to malfunction given the experience of previous users of the MRI system.

Given the relatively small number of 'noisy' data sets available and non-Gaussian distribution of the *δa* estimates (see Appendix A2) the *precision* of the parameter was quantified by the *range* of the measurements (i.e. the difference between the maximum and minimum measurements) for both *δa* and CBF. Maps of the range across 6 CBF and *δa* maps were computed to enable the assessment of any improvements in the precision of the data post-de-noising. Any significant reduction in the 3 median range estimates (1 for each animal) within a cortical ROI following de-noising (see *Figure 3.8*) were determined using a paired t-test.

To assess the *accuracy* of the *in vivo* animal data, the CBF values of the "Gold Standard" maps were treated as true values (θ). Inaccuracy was equated to the absolute difference between the estimates and the "Gold Standard" using:

$$E_{ij}^{\ cbf} = \left| \frac{1}{n_i} \sum_{k=1}^{n_i} \left(\chi_{ijk} - \theta_{ik} \right) \right| \qquad [3.6]$$

where χ_{ijk} is the CBF estimate in the kth pixel of the jth map in the ith animal experiment (i = 1,2,3; j = 1,2,….6; k = 1,2,…n_i; where n_i is the number of pixels within a cortical ROI of relatively homogenous CBF values). $E_{ij}^{\ cbf}$ is the resulting CBF error in the estimate given by the jth map and ith animal experiment. A test based on Mantel-Haenszel statistics and modified ridit scores was used to assess the observed differences between filters, adjusting for the difference between rats and the within-rat occasion effect. To clarify, this test was chosen to account for the variability between the 6 repeats for each rat and between the 3 rats. This analysis was performed using SAS (SAS Institute, Cary, USA). We emphasise that this test does not constitute a hypothesis test because no comparisons were planned in advance. On the contrary, comparisons were decided after visual inspection of the data.

3.4 RESULTS

3.4.1 Simulated data 1

Figure 3.3 shows the mean CBF estimate (± 1 SEM) as a function of the SNR_{PWI} of the simulated perfusion weighted signal (N.B. CBF_{true} = 250ml/100g/min). The bias of the CBF estimates increases with the degree of Gaussian noise and becomes particularly noticeable at $SNR_{PWI} < 5$. Figure 3.3 confirms the tendency of biased CBF estimates with the level of Gaussian noise and provides evidence that the reduction of random errors (e.g. with image de-noising) will result in more accurate CBF estimates (i.e. reduced *bias*). Since some of the fitted δa estimates were less than the minimum PLD, the corresponding graph for δa has not been calculated, given the limitations described above and in appendix A4.

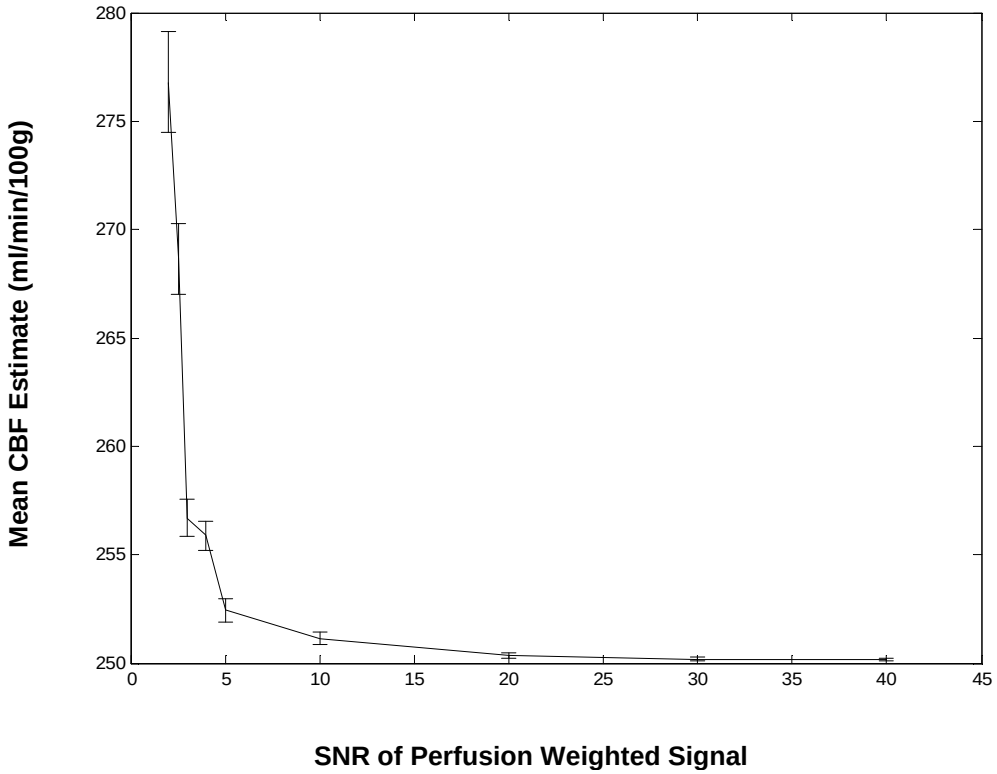

Figure 3.3
Mean simulated CBF estimates (± 1 SEM) at a variety of SNR_{PWI}. The simulated data correspond to CBF_{true} = 250ml/100g/min.

3.4.2 Simulated data 2

Figure 3.4 shows the simulated CBF and δa maps before and after de-noising using ICA. Figure 3.5 shows the mean CBF within a ROI in the CBF maps. ICA_{each} acts to reduce random errors and thus reducing the extent of the bias in the mean CBF estimate. Figure 3.5 suggests that ICA_{all} suppresses the noise to such an extent to remove nearly all the bias from the mean CBF estimates. For the simulated data with changing perfusion values, the mean cortical CBF before de-noising across all 50 CBF maps was 199.5 ± 1.2 for the "low CBF" acquisitions and 250.3 ±1.5 for the "high CBF" acquisitions. After de-noising with ICA the mean cortical CBF was 199.5 ± 0.8 for the "low CBF" acquisitions and 249.4 ± 0.884 for the "high CBF" acquisitions. These results provide evidence that using ICA in this way does not itself introduce marked bias into CBF quantification.

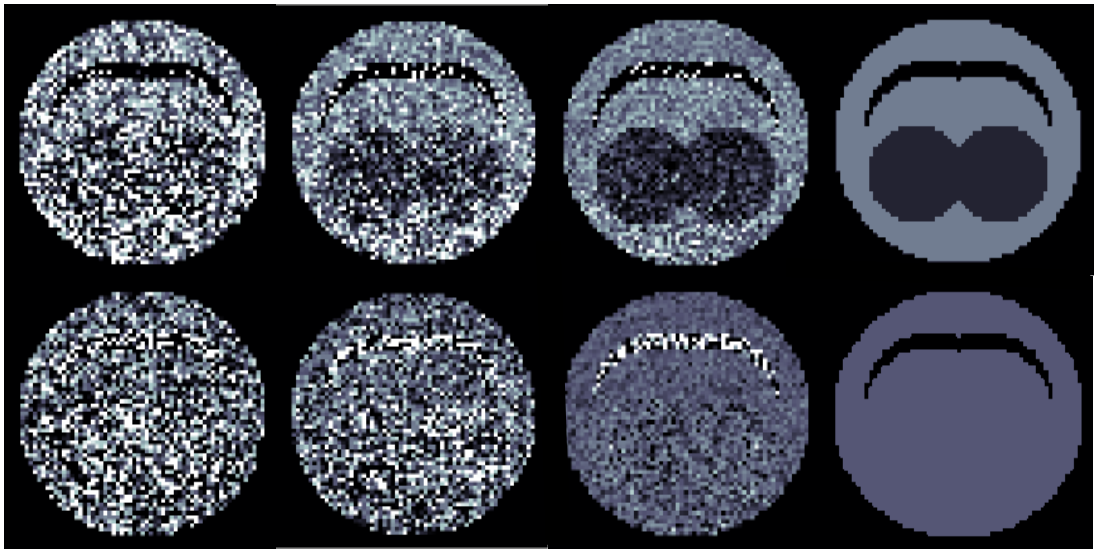

Figure 3.4

The simulated CBF (top row) and δa (bottom row) maps before (original) and after the application of ICA. The true CBF and δa maps are also shown.

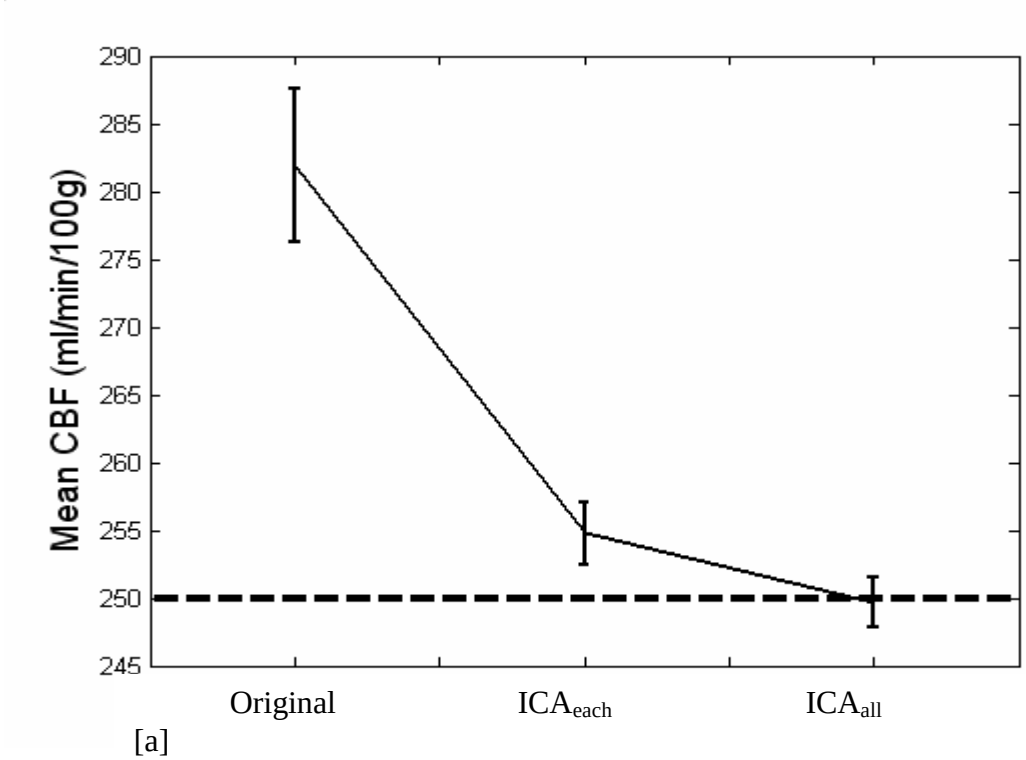

[a]

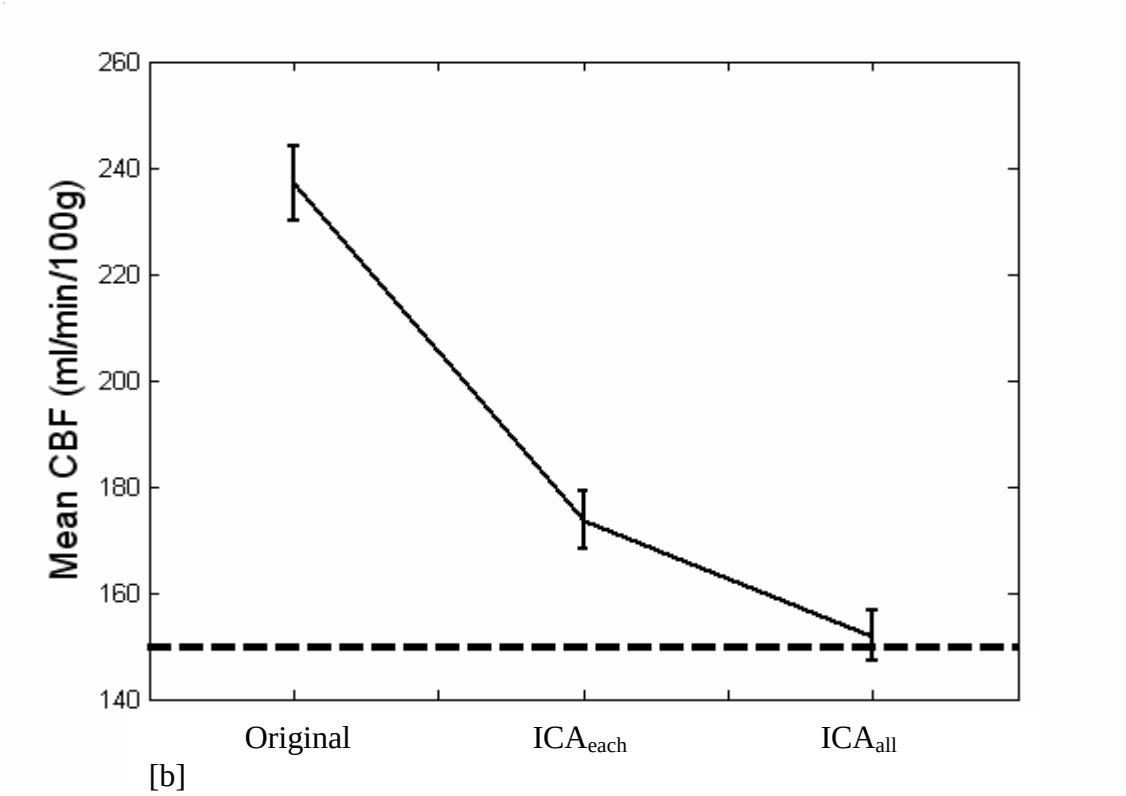

Figure 3.5

The mean CBF of the pixels within a ROI in the cortex [a] and in the striatum [b] of the CBF maps generated using the simulated data before (original) and after the application of ICA. The true CBF values are denoted by a dashed line.

3.4.3 In Vivo Animal Data

Figure 3.6 shows typical 'noisy' CBF and δa maps before and after image de-noising. Clearly the different approaches influence the appearance of the final result and introduce different degrees of spatial smoothing. Visual inspection of Figure 3.6 suggests ICA_{all}, having been applied to the entire data set, is the most proficient at noise removal in the CBF maps while retaining the features of the "Gold Standard'' image with no substantial loss of spatial resolution. When ICA_{each} is applied to individual data sets the improvement, though less than the ICA_{all} method is clearly evident. As expected, the effectiveness of ICA is determined by the number of images acquired within an experiment. Figure 3.6 suggests the technique has great potential if serial data are collected with the intention of monitoring CBF variations with good time

resolution, since in this case data from the whole time course is used to de-noise each individual measurement.

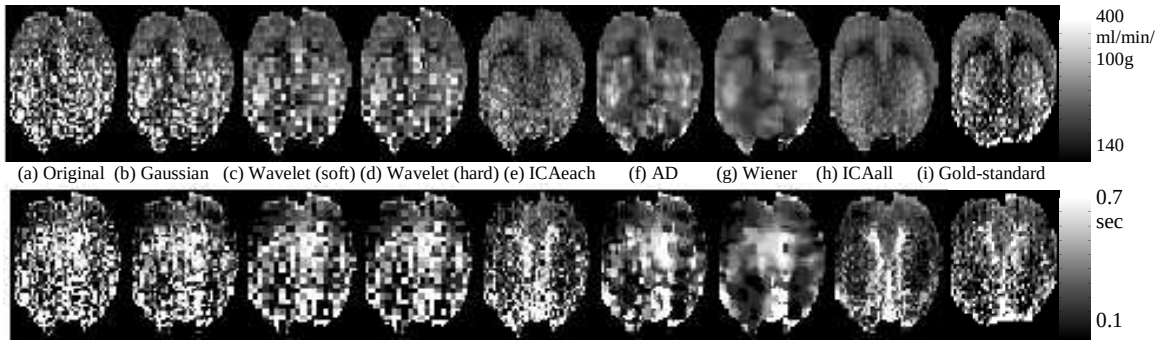

Figure 3.6
Typical CBF (top row) and δa (bottom row) maps generated from 'noisy', 5-average in vivo animal data, before (a) and after image de-noising (b-h). The label 'all' refers to a simultaneous ICA treatment of the entire set of images, while 'each' refers to a procedure in which separate ICA analyses are performed on each of the 6 individual sets. See Methods for additional information. The "Gold Standard" CBF and δa maps (i) are also shown.

Figure 3.7 shows the range (i.e. a measure of precision) of CBF and *δa* values obtained across the 6 maps generated from the 'noisy' data sets before and after application of the de-noising schemes for one of the animal experiments. As expected, in each case, the range increases inferiorly as the surface coil sensitivity and hence SNR decrease. Visual inspection of this figure suggests that the de-noising methods improve the precision of the measurement (Note that the maps are displayed on a common scale, and darker intensity therefore represents increased precision). Once again, ICA_{all} appears to be the most proficient at improving precision. In order to quantify the results of Figure 3.7, Figure 3.8 shows the median parameter range (calculated across the 6 repeats) of pixels within a cortical ROI for all three experiments. The ROI was drawn to encompass a region of relatively homogenous CBF values within the cortex on the "Gold Standard" CBF map. The median range of the CBF estimates in the three experiments decreases following application of each of the de-noising methods ($p<0.05$), denoting increased precision. The application of the AD filter, the Wiener filter, or ICA_{all} significantly reduces the range of the *δa* estimates ($p<0.05$).

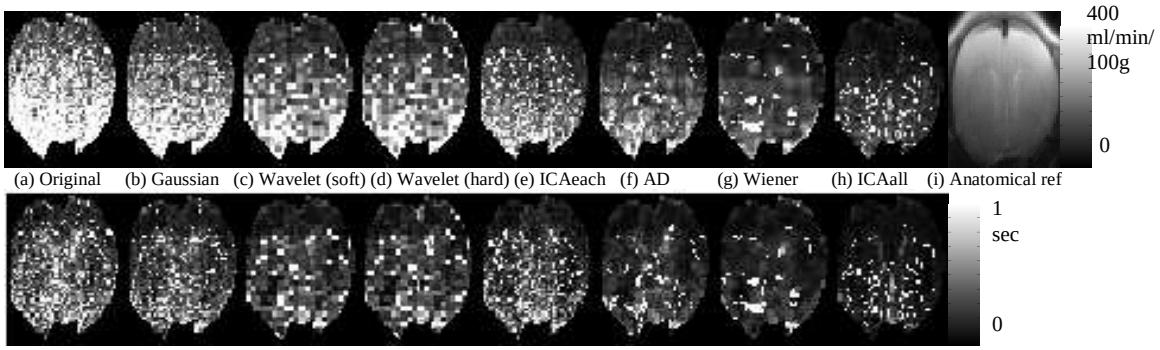

Figure 3.7

Maps of the range (i.e. a measure of precision) across the 6 CBF (top row) and δa (bottom row) maps of a typical animal data set before (a) and after (b-h) de-noising. An anatomical reference is also provided (i).

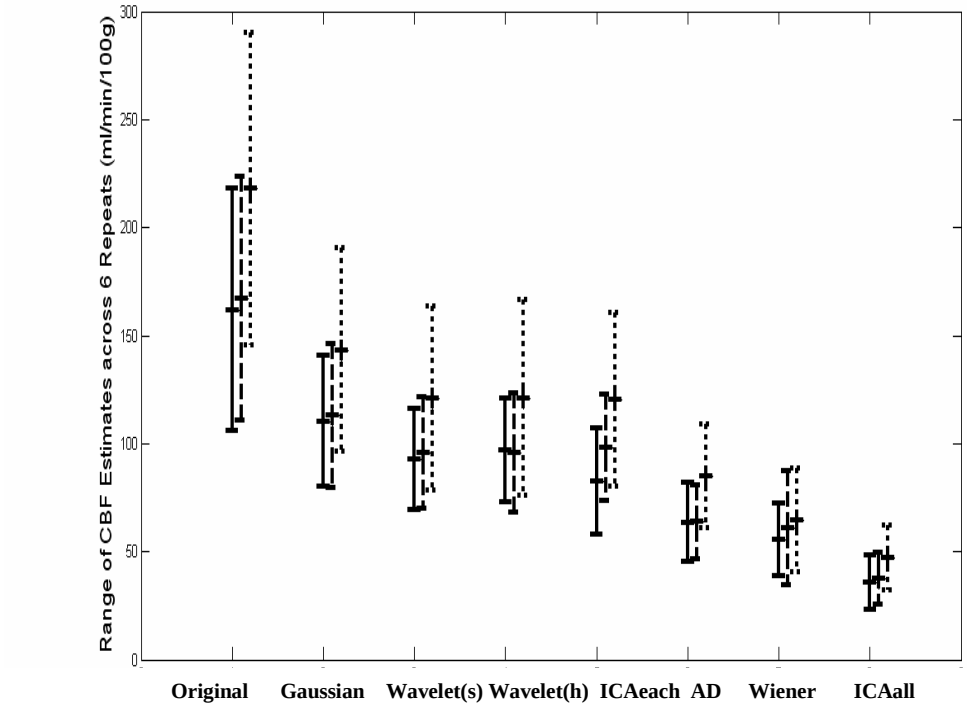
Range of CBF Estimates across 6 Repeats (ml/min/100g)
300
250
200
150
100
50
0
Original
Gaussian
Wavelet(s)
Wavelet(h)
ICAeach
AD
Wiener
ICAall

[a]

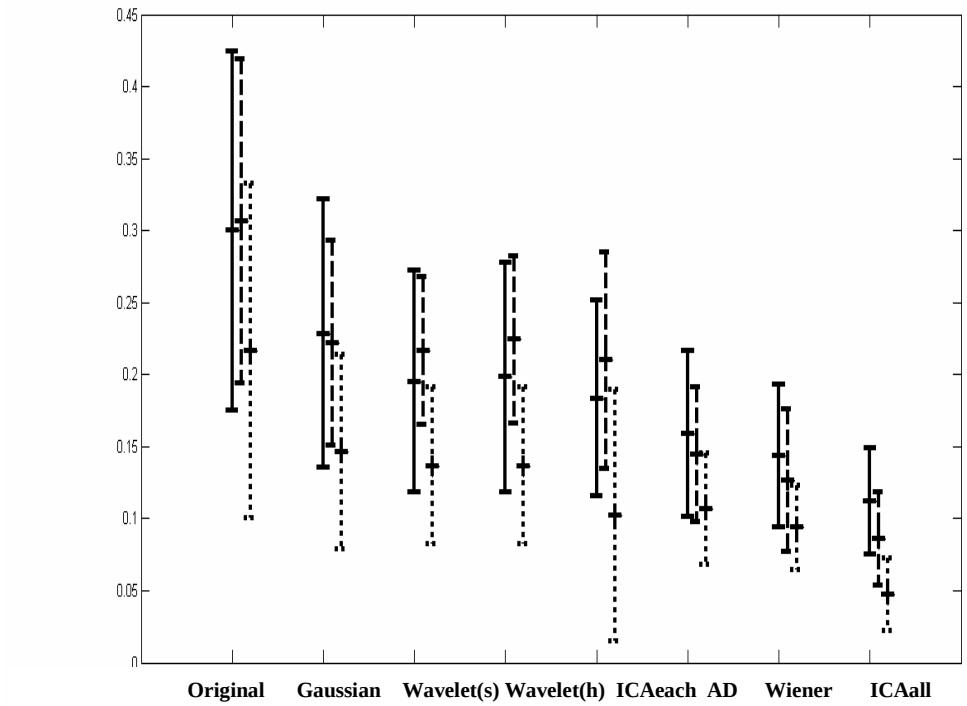
0.45
0.4
0.35
0.3
0.25
0.2
0.15
0.1
0.05
0
Original
Gaussian
Wavelet(s)
Wavelet(h)
ICAeach
AD
Wiener
ICAall

[b]

Figure 3.8

The median range across the 6 repeats (estimate of precision) of the CBF (a) and δa (b) observations of the pixels within a cortical ROI before (original') and after application of the de-noising methods. Error bars denote the inter-quartile range of the range estimates within the ROI. Data are reported for all three experiments (solid line, dashed line, dotted line).

Figure 3.9 shows the mean difference (as a measure of bias) between the CBF estimates and the "Gold Standard" within a cortical ROI (the same ROI used for the analysis in Figure 3.8) for the CBF maps pre- (referred to as 'original' data) and post-de-noising (each line represents a different experimental animal). The mean SNR of the perfusion-weighted signal within the cortical ROI was 2.0, 2.3 and 1.6 in the three animal experiments. $ICA_{all,}$ wavelets (with soft and hard thresholding) and the Wiener and AD filters provide significantly more accurate CBF estimates (as determined by the "Gold Standard" values) in comparison to the original noisy data ($p < 0.05$), consistent with the results from the simulations. Visual inspection of Figure 3.9 suggests that other de-noising schemes also act to reduce the bias of the estimates as most of the mean difference estimates tend to the "Gold Standard" in comparison to the original data. The mean SNR_{PWI} within the cortical ROI of the "Gold Standard" data was 5, 5.6, and 3.7 for each of the animal experiments, providing a considerably more accurate estimate of the CBF in comparison to the 'noisy' data (see *Figure 3.3*). However, due to the relatively low SNR_{PWI} the "Gold Standard" will still possess some bias (see Simulations results in *Figure 3.3*) and is not expected to be more accurate than processed images that possess similar SNR_{PWI} values, such as those processed using the Wiener filter, the AD filter, or using ICA_{all}. The corresponding δa results are not shown because at low SNR some fitted values are less than the minimum PLD and cannot be precisely defined, as previously described (see also Appendix A4).

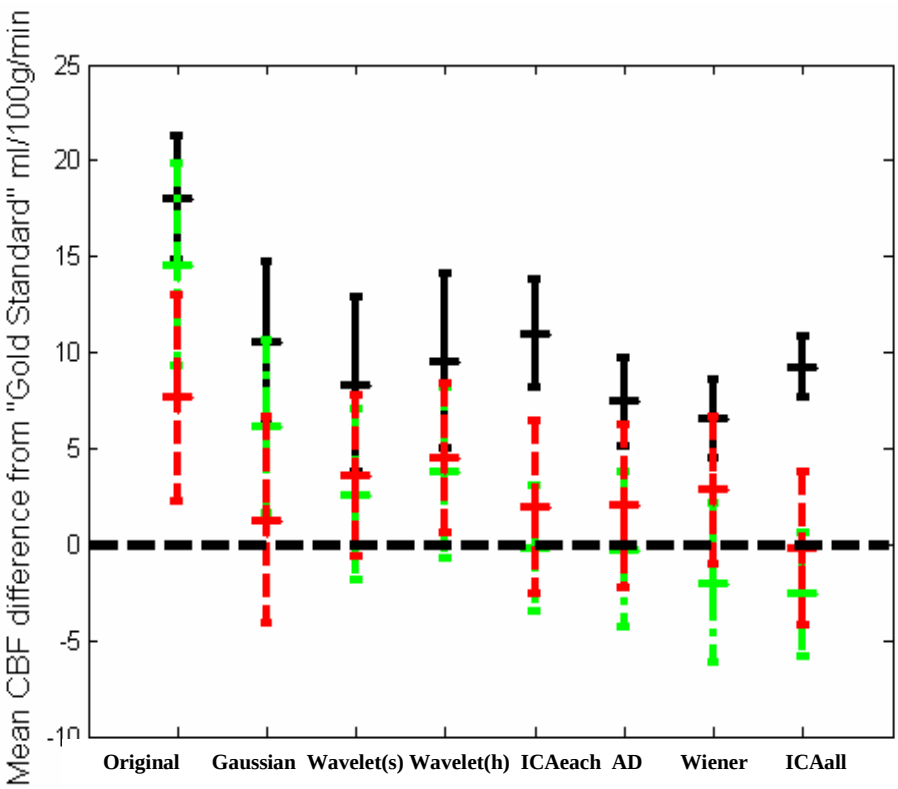

Figure 3.9
The mean difference between CBF estimates and the "Gold Standard" within a cortical ROI. The x-axis labels the pre- (original) and post-de-noising cases. The results from each rat are represented by a different line and error bars denote the standard error across the 6 repeats.

3.4.4 Human Data

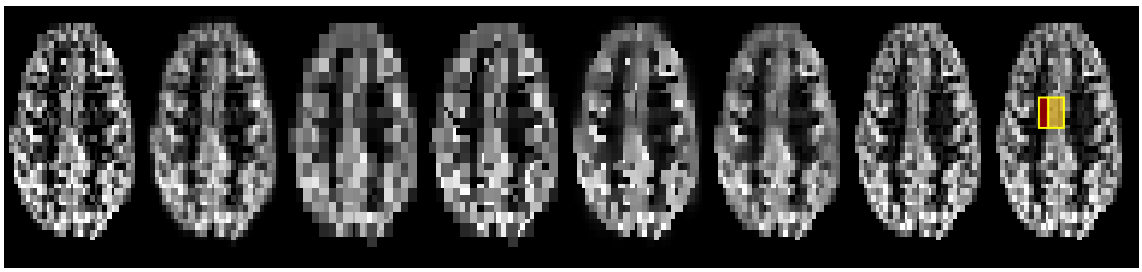

(a) Original (b) Gaussian (c) Wavelet (soft) (d) Wavelet (hard) (e) AD (f) Wiener (g) ICAall (h) Gold-standard

Figure 3.10
Human perfusion weighted images generated from 8 average data before (a) and after (b-g) image de-noising. The 'Gold Standard' (64 average) perfusion-weighted image is also shown (h). The two ROIs used in the CNR measurements in Figure 3.11 are shown in (h). The ROI containing pixels of greater signal intensity was used to calculate the SNR_{PWI} of the images.

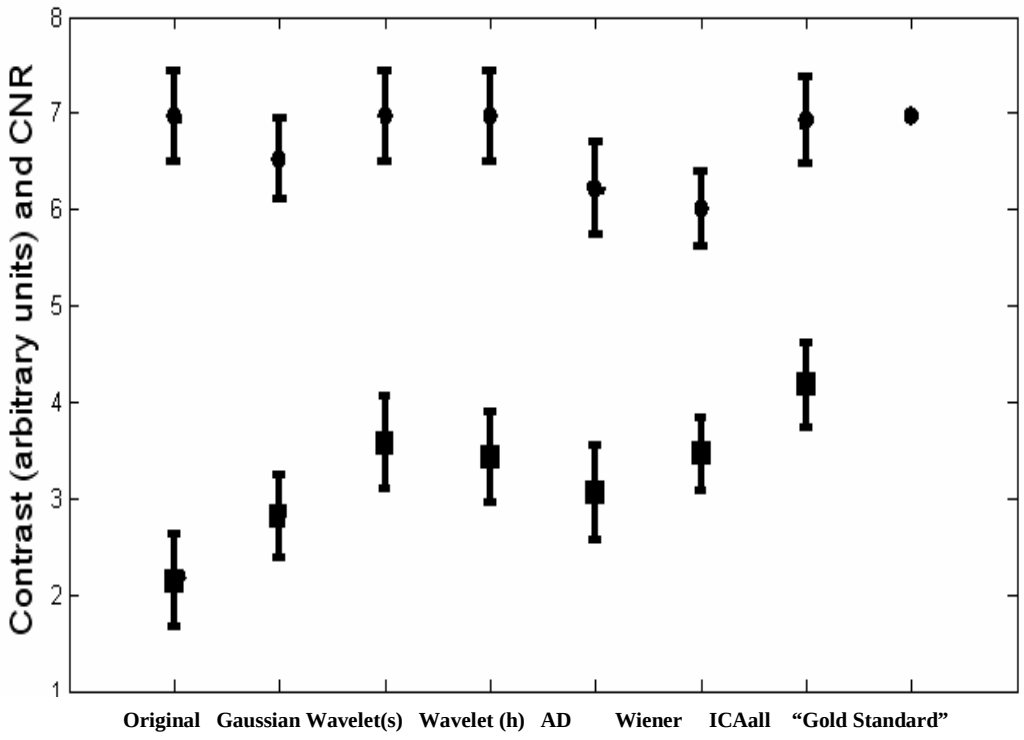

Figure 3.11
The contrast to noise ratio (solid line) across a structural boundary in the human perfusion weighted images, as indicated by the two regions shown in Figure 3.10. The contrast (mean signal region 1 – mean signal region 2) is also reported (dashed line). The "Gold Standard" contrast is also shown. Error bars represent the standard error across the 8 contrast and 8 CNR measurements respectively.

The effect of applying the various de-noising methods to the calculated ASL data is shown in Figures 3.10. The SNR_{PWI} of the human brain data with 8 averages within the ROI shown in Figure 3.10 was 2.6. In order to quantify the structural degradation introduced by the de-noising methods, Figure 3.11 shows the contrast and CNR across the structural boundary highlighted in Figure 3.10(h). The CNR is significantly greater following application of each of the de-noising techniques ($p<0.05$). The animal studies have shown the Wiener filter to perform marked noise suppression yielding more precise CBF estimates (see *Figures 3.7 and 3.8*). It is apparent from Figure 3.10(f) and visual inspection of the contrast reported in Figure 3.11 that the 2D Wiener filter can also introduce marked spatial smoothing (NB. This was apparent from the animal results in Figure 3.6, but became more apparent with the increased contrast observed in human data), though there is no significant change in the contrast following each of the

de-noising methods. Thus one must employ caution with this approach or risk losing distinction between regions of different CBF. In these measurements, 64 control and labelled images were acquired at a single inversion time, limiting the effectiveness of ICA in this case. However, Figures 3.10 and 3.11 provides further evidence that ICA introduces no loss of structure and the images bear a closer likeness to the ‘‘Gold Standard’’ in comparison to the original. Indeed of all the de-noising methods, ICA_{all} returns the greatest contrast and CNR in this data set.

3.5 DISCUSSION

The intrinsically low SNR of the perfusion-weighted measurements is inherently responsible for holding back the progression of ASL to an MRI modality that is more widely used for the research and diagnosis of brain pathology. The results of this study demonstrate the potential benefits of pre-processing de-noising algorithms in ASL applications. It is important to determine whether a de-noising method increases precision at the expense of introducing bias. This study shows that noise reduction methods can improve both the precision of the CBF and δa maps and the accuracy of CBF measurements, as the bias (common to non-linear model estimates [Box. 1987)] with non-zero residual variance) is reduced. Therefore in principle, ASL data with low SNR can be used with an appropriate filter to obtain cerebral haemodynamic estimates of acceptable accuracy and precision. These benefits may translate into improved spatial or temporal resolution or shorter scan times (of particular benefit to the clinical setting). Furthermore suitable pre-processing may make mapping of arterial transit time more feasible in practical acquisition times.

The results show ICA, given a sufficient amount of data (*i.e.* ICA_{all}), is particularly effective at improving the precision of the CBF and δa measurements. On the other hand, if limited data are available the application of the AD or Wiener filters, which can be applied on an image-by-image basis, enhance precision as well as improving the accuracy of the calculated CBF estimates due to the associated reduction of bias (see *Figures 3.8 and 3.9*). The simulation results from Figure 3.3 suggest that the effect of the de-noising methods to reduce bias is particularly important for low SNR_{PWI} values;

for high SNR_{PWI} data (SNR_{PWI} > 10-15) the improvement associated with de-noising will be more limited.

It is not only important to assess the effect on precision and bias for a given de-noising method, but also to ensure it does not introduce unacceptable levels of spatial blurring. Since different de-noising schemes introduce different degrees of spatial smoothing, this important characteristic must be carefully considered during filter selection. The optimal filter is highly dependent on the SNR of the images. For example, although the Wiener filter performs marked noise reduction in the animal data (low SNR, relatively little contrast), the degree of spatial smoothing incurred may be too severe for certain applications (*e.g.* higher SNR, marked contrast human data). In contrast, ICA, for example, maintains boundaries between certain structures in the perfusion-weighted images of the human brain.

We emphasise that in this chapter we chose to implement, as far as possible, automatic criteria for the optimisation of filter parameters associated with each noise reduction technique, to investigate the possibility that image de-noising within ASL can be beneficial even with minimal subjective optimisation. This chapter was not intended to present an exhaustive assessment of all the de-noising methods available and indeed there is certainly scope for improved optimisation of filter parameters. This chapter included some of the most commonly used methods, from very simple methods (e.g. Gaussian filter), edge-preserving filters (e.g. the AD filter), to filters that work in the spatial-temporal domain (e.g. ICA). Many other filters are available, and even alternative implementations of the filters used (*e.g.* see references [Wirestam *et al.,2006;*,Wirestam *et al.,* 2005; Donoho. 1994; Goldstein *et al.,*2006] for variations on wavelets). Nevertheless, the results shown in this study demonstrate that de-noising methods can play an important role in ASL, and in particular ICA was efficient at improving precision and reducing bias, without compromising image contrast. A comprehensive assessment of de-noising methods is however beyond the scope of this thesis chapter.

In this work, ICA reduces random noise with minimal structural degradation, though its application is dependent on the collection of a series of images. ICA exploits the

information of all the available data. Multi-delay time ASL (e.g. based on a Look-Locker acquisition [Guenther *et al.*, 2001]) is being increasingly used as an efficient and robust approach to CBF quantification [Petersen *et al.*, 2008]. Consequently, the potential role of ICA in ASL is likely to become increasingly important and the results from this study suggest it should be an essential pre-processing tool in future ASL studies. ICA has been used in a variety of MRI applications [*e.g.* Thomas *et al.*,2002; Arfanakis *et al.*, 2002; Calamante *et al.*,2004;Carroll *et al.*,2002,Kiviniemi *et al.*,2006], often to identify and remove systematic sources of error in a way that is user-dependent. For this reason, its reproducibility has been criticised. Since we are using ICA purely to remove random noise from the images, minimal subjective input is required and the de-noising protocol should be easily reproducible. ICA takes approximately 30s to de-noise a single time-series of images using a dual core 2.16GHz PC with 3GB of RAM. Currently, each time-series of images must be loaded in individually by the user.

The observed bias in non-linear parameter estimates may be exacerbated by the discontinuities that describe the different stages of the delivery of labelled blood to the tissue within the CBF quantification model. These discontinuities or switching points are present in many of the established ASL CBF quantification models (e.g. [Alsop and Detre. 1996;, Buxton *et al.*,1998]). An example within the model used in this work is the min([δa–PLD],0) term (see Eq.[9] in [Alsop and Detre. 1996]). When this complicated function is fitted to particularly noisy data (SNR_{PWI} <5), the δa estimates will often converge on the PLD at which the perfusion-weighted signal was sampled. Because the CBF is correlated with the δa (when the δa estimate is greater than PLD_{min}) this will influence the distribution of CBF estimates which may contribute to the bias that we have observed with the addition of Gaussian noise. For more information see Appendix A.

Although in the current study ICA_{all} appears to perform particularly well, in general the best filter will depend on the particular ASL dataset (*e.g.* high or low SNR and number of post-labelling delays acquired) and application (*e.g.* measuring low CBF or high CBF), which will determine the degree of spatial filtering that can be tolerated. It should be noted that the findings of this study should be directly extendable to studies

with other ASL sequences or acquired under different experimental conditions, as illustrated by the similar qualitative findings from the experimental animal and human studies (carried out with different ASL sequences on different scanners). The use of de-noising pre-processing may also make the use of more complex ASL models (e.g. two-compartment models [Parkes *et al.*, 2002]) more feasible, since they are currently limited in part by the low SNR in the data.

3.6 SUMMARY

In summary, the results reported in this chapter support the use of image de-noising (and especially ICA) as a pre-processing step to improve the precision of ASL CBF and arterial transit time estimates whilst maintaining the structure of the cerebral parameter maps in both human and animal data. Importantly, the improved precision does not come at the expense of accuracy: as shown in this study, the reduction of random errors also leads to reduced CBF bias. I now continue to chapter 4 where I describe the first successful *in-vivo* application of H-CASL; an efficient method of imaging small-boli of labelled blood in the brain that may have value as a pre-scan for optimisation of ASL imaging parameters.

3.7 REFERENCES

Alsop DC, Detre JA. (1996). Reduced transit-time sensitivity in non-invasive magnetic resonance imaging of human cerebral blood flow. Journal of Cerebral Blood Flow and Metabolism16, 1236-1249

Arfanakis K, Cordes D, Haughton VM, Carew JD, Meyerand ME. (2002). Independent component analysis applied to diffusion tensor MRI. Magnetic Resonance in Medicine 47, 354-363

Behzadi Y, Restom K, Liau J, Liu TT. (2008). A component based noise correction method (CompCor) for BOLD and perfusion based fMRI. Neuroimage 37, 90-101

Box MJ. (1971). Bias in nonlinear estimation. The Journal of the Royal Statistical Society Series B 33, 171-201.

Branch MA, Coleman TF, Li Y. Subspace, Interior, and Conjugate Gradient Method for Large-Scale Bound-Constrained Minimization Problems (1999). SIAM Journal on Scientific Computing 21, 1-23

Buxton RB, Frank LR, Wong EC, Siewert B, Warach S, Edelman RR.(1998). A general kinetic model for quantitative perfusion imaging with arterial spin labelling. Magnetic Resonance in Medicine 40, 383-396

Calamante F, Morup M, Hansen LK. (2004). Defining a local arterial input function for perfusion MRI using independent component analysis. Magnetic Resonance in Medicine 52, 789-797

Calamante F, Thomas DL, Pell GS, Wiersma J, Turner R. Measuring cerebral blood flow using magnetic resonance imaging techniques. Journal for Cerebral Blood Flow and Metabolism 19, 701-35

Carroll TJ, Haughtonb VM, Rowleyb HA. Cordesc D.(2002). Confounding effect of large vessels on MR perfusion images analyzed with independent component analysis. American Journal of Neuroradiology 23, 1007-1012

Detre JA, Leigh JS, Williams DS, Koretsky AP. Perfusion imaging. (1992).Magnetic Resonance in Medicine 23, 37-45

Donoho DL, Johnson IM. (1994). Ideal spatial adaptation by wavelet shrinkage. Biometrika 81, 425-455

Donoho DL. De-noising by soft-thresholding. (1995). IEEE Transactions on Information Theory 41, 613-627

Fernandez-Seara MA, Wang Z, Wang J, Rao HY, Guenther M, Feinberg DA, Detre JA. (2005). Continuous arterial spin labelling perfusion measurements using single shot 3D GRASE at 3T. Magnetic Resonance in Medicine 54, 1241-1247

Goldstein TA, Zhang H, Misselwitz B, Gropler RG, Zheng J. (2006). Improvement of quantification of myocardial first-pass perfusion mapping: a temporal and spatial wavelet de-noising method. Magnetic Resonance in Medicine 56, 439-445

Guenther M, Bock, Schad LR. (2001). Arterial spin labeling in combination with a look-locker sampling strategy: inflow turbo-sampling EPI-FAIR (ITS-FAIR). Magnetic Resonance in Medicine 46**,** 974-84

Herscovitch P, Raichle ME. (1985). What is the correct value for the blood–brain partition coefficient for water? Journal for Cerebral Blood Flow and Metabolism 5, 65–69

Kiviniemi V, Ruohonen J, Tervonen O. (2006). Separation of physiological very low frequency fluctuation from aliasing by switched sampling interval fMRI scans. Magnetic Resonance Imaging 23, 41-46

Lim, Jae S. (1990). Two-Dimensional Signal and Image Processing. Englewood Cliffs, NJ: Prentice Hall 1990.

Martin-Fernandez M, Alberola-Lopez C, Ruiz-Alzola J, Weston CF. (2007). Sequential anisotropic Wiener filtering applied to 3D MRI data. Magnetic Resonance in Medicine 25, 278-292.

Mckeown MJ, Hansen LK, Sejnowski TJ. (2003). Independent component analysis of functional MRI: What is signal and what is noise? Current Opinions in Neurobiology 13, 620-629.

Murase K, Yamazaki Y, Shinohara M, Kawakami K, Kikuchi K, Miki H, Mochizuki T, Ikezoe J. (2001). An anisotropic diffusion method for de-noising dynamic susceptibility contrast-enhanced magnetic resonance images. Physics in Medicine and Biology 46, 2713-2723

Nowak RD. (1999). Wavelet based rician noise removal for magnetic resonance imaging. IEEE Transactions in Image Processing 8, 1408-1419

Parker GJM, Schnabel JA, Symms MR, Werring DJ, Barker GJ.(2000). Nonlinear smoothing for reduction of systematic and random errors in diffusion tensor imaging. Journal of Magnetic Resonance Imaging 11, 702-710

Parkes LM, Tofts PS. (2002). Improved accuracy of human cerebral blood perfusion measurements using arterial spin labelling: accounting for capillary water. Magnetic Resonance in Medicine 48, 27-41

Petersen ET, Zimine I, Ho YC, Golay X. (2006). Non-invasive measurement of perfusion: a critical review of arterial spin labelling techniques. The British Journal of Radiology79, 688-701

Petersen ET, Golay X Is Arterial Spin Labelling Ready for the Prime time? (2008). Prilimary Results from the QUASAR Reproducibility Study. Proceedings of the 16th Annual Meeting of ISMRM, Toronto, Cananda, 2008 (Abstract 191)

Restom K, Behzadi Y, Liu TT. (2006). Physiological noise reduction for arterial spin labelling functional MRI. Neuroimage 31, 1104-1115

Thomas CG, Harshman RA, Menon RS. (2002). Noise reduction in BOLD-based fMRI using component analysis. Neuroimage 17, 1521-1537

Thomas DL, Lythgoe MF, Pell GS, Calamante F, Ordidge RJ. (2002). The measurement of diffusion and perfusion in biological systems using magnetic resonance imaging. Physics in Medicine and Biology 45:R97-138.

Thomas DL, Lythgoe MF, van der Weerd L, Ordidge RJ, Gadian DG. (2006). Regional variation of cerebral blood flow and arterial transit time in the normal and hypoperfused rat brain measured using continuous arterial spin labelling MRI. Journal of Cerebral Blood Flow and Metabolism 26, 274-82

Thomas DL, Lythgoe MF, Gadian DG, Ordidge RJ. (2006). In vivo measurement of the longitudinal relaxation time of arterial blood (T1a) in the mouse using a pulsed arterial spin labelling approach. . Magnetic Resonance in Medicine 55, 943-947

Utting JF, Thomas DL, Gadian DG, Ordidge RJ. (2003). Velocity-driven adiabatic fast passage for arterial spin labelling: results from a computer model. Magnetic Resonance in Medicine 49, 398-401

Wink AM, Roerdink JBTM (2004). De-noising Functional MR Images: A comparison of wavelet de-noising and gaussian smoothing. IEEE Transactions on Medical Imaging 23, 374-387

Wirestam R, Bibic A, Lätt J, Brockstedt S, Ståhlberg F. (2006). De-noising of complex MRI data by wavelet-domain filtering: application to high-b-value diffusion-weighted imaging. Magnetic Resonance in Medicine 56, 1114-1120

Wirestam R, Ståhlberg F. (2005). Wavelet-based noise reduction for improved deconvolution of time-series data in dynamic susceptibility-contrast MRI. MAGMA 18, 113-118.

Zhou J, Wilson DA, Ulatowski JA, Traystman RJ, van Zijl PC. (2002). Two-compartment exchange model for perfusion quantification using arterial spin tagging. Journal of Cerebral Blood Flow and Metabolism 21, 440-55.

CHAPTER 4: *IN-VIVO* HADAMARD ENCODED CONTINUOUS ARTERIAL SPIN LABELLING (H-CASL)

4.1 ABSTRACT

Continuous arterial spin labelling (CASL) measurements over a range of post-labelling delay (PLD) times can be interpreted to estimate cerebral blood flow (CBF) and arterial transit time (δa) with good spatial and temporal resolution. In this work we present an *in-vivo* demonstration of Hadamard-encoded continuous arterial spin labelling (H-CASL); an efficient method of imaging small volumes of labelled blood water in the brain at multiple PLD times. We present evidence that H-CASL is viable for *in-vivo* application and can improve the precision of δa estimation in 2/3 of the imaging time required for standard multi-PLD CASL. Based on these findings we propose that H-

CASL may have application as an efficient pre-scan for optimisation of ASL imaging parameters.

4.2 INTRODUCTION

As previously discussed, arterial spin labelling (ASL) MRI can acquire cerebral blood flow (CBF) weighted images non-invasively with good spatial and temporal resolution [Detre *et al.,* 1992]. However, ASL generally requires long scan times and careful interpretation due to the low signal to noise ratio (SNR) of the measurements and the complexity of accurate CBF quantification. A confounding factor for quantifying CBF with ASL is the transit time of blood water: the time it takes to travel from where it is labelled to where it enters the cerebral tissue. For example, CBF may be underestimated if the bolus of labelled arterial blood has not (or has only partially) arrived in the tissue of interest upon image acquisition. In order to eliminate this problem, ASL measurements with a range of post labelling delays (PLDs) between the end of the labelling pulse and image readout can be performed at the cost of a significantly increased total scan time [Buxton *et al.,* 1998]. This also enables estimation of the arterial transit time (δa), a possible biomarker of cerebral vascular disease [Thomas *et al.,* 2006(a)]. Previous work has demonstrated that the choice of PLD values can be optimised according to the transit times within the tissue of interest to improve the precision of CBF and transit time estimation [Xie *et al*., 2008]. Furthermore, it has been suggested that a multi-PLD pre-scan with low-resolution image acquisition for rapid δa estimation is valuable to guide parameter selection in the main ASL imaging protocol [Dai *et al.,* 2009]. Recently, Hadamard-encoding techniques have been applied to the continuous ASL (CASL) labelling pulse to increase the efficiency of this approach by encoding the signal from small volumes of arterial blood water over a range of PLDs [Gunther, 2007]. However to our knowledge this work has not yet been extended beyond phantom validation. In this study we provide evidence that this new approach is viable *in-vivo* and can be used for accurate CBF and δa estimation. We compare the precision of *in-vivo* CBF and δa estimates derived from multi-PLD CASL to those generated using the Hadamard-encoding method and demonstrate that this novel technique can improve the precision of transit time estimation in 2/3 of the imaging time required for the standard approach. Based on these findings, we propose that

Hadamard encoded CASL (H-CASL) may have application as an efficient pre-scan for optimisation of ASL imaging parameters.

4.2.1 H-CASL Theory

In continuous ASL a spin-labelling pulse is applied to the feeding arteries in the neck (typically for a few seconds) to invert arterial blood water prior to acquisition of a "tagged" image of the brain. A "control" image of the brain is then acquired with no flow-weighting. A simple subtraction of the "tagged" and "control" scans yields a CBF-weighted difference image (ΔM). In H-CASL, the labelling pulse oscillates between the tagging and control phase before each acquisition. The idea is to divide the large tagged bolus into several small sub-boli, each with different effective PLDs (PLD_{eff}). In the case of H-CASL, PLD is replaced with PLD_{eff} as the labelling/control pulse is applied during this period.

Figure 4.1 shows the H-CASL encoding scheme used in this study. Eight images are acquired; each preceded by a different temporal sequence of tagging and control periods. The CBF weighted images derived from the delivery of each of the sub-boli to the tissue are reconstructed using the Hadamard encoding scheme. Each of the 7 sub-boli have 4 control and 4 labelled states. Theoretically, the 8 images can be combined so that for a single sub-bolus each of the 4 control and 4 label phases add constructively - resulting in the net CBF- weighted difference between them. The 8 images can be combined in different ways to reconstruct a CBF- weighted image from each of the 7 sub-boli with different PLD_{eff}. For each reconstruction, both the tagged and control states of the other 6 sub-boli cancel, resulting in zero net signal from these sub-boli. For example, to reconstruct the CBF-weighted image due to the delivery of bolus no. 7 to the observation slice, the 8 acquisitions were combined as follows:

$$\Delta M\ (\text{Bolus No.7}) = \text{image 1} - \text{image 2} - \text{image 3} + \text{image 4} - \text{image 5} + \text{image 6} + \text{image 7} - \text{image 8} \quad [4.1]$$

Therefore 7 CBF-weighted images can be reconstructed (each equal to the difference between 4 labelled and 4 control acquisitions) due to the arrival of each sub-bolus to the tissue of interest. In this way 8 acquisitions can generate a perfusion weighted image from 7 individual sub-boli at different $PLD_{eff,}$ each averaged over 4 images. To generate a single average ΔM image at 7 different PLDs using standard CASL would require 14 acquisitions (7 tagged images and 7 controls). As each of these H-CASL individual boli

have different PLD_{eff} times, this approach can be used to sample the bolus inflow curve with considerable data averaging in a relatively short imaging time which may benefit CBF and δa estimation. It is important to note that non-plug flow (i.e. laminar and/or pulsetile) will "blur the boundaries" of the individual small boli of labelled blood. Such dispersion effects will be more problematic in H-CASL in comparison to standard CASL

Preliminary results (see below) showed that H-CASL yielded precise δa estimates in comparison to CASL. However the precision of CBF estimation using H-CASL was considerably reduced when compared to the standard approach. Therefore in this work as well as investigating the performance of H-CASL independently we also report the results of a hybrid approach where H-CASL images are combined with CASL data at fixed PLD (hybrid H-CASL) and compared to CASL data acquired at a range of PLDs for similar temporal coverage of the dynamic delivery of labelled blood to the tissue in the same total imaging time.

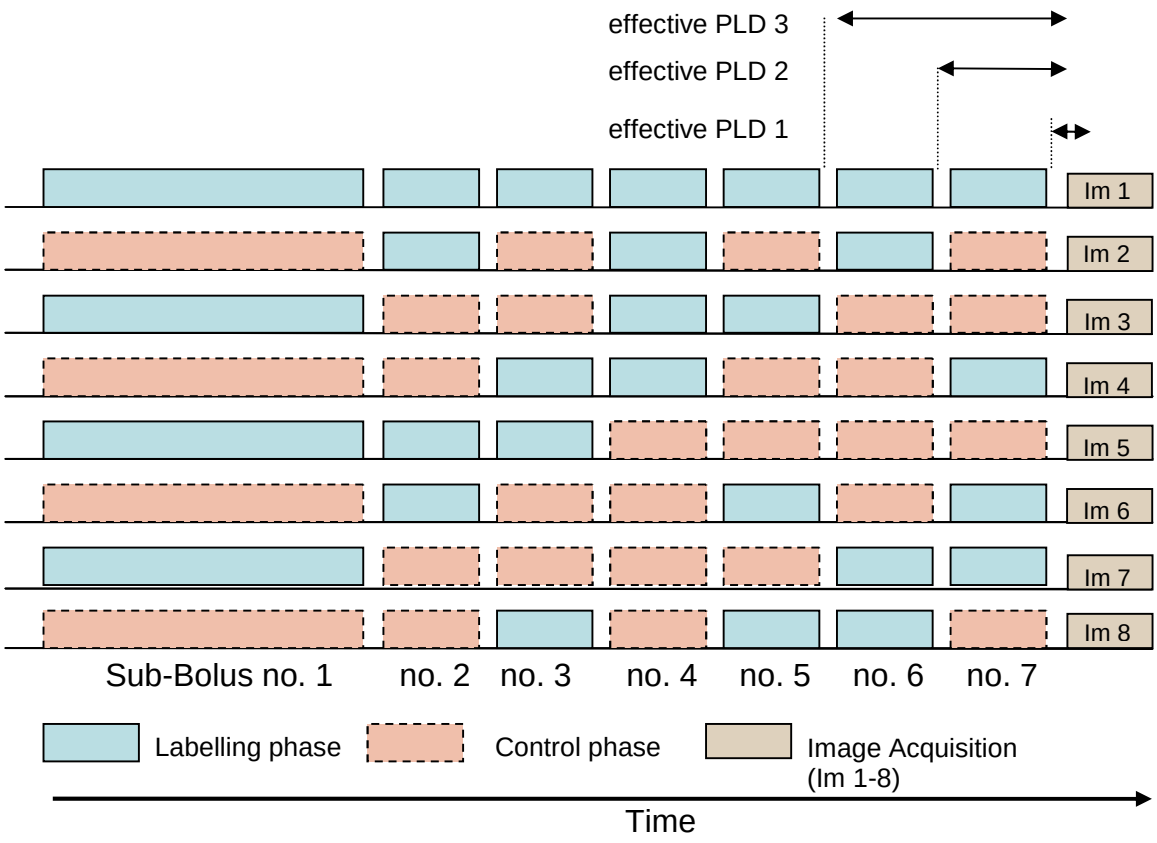

Figure 4.1
The H-CASL encoding scheme [Gunther, 2007]. In this work eight images are acquired that can be combined to extract seven CBF-weighted images due to the delivery of each

sub bolus to the tissue. In this schematic, a delay is present between each sub-bolus for clarity; however there is negligible delay in practice.

4.3 METHOD

4.3.1 Animal Preparation and MRI Hardware

Animals were prepared and imaged using MRI as described in section 1.12 (*MRI Apparatus*).

4.3.2 CASL and H-CASL In-vivo Implementation

The H-CASL scheme was implemented as illustrated in Figure 4.1. The first sub-bolus had a duration of 1.8s. Sub-boli 2-7 had a duration of 0.2s to produce 7 $PLDs_{eff}$ (0.02 0.22 0.42 0.62 0.82 1.02). Spoiler gradients of approximate duration 0.02s are applied between the end of the H-CASL labelling/control phase and the first 90^0 excitation pulse in all the acquisitions. A straightforward single slice CASL approach was used; the plane of the tagging pulse (i.e. neck for label or above the head for control) was changed by altering the offset frequency of the labelling/control pulse during a constant gradient.

The 8 H-CASL acquisitions (see *Figure 4.1*) were followed by 12 standard CASL acquisitions (label and control) at 6 PLDs (0.05, 0.1, 0.2, 0.3, 0.5, 0.8s) with a 3 second labelling duration. These 6 PLD values were chosen as preliminary analyses demonstrated that they were better optimised (Xie *et al*., 2008) for precise δa estimation at the typical transit times in the rat cortex (0.2-0.3s) in comparison to 7 PLD times fixed at the equivalent PLD_{eff} in the H-CASL sequence (data not shown). This exploits the flexibility of PLD selection in CASL which is restricted in H-CASL as the PLD_{eff} values are determined by the sub-bolus duration. Four standard CASL images (2 labelled and 2 control) at fixed PLD of 0.5 seconds were additionally acquired. In this work we investigate the performance of H-CASL (8 acquisitions) independently in addition to a hybrid approach which combines the H-CASL data with the fixed PLD CASL images (Hybrid H-CASL)- 12 acquisitions). For the hybrid approach, the resultant two subtracted (ΔM) images from the four CASL images were then averaged and combined with the reconstructed H-CASL perfusion weighted images for equivalent imaging times between the two methods (12 acquisitions in total). Images

were acquired of a plane approximately 0.2, 0.3 and 0.4 mm caudal to the bregma respectively for the three experiments using a spin echo EPI readout. The position of the slice was changed for the three experiments in this way to examine the performance of the new approach over a range of transit times (which should increase as the slice moves further from the tagging plane). Tagging pulses were applied to a plane 2mm caudal to the cerebellum. The protocol was repeated 15 times. Other acquisition parameters were: slice thickness = 2mm; image matrix size = 128×64; field of view = 40×20mm^2; TE = 36ms; inter-experiment delay = 4s. For each method, all the data were averaged across the 15 repeats to produce a high SNR, "Gold Standard" data set for which CBF and δa maps were generated from the masked images. In addition the data were split into 5 groups of 3 repeats and averaged across the 3 repeats to generate 5 relatively "low SNR" groups. A Gaussian filter with kernel size of [3 x 3] pixels and a standard deviation of 1 was applied to the "Gold Standard" and "low SNR" perfusion weighted images to increase the SNR of the data before CBF and δa estimation. The data were averaged in this way so that the SNR_{pwi} of the *in-vivo* data was more representative of typical applications (see 4.4 *Results*). CBF and δa estimates were calculated for pixels within a cortical ROI for each of the 5 groups to examine their precision (see 4.3.5 *CBF and δa estimation*). In summary, we perform separate analysis on three groups: i) the standard multi-PLD CASL images; ii) The H-CASL acquisitions; iii) The Hybrid H-CASL acquisitions.

4.3.3 Simulations

In the simulations zero mean Gaussian noise was added to modelled data before the precision of the resultant CBF and δa measurements were estimated (see 4.3.4 *CBF and δa Estimation* and 4.3.5 *Data Comparisons*). Simulated CASL data at 6 PLDs (0, 0.3, 0.6, 0.9, 1.2, 1.5) were constructed according to [Wang *et al.*, 2002 (Eq. 2)] with δa values of 0.1, 0.2, 0.3, 0.4, 0.5, 0.6, 0.7, 0.8, 0.9, 1s. Zero mean Gaussian noise were then added to the data for a mean signal to noise ratio of the perfusion weighed signal (SNR_{pws}) of 5.75, the average SNR_{pwi} of the 3 "low SNR" *in-vivo* data. The SNR_{pws} is calculated by taking the mean SNR of the simulated CASL perfusion weighted signal at all PLDs. In the simulations the choice of PLDs were selected for a range of transit times (0.1 -1s) whereas the PLDs in the *in-vivo* data were better optimised for precise δa estimation given the expected transit times in the rat cortex (200-300ms). Throughout

the simulations, the constant coefficients (T1a, α, Mo, R1n, R1s, δ, λ) are fixed at the values used in the *in-vivo* analyses (see 4.3.4 *CBF and δa Estimation*). The "true" CBF was chosen to be 300 ml/100g/min, in overall agreement with the mean cortical *in-vivo* estimates under our anaesthetic conditions (see 3.6 *Results*). For each of the three different *δa* values the process was repeated 100 times and in each case CBF and *δa* were estimated (see 4.3.4 *CBF and δa Estimation*). Simulated reconstructed H-CASL data with the same sub-bolus durations as the *in-vivo* experiment (1.8, 0.2, 0.2, 0.2, 0.2, 0.2, 0.2s) were generated at the appropriate PLD_{eff} according to [Wang *et al.,* 2002. Eq 1].The same degree of zero mean Gaussian noise was then added to the data. These data were then averaged over 4 simulated time courses as intended in the Hadamard reconstruction to generate the simulated H-CASL data, which were then analysed independently. To generate the Hybrid H-CASL data, simulated CASL data with $\tau = 3s$ and fixed PLD of 0.5s were generated according to [Wang *et al.,* 2002 (Eq 2)], to which to same level of Gaussian noise was added. These data were averaged over 2 acquisitions and combined with the simulated H-CASL data to mirror the *in-vivo* protocol.

4.3.4 CBF and δa Estimation

CBF and *δa* estimates were calculated for pixels within a cortical ROI for each of the 5 groups to examine their precision (see *Data Comparisons*). All images were aligned using SPM prior to CBF and *δa* estimation to reduce possible movement artefacts. CBF and *δa* were estimated on a pixel by pixel basis using the model described previously [Wang *et al,* 2002]. For standard CASL, equation 4.2 was used for model fitting to the data. The efficiency of the tagging pulse (α) was assumed to be 0.71 based on previous measurements (Utting *et al.,* 2003); the blood:brain partition coefficient for water (λ) was fixed at 0.9 ml of water per gram tissue/ml water per ml blood [Herscovitch and Raichle, 1985]; instantaneous exchange is assumed where the tissue transit time (*δ*) equals the arterial transit time (*δa*); the longitudinal relaxation constant of the blood (T1a) is assumed to be constant at 1.5s based on previous measurements [Thomas *et al.,* 2006(b)]; the rate of longitudinal relaxation of the brain tissue during and after application of the off-resonance labelling pulse ($R1_s$ and $R1_{ns)}$ was calculated from the PLD dependant longitudinal decay of the mean cortical perfusion weighted signal from

the high SNR, "Gold-Standard", H-CASL and CASL data respectively and were fixed for the calculation of the CBF and δa maps; the tagging duration (τ) was 3s; f is the CBF; the equilibrium magnetisation of the tissue (M_0) was estimated for each voxel by fitting the CASL control images acquired at a range of PLDs to a simple T1 recovery model [Alsop and Detre., 1996]. M_0 as calculated from the CASL images was used to quantify both the CASL and H-CASL perfusion weighted signal. Equation 4.3 was used for model fitting to the H-CASL data where $R1_{app}$ has been replaced by $R1_s$, since the off-resonance labelling/control pulse is applied during PLD_{eff}. In this case τ is 0.2 and 1.8s. The labelled blood water that has exchanged into the tissue is assumed to decay with $R1_s$ during the 0.02 second delay between the end of the H-CASL labelling scheme and imaging acquisition where the spoiler gradients are applied.

For CASL:

Under the condition that $\tau > \delta$:

$$\Delta M = \frac{-2M_0 f\alpha}{\lambda}\left\{\begin{array}{l}\frac{\exp(-\delta R_{1a})}{R_{1ns}}[\exp(\min(\delta - w,0)R_{1ns}) - \exp(-wR_{1ns})] + \\ \frac{\exp(-\delta R_{1a})}{R_{1s}}\exp(-wR_{1ns})[1-\exp(\min(\delta - \tau,0)R_{1s})] + \\ \frac{1}{R_{1a}}[\exp((\min(\delta_a - w,0) - \delta_a)R_{1a}) - \exp((\min(\delta - w,0) - \delta)R_{1a})]\end{array}\right\} \quad [4.2]$$

For H-CASL:

$$\Delta M = \frac{-2M_0 f\alpha}{\lambda}\left\{\begin{array}{l}\frac{\exp(-\delta R_{1a})}{R_{1s}}[\exp(\min(\delta - w,0)R_{1s}) - \exp((\delta - \tau - w)R_{1s})] + \\ \frac{1}{R_{1a}}[\exp((\min(\delta_a - w,0) - \delta_a)R_{1a}) - \exp((\min(\delta - w,0) - \delta)R_{1a})]\end{array}\right\} \quad \tau + w > \delta \quad [4.3]$$

$$\Delta M = \frac{-2M_0 f\alpha}{\lambda R_{1a}}[\exp((\min(\delta_a - w,0) - \delta_\alpha)R_{1a}) - \exp(-(\tau + w)R_{1a})] \times \frac{\min(\delta_a - w - \tau,0)}{(\delta_a - w - \tau)} \quad \tau + w < \delta$$

For the Hybrid H-CASL the data acquired using H-CASL and CASL (at fixed PLD) techniques was simultaneously fitted to equations 4.2 and 4.3 respectively. By

comparing the standard CASL approach to Hybrid H-CASL in this way we are comparing CBF and δa estimates derived from the equivalent volume of labelled blood acquired in the same imaging time.

4.3.5 Data Comparisons

To quantify the precision of the CBF and δa estimates we examine the absolute error of the CBF and δa estimates calculated from the "low SNR" *in-vivo* data and the simulated data with added Gaussian noise from the "true" value. In the case of the simulations the "true" cerebral parameter values are known. For the *in-vivo* data the "true values" are approximated to be the "Gold Standard" CBF and δa maps (assuming the measurement errors to be purely random and not systematic). For CBF, the precision was calculated by quantifying the absolute difference between the estimates and the "true" value (θ) using:

$$E_i^{CBF} = \left| \chi_i - \theta_i \right| \qquad [4.4]$$

where $\chi_{i,}$ is the CBF estimate in the ith pixel or repeat (i = 1,2,…n_i; where for the *in-vivo* data, n_i is the number of pixels within a cortical ROI and for the simulations, n_i is the 100 repeats;). $E_{i,}^{CBF}$ is the resulting CBF error. The precision of the δa estimates is quantified using an identical analysis. The Wilcoxon rank sum test was adopted to determine the probability that a given rank ordering amongst the CBF or δa error observations may have arisen by chance in the absence of an underlying true difference between estimates generated with the CASL and H-CASL methods and between the CASL and Hybrid H-CASL methods. The comparison was performed separately for each of the three *in-vivo* experiments and for each of the simulated δa values.

4.4 RESULTS

Figure 4.2 shows the mean *in-vivo* cortical perfusion weighted signal of the standard CASL and H-CASL data as a function of PLD and $PLD_{eff,}$ together with the respective model fits to the data. The CBF and δa estimates within the cortical ROI are also reported**.** The coefficient of determination of the model fit to the reconstructed H-CASL ΔM signal (0.97, 0.98, and 0.93 for the three subjects respectively) provides some evidence that the scheme has successfully imaged the progression of the Hadamard encoded sub-boli in the brain and that the adapted model is suitable for accurate CBF

and δa quantification. The mean cortical CBF estimates (95% confidence intervals of the fit) over the three experiments were 308 (303,313), 360 (354,371) and 242 (220,264) ml/min/100g using CASL and 297 (272, 321), 378 (351,405) and 256 (222,290) ml/min/100g using H-CASL respectively for the three experiments. The mean cortical δa estimates (s) over the three experiments were 0.20 (0.18, 0.22), 0.23 (0.20, 0.26) and 0.27 (0.14 0.40) using CASL and 0.19 (0.17, 0.22), 0.26 (0.24, 0.28) and 0.31(0.27, 0.34) using H-CASL respectively for the three experiments. For each experiment the mean cortical CBF and δa estimates fall within the 95% confidence intervals of one another between the CASL and H-CASL techniques.

Figure 4.3 shows the perfusion weighted images derived from the delivery of the Hadamard encoded individual sub-boli (top row) and CASL extended bolus (bottom row) to the observation slice at increasing $PLD_{(eff)}$ for the three experiments. The lack of noticeable coherent signal from outside the brain suggests that, in both acquisition schemes, the signal is proportional to CBF as intended. The patches of high intensity in the H-CASL images at the earliest PLD_{eff} are likely to represent the first inflow of labelled blood into the tissue. Though the measured perfusion weighted signal from the H-CASL sub-boli (τ = 0.2s) is a fraction of that from the CASL extended bolus (τ = 3s) the increased data averaging within the H-CASL acquisition and reconstruction reduces the background noise. The mean SNR_{pwi} of the CASL acquisitions for the three experiments was 5.9, 6.7, and 4.7, following application of the Gaussian filter. The mean SNR_{pwi} of the H-CASL acquisitions for the three experiments was 2, 2.4, and 1.6, following application of the Gaussian filter.

Figure 4.4 reports the median $E^{\delta a}$ and E^{CBF} observations across the 5 "low-SNR" groups for the three *in-vivo* data sets using CASL, H-CASL and Hybrid H-CASL. H-CASL returns a significant reduction in the $E^{\delta a}$ values in comparison to standard CASL for each of the 3 *in-vivo* experiments, denoting increased precision ($p < 0.05$). CASL returns a significant reduction in E^{CBF} in comparison to H-CASL and in comparison to Hybrid H-CASL ($p < 0.05$) suggesting that CASL returns the most precise CBF estimates. Figure 4.5 shows the median simulated $E^{\delta a}$ and E^{CBF} values estimated using the standard CASL, H-CASL and Hybrid H-CASL methods models at different simulated δas. Simulated data show that the H-CASL $E^{\delta a}$ population is less than the CASL $E^{\delta a}$ population at 6 of the 10 different simulated arterial transit times ($p<0.05$). However

CASL yields a reduction in E^{CBF} at all 10 simulated transit times in comparison to CASL and at 7 of the 10 simulated transit times in comparison to Hybrid H-CASL.

The *in-vivo* and simulated $E^{\delta a}$ estimates provide evidence that H-CASL can improve the precision of δa estimation in 2/3 of the imaging time required for standard CASL. Conversely simulated and *in-vivo* data show the H-CASL returns significantly greater E^{CBF} values (even with the addition of the standard CASL images (Hybrid H-CASL)) in all three *in-vivo* experiments and at most simulated transit times, demonstrating greater precision in CBF estimation using standard CASL.

Figure 4.6 shows the "Gold-Standard" CBF and δa maps acquired with the H-CASL and standard CASL schemes. Visual assessment demonstrates the similarity of contrast in each of the cerebral parameter maps between the two imaging techniques, despite the marked difference in acquisition methods and the interpretation of the ΔM signal from a steady state technique (CASL τ = 3s) and H-CASL (τ = 0.2s).

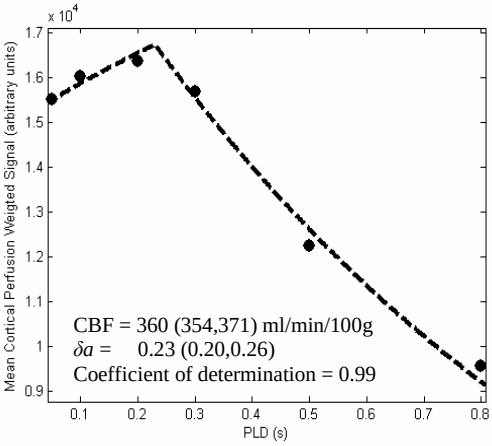
x 10^4
Mean Cortical Perfusion Weighted Signal (arbitrary units)
PLD (s)
CBF = 360 (354,371) ml/min/100g
δa = 0.23 (0.20,0.26)
Coefficient of determination = 0.99

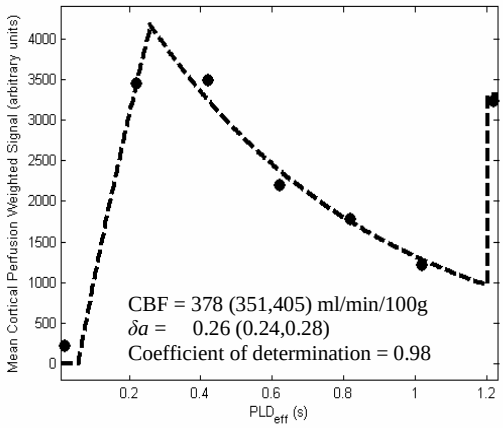
Mean Cortical Perfusion Weighted Signal (arbitrary units)
PLD_eff (s)
CBF = 378 (351,405) ml/min/100g
δa = 0.26 (0.24,0.28)
Coefficient of determination = 0.98

[a]

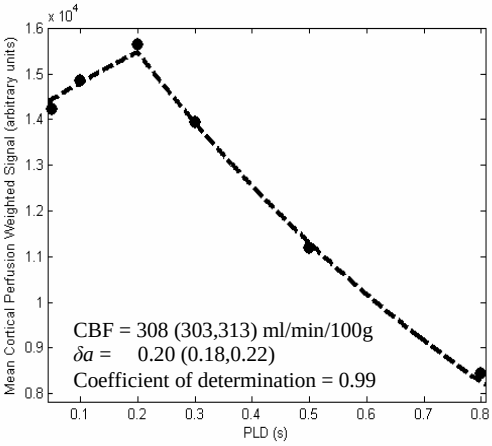
x 10^4
Mean Cortical Perfusion Weighted Signal (arbitrary units)
PLD (s)
CBF = 308 (303,313) ml/min/100g
δa = 0.20 (0.18,0.22)
Coefficient of determination = 0.99

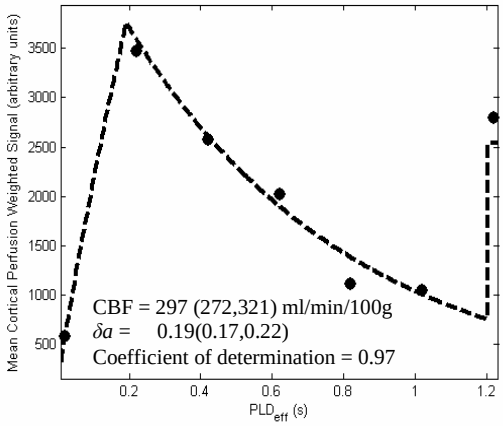
Mean Cortical Perfusion Weighted Signal (arbitrary units)
PLD_eff (s)
CBF = 297 (272,321) ml/min/100g
δa = 0.19(0.17,0.22)
Coefficient of determination = 0.97

[b]

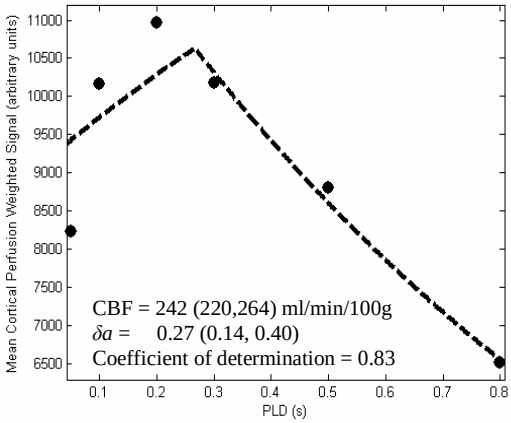
Mean Cortical Perfusion Weighted Signal (arbitrary units)
PLD (s)
CBF = 242 (220,264) ml/min/100g
δa = 0.27 (0.14, 0.40)
Coefficient of determination = 0.83

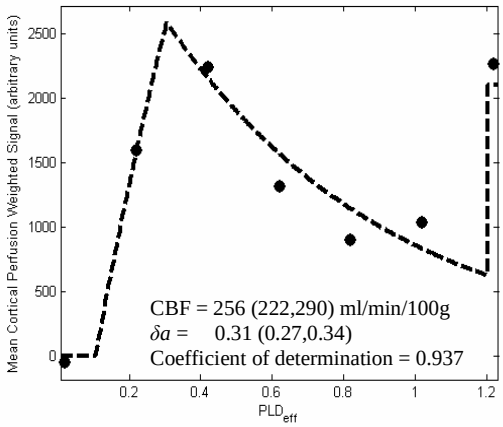
Mean Cortical Perfusion Weighted Signal (arbitrary units)
PLD_eff
CBF = 256 (222,290) ml/min/100g
δa = 0.31 (0.27,0.34)
Coefficient of determination = 0.937

[c]

Figure 4.2

The mean in-vivo cortical perfusion weighted signal against $PLD_{(eff)}$ for the CASL (1^{st} row) and H-CASL (2^{nd} row) sequences. Also plotted are the model fits to the data together with the estimated CBF and δa. Results are reported for all three experiments (a-c). The discontinuity in the H-CASL data at PLD_{eff} of 1.2 seconds is due to the increase in the tagging duration from 0.2s to 1.8s at the greatest PLD (1.22s) – corresponding to the CBF-weighted signal from bolus no.1 in the cortical ROI. In this figure the scales of the y-axis are different: the H-CASL perfusion weighted signal is considerably smaller then the CASL ΔM signal.

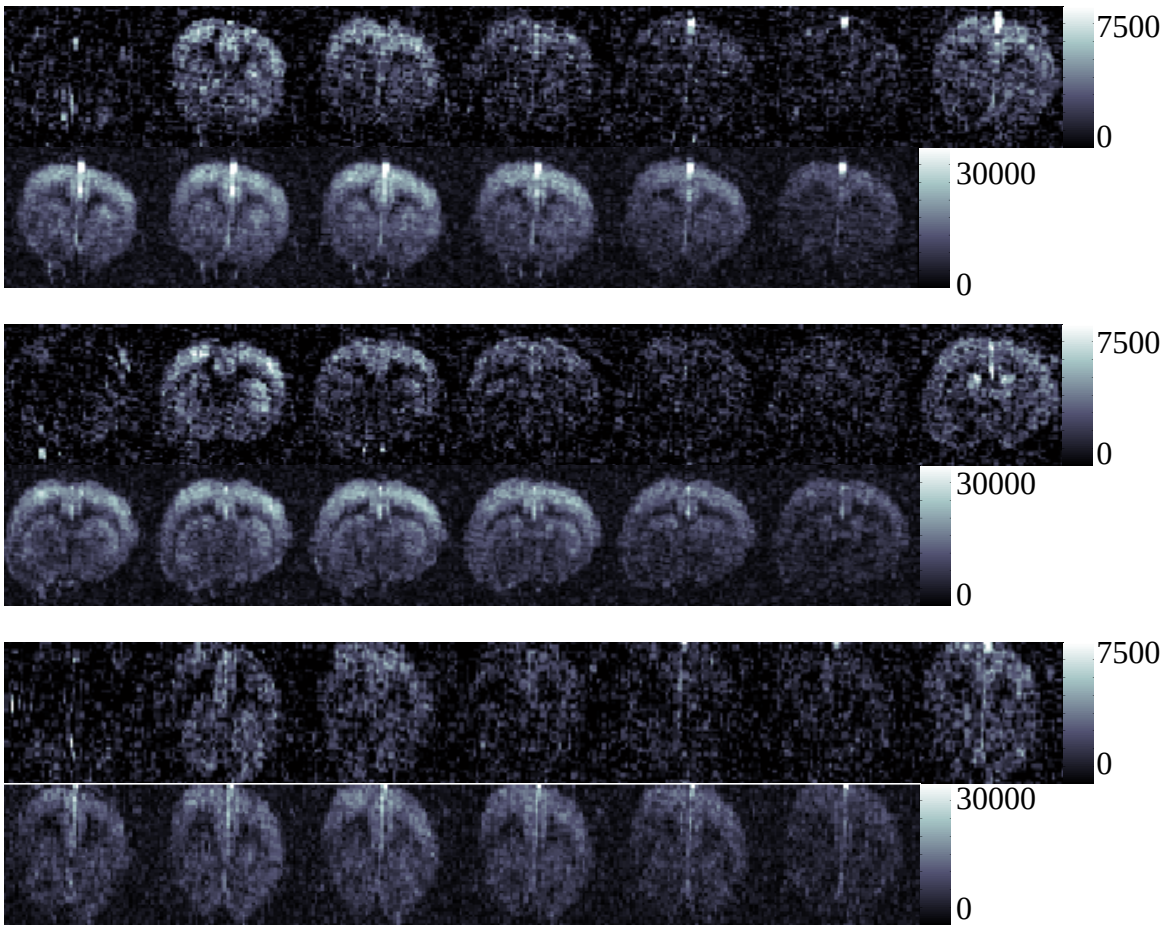

PLD_{eff} (s)

0.02	0.22	0.42	0.62	0.82	1.02	1.22

PLD (s)

0.05	0.1	0.2	0.3	0.5	0.8

Figure 4.3

The in-vivo perfusion weighted images (arbitrary units) derived from the delivery of the H-CASL (top row) and standard CASL bolus at increasing $PLD_{(eff)}$ times (left to right) for all three experiments.

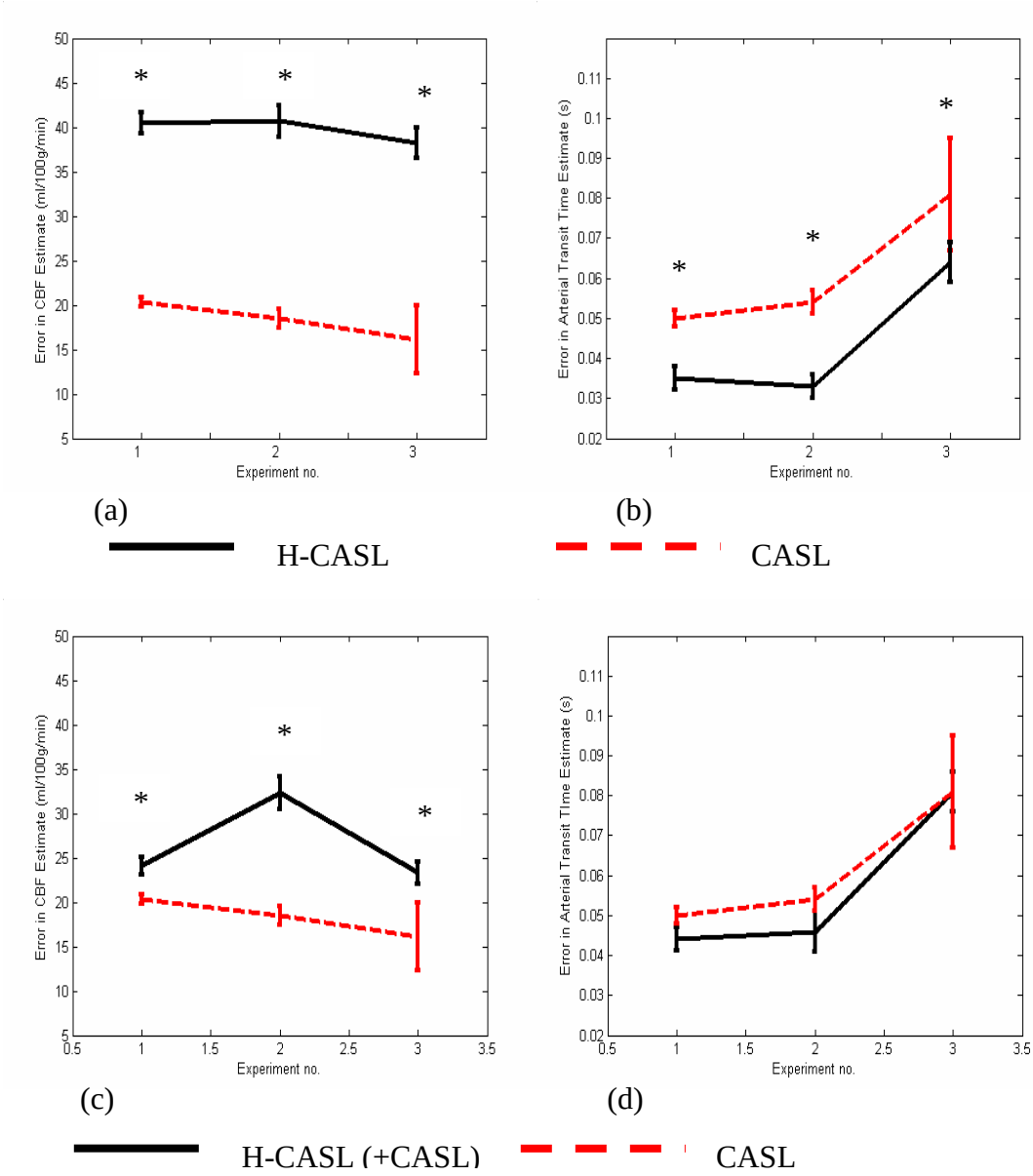

Figure 4.4

The median E^{CBF} and $E^{\delta a}$ estimates from the three in-vivo experiments (± 1 SEM). The first row (a and b) shows the CASL and H-CASL results. The second row (c and d) shows the CASL and Hybrid H-CASL *results. The Median is reported as a summary measurement to reduce the possible influence of outliers. Any significant differences in the CASL and H-CASL error populations and between the CASL and Hybrid H-CASL error populations at each simulated transit time or each different experiment are denoted by *.*

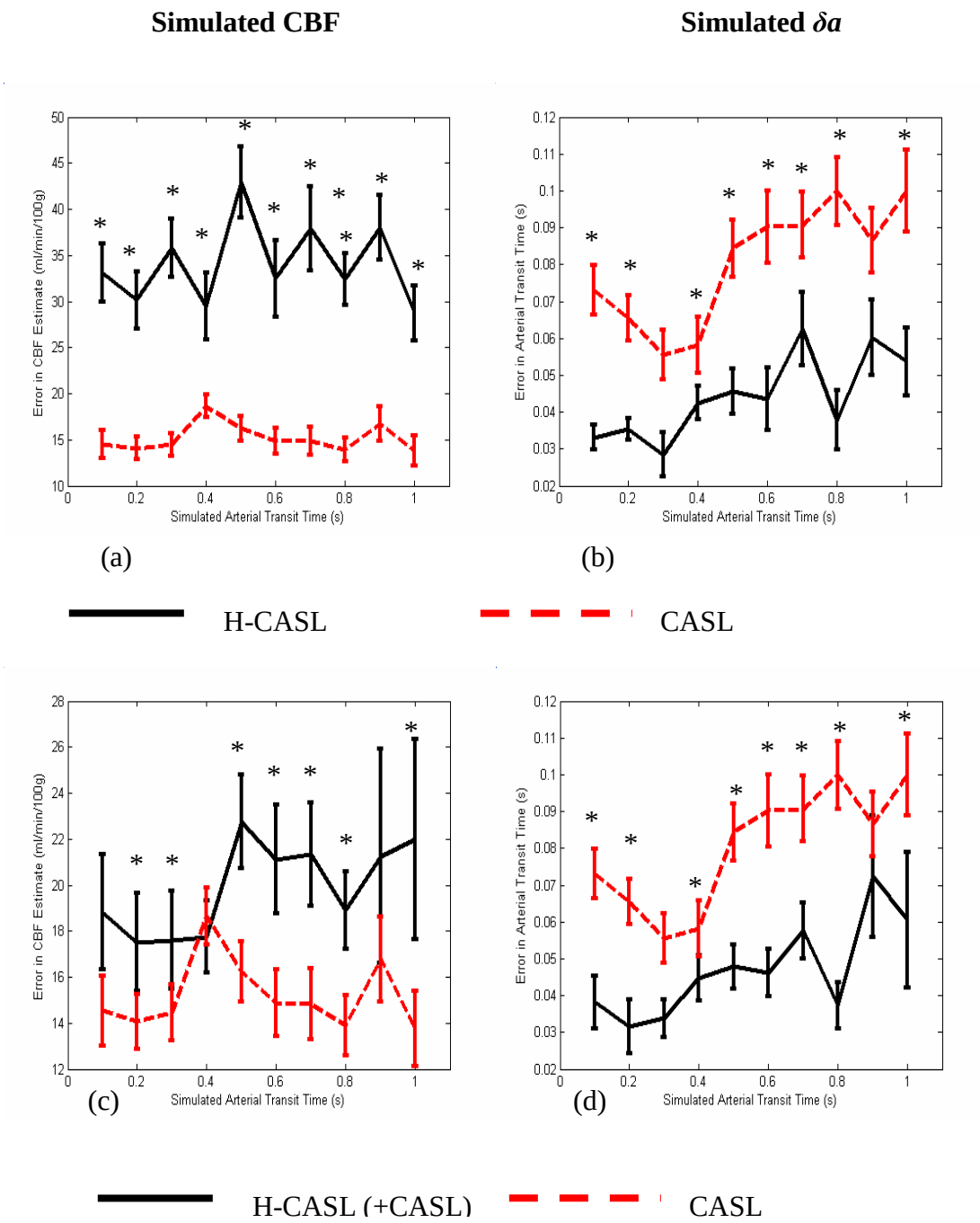

Figure 4.5

*The median E^{CBF} and $E^{\delta a}$ estimates from the simulations (± 1 SEM). The first row (a and b) shows the CASL and H-CASL results. The second row (c and d) shows the CASL and Hybrid H-CASL results. Any significant differences in the CASL and H-CASL error populations and between the CASL and Hybrid H-CASL error populations at each simulated transit time or each different experiment are denoted by *. The distinct fluctuations in the simulated CBF and δa error observations reflects how well the PLD*

times are optimised for a given simulated transit time. As shown by Xie et al., [Xie et al., 2008] the choice of PLD values for a given transit time can have a significant influence on the precision of CBF and δa estimates

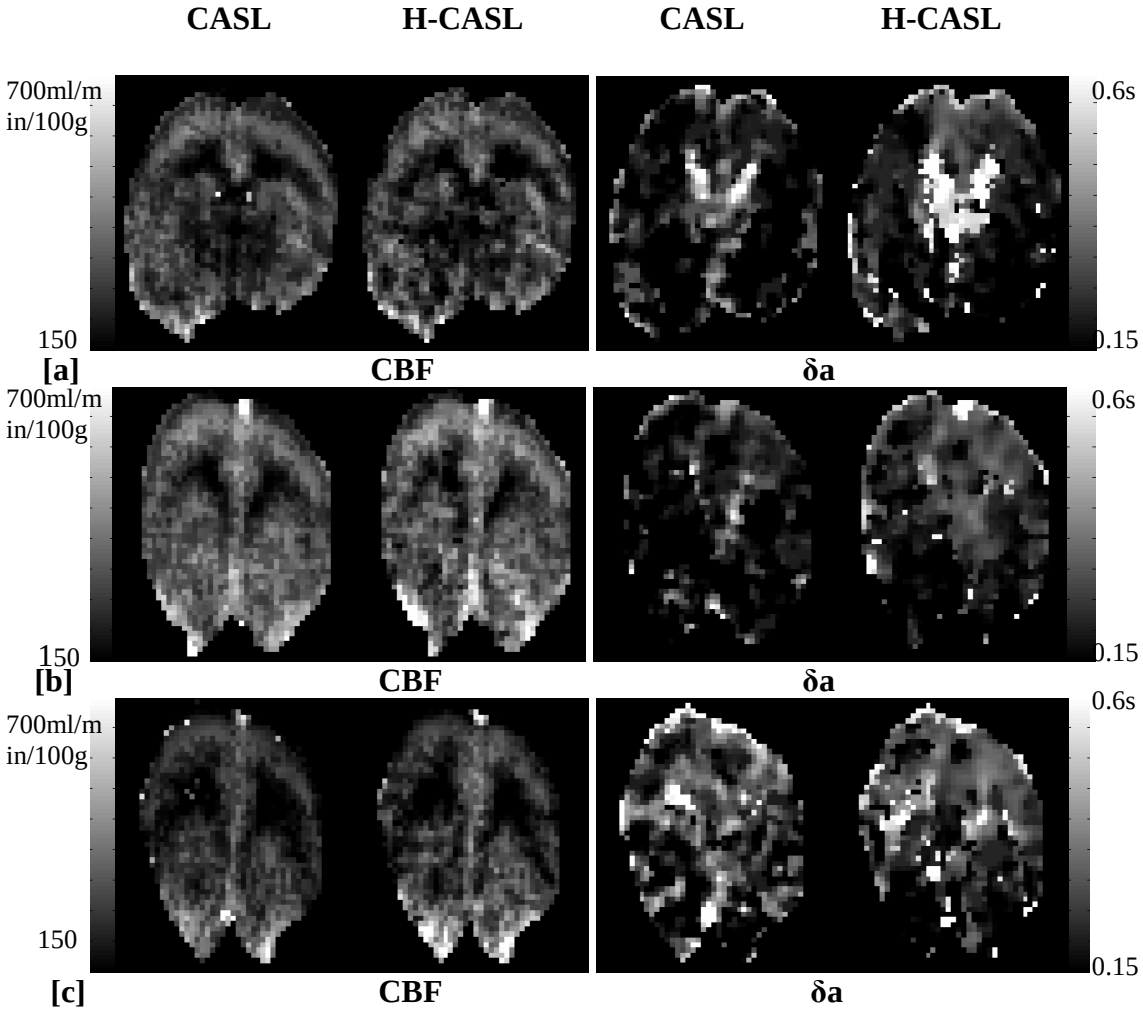

Figure 4.6
The in-vivo CBF and δa maps generated from the CASL and H-CASL schemes for the three subjects (a-c).

4.6 DISCUSSION

This study demonstrates the potential utility of the H-CASL sequence in CBF and *δa* quantification. Several factors demonstrate that this novel approach is viable for accurate cerebral parameter estimation: (i) the good model fit to the data (Figure 4.2) (ii) the noticeable lack of artefacts in the H-CASL perfusion weighted images (Figure 4.3) (iii) the similarity of contrast within each of the cerebral parameter maps between the H-CASL and CASL methods (Figure 4.6). Furthermore, simulated and *in-vivo* data suggest that H-CASL can improve the precision of *δa* estimation in 2/3 of the imaging time required for standard multi-PLD CASL. Thus this new technique may have

particular application as an efficient pre-scan for optimisation of PLD value(s) prior to the main ASL imaging protocol [Dai *et al.*, 2009; Xie *et al.*, 2008].

H-CASL can yield precise δa estimates due to the sensitivity of the measured ΔM signal to the post-labelling delay, at which the small boli of labelled blood first arrives in the imaging region (i.e. the transit time). Once the small bolus of labelled blood water has exchanged into the tissue it rapidly decays according to $T1_{sat}$ (Alsop *et al.*, 1996) which is likely to further increase the sensitivity of the measurements to δa (see *Figure 4.2*). Given that the estimated CBF is correlated with the transit time (i.e. errors in the estimated transit time will reduce the precision of the calculated CBF) any such improvement will aid the precision of CBF estimation. However, as expected, the perfusion weighted signal from the H-CASL images (τ = 0.2s) is considerably lower than the standard CASL approach (τ =3s). Consequently standard CASL possesses a distinct advantage in CBF estimation (where the flow is proportional to the measured ΔM signal in standard quantification models) despite the additional data averaging within the H-CASL reconstruction. Therefore our aim was to combine the H-CASL images (good δa estimation) with standard CASL images at fixed PLD (good CBF estimation) and compare this approach with standard multi-PLD CASL. The simulated and *in-vivo* error observations demonstrated that this hybrid approach considerably improved the precision of the CBF estimates in comparison to the individual H-CASL measurements. However despite the addition of the standard CASL images, the hybrid approach could still not match the precision of CBF measurements generated from the multi-PLD CASL images (the standard approach). Furthermore Figure 4.4 shows that the introduction of the CASL images resulted in a small reduction in the precision of the *in-vivo* δa observations. This may reflect the difficulty of devising a model that describes the signal from small boli of labelled blood equally well as the steady state signal from a large tagged bolus. Therefore although the hybrid approach may have limited application, we propose that H-CASL on its own has value as a quick pre-scan for precise δa estimation to guide ASL imaging parameter selection.

In this work the recovery of the CASL control images at increasing PLD is used to estimate M_0. To our knowledge, the H-CASL data cannot be used in a similar way to estimate M_0. Knowledge of this parameter is essential for CBF quantification but does not influence to the precision of δa estimation. In general, the increased susceptibility

of H-CASL to systematic errors (since any systematic error present in one of the eight H-CASL acquisitions will propagate throughout the entire reconstruction) may prove more challenging to overcome in human application where errors due to subject movement and pulsetile motion can be more prominent. H-CASL is also likely to be more susceptible to dispersion of labelled blood in transit to the brain (due to non plug flow) in comparison to CASL. Indeed as dispersion is a non-linear process it is likely to significantly affect the accuracy of H-CASL as the technique assumes linear delivery of labelled blood to the tissue. Furthermore, in CASL we are estimating δa by focusing on the tail of the tagged bolus of blood. In H-CASL we measure the first delivery of the small boli to the imaging volume to determine δa. Therefore conceptually it can be seen that dispersion effects may lead to a systematic disagreement between δa as estimated using these two approaches (H-CASL and CASL underestimating and overestimating δa respectively). In this work we have observed good agreement between the H-CASL and CASL CBF and δa estimates, which suggest that dispersion effects are not acting as a significant confounding factor in our acquisitions. This may be a consequence of the high flow rate of blood in the feeding arteries of the rat. This high flow rate ensures that a relatively large volume of blood is labelled in 0.2s and minimises the transit time (0.2-0.3s) which limits the extent of dispersion en-route to the imaging region. In humans, dispersion of the encoded sub-boli is likely to be more of an issue and greater sub-bolus duration may be necessary to reduce the influence of such affects. Indeed, longer sub-bolus duration may also be desirable due to the increased range of transit times in the human brain.

In pilot experiments it was noted that the slightest shift of the brain within the field of view (due to eddy currents or “warming up” of the imaging gradients and/or amplifier for example) has severe implications for the reconstructed H-CASL perfusion weighted images. Therefore H-CASL should be implemented with caution as any such instabilities are likely to confound the reconstructed images. In general, the increased susceptibility of H-CASL to systematic errors (since any systematic error present in one of the eight H-CASL acquisitions will propagate throughout the entire reconstruction) may prove more challenging to overcome in human application where errors due to subject movement and pulsetile motion can be more prominent The implementation of post-acquisition co-registration algorithms such as those in FSL [FMRIB, Oxford, UK]

or SPM [FIL, UCL, London] may help make this approach more viable in human studies. The efficient acquisition of perfusion weighted images derived from the delivery of small boli of blood to the brain may particularly benefit studies focusing on the location (e.g. intra/extravascular) of the ASL signal [eg. Chapter 2 of this thesis; Silva *et al.*, 1997; Wang *et al*., 2007] as the tagged blood is likely to be less dispersed throughout different cerebral compartments.

4.7 SUMMARY

To conclude, this study provides evidence that H-CASL is viable *in-vivo* and can be used for accurate CBF and δa measurement. The benefits to the precision of δa estimation suggest H-CASL may be ideally suited as a quick pre-scan to guide ASL imaging parameters [Dai *et al.*, 2009; Xie *et al.*, 2008].

4.8 REFERENCES

Alsop DC, Detre JA. (1996). Reduced transit-time sensitivity in non-invasive magnetic resonance imaging of human cerebral blood flow. Journal of Cerebral Blood Flow and Metabolism 16, 1236-1249.

Buxton RB, Frank LR, Wong EC, Siewert B, Warach S, Edelman RR.(1998). A general kinetic model for quantitative perfusion imaging with arterial spin labelling. Magnetic Resonance in Medicine 40, 383-396.

Detre JA, Leigh JS, Williams DS, Koretsky AP.(1992). Perfusion imaging. Magnetic Resonance in Medicine 23**,** 37-45.

Garcia DM, Duhamel G, Alsop DC. (2005). Efficiency of inversion pulses for background suppressed arterial spin labelling. Magnetic Resonance in Medicine 54, 366-72.

Herscovitch P, Raichle ME. (1985). What is the correct value for the blood–brain partition coefficient for water? Journal of Cerebral Blood Flow and Metabolism 5, 65–69

Thomas DL, Lythgoe MF, van der Weerd L, Ordidge RJ, Gadian DG. (2006a). Regional variation of cerebral blood flow and arterial transit time in the normal and hypoperfused rat brain measured using continuous arterial spin labelling MRI. Journal of Cerebral Blood Flow and Metabolism 26, 274-82.

Thomas DL, Lythgoe MF, Gadian DG, Ordidge RJ. (2006(b)). In vivo measurement of the longitudinal relaxation time of arterial blood (T1a) in the mouse using a pulsed arterial spin labelling approach. Magnetic Resonance in Medicine 55, 943-947

Gunther M. (2007) Highly efficient accelerated acquisition of perfusion inflow series by Cycled Arterial Spin Labeling. Presented at the 15th ISMRM , Berlin abstract 380.

Silva AC, Williams DS, Koretsky AP.(1997(a)). Evidence for the exchange of arterial spin labelled water with tissue water in rat brain from diffusion-sensitized measurements of perfusion. Magnetic Resonance in Medicine 38, 232-237.

Thomas DL. 1999. Magnetic resonance imaging of diffusion and perfusion: techniques and applications to cerebral ischaemia. Ph.D Thesis.

Wang J, Alsop DC, Li L, Listerud J, Gonzalez-At JB, Schnall MD, Detre JA (2002). Comparison of quantitative perfusion imaging using arterial spin labelling at 1.5 and 4.0 Tesla. Magnetic Resonance in Medicine 48, 242-254

Wang J, Fernandez-Serra MA, Wang S, St. Lawrence KS.(2007). When perfusion meets diffusion: in vivo measurements of water permeability in human brain. Journal of Cerebral Blood Flow and Metabolism 27, 839-49.

Xie J, Gallichan D, Gunn RN, Jezzard P. Optimal Design of Pulsed Arterial Spin Labelling MRI Experiments. Magn Reson Med. 2008. Apr;59(4):826 -34.

CHAPTER 5: FINAL DISCUSSION AND FUTURE WORK

5.1 SUMMARY

The main results from the previous experimental chapters can be summarised as follows:

- By measuring the transverse decay of the ASL signal over a range of tagging durations and post-labelling delay times with and without vascular crusher gradients we have estimated the dynamic distribution of the signal deriving from labelled water in the brain within the intra-vascular, and intra-cellular and extra-cellular tissue space. Our results provide evidence for rapid exchange of labelled water into the intra-cellular space relative to the transit-time through the vascular bed, and provide a more solid foundation for CBF quantification using ASL techniques.
- Secondly, we have demonstrated the potential of image de-noising methods to reduce random errors in perfusion weighted images for more precise and accurate CBF estimates.
- Finally we have presented the first *in-vivo* demonstration of Hadamard encoded CASL and have provided evidence of the value of this technique for precise transit time estimation.

5.2 CHARACTERISING THE ORIGIN OF THE ARTERIAL SPIN LABELLING SIGNAL IN MRI USING A MULTI-ECHO ACQUISITION APPROACH

The estimated $T2_{IV}$ (see *Figure 2.27*) at brief tagging duration (τ =500-1000ms) was initially a considerable source of uncertainty as it appeared to contradict a number of previous experiments. Intuitively we would expect the vascular portion of the ASL

signal to be confined to the arterial side at short τ and PLD. We were originally of the opinion that the T2 of the arterial blood should be around 3 times greater than that of the tissue [Stanitz *et al.*, 2005; Thomas *et al.*, 2001] and were surprised when the measured $T2_{IV}$ was found to be very similar to the T2 of the labelled water that had exchanged into the tissue. We initially suspected that this outcome may reflect a systematic error in the imaging protocol that was confounding our $T2_{IV}$ estimates. Further reading into the literature provided evidence that the arterial side of the vasculature contains blood that is not 100% saturated with oxygen in the rat brain [e.g. Vazquez *et al.*, 2009, Lin *et al.*, 1998]. It is known that the T2 of blood is sensitive to its oxygen saturation [Zhou *et al.*, 2007] which provided a rational physiological explanation for our $T2_{IV}$ measurements.

The main problem encountered in this chapter is one of the sum of exponentials. This is a problem that has been encountered previously in the MR literature e.g. in the context of IVIM for perfusion imaging, which uses a bi-exponential model for diffusion to differentiate the intra-vascular and extra-vascular compartments. As shown by King et al., [King *et al.*, 1991], the problems associated with obtaining reliable parameter estimates from the data fitting process are such that the precision of parameter estimation is limited in practice, despite the validity of the model. Very high SNR (noise referring to random and systematic error) measurements are required for precise parameter estimation". As previously discussed, the uncertainty of the $T2_{IC}$ and $T2_{EC}$ values restricts the extent of interpretation of our data. Our study was originally designed to estimate the EC to IC origin of the ASL signal from the measured transverse decay curves using results from previous work which obtained precise $T2_{IC}$ and $T2_{EC}$ measurements (57ms and 174ms) in the grey matter of the rat brain at the same field strength [Haida *et al.*, 1987]. Our choice of $T2_{IC}$ and $T2_{EC}$ measurements from the literature was partially vindicated by a recent *in*-vivo study that measured similar $T2_{IC}$ and $T2_{EC}$ values (64ms ±10 and 184ms ±50), although this was at a different field strength [Lascialfari *et al.*, 2005]. However although these estimates are from the rat brain cortical grey matter at the same field strength, they are from an ex-vivo sample and therefore may not be exactly relevant to our *in-vivo* data. Ideally we would use our own data to estimate $T2_{IC}$ and $T2_{EC}$, rather than taking values from the literature. However we were not able to achieve reasonable precision in the estimated $T2_{IC}$ and $T2_{EC}$ by fitting to our data due to the limited coverage of the transverse decay curve as well as the SNR of our *in-vivo* measurements. The results of simultaneously estimating

$T2_{IC}$ and $T2_{EC}$ as well as the proportion of the signal originating from the two compartments (IC and EC) from our 9 *in-vivo* subjects (experiments) are presented in appendix B2. Unfortunately, the huge 95% confidence intervals of the fitted parameters demonstrate that the precision of the $T2_{EC}$ and $T2_{IC}$ values is limited to the extent that it would be almost meaningless to take $T2_{EC}$ and $T2_{IC}$ estimates from our data. We also present simulated data (appendix B1) which demonstrates that this imprecision does not reflect systematic errors in our measurements but rather the difficulty of fitting experimental data to a bi-exponential decay model (with no fixed parameters). Therefore, although this is not ideal, we took values from previous studies that were specifically designed to estimate $T2_{IC}$ and $T2_{EC}$ with some precision [Haida *et al.,* 1987; Matsumae *et al.,* 2003]. The question of the reliability of these studies is open to debate. It could be argued that the Haida experiment is sufficiently similar to our study that taking their $T2_{IC}$ and $T2_{EC}$ estimates is a sensible and pragmatic approach particularly given the reasonable agreement in the estimated $T2_{IC}$ and $T2_{EC}$ values from a recent *in-vivo* study [Lascialfari *et al.,* 2005]. However others may quite legitimately question the validity of this decision. I feel though, that I have openly confronted this point of controversy in the chapter. To ensure that the limitations of this approach were made clear to the reader of my thesis, I discuss the justification and implications of this approach in the text and present two versions of Figure 2.28 to show how this source of uncertainty impacted the plots. I believe that this provides the most transparent account of the limitations of our methodology and how this choice impacts the results displayed in Figure 2.28.

However whilst this is a crucial consideration, it is important to emphasise that this study presents several novel findings that do not rely on precise knowledge of $T2_{EC}$ and $T2_{IC.}$

For example:

1) The relatively narrow range of $T2_{app}^{\Delta M}$ and $T2_{app}^{ctrl}$ observations suggests that T2 effects are unlikely to be a significantly confounding factor in quantitative ASL CBF rodent studies, particularly at short echo times (Figure 2.24). However the significantly increased $T2_{app}$ of the perfusion-weighted signal in comparison to the control may result in a small overestimation in CBF using

standard quantification methods (e.g. Alsop *et al.,* 1996, Buxton *et al.,* 1998) as the equilibrium magnetisation of the tissue (M_0) is assumed to decay with the same T2 as the labelled ASL signal in the brain.

2) The choice of $T2_{IC}$ and $T2_{EC}$ will have negligible effect on Figure 2.27 which presents the $T2_{IV}$ observations (which may provide a surrogate index of oxygen saturation) and provides evidence for the timescale of labelled blood water, which has not exchanged into the tissue due to limited permeability of the blood-brain barrier, to traverse the capillary bed.

In addition there are possible interpretations of Figure 2.28 regarding the delivery of labelled blood water to the brain that (whilst relying on $T2_{IC}$ being approximately equal to the overall T2 of the tissue and $T2_{EC}$ being significantly greater) do not require precise knowledge of $T2_{IC}$ and $T2_{EC}$. There are a number of studies that (although they do not estimate $T2_{IC}$ and $T2_{EC}$ explicitly) do conclude that $T2_{EC} >> T2_{Tissue}$ as stated in the introduction of chapter 2. Figure 2.28 does still provide novel evidence in relation to the delivery of blood water to the brain. For example:

3) The constancy of the $\Phi_{IC}^{\Delta M}$ and $\Phi_{EC}^{\Delta M}$ estimates at τ = 1s and τ =3s suggests that a dynamic equilibrium is established between labelled water in the intra-and extra-cellular tissue space by τ = 1s.

4) The ΔM signal is weighted towards the extra-cellular space, relative to the control signal, even when τ=3s and with extended PLD. The short mean residence time (120ms) of the extra-cellular spins relative to the τ and PLD timescale, as well as the aforementioned evidence for establishment of a dynamic equilibrium, suggests this may be due to gradual exchange of labelled blood from the vascular compartment to the tissue at increasing PLD.

In summary, we are not able to generate meaningful values of $T2_{IC}$ and $T2_{EC}$ from our data. Therefore we take $T2_{IC}$ and $T2_{EC}$ from the most relevant study that aimed to precisely measure these parameters. Accepting the limitations of this approach we present two versions of Figure 2.28 (a and b) to clearly illustrate the implications of this source of uncertainty on $\Phi_{IV}^{\Delta M}$,$\Phi_{EC}^{\Delta M}$, $\Phi_{IC}^{\Delta M}$ and Φ_{IV}^{Ctrl}, Φ_{EC}^{Ctrl}, Φ_{IC}^{Ctrl}.

In this way I believe that I have clearly communicated how this limits the strength of interpretation of Figure 2.28. Finally it is important to emphasise that this study provides novel findings that do not rely on precise knowledge of $T2_{IC}$ and $T2_{EC}$.

Ideally I would have implemented separate experiments designed to retrospectively measure $T2_{IC}$ and $T2_{EC}$ by acquiring a high SNR multi-TE data set on the 2.35T system. However given the limitations in terms of the strength of the gradients (and therefore the minimum echo time) it is unlikely that we would be able to estimate $T2_{IC}$ and $T2_{EC}$ with significantly greater precision than [Lascialfari *et al.,* 2005].

The natural development of this technique would be to apply it to an animal model of disease (a brain tumour for example). However, assuming $T2_{EC}$ and $T2_{IC}$ are the same in normal and diseased tissue may not be correct and may yield misleading results. Again, it may be necessary to acquire estimates of $T2_{EC}$ and $T2_{IC}$ for healthy and diseased tissue using standard multi-TE image acquisitions before applying the methods described in chapter 2 on an animal model of disease.

I am very pleased with the concordance of the trends in Figures 2.25 and Figure 2.26 (the individual $T2_{app}$ estimates from each of the 9 experiments with and without VCGs) as these suggest that random and systematic errors have been well suppressed in these experiments. Indeed the dominant affect that determines the size of the error bars in Figure 2.24 seems to be an offset between the estimated T2 values between the 9 experiments; the trends at increasing τ and PLD themselves appear to be fairly concordant. This offset may be due to slight differences in the calibration of the 90^o and 180^o excitation and re-focussing pulses between experiments, differences in the shim or genuine inter-animal physiological variation. In particular, the rate of change of $T2_{app}{}^{\Delta M}$(VCGs-off) from τ=1s to τ=3s does appear to be noticeably concordant between the 9 subjects. I think that one of the main reasons we were able to achieve this relatively high precision was by extensive interleaving of the different sequence parameters in combination with long scan times; any systematic errors are likely to be "evened" out over the course of a 4 hour acquisition protocol. Therefore despite the limitations in the design of the pilot studies, there is no doubt that the final results benefited from the experience of my previous experiments in relation to minimising random and systematic errors in the experimental protocol.

Our results provide evidence for the rapid exchange of labelled water into the brain tissue. In fact it was surprising that only around 20% of the ASL signal derived from the IV space at τ = 500ms and PLD =50ms, considering that the transit time from the labelling plane to the ROI is approximately 250ms. Conceptually, it is somewhat difficult to fathom how such a significant majority of labelled blood resides in the tissue at these sequence timing parameters. However the marked deceleration of the blood from the site of labelling (carotid and vertebral arteries) to the capillaries perhaps provides an explanation for this behaviour. Blood is travelling at approximately 1m/s in the carotid arteries as it leaves the heart which beats at about 400 beats per minute [Utting *et al.*2003]. In the capillaries it travels at around 0.5mm/s [Villringer *et al.*, 1994]. This rapid deceleration is due to the branching and narrowing of the arteries into arterioles and capillaries as blood flows up the vascular tree. Therefore it is perhaps this pressure gradient that quickly forces the water into the tissue through the capillaries. It is important to consider that the $\Phi_{IV}^{\Delta M}$ estimates are dependent on the extent of vascular suppression. The $\Phi_{IV}^{\Delta M}$ values reported in this work may be underestimated because signal from labelled blood water in the vasculature has not been significantly attenuated by the VCGs. Our $\Phi_{IV}^{\Delta M}$ estimates are in agreement with previous MR studies under similar experimental conditions and imaging parameters. Indeed the use of diffusion gradients to remove the vascular ASL signal is fairly established in human studies [e.g. Petersen *et al.*, 2005]. However the assumption that diffusion gradients can efficiently remove the vascular signal is contentious, particularly given evidence suggesting that blood does not flow for a time in some capillaries [Villringer *et al*., 1994]. Therefore it is possible that significant vascular signal remains with VCGs and the assumption of pure tissue signal may not hold true in practice."

The Hadamard encoded CASL study described in chapter 4 provides corroborative evidence for the rapid exchange of labelled blood water into the tissue. The mean *in-vivo* cortical perfusion weighted measurements from the reconstructed H-CASL small boli suggest that the labelled water rapidly decays once it has arrived in the cortex (see *Figure 4.2*). The T1 constant that describes this decay is just over 0.65s which is equivalent to T1sat [Alsop and Detre, 1996] as measured from the recovery of the standard CASL control images at increasing PLD. If the small volumes of labelled blood water did not exchange into the tissue and remained in the vessels for a certain

time prior to exchange then the rate of the decay would be more similar to that of blood (T1 ~ 1.5s). The observation of rapid decay T1 decay provides evidence for fast exchange.

In this work we present the proportion of the measured ASL signal originating from the three compartments (IV, IC, EC). The longitudinal relaxation of tagged spins following labelling plays a significant role in the tri-compartmental distribution of the ASL signal. For example, blood water that has exchanged into the tissue during labelling will be relaxing according to T1sat [Alsop and Detre, 1996] whereas labelled blood in the vasculature will be recovering at a slower rate (T1b) [Alsop and Detre, 1996]. Therefore it is likely that T1 acts to preferentially attenuate the signal from labelled blood water in the tissue space in comparison to blood water that remains in the IV compartment following labelling. However it is difficult to speculate in any greater detail how the reported relative population estimates may change by taking the longitudinal relaxation effects into account. For us to do this would require knowledge of the T1 relaxation history of the labelled blood water in the different compartments, which is an unknown parameter. For example, we do not know whether labelled blood water in the venous vessels has flowed through the vasculature (due to the limited permeability of the blood brain barrier) or whether it has exchanged into the tissue and then exchanged back into the venules. We could impose a model on our data in order to estimate the T1 relaxation history of the labelled blood water in the different compartments. However our data does not necessarily follow the ASL CBF quantification models described in for example [Detre *et* al., 1992; Alsop *et al.*, 1996; Parkes and Tofts 2002]. Indeed the basic hypothesis that with CASL, you need to be in steady-state, which you can only reach if t >> 2-3 times T_{1b}.This is not the case in the ΔM images acquired at $\tau < 3000$ms (i.e. 500ms, 1000ms, 1500ms). Therefore the standard CASL CBF quantification models may not accurately describe the distribution of labelled blood in the brain at these sequence timings. Our work is an exploratory study – we report the observed changes in the measured ASL signal without imposing a model. We hope that our data may perhaps be helpful to guide future ASL CBF quantification models that describe the delivery of blood into the brain.

It would have been interesting to measure the transverse decay of the ASL signal at shorter τ (<500ms) and longer PLD (>1200ms) to investigate the tri-compartmental

distribution of the ASL signal at an earlier or later point during the labelled water's journey into the brain. This would likely have increased the dynamic range of the $T2_{app}$ estimates reported in Figure 2.24. However pilot experiments suggested that the SNR at these sequence timing parameters would significantly reduce the precision of the $T2_{app}$ estimates. Therefore I choose τ = 500ms and PLD =1200ms to ensure that there was reasonable SNR in the ΔM measurements.

5.3 REDUCTION OF ERRORS IN ASL CEREBRAL PERFUSION AND ARTERIAL TRANSIT TIME MAPS USING IMAGE DE-NOISING

Chapter 3 highlights the benefits of image de-noising in quantitative ASL studies. Given that post-acquisition image processing methods provide most benefit to low SNR data, it is perhaps surprising that they have not become more prominent within ASL MRI, given the intrinsically low SNR of the measurements. Our findings provide convincing evidence that ICA can benefit multi time-point ASL data without introducing marked spatial smoothing to the quantitative CBF and δa maps. I have since applied ICA to multi-TI ASL human data, acquired at a number of different MRI centres. For example, Figure 5.1(a) shows perfusion weighted images of an infant brain at 32 different inflow times, acquired using a Look-Locker acquisition. Figure 5.1(b) shows the same images following application of ICA to remove random errors. Although no formal comparisons were performed on these data, visual inspection suggests that ICA acted to significantly reduce random errors as intended. I hope to be able to publish the results described in chapter 3 so that removal of random errors using ICA may soon become common practice in future multi-time-point (PLD inflow times) ASL studies.

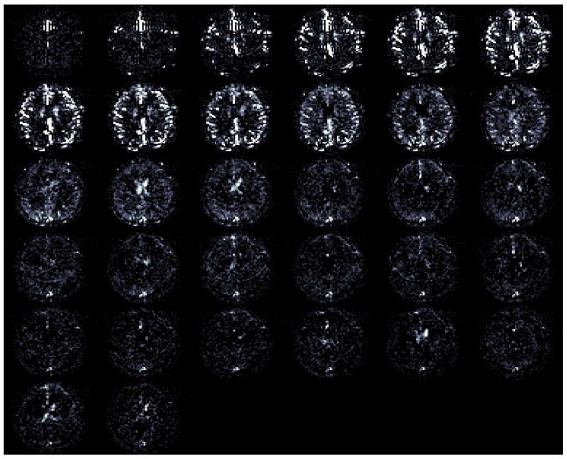

[a]

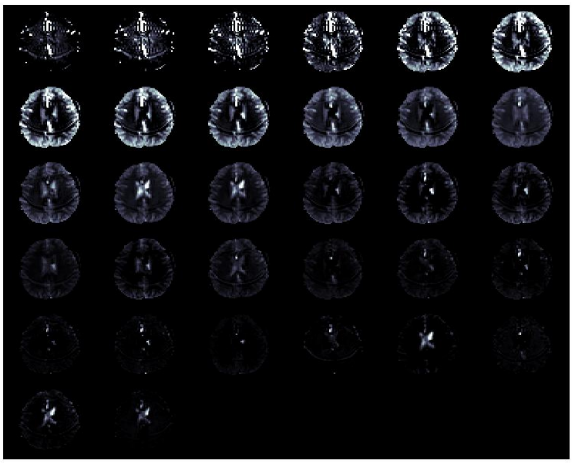

[b]

Figure 5.1

Perfusion Weighted images acquired at 32 different inflow times using a Look-Locker acquisition before (a) and after (b) application of ICA to remove random errors.

It was difficult to devise a fair comparison between different de-noising methods. An obvious criticism of our methodology is the comparison of ICA (which operates on a 3D data set - 2D images at different PLDs) with 2D spatial filters. It could be argued that a fairer comparison would be ICA against a 3D Wiener or AD filter. However it seemed unintuitive to smooth the images in the “time” dimension before fitting the data to a least squares model, particularly given that the CBF related information is contained within the “high frequency” part of the PLD dependant time-course (see *Figure 3.1*). As ICA works in a very different way to standard smoothing methods we

found that this introduced no noticeable bias to the CBF and δa estimates (see 3.4.2 *Results: Simulated data 2*). However for these reasons when discussing the results, I do not to make strong judgements in regards to which de-noising method is best but rather emphasise the benefit of de-noising in comparison to not applying any such post-processing. As discussed in section 3.5, the optimal filter will depend on each particular data set which limits the relevance of comparisons between different de-noising methods, made on the basis of our data sample.

In our analyses, we chose to determine the degree of smoothing (or "threshold") according to the automated threshold selection algorithms associated with each filter (apart from the Gaussian filter). Some would argue that it may have been fairer to standardise the level of smoothing based on visual inspection of the images. For example we could increase the degree of smoothing until a certain boundary is determined to be degraded. However this subjective measure would have been challenging to implement in a fair manner as the AD filter (for example) is designed to maintain boundaries between regions of marked contrast. We chose instead to implement the "optimisation" algorithms that accompany each de-noising method. These should automatically "optimise" the extent of smoothing by estimating the degree of random errors in the image. In this way we sought to examine whether de-noising can benefit CBF and δa maps with minimal subjective optimisation.

5.4. *IN-VIVO* HADAMARD ENCODED CONTINUOUS ARTERIAL SPIN LABELLING (H-CASL)

The difficulty with imaging small boli of labelled water is that relatively few tagged spins contribute to the perfusion weighted signal and therefore the SNR of the ΔM images is considerably reduced in comparison to standard multi-PLD CASL (τ = 3s). Although there is significantly more effective "averaging" in the H-CASL reconstruction (in a given imaging time) in comparison to CASL, the increase in SNR is proportional to the square route of the number of averages and so the benefits to the SNR are restricted in this way. Since the CBF is proportional to the perfusion weighted signal in most ASL CBF quantification models [e.g. Alsop *et al.*, 1996; Buxton *et al.*,

1998] this means that the precision of CBF estimation using H-CASL (τ = 0.2s) is severely limited in comparison to the standard method (τ =3s).

The inventor of this technique, Matthias Günther, intended the data to be flexible in terms of the potential to re-combine it in different ways. He proposed that you do not lose anything by acquiring the data in this way since you can generate the equivalent images to those produced using standard CASL (the perfusion weighted image from a 3 second tagged bolus) by recombining the acquired images in a different way. The data can then be additionally reconstructed to generate the perfusion weighted signal from small boli of labelled blood to the brain as described in chapter 4, to provide additional information (e.g. precise δa measurements).

For example, to generate the equivalent data to the standard CASL experiment the images can be combined in the following way (see Figure 4.1):

7 x Image 1 – Image 2 – Image 3 – Image 4 – Image 5 – Image 6 –Image 7 – Image 8. [5.1]

The results of this reconstruction are shown in Figure 5.2. The CASL image was acquired at a single PLD time (0.5s) and was averaged over all 15 repeats. All 8 H-CASL images (each averaged over the 15 repeats) were used to reconstruct figure 5.2(b). Therefore in this example H-CASL required four times more imaging time in comparison to standard single PLD CASL. Even though all 8 acquisitions contribute to this image, visual inspection reveals that the SNR is lower than standard CASL. This may be because each acquisition (with the same noise level) is not given equal weight within the reconstruction. For example, the first acquisition is used seven times more than each of the other images in this reconstruction. Therefore this approach is not optimised to minimise the noise within the reconstructed perfusion weighted image. Consequently I do not think that this is an efficient way to combine the data in relation to the SNR of the perfusion weighted images. The method of reconstruction presented in chapter 5 makes the most efficient use of the data since each image is given equal weighting.

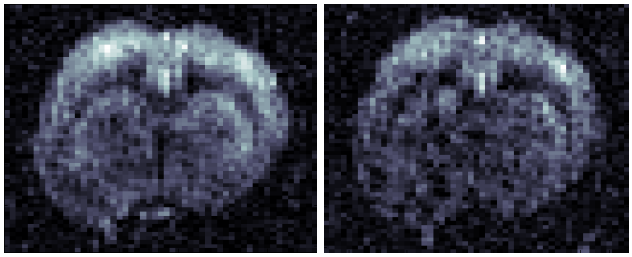

(a) (b)

Figure 5.2.
The perfusion weighted images derived from the standard CASL approach (a) and the H-CASL approach (b) where the images are combined as described in equation 5.1. The data presented is averaged over all the acquisitions for each technique from Experiment 1 (of 3).

I spent some time trying to optimise the sub-boli durations within the H-CASL scheme for precise CBF and δa estimation. Initially I chose a sub-bolus duration of 0.3s. However the reconstructed perfusion weighted images at PLD(eff) of 1.2,1.5 and 1.8s provided little useful information at the typical transit times in the rat brain as the labelled spins had undergone significant longitudinal relaxation according to $T1_{sat}$ at the long PLD_{eff} times. As demonstrated by Figure 5.3 below, the signal from sub-bolus 5, 6 and 7 had almost completely decayed at PLD_{eff} of 1.22, 1.52 and 1.82s which limited the benefits of H-CASL.

I hypothesised that a sensible approach may be to try and account for longitudinal relaxation at increasing PLD by having variable sub-bolus duration. The idea was to increase the duration of the sub-boli at increasing PLD(eff) so that perfusion weighted signal would no longer be negligible at increased PLD(eff). The duration of the sub-bolus was 0.05, 0.1, 0.15, 0.2, 0.25, 0.30 and 0.35s giving a PLD(eff) of 0.02, 0.07, 0.17, 0.32, 0.52, 0.82 and 1.22s. The images generated using this revised approach are shown in Figure 5.4. Although this method successfully increased the SNR of the perfusion weighted images derived from the delivery of sub-bolus 5, 6 and 7 to the tissue, the sensitivity of the inflow curve to δa was significantly decreased, restricting the precision of transit time estimation. As the fixed sub-bolus duration method had already shown promising results in relation to the precision of transit time estimation, it seemed that the utility of this variable sub-bolus duration approach was limited.

I was now satisfied that using fixed sub-bolus duration was the best way to proceed. I continued to try to optimise the duration of the sub-boli. Using short sub-boli ensured that the bolus inflow curve could be frequently sampled so that the PLD at which labelled blood first arrives in the imaging slice can be precisely defined. Using long sub-boli restricted the density of the PLD_{eff} sampling points, limiting the precision of δa estimation. However if the duration of the sub-boli is too short then the SNR_{PWI} was too low to provide useful information. Therefore a sub-bolus duration of 0.2s was chosen as a compromise between reasonable SNR_{PWI} and sampling frequency. The final version of H-CASL presented above also includes a long sub-bolus which was intended to provide a high SNR_{PWI}, transit time insensitive [Alsop *et al.,* 1996] perfusion weighted measurement.

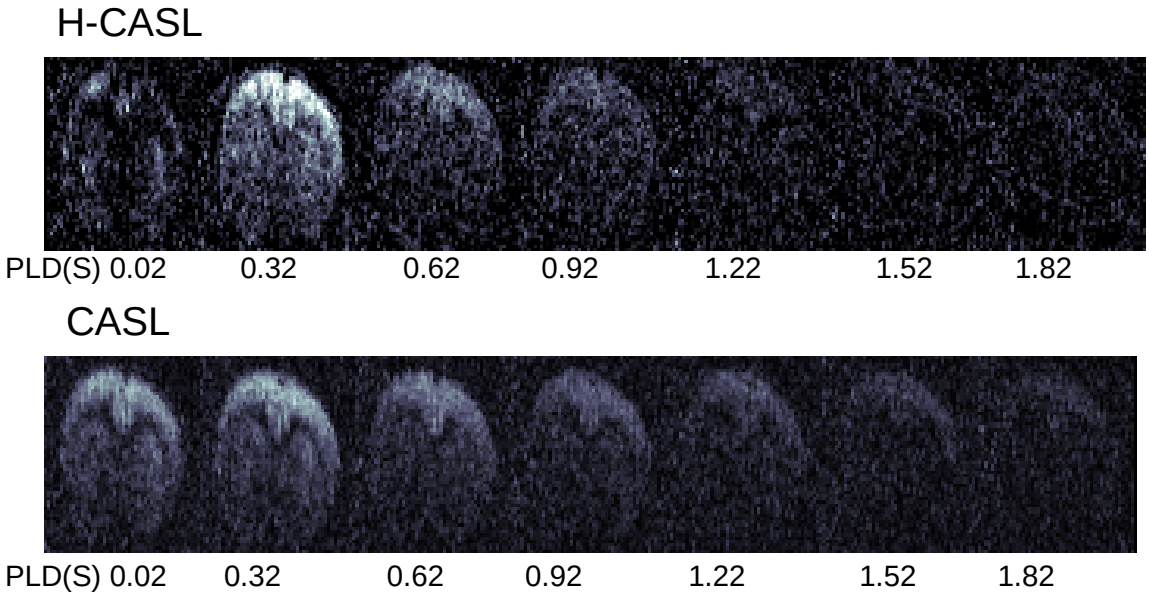

Figure 5.3

The implementation of the H-CASL scheme with a sub-bolus duration of 0.3s. The standard CASL images are shown below.

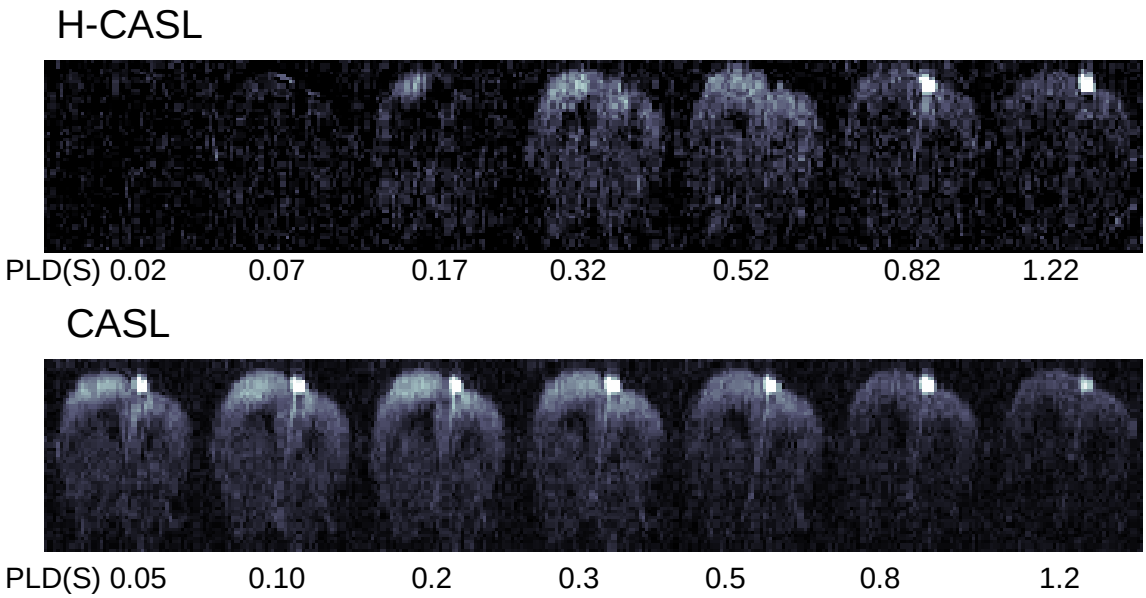

Figure 5.4

The implementation of the H-CASL scheme with variable sub-bolus duration (top row). The standard CASL images are shown below.

Initially H-CASL was a challenging technique to implement reproducibly. The slightest shift of the brain within the field of view had dire implications for the reconstructed ΔM images. However once the imaging protocol was optimised in terms of the level of rigid motion prevention, the technique was re-producible and we performed several consecutive experiments without any obvious artefacts present in the H-CASL perfusion weighted images. Based on my experience of experimental MRI and the problems associated with H-CASL as well as my limited experience with human scanners, I do have some doubt as to whether H-CASL is a viable sequence in human studies. This is mainly because systematic errors (e.g. subject movement, pulsetile motion) are more problematic when compared to pre-clinical rodent imaging. However with background suppression and post-acquisition re-alignment, H-CASL may well be clinically feasible.

5.5 FINAL CONCLUSION

In conclusion, ASL undoubtedly represents a promising approach to cerebral perfusion measurement. However it suffers from low SNR and can be confounded by the effects of neuropathology. Indeed, although a recent study has provided evidence supporting the reproducibility of ASL for perfusion measurement in healthy volunteers [Petersen *et*

al., 2008], accurate and robust CBF quantification in the diseased brain still represents a significant challenge. Pathology may result in reduced CBF, increased transit time and may introduce differences in T2 (ΔM) between healthy and diseased tissue. We hope that the experimental work described in this thesis may be particularly helpful at improving the utility of ASL in such applications.

5.6 REFERENCES

Alsop DC, Detre JA. (1996). Reduced transit-time sensitivity in non-invasive magnetic resonance imaging of human cerebral blood flow. Journal of Cerebral Blood Flow and Metabolism 16, 1236-1249

Buxton RB, Frank LR, Wong EC, Siewert B, Warach S, Edelman RR.(1998). A general kinetic model for quantitative perfusion imaging with arterial spin labelling. Magnetic Resonance in Medicine 40, 383-396

King MD, van Bruggen N, Busza AL, Houseman J, Williams SR, Gadian DG. Perfusion and diffusion MR imaging. Magnetic Resonance in Medicine 24:288-301

Lin W,Paczynski RP, Celik A, Karthikeyan K, Hsu CY, Powers WJ. (1998). Experimental Hypoxia: Changes in R_2* of Brain Parenchyma Accurately Reflect the Combined Effects of Changes in Arterial and Cerebral Venous Oxygen Saturation. Magnetic Resonance in Medicine 39, 374-481

Petersen ET, Lim T, Golay X.(2006). Model-free arterial spin labelling quantification approach for perfusion MRI. Magnetic Resonance in Medicine 55, 219-32.

Petersen ET, Golay X Is Arterial Spin Labelling Ready for the Prime time? (2008). Prilimary Results from the QUASAR Reproducibility Study. Proceedings of the 16th Annual Meeting of ISMRM, Toronto, Cananda, 2008 (Abstract 191)

Stanitz GJ, Odrobina EE, Pun J, Escaravage M, Graham SJ, Bronskill MJ, Henkelman RM.(2005). T1, T2 relaxation and magnetization transfer in tissue at 3T. Magnetic Resonance in Medicine 54, 507-12

Thomas DL, Lythgoe MF, Calamante F, Gadian DG, Ordidge RJ (2001) Simultaneous non-invasive measurement of CBF and CBV using double-echo FAIR (DEFAIR). Magnetic Resonance in Medicine 45, 853-63

Utting JF, Thomas DL, Gadian DG, Ordidge RJ. (2003). Velocity-driven adiabatic fast passage for arterial spin labelling: results from a computer model. Magnetic Resonance in Medicine 49, 398-401

Vazquez AL, Fukuda M, Kim S. (2009). Changes in arterial oxygen tension with evoked stimulation in the rat somato-sensory contex; Implications for quantitative fMRI. 17th annual ISMRM Hawaii. Abstract no. 217

Villringer A, Them A, Lindauer U, Einhaupl K, Dirnagl U. (1994). Capillary perfusion of the rat brain cortex. An in vivo confocal microscopy study. Circulation Research 75, 55-62

Zhao JM, Clingman CS, Narvainen MJ, Kauppinen RA, van Zijl PCM (2007) Oxygenation andHematocrit Dependence of Transverse Relaxation Rates of Blood at 3T. Magnetic Resonance in Medicine 58, 592-596

APPENDIX A: THE DISCRETE DISTRIBUTION OF TRANSIT TIME ESTIMATES

A1. INTRODUCTION

We encountered unexpected results when implementing multiple fits of noisy data to Alsop's standard CBF quantification model [Alsop and Detre, 1996].

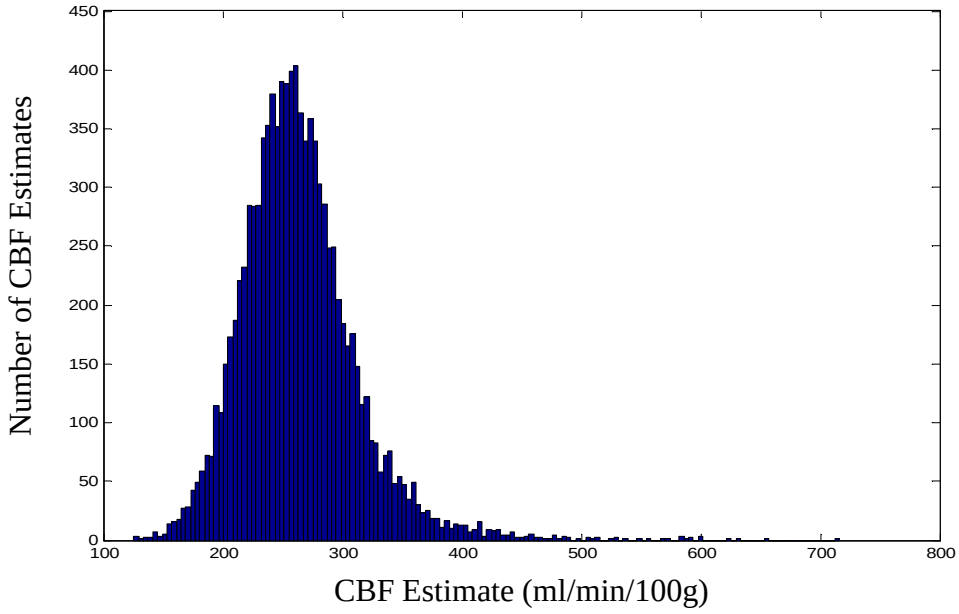

Figure A1
The distribution of CBF estimates calculated from the simulated data with a SNR_{pwi} of 2.

The distribution of CBF values appears to be approximately Gaussian about the true CBF of 250ml/100g/min. However closer visual inspection suggestions it is skewed towards greater CBF values. Initially we hypothesised that this was a result of the documented bias behaviour of the estimates of non-linear models as previously described; why we see an overall increase in the apparent CBF with random errors. However the distribution of the δa estimates (Figure A2) is curious and likely provides an additional explanation for the observed bias of the CBF estimates.

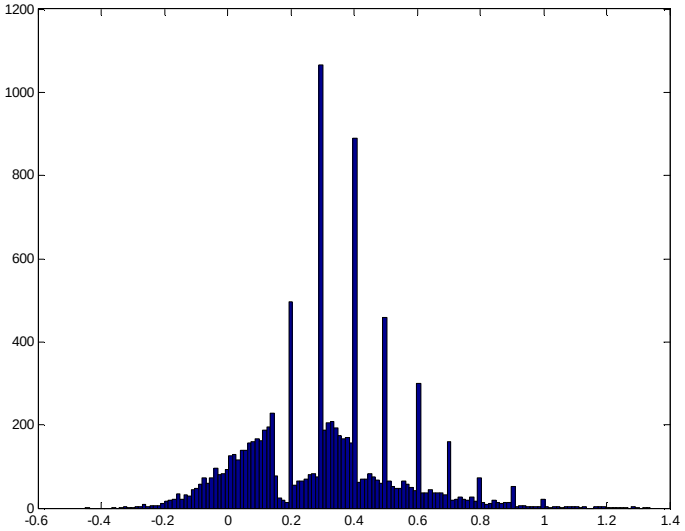

Figure A2
The distribution of δa estimates calculated from the simulated data with a SNR_{pwi} of 2.

Many of the *δa* estimates are falling on the exact discrete PLD times at which the ASL signal is measured. Our initial explanation of this unexpected behaviour was "non-convergence" of the fitting procedure. If this was the case then this would have a significant influence on the resultant CBF and *δa* distributions. In chapter 3, we examine the extent of any bias present in the CBF estimates. It was therefore imperative to ensure that any measured bias was not dominated by errors in the fitting procedure.

In appendix A2 we examine the possibility of non-convergence and propose an explanation for the discrete nature of the *δa* estimates.

A2. ASSESSING CONVERGENCE

Fits were performed using the MatLab 6.5 curve fitting toolbox functions. The first step was to examine the response of the fitting algorithm itself. The fitting algorithms can be implemented to "flag" whether the function has converged to a solution. This parameter indicated that convergence was achieved for each one of the simulated and *in-vivo* time-courses. Convergence was checked in this way for all the fits to the simulated and *in-vivo* data.

The non-linear-least-squares fitting algorithm aims to find the best model fit to the data by minimising the squared residuals. However it was possible that the fitting algorithm was stuck in a local minimum. This would perhaps explain why the δa estimates were falling on the discreet values of the PLD at which the signal is sampled, while the function was apparently converging. Therefore to check that the fitting algorithm was indeed converging on the CBF and δa that resulted in the least squared residuals, I took the following steps:

A simulated data set was generated with a true CBF of 250ml/100g/min and an arterial transit time of 0.3s at the same PLDs used in the *in-vivo* analyses (0.15,0.2,0.3,0.4,0.5,0.6,0.7,0.8,0.9,1,1.5,2). Gaussian noise was then added to the data for a SNR of 5. These data are referred to as the noisy time-course.

CBF and δa estimates were then generated by fitting the noisy time-course to the model as before using the Marlab curve-fitting toolbox functions. Several alternate time-courses with a range of δa and CBF values were then generated. For each of these time-courses, the mean squared difference between the noisy time-course and each time-course with different CBF and δa values (without any added noise) was calculated. Figure A3 shows an example surface plot of the mean squared difference between the noisy data and each of the time courses with different CBF (x-axis) and δa values (y-axis). The minimum mean squared difference occurs when δa is equal to exactly 0.2s which is different to the true δa that was originally defined (0.3s). Fitting the noisy-time course to the fitting algorithm returns the same δa value (0.2s).

This process was repeated over a range of noisy-time courses and in each case, the CBF and δa estimates generated using the two approaches were in good agreement with the exception of when the δa value that the fit returns is less than the minimum PLD time (see A4 *The Problem when δa estimate < 0.15s (the minimum PLD time*))

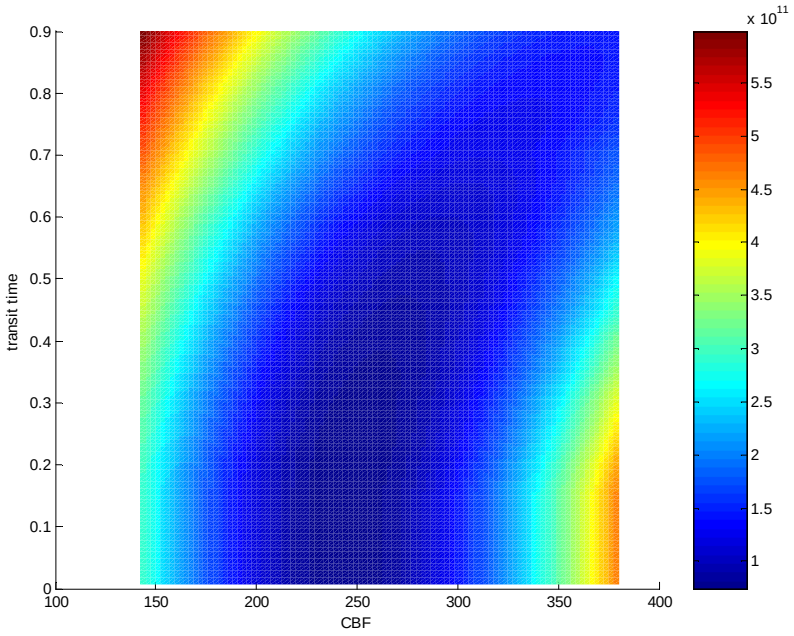

Figure A3
Surface plot showing the mean squared difference between a simulated noisy time-course and the modelled time-courses with different CBF (x-axis) and δa (y-axis) values.

These calculations provided convincing evidence that the fits were indeed converging to the minimum squared residual. Therefore non-convergence was unlikely to be the reason for the tendency of the δa estimates to fall on the post-labelling delay at which the signal is sampled. The next section presents an explanation for this behaviour.

A3. AN EXPLANATION FOR THE DISCRETE NATURE OF THE ARTERIAL TRANSIT TIME ESTIMATES

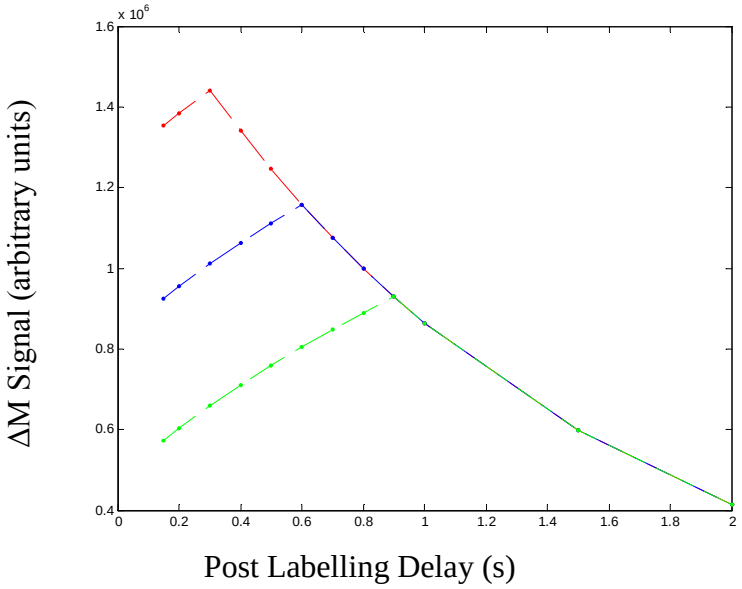

Figure A4

The CBF quantification model at a range of arterial transit times (δa = 0.3s [red], δa = 0.6s [blue], δa = 0.9s [green]).

Figure A4 shows the standard CBF quantification equation modelled at a range of arterial transit times. The apparent turning point is due to the "broken" behaviour of the function, namely the switching condition for when PLD > *δa*. This represents the point at which the tagged bolus of arterial blood has arrived in the region of interest. This demonstrates that the model is insensitive to the transit time when *δa* is less than the PLD at which the signal is sampled (with a fixed *δ*). Indeed this was one of the main "take home messages" in this paper: as long as the PLD is greater then *δa*, the measurement is relatively insensitive to the transit time. This property in combination with the limited number of PLD times at which inflow curve is measured can explain why the *δa* estimates are falling on the exact PLD times at which the perfusion weighted signal is measured.

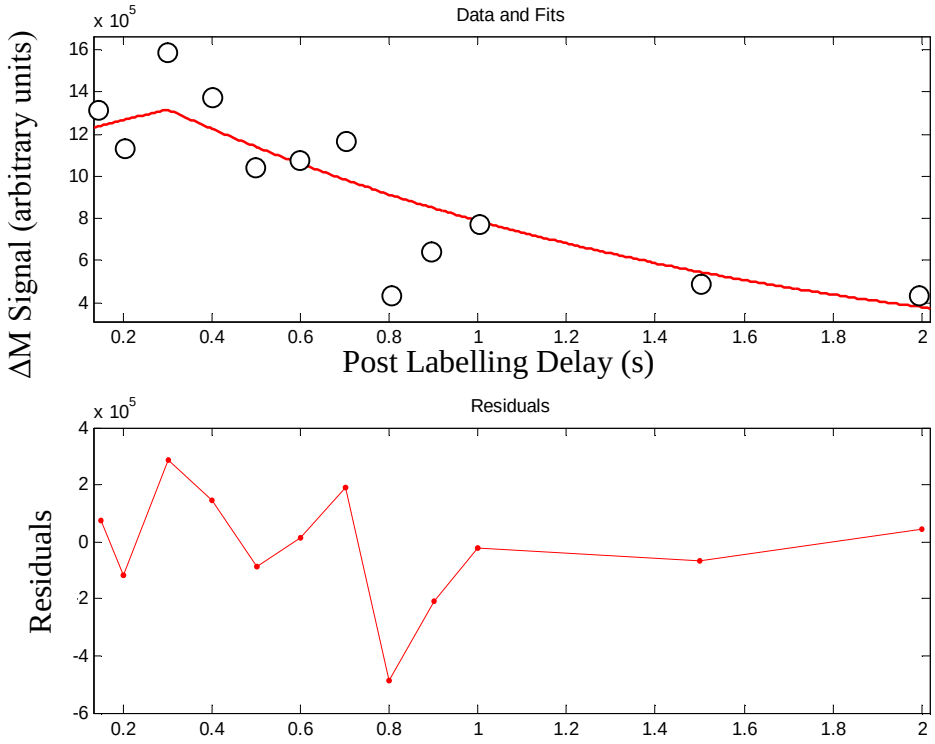

Figure A5

Noisy time-course (black circles) and resultant model fit to the data (red line). The residuals of the model fit to the data are also reported below. The fitted arterial transit time is exactly 0.3s.

Figure A5 shows a simulated multi-PLD CASL time-course with added zero mean Gaussian noise together with the model fit to the data. The model fit to the data yields a transit time of 0.3s – one of the PLD times at which the perfusion-weighted signal was sampled. An intuitive explanation for this behaviour is as follows:

Firstly the fitting algorithm estimates the CBF (which is a linear multiplying factor for all the ΔM values) to minimise the residuals of the fit. The algorithm then estimates the transit time for a given CBF that again minimises the residuals. The fitting algorithm computes the transit time to be at the most 0.3s. This is to minimise the residual at PLD = 0.3s. If the fitted transit time was greater than 0.3s then the residual at PLD = 0.3s would be increased for a given CBF but as long as it is equal to or less then 0.3s then this residual is the same. This is because the objective function is insensitive to δa as long as the PLD at which the signal is sampled is greater then δa as illustrated in Figure A4.

Now the fitting algorithm finds the transit time under the condition that δa <=0.3s that results in the best fit to the data by minimising the residuals at PLD = 0.15 and PLD = 0.2s. Because the noise has acted to considerably reduce the signal at PLD =0.2s then the model minimises the residual at PLD = 0.2s by taking the greatest δa it can up to 0.3s. Therefore the estimated transit time resides on exactly 0.3s. Further examples are displayed in Figure A6 and A7 where the true δa was set to 0.5s. Model fitting to the data reported in Figure A6 and A7 yields a δa of exactly 0.5s and 0.3s respectively. This can be explained using the same reasoning, behaviour which can be summarised as a consequence of the fitting a model that includes "switching functions" to noisy data, sampled at finite intervals. The use of fitting routines such as the "Trust Region algorithm" [Branch *et al*., 1999] is normally only intended in continuously differentiable functions, which is not the case here. Therefore although these findings are still relevant (as these fitting routines are commonly employed to model fit ASL timecourse data) it is important to note that these observations may not apply to alternative fitting routines.

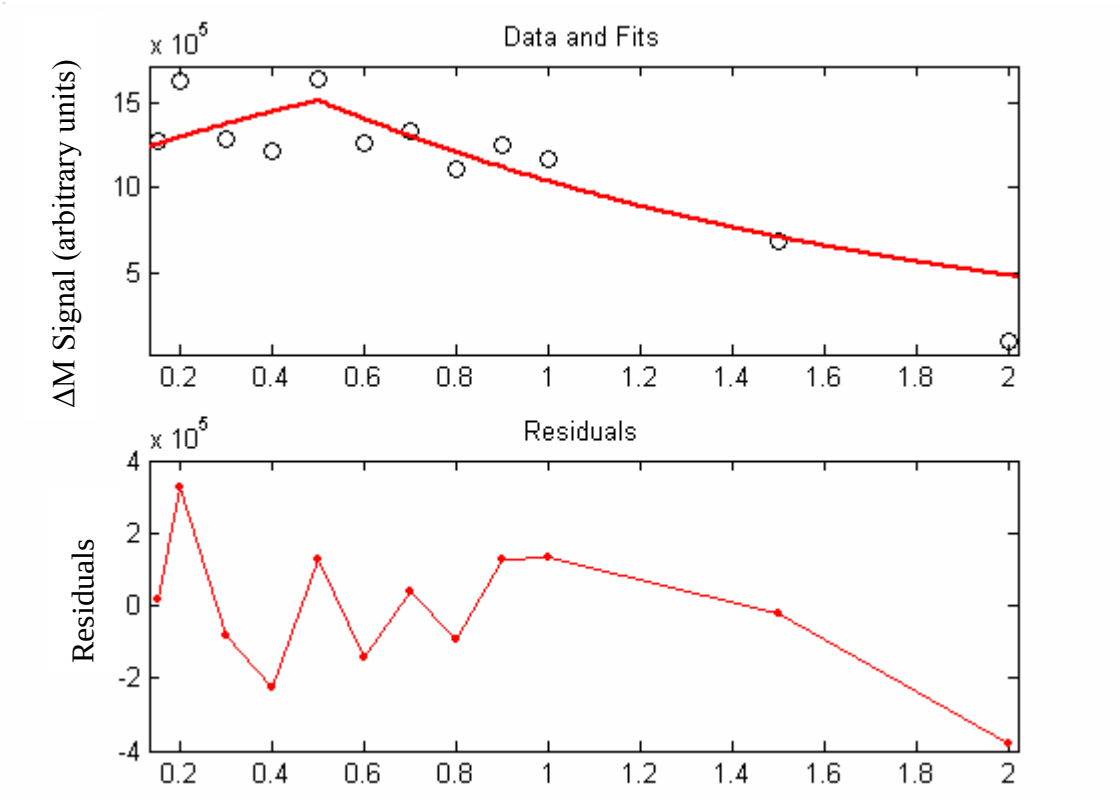

Figure A6

Noisy time-course (black circles) and resultant model fit to the data (red line). The residuals of the model fit to the data are also reported below. The fitted arterial transit time is exactly 0.5s.

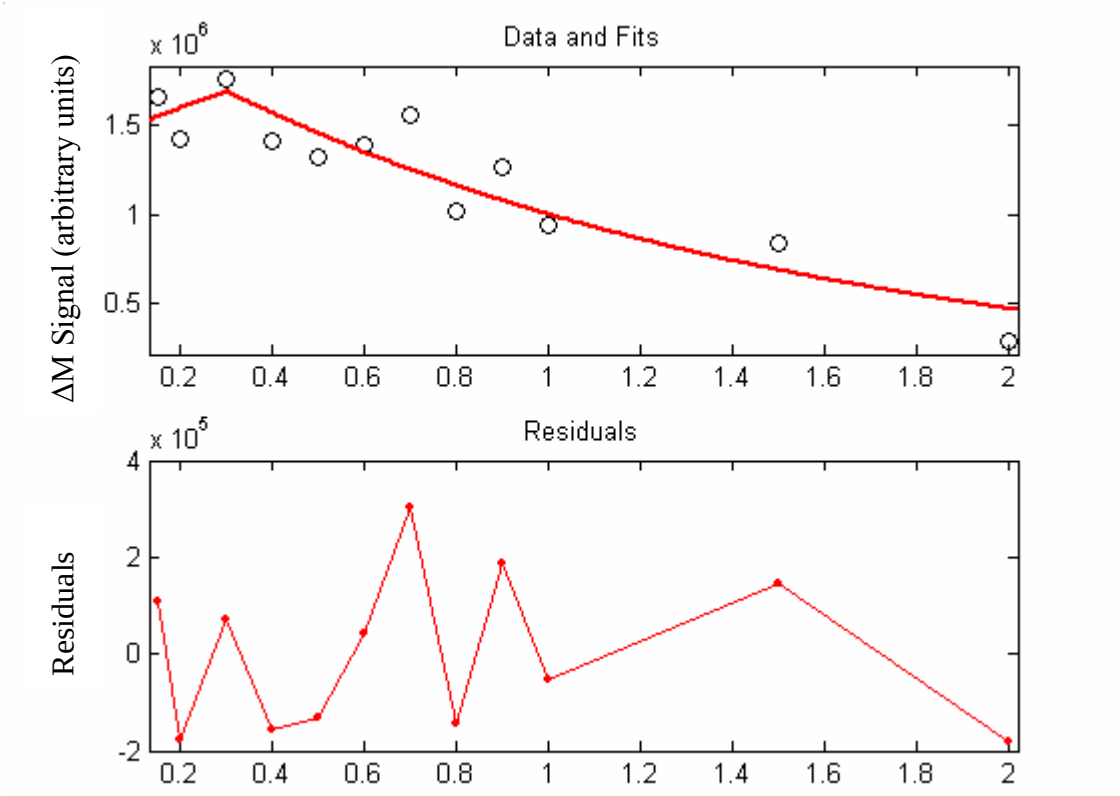

Figure A7

Noisy time-course (black circles) and resultant model fit to the data (red line). The residuals of the model fit to the data are also reported below. The fitted arterial transit time is exactly 0.3s.

A4.THE PROBLEM WHEN THE ARTERIAL TRANSIT TIME < THE MINIMUM PLD TIME.

If the best fit to the noisy data returns a transit time that is less than the minimum PLD at which the perfusion weighed signal is sampled (0.15s in the case of chapter 4) then the transit time cannot be estimated with precision any greater then between 0 (physiological limitations) and 0.15s. This is because changing the arterial transit time in this range has no effect on Alsop's model because the arterial transit time is only present in the following term:

$$\exp((\min(\delta a\text{-PLD},0)-\delta a).*\text{R1a})$$

Consequently, changing δa will have no effect on the resultant function if it is less than the minimum PLD. The minimum PLD in the experiments described in chapter 4 was

fixed at 0.15s. Therefore when the least square fit to the noisy data produces a δa which is less than 0.15 there is no way of estimating δa with any more precision. However this issue does not affect the distribution of the CBF estimates as changing δa in this range does not affect the resultant function. Therefore although we are not able to report the mean value of the δa estimates, the mean value of the CBF estimates has been reported to assess possible bias with the addition of Gaussian noise.

APPENDIX B: ESTIMATION OF $T2_{IC}$ AND $T2_{EC}$

B1 INTRODUCTION

In appendix B, I use a simple simulation, which mimics the experimental protocol described in chapter 2 to demonstrate the difficulty of fitting experimental data to a bi-exponential decay model (with no fixed parameters). I then continue to report the results of fitting the model to the *in-vivo* data acquired in Chapter 2.

B2 SIMULATIONS

The plot below (*Figure B1*) shows simulated data generated using the bi-exponential model described in Equation 2.2, at the same echo times as our study. 95 % of the simulated signal arises from the IC compartment ($T2_{IC}$ =57ms) and 5% from the EC compartment ($T2_{EC}$ = 174ms). A small degree of Gaussian noise is added to the simulated data to give a SNR at the first echo time (29ms) of 80 (in approximate agreement with the SNR of the control base images in our data). The simulated data are then fitted to the bi-exponential model described in Equation. 2.2 but in this case $T2_{IC}$ and $T2_{EC}$ are not fixed but are estimated in the fitting process. The model fit to the data is shown by the solid line:

.

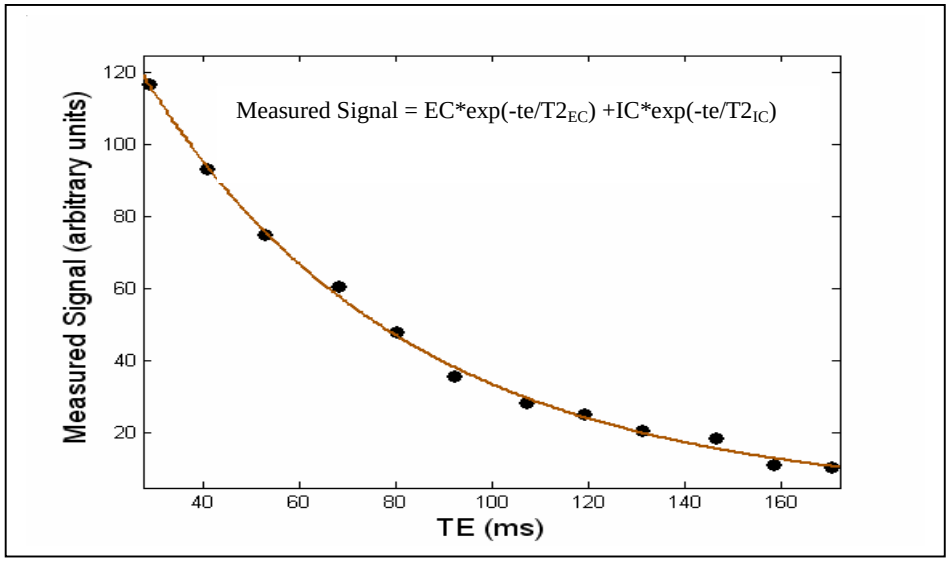

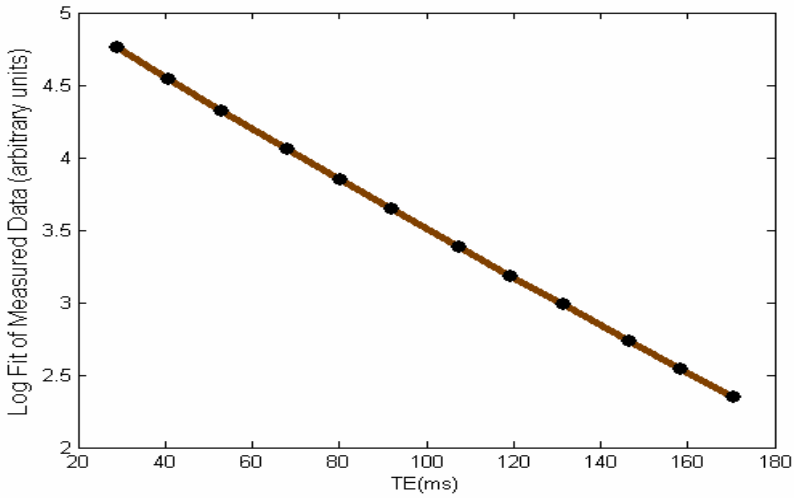

Figure B1

[a] Simulated bi-exponential transverse decay with a small degree of added Gaussian noise (black dots) together with the model fit to the data (solid line) at the echo times used in our study. [b] The log plot of the fit.

The model fit returns the following estimates of the 4 parameters (95% confidence intervals of the fit):

EC = 81.7 (-2176, 2339)
IC = 117 (-2099, 2333)
$T2_{EC}$ = 72.84 (-382.2, 527.9) ms

$T2_{IC}$ = 45 (-200.1, 290.1) ms
[R-square = 0.9977]

The inaccuracy and considerable uncertainty in the four parameter fit demonstrates the difficulty of using our data to estimate the $T2_{EC}$ and $T2_{IC}$. We could estimate $T2_{EC}$ and $T2_{IC}$ using our data but the precision of the fit would severely limit any interpretation of the values. We could impose fitting constraints; however in this case the estimated $T2_{EC}$ and $T2_{IC}$ will often fall on the upper or lower limit of these constraints making the resultant estimates dependent on the imposed limits.

However, if we assume the correct T2 values (as in the present analysis) then the fit returns EC and IC values with reasonable certainty:

EC = 6.6 (2.0, 11.2) ; IC = 189 (179, 198.9)

We have performed further simulations which suggest that it would require acquisitions at many more echo times and increased SNR in order to achieve reasonable precision in the $T2_{IC}$ and $T2_{EC}$ parameter estimates. For example, [Matsumae *et al.*, 2003] acquired data at 60 echo times with 100 averages. The estimates are very sensitive to physiological noise which may be why *ex-vivo* experiments were performed. The *ex-vivo* transverse relaxation studies also allowed measurements at very short echo times, improving the dynamic range of the measured transverse decay.

The plot below shows simulated data generated using the bi-exponential model at 60 echo times. 95 % of the simulated signal arises from the IC compartment ($T2_{EC}$ =57ms) and 5% from the EC compartment (EC = 174ms). A small degree of Gaussian noise is added to the simulated data to give a SNR at TE = 30ms of 250, reflecting the greater number of averages and reduced physiological noise of the *ex-vivo* acquisitions in their work [Matsumae *et al.*, 2003].

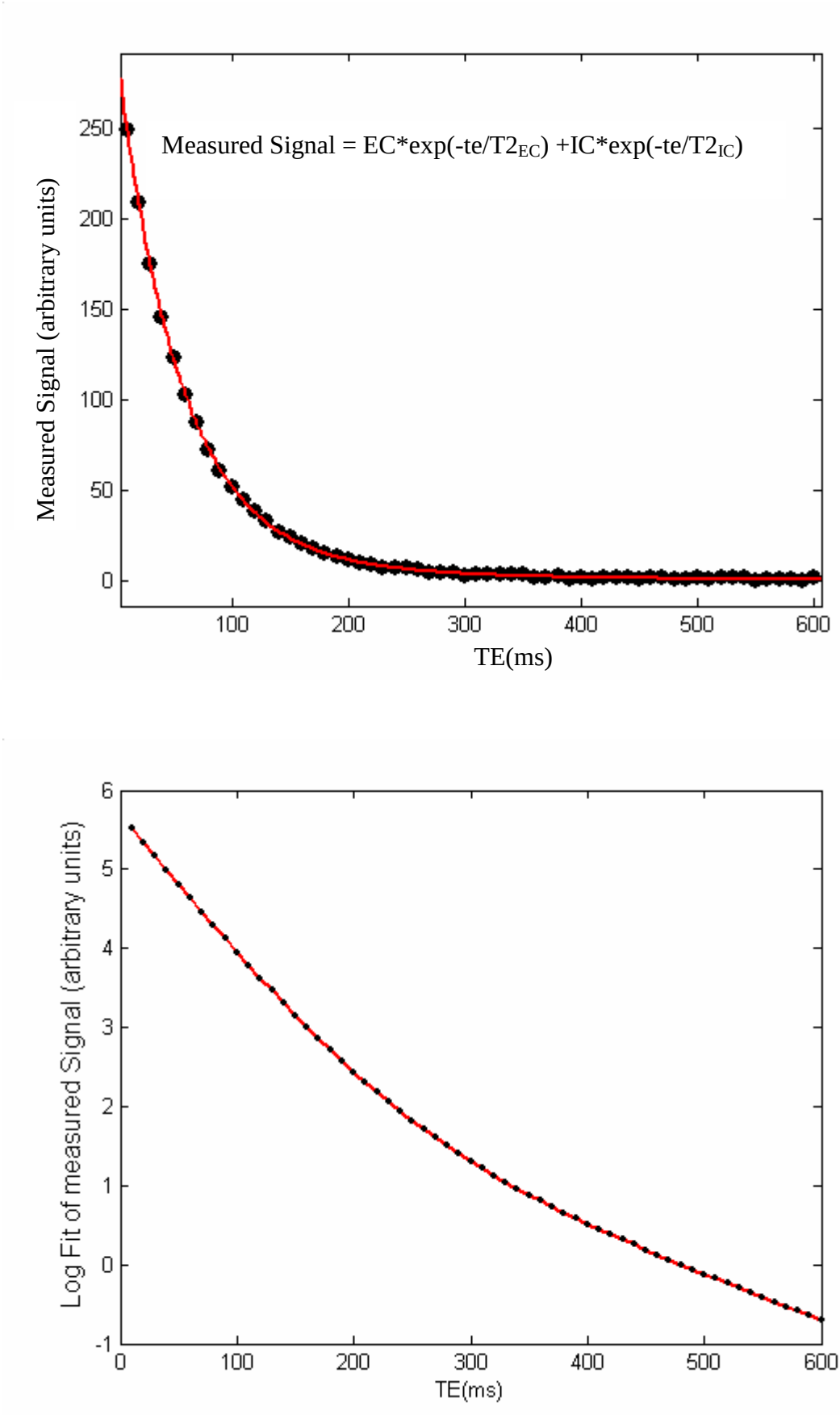
Measured Signal = EC*exp(-te/T2EC) +IC*exp(-te/T2IC)
Measured Signal (arbitrary units)
TE(ms)
Log Fit of measured Signal (arbitrary units)
TE(ms)

Figure B2

[a] Simulated bi-exponential transverse decay with a small degree of added Gaussian noise (black dots) together with the model fit to the data, based on the methodology proposed in [Matsumae et al., 2003].[b] The log plot of the fit.

EC = 14.23 (8.491, 19.97)
IC = 284.8 (279.7, 290)
$T2_{EC}$ = 178.3 (139.9, 216.7) ms
$T2_{IC}$ = 53.48 (52.42, 54.54) ms
[R-square: 0.9999]

Although the precision of the estimates is considerably improved, the 95% confidence intervals of the fit indicate that there is still some uncertainty in the estimates, even with such rigorous coverage of the transverse decay curve.

B3 *IN-VIVO* DATA

The results of simultaneously estimating $T2_{IC}$ and $T2_{EC}$ as well as the proportion of the signal originating from the two compartments (IC and EC) from our 9 *in-vivo* subjects (experiments) are presented in the table below. Also shown is an example of the fitted curve to one of the 9 data sets.

Measured mean cortical control signal (VCGs – on, τ=3000 , PLD = 1200s) =

$$IC\exp(-te/T2_{IC}) + EC\exp(-te/T2_{EC}) \qquad \text{(Eq. B1)}$$

Subject (Experiment) Number	IC (95% Confidence Interval) Arbitrary Units	EC (95% Confidence Interval) Arbitrary Units	$T2_{IC}$ (95% Confidence Interval) Ms	$T2_{EC}$ (95% Confidence Interval) ms
1	49.28 (-664.3, 762.9)	62.55 (-606.8, 731.9)	39.27 (-164.5, 243.1)	78.57 (-286.8, 444)
2	50 (-1.123e+004, 1.133e+004)	41.21 (-1.125e+004, 1.134e+004)	54.83 (-1457, 1567)	69.09 (-2051, 2189)
3	95.4 (-1566, 1757)	4.898 (-1678, 1688)	61.8 (-276.3, 399.9)	110.3 (-1.111e+004, 1.133e+004)
4	92.34 (-741.2, 925.9)	17.89 (-846.6, 882.3)	50.69 (-149.2, 250.6)	104.4 (-1723, 1932)
5	43.22 (-8.73e+007, 8.73e+007)	38.86 (-8.73e+007, 8.73e+007)	62.48 (-4.006e+004, 4.019e+004)	62.47 (-5.234e+004, 5.247e+004)
6	45.65 (-1.935e+008, 1.935e+008)	27.95 (-1.935e+008, 1.935e+008)	63.27 (-2.694e+007, 2.694e+007)	63.27 (-4.4e+007, 4.4e+007)
7	103.1 (-87.22, 293.4)	0.8296 (-203.4, 205.1)	63.11 (-23.71, 149.9)	250 (-5.766e+004, 5.816e+004)
8	50.18 (-3.965e+007, 3.965e+007)	37.18 (-3.965e+007, 3.965e+007)	61.98 (-4.713e+005, 4.715e+005)	61.1 (-3.461e+005, 3.462e+005)
9	97.13 (-434, 628.3)	A = 3.929 (-550.8, 558.6)	56.41 (-104.2, 217)	137.7 (-9272, 9547)

Table B1

Table 1 shows the results of fitting the mean control perfusion weighted signal (acquired with vascular crusher gradients (VCGs) at tagging duration (τ) = 3000ms and post labelling delay (PLD) = 1200ms) to a bi-exponential model whilst simultaneously fitting for all four unknown variables (IC, EC, $T2_{IC}$, $T2_{EC}$).

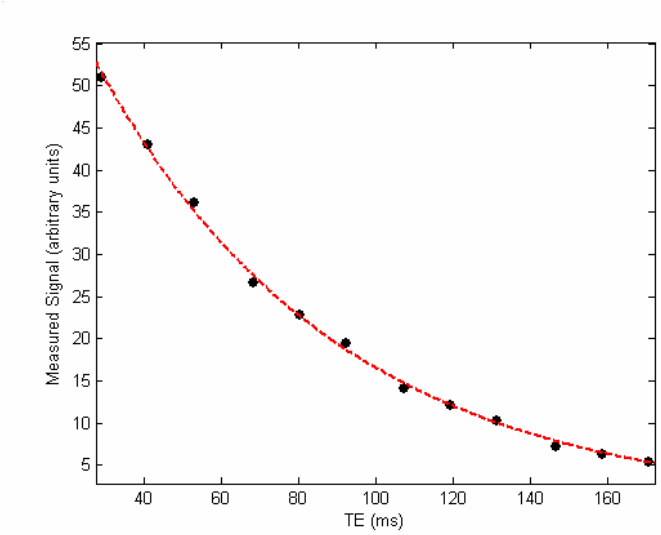

Figure B3

The transverse decay of the mean control signal (VCGs on, τ=3000ms, PLD = 1200ms) from subject no. 6 as a function of echo time (black dots) together with the model fit to the data (red dashed line)

Unfortunately, the huge 95% confidence intervals of the fitted parameters demonstrate that the precision of the $T2_{EC}$ and $T2_{IC}$ values is limited to the extent that it would be almost meaningless to take $T2_{EC}$ and $T2_{IC}$ estimates from our data. This does not reflect systematic errors in our measurements (as highlighted by the simulations described above in B1) but rather the need for much more rigorous coverage of the transverse decay curve and higher SNR to precisely estimate the four parameters simultaneously.

Therefore we took values from previous studies that were specifically designed to estimate $T2_{IC}$ and $T2_{EC}$ with some precision [Haida *et al.*, 1987; Matsumae *et al.*, 2003].